The Dissertation Committee for Kirsten Viering
certifies that this is the approved version of the following dissertation:

Experiments to Control Atom Number and Phase-Space Density in Cold Gases

Committee:

Mark G. Raizen, Supervisor

Arno Boehm

Paul Shapiro

Chih-Kang Shih

George Shubeita

Experiments to Control Atom Number and Phase-Space Density in Cold Gases

by

Kirsten Viering, M.A.

DISSERTATION

Presented to the Faculty of the Graduate School of

The University of Texas at Austin

in Partial Fulfillment

of the Requirements

for the Degree of

DOCTOR OF PHILOSOPHY

THE UNIVERSITY OF TEXAS AT AUSTIN

August 2012

For Adam

Acknowledgments

First of all, I would like to thank my advisor Mark Raizen. Mark approaches physics with great excitement and his intuition for interesting experiments is exceptional. I am immensely grateful for all the support he provided over the years. It has been a great privilege working in his lab.

Experimental research is a collaborative effort, and it has been my pleasure to work with a number of bright and enthusiastic people on a variety of experiments. For the first part of my PhD I worked with Gabriel Price and Travis Bannerman on the rubidium single-photon cooling experiment. Both are very knowledgeable experimental physicists, and it was a great experience working with them.

After shutting down the rubidium experiment I joined Hrishikesh Kelkar, Tongcang Li and David Medellin on the sodium experiment. Hrishi is amazingly friendly and impressively patient. Tongcang is an incredible bright physicist and I am sure that he will come up with many more amazing experiments in the future.

My final project in the lab was done in collaboration with David Medellin and Jianyong Mo, who joined the lab just when we started the lithium experiment. David's knowledge of mathematics and physics theory is very impressive and was invaluable for our work. Jianyong has shown great enthusiasm throughout every single stage of the experiment. Both David and Jianyong are very hardworking and I am confident that they will produce many exciting results with the lithium setup.

I would like to thank Adam Libson for all his love and support, inside and outside the lab. I am looking forward to starting the rest of my life with him.

I also want to thank all the other students and postdocs who contributed to making this such an enjoyable PhD time. Everybody always seems willing to help one another and the diversity and combination of personalities has made the Raizen lab a great place to work. I therefore thank Ed Narevicius, Charlotte Sanders, Tom Mazur,

Isaac Chavez, Melissa Jerkins, Simon Kheifets, Akarsh Simha, Rodrigo Castillo-Garza, Bruce Klappauf, Jamie Gardner, Rob Clark, Christoph Schaeff, Christian Parthey and Maria Becker.

During my time as a PhD student I also had the opportunity to work a few months with Professor Selim Jochim's group at the Max-Planck-Institute for Nuclear Physics in Heidelberg, Germany. Selim's enthusiasm for his work was truly inspiring and was echoed by the interactions I had with the members of his group: Timo Ottenstein, Thomas Lompe, Gerhard Zuern, Friedhelm Serwane, Martin Ries and Philipp Simon. I am truly grateful for the knowledge and experience I gained during those few months.

I would also like to thank the administrative staff of the Center for Nonlinear Dynamics, Olga Vera, Marybeth Casias and Elena Simmons, for all their help during these years. I am very grateful towards Allan Schroeder and the physics machine shop who did a terrific job with all the machining projects we had. Without this resource much of this work would not have been possible. Lanny Sandefur and Ed Baez have provided excellent support in the cryogenics shop. I would also like to thank Jack Clifford for all the help he provided in the student machine shop.

Ein ganz besonderer Dank geht auch an meine Familie, die mich immer ermutigt hat meinen eigenen Weg zu gehen. Die Gewissheit, dass sie mich immer unterstuetzen wird, ist unbezahlbar.

I am also grateful to have the support from my new family.

Kirsten Viering

Experiments to Control Atom Number and Phase-Space Density in Cold Gases

Kirsten Viering, Ph.D.
The University of Texas at Austin, 2012

Supervisor: Mark G. Raizen

This dissertation presents the development and implementation of two novel experimental techniques for controlling atom number and phase-space density in cold atomic gases.

The first experiment demonstrates the method of single-photon cooling, an optical realization of Maxwell's demon, using an ensemble of rubidium atoms. Single-photon cooling increases the phase-space density of a cloud of magnetically trapped atoms, reducing the entropy of the ensemble by irreversibly transferring atoms through a one-way wall via a single-photon scattering event. While traditional laser cooling methods are limited in their applicability to a small number of atoms, single-photon cooling is much more general and should in principle be applicable to almost all atoms in the periodic table. The experiment described in this dissertation demonstrates a one-dimensional implementation of the cooling scheme. Complete phase-space compression along this dimension is observed. The limitations on the cooling performance are shown to be given by trap dynamics in the magnetic trap.

The second part of this dissertation is dedicated to the experiment built to control the atom number of a degenerate Fermi gas on a single particle level. Creating Fock states of atoms with ultra-high fidelity is a mandatory step for studying quantum entanglement on a single atom level. The experimental technique implemented to control the atom number in this experiment is called laser culling. Decreasing the trapping potential reduces the atom number in a controlled way, giving precise control over the number of atoms remaining in the trap. This dissertation details the design and construction

of this experiment and reports on the progress towards the creation of neutral lithium Fock states.

Table of Contents

List of Tables

List of Figures

Chapter 1

Introduction

Atomic physics is the study of the atomic energy level structure and of atomic interactions with other particles, external magnetic fields, and external electric fields. It has also been a testing ground for theories of quantum mechanics. As such, it is a research field with a long tradition.

One could argue that modern atomic physics started with J.J. Thomson's discovery of the electron [1]. Ernest Rutherford, and the discovery of atomic structure consisting of a nucleus surrounded by a cloud of orbiting electrons, was the next step only a few years later [2]. Max Planck's postulate of energy quantization of oscillators in a black body, and Niels Bohr's model of the atomic nucleus surrounded by electrons moving in circular orbits were the first attempts to explain quantum phenoma such as the spectral emission lines of hydrogen in terms of the underlying atomic structure [3, 4]. In the following years of the early 20th century many exciting discoveries were made and theories developed, including work by Einstein and deBroglie, ultimately leading to the development of quantum mechanics by Heisenberg, Schrödinger and others.

Even though much progress in the understanding of atomic structure was made during the mid 20th century, the experimental techniques used in this dissertation were not developed until the 1980s, when William Phillips, Harold Metcalf and co-workers developed the Zeeman slower to reduce the velocity of an effusive atomic beam [5–7]. Following this development was the experimental realization of optical molasses and magneto-optical trapping in 1987 [8], work for which Steven Chu was awarded the nobel prize in 1997, together with Claude Cohen-Tannoudji and William Phillips. These are still the standard techniques used today to cool and trap neutral atoms, and they have led to the realization of Bose-Einstein condensates [9–11] and degenerate Fermi gases [12–14].

The development of techniques to laser-cool atoms has enabled many interesting studies based on the ability to control temperature and internal states of trapped atomic ensembles. Their applicability, however, is restriced to a limited number of atoms, mostly the alkaline atoms. By gaining a similar amount of control over all atomic species new fundamental research relying on properties specific to each atom becomes feasible. For example, measuring the isotopic shifts in hydrogen with an increased precision would provide further testing ground for theories of nuclear few-body systems. Cooled atomic ensembles of deuterium and tritium could potentially lead to such improved measurements.

Moreover, in general, the number of atoms in an atomic ensemble is subject to Poissonian fluctuations and is not controllable in standard cold gases experiments. The atom number, however, is an important parameter in many interesting quantum-mechanical systems. Precise control of the number is required for studying phenomena like quantum entanglement and for understanding the physics of cold atomic collisions. Control of the atom number is therefore mandatory for quantum simulation and quantum computing experiments.

This dissertation presents two techniques that allow for general control of phase-space density and atom number in cold atomic gases; single-photon cooling and laser culling. Chapter 2 summarizes the basic theory of atomic interactions with external fields and introduces standard atomic physics techniques as far as they pertain to the experiments described in this dissertation. Chapters 3, 4, and 5 describe the technique of single-photon cooling, the experimental apparatus used for the implementation using rubidium, and the results of the proof-of-principle experiment.

The method of laser culling paves the way towards studying trapped samples with a defined number of atoms by offering the ability to control the number of atoms down to a single atom level. Chapter 6 introduces the general idea of laser culling. Chapter 7 summarizes the experimental apparatus built for a laser culling experiment of a trapped sample of fermionic lithium, and chapter 8 outlines the progress made towards creating Fock states of neutral atoms.

Chapter 2

Cold Atomic Gases

This dissertation is ultimately about atomic cooling, trapping, and the manipulation of cold atomic ensembles. This chapter addresses the standard experimental techniques used in cold atom experiments as well as the fundamental physical interactions between atoms and electromagnetic fields relevant to these techniques.

2.1 ^{87}Rubidium

Rubidium (Rb), being an alkali metal, has only one electron in the valence shell. This common feature in alkali atoms gives rise to a relatively simple energy level structure and makes alkali atoms a popular choice for cold atom experiments. The most abundant natural isotope of rubidium is ^{85}Rb (nuclear spin $I = 5/2$), with a natural abundance of 72.17(2)%. The work in this dissertation however was performed using ^{87}Rb (nuclear spin $I = 3/2$). ^{87}Rb has a half-life time of about 4.88×10^{10} years and a natural abundance of 27.83(2)%. Rubidium melts at 312.46 K and boils at 961.15 K [15].

The vapor pressure of rubidium is an important parameter for the experiment. Fortunately the vapor pressure of rubidium is high enough that atoms can be trapped directly from the background pressure. The vapor pressure P_v in torr for solid Rb is given in [16] by

$$log_{10} P_v = 2.881 + 4.857 - \frac{4215}{T}, \tag{2.1}$$

where T is the temperature in Kelvin. Figure 2.1 shows the vapor pressure of solid rubidium.

Some important physical properties of ^{87}Rb are summarized in table 2.1. A more complete summary of the properties of ^{87}Rb can be found in [17].

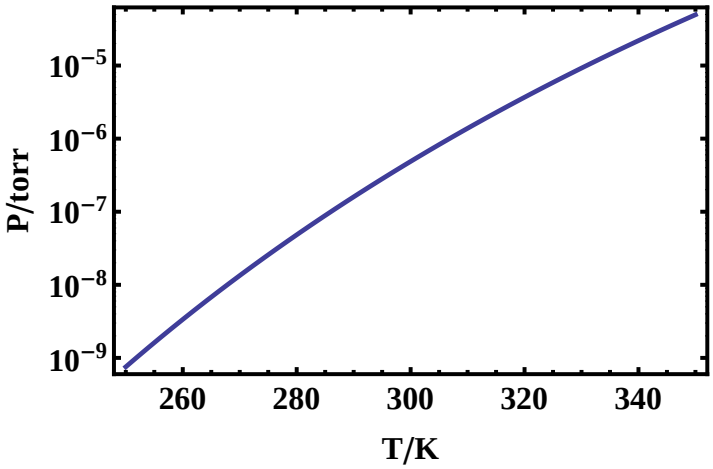

Figure 2.1: Vapor pressure of solid rubidium as a function of temperature.

Property	Symbol	Value	Reference
Atomic numer	Z	37	
Nucleons	Z+N	87	
Natural abundance	η	27.83(2)%	[15]
Atomic mass	m	86.909180 u 1.443160×10^{-25} kg	[18]
Nuclear spin	I	3/2	
Electronic spin	S	1/2	

Table 2.1: Physical properties of ^{87}Rb

2.2 ^{6}Lithium

Lithium is the lightest of the alkali atoms. It has three electrons, one being unpaired in the outer shell. There are two naturally abundant isotopes of lithium, fermionic ^{6}Li (nuclear spin $I = 1$) and bosonic ^{7}Li (nuclear spin $I = 3/2$). The natural abundance of ^{6}Li is approximately 7.6%. The melting point of lithium is 453.69 K; the boiling point lies well above all relevant temperature scales of this work at 1615 K [15].

The vapor pressure of lithium is an important parameter for the experiment. In the solid and liquid phases the vapor pressure is given by [19]

$$\log_{10} P_{Vsol} = -54.87864 - \frac{6450.944}{T} - 0.01487480T + 24.82251 \log_{10} T \quad (2.2)$$

$$\log_{10} P_{Vliq} = -10.34540 - \frac{8345.574}{T} - 0.00008840T - 0.68106 \log_{10} T. \quad (2.3)$$

A plot of the vapor pressure in the liquid phase is shown in figure 2.2.

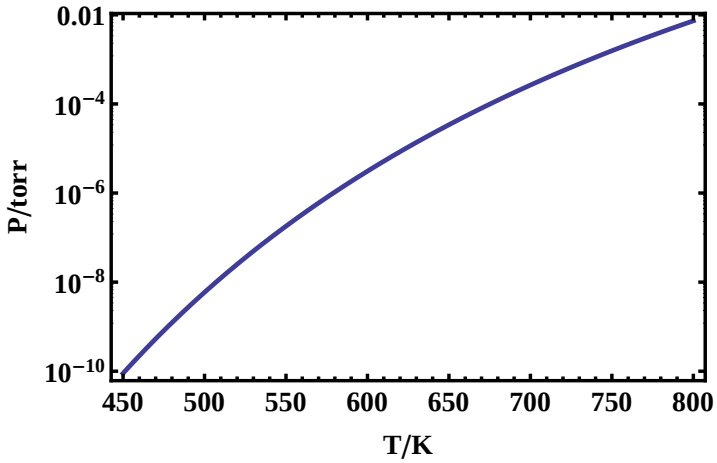

Figure 2.2: Vapor pressure of liquid lithium as a function of temperature.

The work in this dissertation is entirely performed using ^{6}Li, and thus all properties given relate to this isotope. Table 2.2 summarizes some important physical properties. A more comprehensive summary of physical properties is given in [20].

Property	Symbol	Value	Reference
Atomic numer	Z	3	
Nucleons	Z+N	6	
Natural abundance	η	7.6%	[15]
Atomic mass	m	6.0151214 u $9.9883414 \times 10^{-27}$ kg	[21]
Nuclear spin	I	1	
Electronic spin	S	1/2	

Table 2.2: Physical properties of ^{6}Li

2.3 Fine and Hyperfine Structure

Even in the absence of any external electromagnetic fields, interactions between the subatomic particles within the atoms will give rise to a splitting of the energy levels. Relativistic energy corrections, spin-orbit coupling and the Darwin term give rise to the fine-structure. The interaction between the nuclear spin I and the electron angular momentum J leads to the hyperfine structure. More detail on these interactions is given in the following sections.

2.3.1 Fine Structure

Alkali atoms have a single unpaired electron in the valence shell. The ground and first excited state configurations for lithium are $1s^2 2s^1$ and $1s^2 2p^1$ respectively. For rubidium the ground state configuration is $[Kr]5s^1$ and $[Kr]5p^1$ describes the excited state. The transition between these two states is usually called the D-line. This is the energy level structure one derives from the central potential (spin-independent) approximation.

Relativistic energy corrections, spin-orbit coupling, and the Darwin term lead to an energy splitting called fine-structure. The Hamiltonian describing the interaction between the orbital angular momentum $\vec{L}$ and the spin angular momentum $\vec{S}$ can be written as [22–25]

$$H_{fs} = A\,\vec{L} \cdot \vec{S}, \tag{2.4}$$

where A is the constant parameterizing the strength of the interaction. The coupling

of the two angular momenta can be expressed by the total electron angular momentum $\vec{J} = \vec{L} + \vec{S}$. Noting that

$$J^2 = S^2 + L^2 + 2\,\vec{L} \cdot \vec{S} \tag{2.5}$$

the fine structure Hamiltonian (2.4) can be rewritten as

$$H_{fs} = \frac{A}{2}(J^2 - L^2 - S^2). \tag{2.6}$$

The energy-splitting due to the fine structure can be treated as a perturbation to the central potential approximation. The difference in the energy levels is hence given by

$$\Delta E = \frac{\hbar A}{2}[J(J+1) - S(S+1) - L(L+1)]. \tag{2.7}$$

The resulting energy level structure and configurations for the cases of ^{87}Rb and ^{6}Li are shown in figure 2.3. The coupling of the angular momenta leads to $J = 1/2$ for the ground state and $J = 1/2$ or $J = 3/2$ for the excited state.

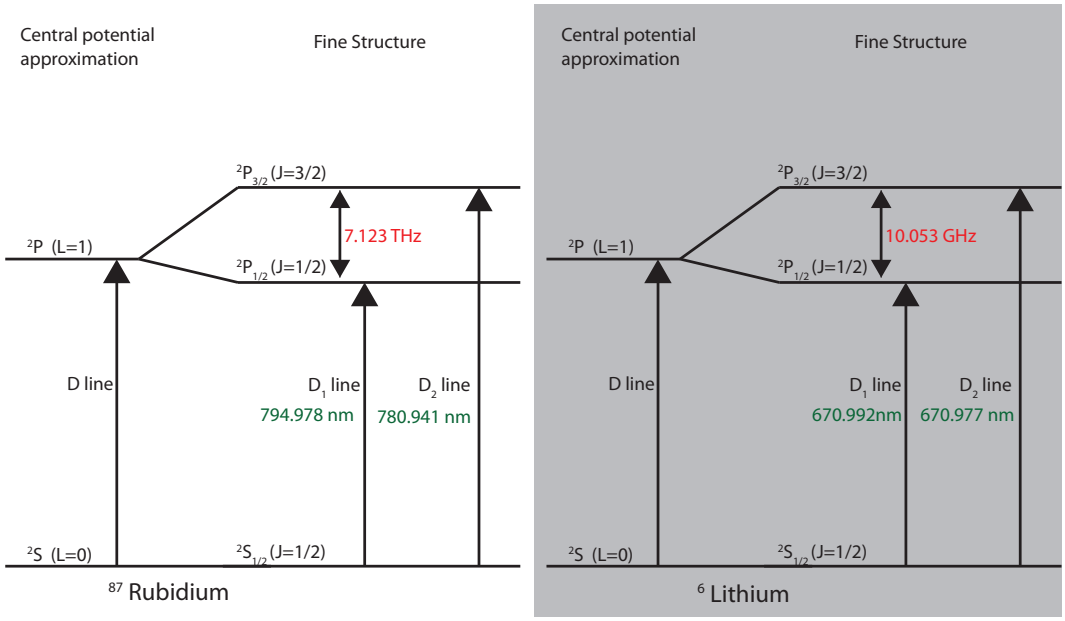

Figure 2.3: Ground and first excited states of ^{87}Rb and ^{6}Li in the central potential and fine structure approximations. Energy splittings are not to scale.

The D-line transition is split into two separate lines, called the D_1 and D_2line. The D_2-line transition is the transition relevant to the experiments described in this dissertation.

2.3.2 Hyperfine Structure

So far the analysis has neglected the interaction with the total angular momentum I of the nucleus. This interaction is significantly smaller than the fine structure interaction; however, it is still possible to observe the hyperfine structure in many atomic transitions, as for example in ^{87}Rb. For the case of ^{6}Li however, the hyperfine structure can only be resolved in the ground state, not in the $2^2P_{3/2}$ excited state, where the linewidth of the transition is larger than the hyperfine splitting.

The Hamiltonian describing the hyperfine interactions, including the magnetic dipole moment and the electric quadrupole moment of the nucleus, is given by [25]

$$H_{hfs} = A_{hfs}\,\vec{I}\cdot\vec{J} + B_{hfs}\,\frac{3(\vec{I}\cdot\vec{J})^2 + \frac{3}{2}(\vec{I}\cdot\vec{J}) - I(I+1)J(J+1)}{2I(2I-1)J(2J-1)}. \tag{2.8}$$

A_{hfs} is the magnetic dipole constant, B_{hfs} is the electric quadrupole constant. Defining the total atomic angular momentum $\vec{F} = \vec{I} + \vec{J}$ leads to the following solution for the energy splitting

$$\Delta E_{hfs} = \frac{1}{2}A_{hfs}\,K + B_{hfs}\,\frac{\frac{3}{2}K(K+1) - 2I(I+1)J(J+1)}{4I(2I-1)J(2J-1)}, \tag{2.9}$$

where $K = F(F+1) - I(I+1) - J(J+1)$. The resulting energy structure is shown in figures 2.4 and 2.5. The difference in the magnitude of the hyperfine splitting, especially in the $^2P_{3/2}$ excited state, has large consequences for the experimental sequence and absorption imaging in particular (see chapter 7.5.1).

2.4 Branching Ratios

Transitions between different energy levels are governed by electric dipole transition rules. The relative probabilities for the different decay channels from the excited state are known as branching ratios. Traditional laser cooling techniques, like the magneto optical trap, see chapter 2.9, work best on a true two-level atom, and any additional decay channels complicate the experimental setup, effectively limiting the applicability to a small number of elements. For single-photon cooling on the other hand, having at least three energy levels is essential. The branching ratios have a large effect on the efficiency of single-photon cooling, see chapters 3 and 5.

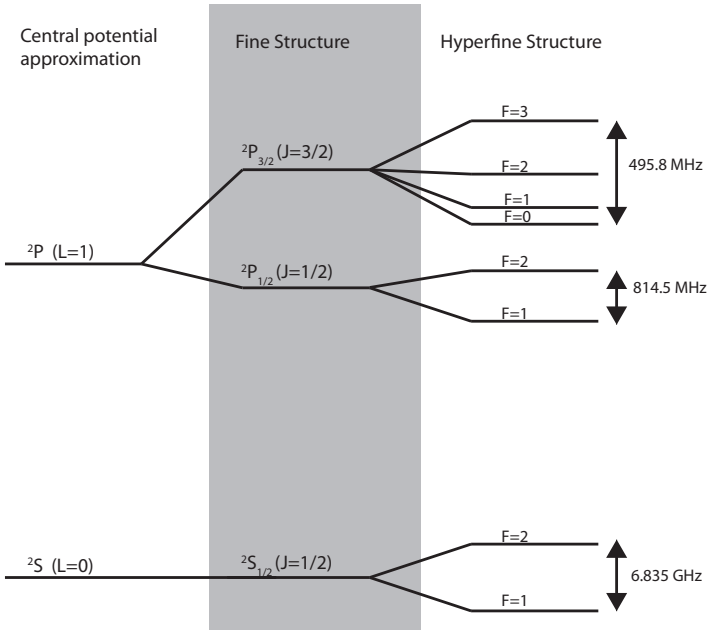

Figure 2.4: Central potential approximation, fine, and hyperfine structure of ^{87}Rb. Energy splittings are not to scale.

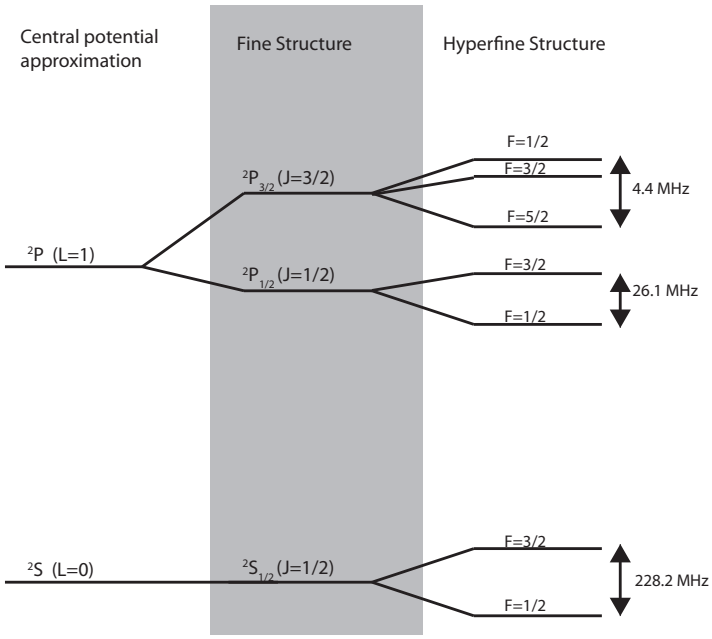

Figure 2.5: Central potential approximation, fine, and hyperfine structure of ^{6}Li. Energy splittings are not to scale.

The Wigner-Eckhart theorem can be used to determine the relative strength of each of the allowed transition by reducing the transition matrix element [26],

$$\langle F, m_F|\mu_q|F', m_{F'}\rangle = \langle F||\mu||F'\rangle(-1)^{F'-1+m_F}\sqrt{2F+1}\begin{pmatrix} F' & 1 & F \\ m_{F'} & q & -m_{F'}\end{pmatrix}, \quad (2.10)$$

where $|F, m_F\rangle$ ($|F', m_{F'}\rangle$) are the ground (excited) state hyperfine quantum numbers, μ_q is the component of the spherical electric dipole operator for polarization q and the quantity in parentheses is known as the Wigner 3-j symbol. Applying the Wigner-Eckhart theorem again, the transition matrix element reduces even further to

$$\langle F||\mu||F'\rangle = \langle J||\mu||J'\rangle(-1)^{F'+J+1+I}\sqrt{(2F'+1)(2J+1)}\begin{Bmatrix} J & J' & 1 \\ F' & F & I\end{Bmatrix}, \quad (2.11)$$

with the use of the Wigner 6-j symbol.

The matrix element $\langle J||\mu||J'\rangle$ can be determined experimentally by measuring the transition frequency and the lifetime of a given transition, where

$$\frac{1}{\tau} = \frac{\omega^3}{3\pi\epsilon_0\hbar c^3}\frac{2J+1}{2J'+1}\left|\langle J||\mu||J'\rangle\right|^2. \quad (2.12)$$

Values of $\langle J||\mu||J'\rangle$ for ^{87}Rb and ^{6}Li can be found in [17, 20].

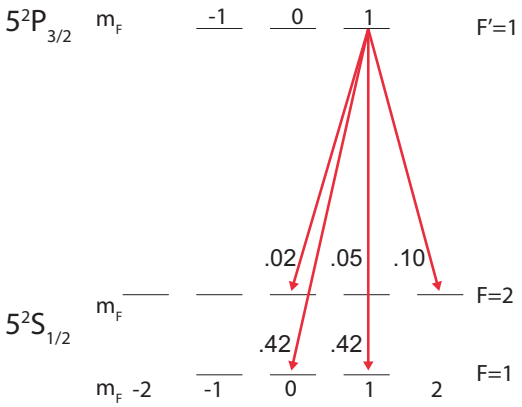

Figure 2.6: Branching ratios for the ^{87}Rb transitions for the implementation of single-photon cooling.

Figure 2.6 shows the relevant branching ratios for the transition for the implementation of single-photon cooling in rubidium.

2.5 Magnetic Interactions with Atoms

This section describes the effect of an external magnetic field on the atomic energy structure (anomalous and normal Zeeman effect) and on the scattering properties of atoms (magnetic Feshbach resonance). The Zeeman effect is utilized both in the Zeeman slower (see chapters 2.7 and 7.2.1) in a magneto-optical trap. In addition, magnetic trapping of atoms would not be possible without the Zeeman effect. Magnetic Feshbach resonances lead to a strong dependence between the scattering length of the atoms and an externally applied homogeneous magnetic field. This effect can be exploited, for example, to decrease evaporation times, see chapter 2.10.

2.5.1 Anomalous and Normal Zeeman Effect

The anomalous Zeeman effect describes the energy shift of atomic states in the presence of a weak external magnetic field. Weak in this context means that the interaction energy between the total angular momentum of the atom and the external magnetic field is small compared to the interaction energy between the electron spin and the nuclear spin of the atom. This means that the total angular momentum $\vec{F}$ will precess along the magnetic field axis, see figure 2.7. In stronger magnetic fields, angular momenta start to decouple. This is described by the normal Zeeman effect and the Paschen-Back effect.

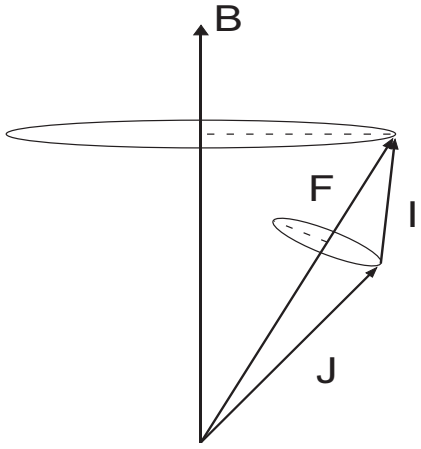

Figure 2.7: In the anomalous Zeeman regime the total angular momentum $\vec{F} = \vec{I} + \vec{J}$ precesses around the magnetic field axis. Figure courtesy of Gabriel Price.

The total magnetic moment of an atom is given by the sum of its electronic and nuclear moments,

$$\vec{\mu} = \mu_B(g_J\vec{J} + g_I\vec{I}), \tag{2.13}$$

where μ_B is the Bohr magneton, $\vec{J}$ and $\vec{I}$ are the electronic angular momentum and nuclear spin, and g_J and g_I are the electronic and nuclear magnetic g-factors. The Hamiltonian describing the interaction between the atomic magnetic moment $\vec{\mu}$ and the external magnetic field $\vec{B}$ is given by [22, 23, 25]

$$H = -\vec{\mu} \cdot \vec{B}. \tag{2.14}$$

This Hamiltonian can be diagonalized in the hyperfine basis $|F, m_F\rangle$. Each of the hyperfine levels F consists of $2F + 1$ magnetic sublevels (m_F), corresponding to the different projections of the total atomic angular momentum along the quantization axis given by the direction of the magnetic field. The associated energy shift of the state $|F, m_F\rangle$ is given by

$$\Delta E = \mu_B g_F m_F |B|, \tag{2.15}$$

where

$$g_F = g_J \frac{F(F+1) - I(I+1) + J(J+1)}{2F(F+1)} + g_I \frac{F(F+1) + I(I+1) - J(J+1)}{2F(F+1)}. \tag{2.16}$$

Table 2.3 summarizes the values of g_I and g_J for the transitions important to this dissertation for both rubidium and lithium.

Rubidium	
g_I	-0.0009951414(10)
$g_J(5^2S_{1/2})$	2.00233113(20)
$g_J(5^2P_{1/2})$	2/3
$g_J(5^2P_{3/2})$	1.3362(13)

Lithium	
g_I	-0.0004476540
$g_J(2^2S_{1/2})$	2.00233113(20)
$g_J(2^2P_{1/2})$	0.6668
$g_J(2^2P_{3/2})$	1.335

Table 2.3: g-factors for rubidium and lithium

Figure 2.8 shows the anomalous Zeeman splitting of the ground state of ^{87}Rb. The magnetic field strengths used during the course of the rubidium single-photon cooling experiment remain in the anomalous Zeeman regime. This figure shows that it is possible

to magnetically trap an ensemble of rubidium atoms at a local magnetic field minimum, if the atoms are in the low-field seeking states. This is routinely done in many cold atom experiments [27].

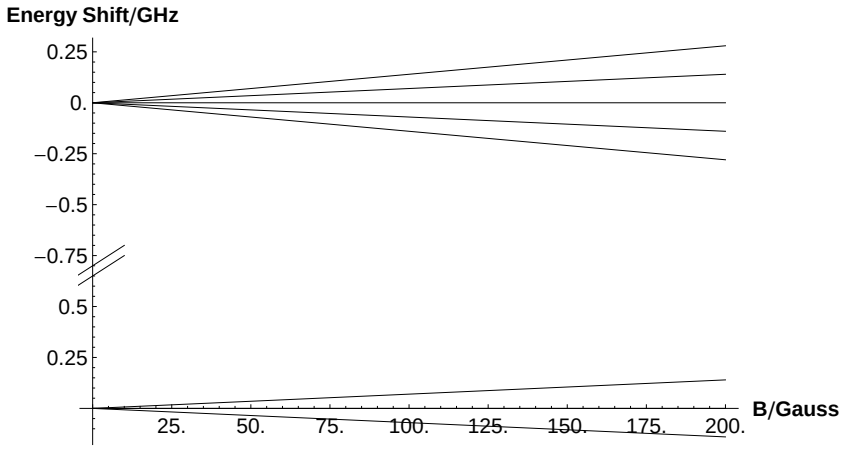

Figure 2.8: Anomalous Zeeman shift of the hyperfine energy level structure in ^{87}Rb.

In lithium the anomalous Zeeman regime only extends for a few tens of Gauss, even for the ground state. It is therefore important to understand the normal Zeeman effect in addition to the anomalous Zeeman effect.

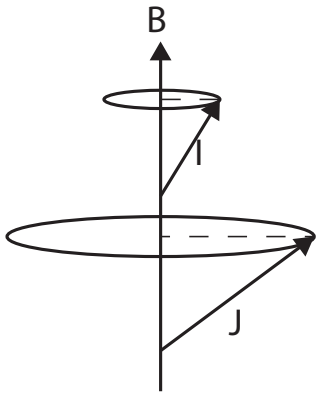

Figure 2.9: In the normal Zeeman effect regime the angular momentum spin $\vec{J}$ and nuclear spin $\vec{I}$ precess around the external magnetic field axis individually.

As mentioned above, in the normal Zeeman regime the angular momentum $\vec{J}$ and the nuclear spin $\vec{I}$ decouple and precess around the external magnetic field individually, see figure 2.9. This happens when the interaction energy $\mu \cdot \vec{B}$ exceeds the fine structure

interaction. The shift in the energy states is then well approximated by

$$\Delta E \approx \mu_B g_J m_J B \tag{2.17}$$

The energy level structure of lithium in the Zeeman regime is shown in figure 2.10. Even though the highest three magnetic states (labeled $|4\rangle$, $|5\rangle$ and $|6\rangle$ in figure 2.10) are low-field seeking states, it is unfortunately not possible to evaporatively cool ^{6}Li atoms confined in a magnetic trap. Scattering events during evaporation causes spin-flips to anti-trapped states leading trap loss [28].

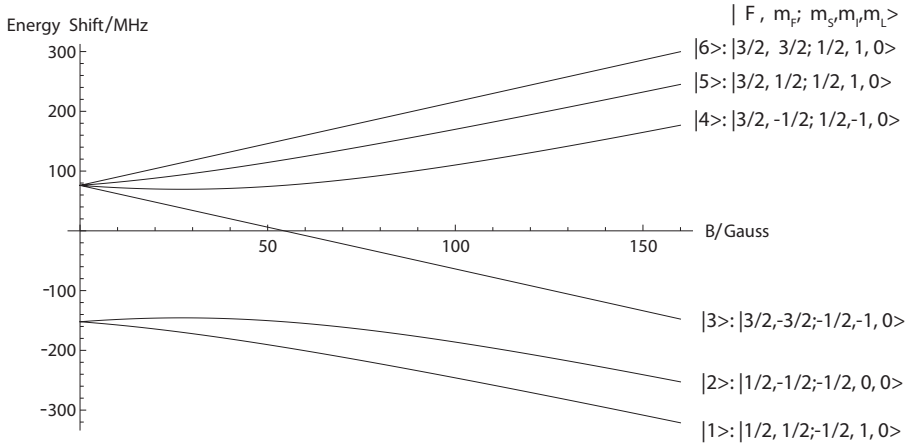

Figure 2.10: Energy shift of the ^{6}Li ground state in an external magnetic field. For small magnetic field strengths the energy level splitting follows the anomalous Zeeman-effect. Above about 30 Gauss angular momenta decouple and the energy splitting is described by the normal Zeeman effect.

2.5.2 Magnetic Feshbach Resonance

A Feshbach resonance is a quantum mechanical scattering resonance, which was first encountered in the context of nuclear physics [29]. In general, a Feshbach resonance can be induced optically as well as magnetically, however, this discussion is limited to the magnetic case. A simple model is used to describe the general phenomenon.

Consider two potential curves V_{bg} and V_C, and two atoms colliding with the small energy E as shown in figure 2.11 [30]. For large atomic separations R the potential V_{bg} asymptotically connects to two free atoms. For small energies E the potential V_{bg}

represents the energetically open channel, also called the entrance channel. The second potential, V_C, is known as the closed channel. This potential (V_C) can support a bound molecular state near the threshold of the entrance channel.

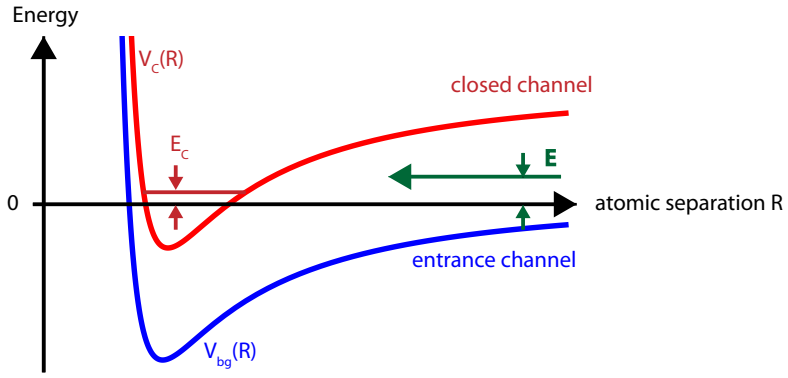

Figure 2.11: Two channel model for a Feshbach resonance. Consider two atoms scattering with energy E and the existence of a closed channel V_C that can support a bound state with energy E_C. If resonant coupling to the closed channel exists, for example through hyperfine interactions, the phenomenon of a Feshbach resonance occurs. For cold atoms, where $E \to 0$, resonant coupling can be realized by tuning E_C towards zero by means of an external magnetic field, if the magnetic moments of the entrance and closed channels differ.

When the energy of the bound state E_C approaches the energy of the scattering state of the entrance channel, small interactions, for example hyperfine interactions, lead to a strong mixing between the two channels and a Feshbach resonance occurs, see figure 2.12. For cold atoms, where $E \to 0$, resonant coupling can be realized by tuning E_C towards zero by means of an external magnetic field, if the magnetic moments of the entrance and closed channels differ.

In case of a magnetically tuned Feshbach resonance the s-wave scattering length can be described by a simple model [31],

$$a_s(B) = a_{bg}\left(1 - \frac{\Delta}{B - B_0}\right), \tag{2.18}$$

where a_{bg} is the background scattering length, B_0 describes the resonance position and the parameter Δ describes the width of the resonance.

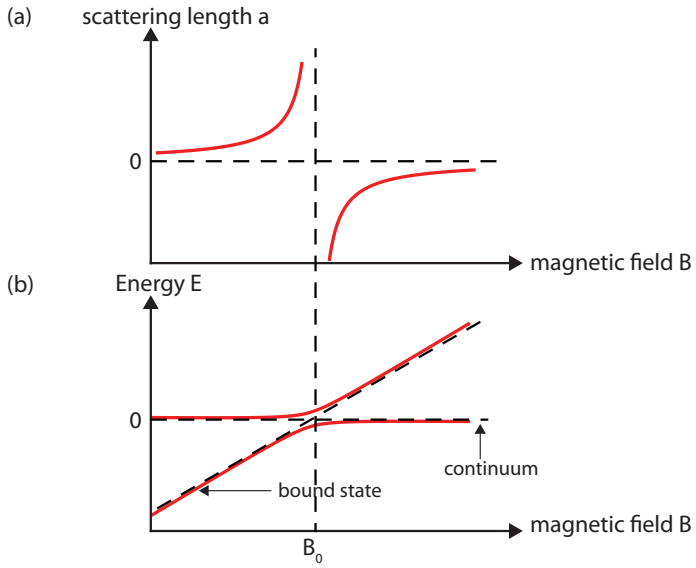

Figure 2.12: Scattering length and molecular state energy near a magnetic Feshbach resonance. (a) The scattering length varies with the magnetic field strength, if the magnetic moments of the entrance and closed channels differ. (b) The hyperfine coupling between the entrance and closed channel leads to an avoided crossing between the free atomic state and the bound molecular state.

Because Feshbach resonances allow tuning of the s-wave scattering length, they are a very useful tool during evaporative cooling of cold atomic clouds, see chapter 2.10. Evaporative cooling using two different spin states in ^{6}Li is typically done using states $|1\rangle$ and $|2\rangle$, see figure 2.10. For these states a Feshbach resonance with a width of $\Delta \approx -300$ G is located at 834 G [30]. The broad width of this resonance makes it particularly useful [32]. The scattering length of these states as a function of the magnetic field B can be found in [32–34].

2.6 Interaction of Atoms with Light

One of the most powerful methods to trap, cool, and manipulate the internal quantum states of atoms is through interaction with light. One can roughly distinguish between two regimes that will be treated separately in this discussion: the interaction with near-resonant light, which leads to a strong scattering force, and the far-detuned regime, which leads to an AC Stark shift or an optical dipole force. Both regimes are

used during the course of the experiments described in this dissertation: Near-resonant light slows atoms in a Zeeman slower and traps atoms in a magneto-optical trap; far-off resonant light on the other hand creates optical dipole traps. In the lithium experiment an optical dipole trap is used for optical evaporation in order to cool the atoms to degeneracy. In the rubidium experiment an optical dipole trap stores the atoms after they have undergone single-photon cooling.

2.6.1 Near-Resonant Light - Scattering Force

The dominant effect of near-resonant light is the creation of a strong scattering force. If an atom absorbs a photon, the photon momentum is transferred to the atom. If the absorption of the photon is followed by a spontaneous emission process, on average the emission will not cause a change in the momentum of the atom. The net force an atom experiences from absorption is thus given by [35]

$$F_{scatt} = \hbar k \Gamma \rho_{ee}, \tag{2.19}$$

where $\hbar k$ is photon momentum, Γ is the rate of the process and ρ_{ee} is part of the density matrix and describes the probability to find an atom in the excited state. Choosing ρ_{ee} over ρ_{gg} includes the effects of saturation and detuning. The expression for ρ_{ee} can be derived from the optical Bloch equations and is given by [35]

$$\rho_{ee} = \frac{1}{2} \frac{I/I_{sat}}{1 + (I/I_{sat}) + 4(\Delta/\Gamma)^2}, \tag{2.20}$$

where $\Delta = \omega_{laser} - \omega_{resonant}$. This implies that the scattering rate and scattering force are given by

$$R_{scatt} = \frac{\Gamma}{2} \frac{I/I_{sat}}{1 + (I/I_{sat}) + 4(\Delta/\Gamma)^2} \tag{2.21}$$

$$F_{scatt} = \hbar k \frac{\Gamma}{2} \frac{I/I_{sat}}{1 + (I/I_{sat}) + 4(\Delta/\Gamma)^2}. \tag{2.22}$$

2.6.2 Far-Detuned Light - AC Stark Shift and Optical Dipole Force

Far-off resonant light creates an AC Stark shift, while scattering forces are negligible in this regime. Consider an atom placed into an electric field $\vec{E}$ generated by

a laser field with frequency ω. This electric field induces an atomic dipole moment $\vec{p}$, where [36]

$$\vec{p} = \alpha(\omega)\vec{E}. \tag{2.23}$$

$\alpha(\omega)$ is the complex polarizability, which depends on the laser frequency ω. The induced dipole gives rise to an energy shift given by

$$\Delta E_{AC} = -\frac{1}{2}\langle \vec{p} \cdot \vec{E} \rangle = -\frac{1}{2\epsilon_0 c} Re(\alpha) I, \tag{2.24}$$

where the angular brackets indicate the time average. The intensity I is given by $I = 2\epsilon_0 c|\vec{E}|^2$.

In a quantum-mechanical description the scalar polarizability α is given by

$$\alpha = \frac{1}{2\hbar} \sum_k |\langle k|\vec{\mu}|j\rangle|^2 \left(\frac{1}{\omega_{kj} + \omega} + \frac{1}{\omega_{kj} - \omega} \right). \tag{2.25}$$

The energy shift of an energy level j in the presence of a laser beam with intensity I is thus described by

$$\Delta E_{AC} = -\frac{1}{4\epsilon_0 \hbar c} \sum_k |\langle k|\vec{\mu}|j\rangle|^2 \left(\frac{1}{\omega_{kg} + \omega} + \frac{1}{\omega_{kg} - \omega} \right) I, \tag{2.26}$$

where the sum is over all possible energy levels k. This formula is evaluated further in appendix A.

In a semi-classical approximation the AC-Stark shift of the ground state, typically called the dipole potential, can be expressed by

$$U_{dip}(r) = -\frac{\hbar \Gamma_{D2}^2}{8 I_{sat}} \left(\frac{1}{\omega_{D2} + \omega} + \frac{1}{\omega_{D2} - \omega} \right) I(r), \tag{2.27}$$

where Γ_{D2} is the D_2-line transition linewidth and I_{sat} is the saturation intensity. In cases where the rotating wave approximation can be invoked, this equation simplifies to

$$U_{dip}(r) = \frac{3\pi c^2}{2\omega^3} \frac{\Gamma}{\Delta} I(r), \tag{2.28}$$

where the expression of the saturation intensity is inserted [36], and Δ describes the detuning from resonance, $\Delta \equiv \omega_{laser} - \omega_{D2}$. The dipole potential then scales as $\frac{I}{\Delta}$. Depending on the sign of Δ, a repulsive (for blue-detuned light) or an attractive (for

red-detuned light) potential is created. In the experiments described in the following chapters, an attractive dipole potential for lithium atoms is formed by focusing a CO_2 laser beam ($\lambda = 10.6$ μm), and repulsive potentials for rubidium atoms are created by multiple laser beams at a wavelength of $\lambda = 532$ nm.

2.7 Zeeman Slower

A magneto-optical trap, see chapter 2.9, is able of capturing atoms at a speed of a few tens of m/s. However, to get a large enough number of lithium atoms into the gas phase to create an effusive atomic beam, it is necessary to heat the lithium reservoir to a temperature of about 350°C. At this temperature atoms within the effusive beam move at a mean velocity of 1100 m/s (the most probable velocity is about 860 m/s) and are thus too fast to be captured directly in the MOT. The standard way of slowing atoms to lower speeds is to use a Zeeman slower [5–7, 22, 35]. Due to the higher vapor pressure of rubidium, a Zeeman slower is not needed in the rubidium setup. Instead a double MOT setup is used, see chapter 4.

A Zeeman slower has two main components: a magnetic field which strength varies along the propagation axis of the atomic beam, and a counter-propagating laser beam. This basic setup is schematically shown in figure 2.13. The Zeeman slower decelerates atoms in the effusive atomic beam by transferring momentum from the scattered photons from the resonant laser beam to the atoms. With each scattering event an atom in the atomic beam loses on average a momentum of $p = h/\lambda$. In order to transfer momentum efficiently from the photons to the atoms, the frequency of the laser beam has to be close to the resonant frequency. As the speed of the atoms decreases, the transition frequency changes as a consequence of the Doppler-effect. A spatially varying external magnetic field (usually created by electromagnetic coils) induces a Zeeman-shift of the energy levels of the atoms. By matching the Doppler- and Zeeman-shifts it is possible to maintain a resonant scattering condition and thus a large scattering rate. The ideal magnetic field is thus given by

$$\omega_0 + \frac{\mu_B B(z)}{\hbar} = \omega_{laser} + kv. \tag{2.29}$$

Here ω_0 is the resonance frequency at zero magnetic field, ω_{laser} the laser frequency, and v the speed of the atoms. A schematic of a Zeeman slower and the ideal magnetic field profile are shown in figure 2.13.

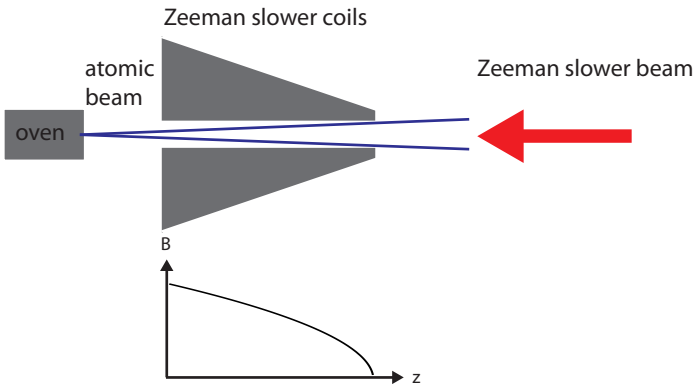

Figure 2.13: Zeeman slower setup in decreasing field configuration. An effusive atomic beam is created by heating the oven housing a reservoir. The beam then travels along the Zeeman slower axis. The atoms scatter photons from a counter-propagating laser beam and are decelarated by the exerted scattering force. A magnetic field created by electromagnetic coils causes a Zeeman shift, keeping the laser frequency on resonance with the atomic transition as the Doppler shift of the atom changes due to deceleration. The ideal profile of the magnetic field is shown below the magnetic field region.

2.8 Optical Molasses

Optical Molasses is a laser cooling technique solely relying on the transfer of momentum from photons to atoms. The standard configuration of an optical molasses setup consists of three pairs of counter-propagating laser beams [22, 35], see figure 2.14. All beams have the same frequency, tuned slightly below resonance, and each pair has balanced intensities. The effect of this configuration is understood the easiest in one dimension. A stationary atom experiences no net force and on average the interaction vanishes. However, if an atom is moving, the symmetry of the situation is broken.

Consider an atom moving to the right with velocity v as shown in figure 2.14. Due to the Doppler-shift, the atom will then scatter more photons from the beam coming

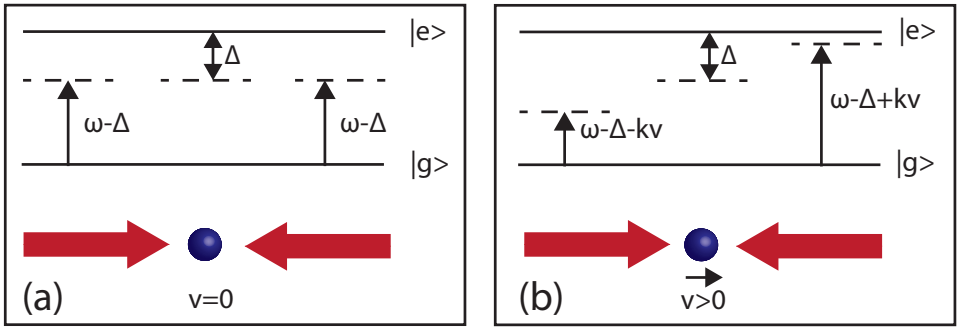

Figure 2.14: 1D optical molasses consist of a pair of counter propagating beams, detuned below the atomic resonance frequency, impinging on the atom. (a) If the atom is at rest, both beams are equally detuned from resonance, and the number of photons scattered from each beam is on average the same. (b) If the atom is in motion, the Doppler effect shifts the beam opposing the atomic motion closer to resonance and the atom scatters photons preferentially from this beam, effectively slowing the atom.

from the right hand side than from the beam coming from the left hand side. Thus the velocity of the atom is decreased.

More quantitatively, the overall force on the atom in optical molasses is determined by the scattering forces caused by the counter-propagating beams. In the one dimensional situation described above, the net molasses force on the atoms is thus given by

$$F_{molasses} = F_{scatt}(\omega - \omega_0 - kv) - F_{scatt}(\omega - \omega_0 + kv). \tag{2.30}$$

For small velocities this simplifies to

$$F_{molasses} = \alpha v, \tag{2.31}$$

where $\alpha = 4\hbar k^2 \frac{I}{I_{sat}} \frac{-2\Delta\Gamma}{(1+(2\Delta/\Gamma)^2)^2}$, and the force on the atom is proportional to the velocity of the atom [22, 35].

The lowest temperature possible in a true two-level system cooled by optical molasses is determined by the Doppler temperature $T_D = \frac{\hbar\Gamma}{2k_B}$ [22, 35]. In a multi-level atom it is possible to beat the Doppler limit in the optical molasses configuration due to the Sisyphus cooling effect. This effect has been observed in the heavier alkali atoms. For lithium, the lowest temperatures reported in an optical molasses are around the Doppler temperature.

Optical molasses do not provide a spatial confinement, and are thus a cooling and not a trapping method.

2.9 Magneto-Optical Trap

While optical molasses provides an effective method to cool atoms, it cannot confine atoms for an extended period of time; optical molasses is not an optical trap for atoms. The extension of the idea of optical molasses to create a trap is called magneto-optical trap (MOT) [37].

Adding a quadrupole magnetic field, created by a pair of anti-Helmholtz coils, to the three pairs of counter-propagating laser beams creates a magneto-optical trap. A schematic of the setup is shown in figure 2.15. The restoring force towards the center of the trap is again provided by photons scattered from the laser beams. Because the magnetic field defines a quantization axis, the polarization of the laser beams is important. The beams have to be circularly polarized, where opposing beams have opposite handedness [22, 35].

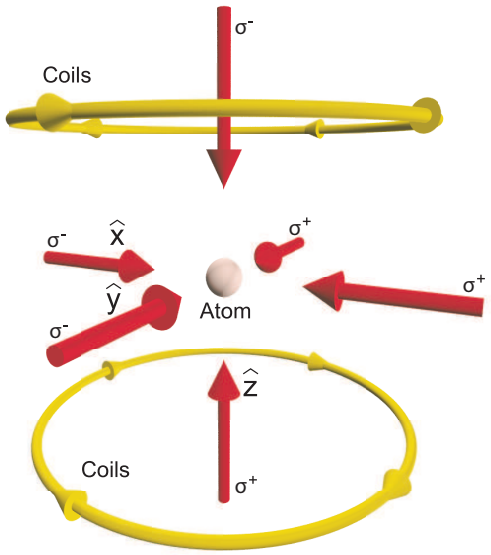

Figure 2.15: Schematic of a magneto-optical trap setup. A pair of anti-Helmholtz coils produces a quadrupole magnetic field. Three pairs of counter-propagating laser beams with opposite circular polarization cause a restoring force, pushing atoms towards the center of the magnetic quadrupole field. Figure courtesy of Gabriel Price.

The magnetic field gradients introduce a position-dependent scattering force on the atoms, confining the atoms within the magneto-optical trap radius. For simplicity consider a one-dimensional setup and an atom with the ground state $J = 0$ and an excited state $J = 1$. In the presence of the quadrupole magnetic field, the Zeeman effect splits the excited state into three states, denoted by $m = +1$, $m = 0$ and $m = -1$, see figure 2.16. The transition frequency between the ground and the excited states $m \pm 1$ is thus varying along the quadrupole field. The laser beams are red-detuned from the transition frequency (ω_0) at zero magnetic field by an amount Δ . At the position $z = z'$ the transition frequency from the ground state to the excited state with $m = -1$ is then resonant with the laser frequency, $\omega(z = z') = \omega(z = 0) - \Delta$. This transition is driven by σ^- circularly polarized light, the beam impinging from the right hand side. Because the detuning for the transition between the ground state and the $m = +1$ state is 2Δ, the atom is more likely to scatter photons from the laser beams coming from the right than from the beam coming from the left hand side having σ^+ polarization. This imbalance in scattering events moves the atom back towards the center of the quadrupole field. If the atom is displaced along the other direction, the selection rules for driving a transition now imply that the atom will scatter more photons from the beam coming from the left than from the beam coming from the right, again moving the atom back towards the center of the trap. This scheme only works as long as atoms return to the same ground state. This type of transition is then called a cycling transition.

Quantitatively the restoring force is described by adding the Zeeman shift into equation 2.30.

$$F_{MOT} = F^{\sigma^+}_{scatt}(\omega - (\omega_0 + \beta z) - kv) - F^{\sigma^-}_{scatt}(\omega - (\omega_0 + \beta z) + kv), \tag{2.32}$$

where $\beta = \frac{g\mu_B}{\hbar}\frac{dB}{dz}$. Near the trap center it follows that

$$\begin{aligned} F_{MOT} &\approx -2\,\frac{\partial F}{\partial \omega} kv + 2\,\frac{\partial F}{\partial \omega_0}\beta z && (2.33)\\ &= -2\,\frac{\partial F}{\partial \omega}(kv + \beta z) && (2.34)\\ &= -\alpha v - \frac{\alpha\beta}{k} z. && (2.35) \end{aligned}$$

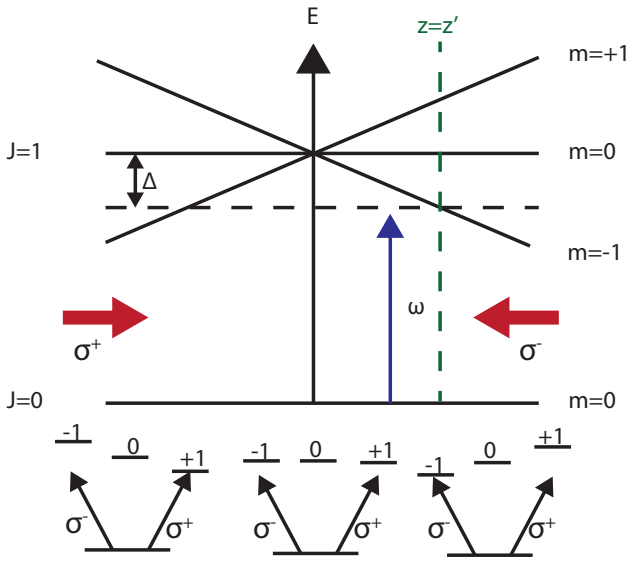

Figure 2.16: 1D magneto optical trap setup for the case of an atom with ground state $J = 0$ and excited state $J = 1$. The quadrupole magnetic field causes a Zeeman splitting of the excited state magnetic levels. At the position $z = z'$ the $|J = 0, m = 0\rangle \rightarrow |J = 1, m = -1\rangle$ transition is resonantly driven by a laser with frequency $\omega = \omega_0 - \Delta$. This transition is driven by σ^- circularly polarized light. This implies that the atom scatters more photons from the beam coming from the right than from the beam coming from the left, where the laser frequency is detuned by 2Δ from resonance. This imbalance in scattering events forces the atom back towards the center of the trap.

The final form of the equation emphasizes the emergence of the restoring force due to the imbalance in the number of scattering events caused by the Zeeman shift of the energy levels.

Unfortunately neither rubidium nor lithium have a level structure as simple as the one in the example above. Figures 2.17 and 2.18 show the energy level structure of rubidium and lithium and the transitions used in the implementation of the magneto-optical trap.

Even the relatively simple level structure of the alkali atoms does not offer a completely closed cycling transition. Because the ground state consists of two hyperfine states, a repump laser has to be added to the setup. This repump laser allows atoms to be pumped back into the cooling cycle driven by the MOT transition. The necessary strength of the repump light depends on the branching ratios. For rubidium the required amount repump light is small, making it possible to use a single repump beam. Lithium

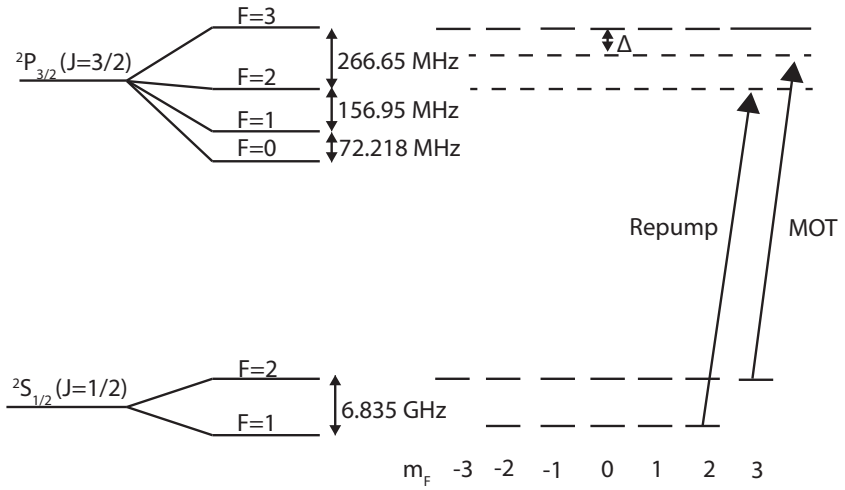

Figure 2.17: MOT and repump transition in ^{87}Rb. The MOT transition drives the atoms from $|F = 2\rangle$ to $|F' = 3\rangle$, the repump drives the $|F = 1\rangle$ to $|F' = 2\rangle$ transition.

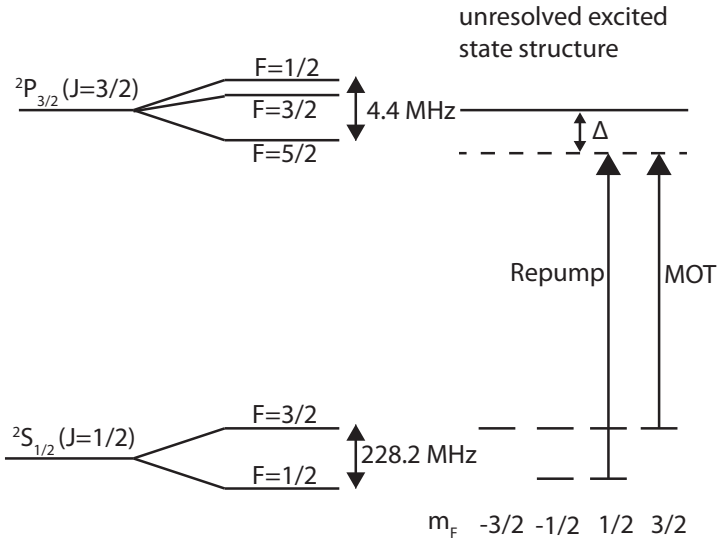

Figure 2.18: MOT and repump transition in ^{6}Li. The MOT transition drives the atoms from $|F = 3/2\rangle$ the unresolved excited state. The repump transition goes from the $|F = 1/2\rangle$ to the excited state.

on the other hand requires a significant amount of repump power. It is therefore advantageous to use the repump light as a cooling transition as well. This requires a total of six repump beams co-propagating with the MOT beams and the polarization to be identical to the MOT beam.

Typical phase-space densities in a MOT are on the order of $\rho \approx 10^{-6}$. The

phase-space density is defined as $\rho \equiv n\lambda_{dB}^3$, $\lambda_{dB} = \frac{\hbar\sqrt{2\pi}}{\sqrt{mk_BT}}$, where n is the spatial density of atoms with mass m at temperature T. The phase-space density is limited by the temperature achievable in a MOT as well as by the spatial density of atoms (typically on the order of $\approx 10^{11}$ cm^{-3}) [38]. Once the density exceeds a critical value atoms start absorbing fluorescent light emitted by other atoms. This leads to a repulsive force between the atoms limiting the maximum density [35].

2.10 Evaporative Cooling

The phase-space density in a magneto-optical trap is still about 6 orders of magnitude below degeneracy. The standard method of cooling alkali atoms further is evaporative cooling. This can happen in either a magnetic trap using an RF-knife, as is typically done for ^{87}Rb or ^{23}Na, or in an optical dipole trap, as is typically done for ^{6}Li, where evaporative cooling in a magnetic trap is not possible, see chapter 2.5.1. The basic principle of evaporative cooling is illustrated in figure 2.19.

Consider an atomic cloud trapped in an optical dipole trap of trap depth U. If the thermal tail extends above the trap depth, the hottest atoms with $E > U$ will leave the trap, effectively lowering the average energy of the remaining atoms. The remaining atoms then rethermalize through collisions, thus lowering the average temperature of the trapped atoms. Both of these processes happen simultaneously, until the thermal tail no longer extends above the trap depth and evaporation stops. The evaporative cooling process can be forced to continue by reducing the trap depth U.

Evaporative cooling can only be applied successfully if elastic collisions between atoms dominate over inelastic collisions. This is true for both fermions and bosons. However, fermions cannot scatter with other fermions in the same state, due to the anti-symmetric nature of their wavefunction. Evaporative cooling can therefore only be done using either atoms in two different states [39], using two different atoms, or by sympathetic cooling [14]. The condition of a dominating elastic cross section is satisfied for the two lowest states of ^{6}Li, $|F = 1/2, m_F = 1/2\rangle$ and $|F = 1/2, m_F = -1/2\rangle$, and it is therefore possible to use these states for evaporative cooling.

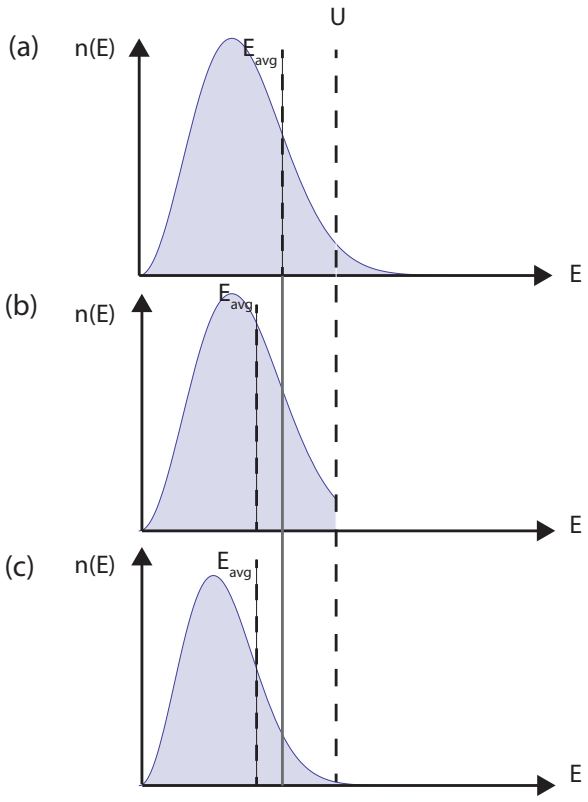

Figure 2.19: Evaporative Cooling Process. (a) The thermal distribution of the trapped cloud of atoms extends far above the well depth U of the optical trap. (b) The hottest atoms leave the atoms, effectively reducing the average energy of the trapped atoms. (c) Collisions between the atoms lead to a rethermalizing of the cloud at a lower temperature. The process then repeats itself. The processes of leaving the trap and rethermalization happen continously and is not a discrete process. Once the thermal tail does not extend above the trap depth anymore, additional techniques (i.e. lowering of the trap depth) are required to continue the evaporative cooling process.

The speed of evaporative cooling is highly dependent on the timescale of rethermalization and thus on the scattering cross section of the atoms. Using the broad Feshbach resonance in ^{6}Li the scattering cross section can be significantly increased, thus reducing evaporation times dramatically.

The efficiency of the evaporative cooling process will depend on the shape of the trap depth lowering curve. For an energy-independent scattering cross section the ideal shape is given by [40]

$$\frac{U(t)}{U_0} = \left(1 + \frac{t}{\tau}\right)^{-2(\eta-3)/\eta}, \tag{2.36}$$

which maintains a constant $\eta = U/k_BT$ during the evaporation process. Near the Feshbach resonance, in the unitary regime, the scattering cross section becomes energy-dependent. The ideal shape of the trap depth lowering curve is then described by [41]

$$\frac{U(t)}{U_0} = \left(1 - \frac{t}{\tau}\right)^{2(\eta-3)/(\eta-6)}. \tag{2.37}$$

2.11 Degenerate Fermi Gas

In the quantum regime the properties of bosons and fermions are very different. While the wave-function of bosons, like ^{87}Rb, is symmetric under the exchange of two particles, the wavefunction of fermions, like ^{6}Li, is anti-symmetric under the exchange. In addition, fermions obey the Pauli-exclusion principle and two indistinguishable fermions cannot occupy the same energy level. These differences lead to bosons following Bose-Einstein statistics and fermions obeying Fermi-Dirac statistics. In the thermal regime the difference between bosons and fermions can be neglected, both following Maxwell-Boltzmann statistics. However, as the temperature of the gas falls below a transition temperature and degeneracy is approached, exciting new physics can be discovered. This section focuses on properties of degenerate non-interacting fermions.

For non-interaction fermions the Fermi-Dirac distribution is given by

$$f(\epsilon_\nu) = \frac{1}{exp\left(\frac{\epsilon_\nu - \mu}{k_BT}\right) + 1}, \tag{2.38}$$

where μ is the chemical potential [42]. At zero temperature the energy distribution is $f(\epsilon) = 1$ below the Fermi energy $E_F = \mu(T = 0, N)$ and $f(\epsilon) = 0$ above. For higher temperatures the distribution is smeared out around E_F. In a harmonic trap the density of states is given by [43]

$$g(\epsilon) = \frac{\epsilon^2}{2\hbar^3\omega_x\omega_y\omega_z} = \frac{\epsilon^2}{2\hbar^3\bar{\omega}^3}, \tag{2.39}$$

where ω_i are the trapping frequencies and $\bar{\omega}^3 \equiv \omega_x\omega_y\omega_z$. The total number of particles is therefore determined by

$$N = \int d\epsilon\, f(\epsilon)g(\epsilon). \tag{2.40}$$

At $T = 0$ the non-interacting fermions will fill the trap up to the Fermi-Energy $E_F = \mu$

$$E_F = \hbar\bar{\omega}\,(6N)^{1/3} = k_B T_F. \tag{2.41}$$

and the radius of the trapped degenerate cloud is given by

$$R_i = \sqrt{\frac{2E_F}{m\bar{\omega}^2}}. \tag{2.42}$$

The Fermi-Dirac distribution implies that at low temperatures ($T \approx T_F$) the lowest energy levels of the trap will be filled with almost unit probability. Deviations from the maximum filling are most likely to occur in the energy levels close to the Fermi-energy. In the absence of additional excitation mechanisms, for example scattered photons, the lowest energy levels of the trap will remain filled, and the smaller the final temperature, the smaller the likelihood of finding vacancies within the distribution.

2.12 Spectroscopy

The frequency of the (near-)resonant laser beams in the experiment have to be very well controlled. Close to resonance even small changes have a big impact on the scattering rate and scattering force. It is therefore necessary to lock the laser system directly to a spectroscopic line.

The natural linewidths of the D_2 transitions in alkali atoms are on the order of a few MHz. Unfortunately this narrow linewidth will be smeared out to hundreds of MHz by Doppler-broadening. The source of this broadening lies, as the name suggests, in the Doppler-effect. Consider an atom moving with velocity $\vec{v}$ in the lab frame. In the reference frame of this atom the laser frequency ω is shifted to $\omega' = \omega - \vec{k} \cdot \vec{v}$. This particular atom will thus absorb a photon with frequency ω'. In an ensemble of atoms with a Maxwell-Boltzmann velocity distribution the natural linewidth will thus be broadened due to the different velocities of the atoms of the ensemble [22, 44].

Fortunately, Doppler-free spectroscopy methods exist which suppress the effect of Doppler-broadening.

2.12.1 Saturated Absorption Spectroscopy

Saturated absorption spectroscopy is one method frequently used to maintain a Doppler-free spectroscopy signal. Consider the setup shown in figure 2.20. The laser beam is split into two separate beams, a strong pump and a weak probe beam, counter-propagating through the spectroscopy cell. The transmitted power of the pump beam is monitored as a function of the laser frequency.

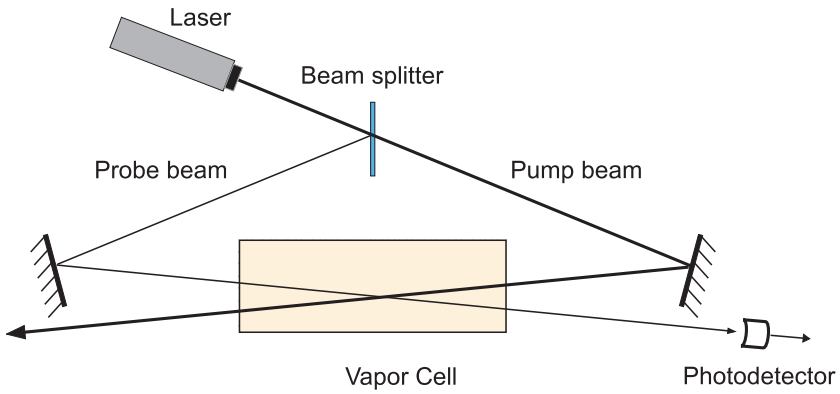

Figure 2.20: Saturated absorption spectroscopy setup. The laser beam is split into two paths: a strong pump and a weak probe beam, counter-propagating through the spectroscopy cell. The transmitted power of the probe beam is detected by a photodiode as a function of the laser frequency. Figure adapted from Gabriel Price.

In the absence of the pump beam the spectrum of the transmitted power on the probe beam is the Doppler-broadened profile with width $\Delta\omega_D$, see figure 2.21. In the presence of the pump beam the spectrum significantly changes and a narrow peak appears on top of the Doppler-broadened background. This is known as hole-burning or Lamb dip. In the presence of the pump beam a significant fraction of atoms in the spectroscopy cell are pumped into the excited state. If, at a given laser frequency, preferably atoms moving at a velocity v are excited, the same frequency will not be on resonance for the counter-propagating probe beam and thus only small amount of light will be absorbed. However, if the laser beam is on resonance for atoms at rest ($v = 0$), both pump and probe beams interact with the same velocity group. Because the pump beam excites atoms, a smaller amount of light of the pump beam is absorbed at this frequency than without the presence of the pump beam [22, 44].

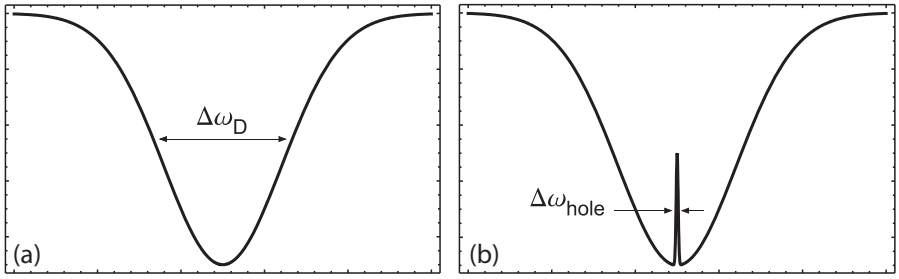

Figure 2.21: Saturated absorption spectroscopy spectrum. (a) In the absence of the pump beam, the spectrum shows the Doppler-broadened profile. (b) In the presence of the pump beam, a narrow peak appears in the spectrum, known as Lamb dip or hole burning. Figure courtesy of Gabriel Price.

Assume there exists more than one transition separated by less then the Doppler width, e.g. two distinct excited states. The spectrum will then display three lines. Two of these lines are associated with the transitions from the ground to the two distinct excited states. The third line is located midway between these transitions and is known as cross-over transition or cross-over resonance. The emergence of this line is connected with a group of atoms moving at a velocity v such that one transition is resonant with the probe while the other is resonant with the pump beam.

The Doppler-broadend background can be removed by adding an acousto-optic modulator (AOM) to the setup, see figure 2.22. In addition to the slow frequency sweep of the laser frequency, a fast dithering frequency (f_{dither}) is added to the pump beam. The photodiode signal and the dither frequency f_{dither} are then mixed in a lock-in amplifier. Away from a transition the dither will not induce a change in the power of the probe beam, and the signal from the lock-in amplifier will be close to zero. Near the resonance however, the small change in the pump laser frequency dramatically changes the absorption profile. The generated error signal is proportional to the slope of the saturation absorption spectrum and the error signal is thus the Doppler-free derivative of the spectrum. This error signal provides a good signal for a frequency feedback loop.

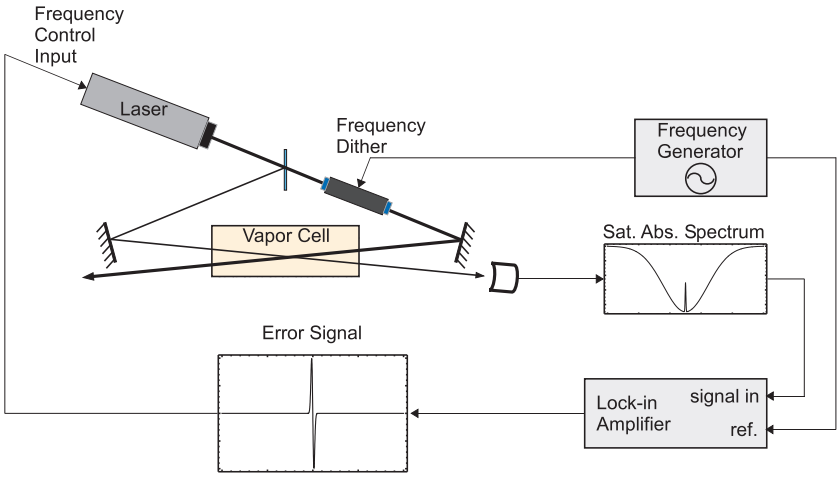

Figure 2.22: Saturation absorption spectroscopy setup used for locking the laser frequency. A slow sweep over the atomic transition yields the spectrum as shown. A fast frequency dither is added to the pump beam. The spectrum and the dithering frequency are mixed in a lock-in amplifier to generate the Doppler-free error signal. Away from the transition a change in the pump frequency does not cause changes in the transmitted power of the pump beam. Close to the transition small changes lead to large changes in the transmitted signal. The final error signal is thus the Doppler-free derivate of the spectrum detected by the photodiode. Figure courtesy of Gabriel Price.

2.12.2 Phase Modulation Spectroscopy

Phase-modulation (FM) spectroscopy is a second method frequently used to generate an error signal usable for locking the laser frequency. It is closely related to the Pound-Drever-Hall technique usually utilized to lock cavities [45–50].

Consider the setup in figure 2.22 again. Rather than inserting an AOM into the pump beam, consider adding an electro-optic modulator (EOM) into the path of the probe beam. This EOM adds sidebands to the laser frequency at a frequency of ω_m. Taking only the two nearest sidebands into account, the electric field of the probe beam after the EOM is given by

$$E_{FM} = \frac{E_0}{2}\left(J_0(\delta)\, e^{i\omega t} + J_1(\delta)\, e^{i(\omega+\omega_m)t} - J_1(\delta)\, e^{i(\omega-\omega_m)t}\right) + c.c., \tag{2.43}$$

where $\delta \ll 1$ is the modulation depth, ω the laser frequency and J are Bessel-functions. All three frequency components will interact differently with the atoms in the spectroscopy cell. Combining the absorption (α_l) and the optical phase shift (dispersion)

(ϕ_l) effects into one factor, $T_l = exp(-\alpha_l - i\phi_l)$, where $l = 0, \pm 1$ for the three frequency components, the electric field of the probe beam after the spectroscopy cell is given by

$$E_{FM} = \frac{E_0}{2}\left(T_0\, e^{i\omega t} + T_1\frac{\delta}{2}\, e^{i(\omega+\omega_m)t} - T_1\frac{\delta}{2}\, e^{i(\omega-\omega_m)t}\right) + c.c.. \tag{2.44}$$

The photodiode will thus record an intensity of the form

$$I \propto e^{-2\alpha_0}\left|e^{-i\phi_0}e^{i\omega t} + \frac{\delta}{2}e^{-i(\alpha_0-\alpha_1)}e^{-i\phi_1}e^{i(\omega+\omega_m)t} - \frac{\delta}{2}e^{-i(\alpha_0-\alpha_{-1})}e^{-i\phi_{-1}}e^{i(\omega+\omega_m)t}\right|^2. \tag{2.45}$$

To first order the signal is thus given by

$$I \propto e^{-2\alpha_0}\left(1 + (\alpha_{-1} - \alpha_1)\,\delta\, cos(\omega_m t) + (\phi_1 - 2\phi_0 + \phi_{-1})\,\delta\, sin(\omega_m t)\right). \tag{2.46}$$

This form clearly shows two contributions to the overall signal: an in-phase signal proportional to the difference in absorption of the low and the high-frequency sidebands, and an out-of-phase contribution proportional to the phase differences. Mixing this signal in a lock-in amplifier with the driving frequency allows for generating an error-signal showing either the absorption or the dispersion signal, where the phase has to be chosen such that mixing between these two extreme cases does not occur.

The lineshape of an atomic transition is typically described by a Lorentzian. Equation 2.46 suggests that the error signal consists of two symmetric lines centered around $\omega \pm \omega_m$ for the in-phase signal and of a superposition of the three dispersive signals at $\omega - \omega_m$, ω, and $\omega + \omega_m$. The lineshape of an atomic transition, the associated dispersion signal, the in-phase, and out-of-phase error signals are shown in figure 2.23.

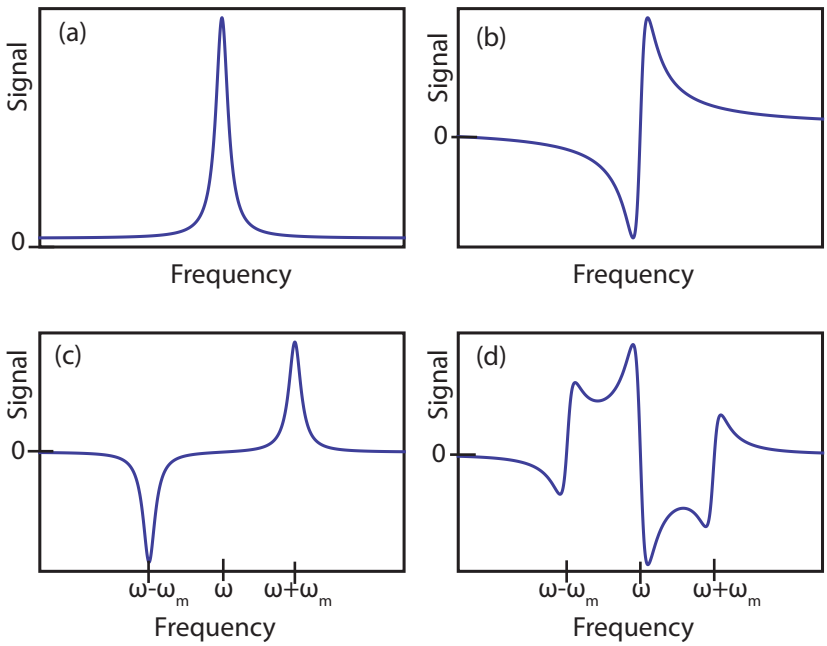

Figure 2.23: (a) Lorentzian lineshape of an atomic signal. (b) Dispersive signal of an atomic transition. (c) In-phase / amplitude contribution of the FM error signal. The two lines are centered around $\omega \pm \omega_m$. (d) Out-of-phase / dispersive contribution of the FM error signal. The three dispersion lines are centered around $\omega - \omega_m$, ω and $\omega + \omega_m$.

2.13 Imaging Techniques

The standard technique to obtain information about an ultracold ensemble of atoms is to use various imaging techniques. In-situ and time-of-flight imaging techniques allow the study of trapped atomic samples. Two forms of imaging known as absorption and fluorescence imaging are used in the experiments described in this dissertation. Additional imaging techniques include phase-contrast imaging, dark-ground imaging, and polarization-contrast imaging [51].

2.13.1 Absorption Imaging

Absorption imaging relies on imaging a resonant or near-resonant laser beam that passes through the atomic cloud. When passing through the atomic cloud, the atoms will scatter photons out of the beam, leaving a shadow of the cloud on the laser beam profile.

The scattering cross section of a two-level atom is given by

$$\sigma(z) = \sigma_0 \frac{1}{1 + 4(\Delta/\Gamma)^2 + I(z)/I_{sat}}, \tag{2.47}$$

where $\sigma_0 = \frac{3\lambda^2}{2\pi}$. As the laser beam passes through the cloud, the intensity of the laser beam will be attenuated according to Beer's law:

$$\frac{dI}{dz} = -\sigma(z)\, n(x,y,z) I. \tag{2.48}$$

Direct integration of this equation leads to

$$I(x,y) = I_0(x,y)\, e^{-\sigma \int n(x,y,z) dz}. \tag{2.49}$$

This requires the intensity of the laser beam I to be much smaller than I_{sat}, $I \ll I_{sat}$, so that the scattering cross section is independent of the intensity of the laser beam. The integrated column density $\int n(x,y,z)dz$ can then be determined, if the scattering cross section as well as $I(x,y)$ and $I_0(x,y)$ are known. Absorption imaging thus requires to take two CCD images; one in the presence of the atoms to determine $I(x,y)$, and a second picture without the atoms as a reference picture to determine $I_0(x,y)$. With this information the optical density of the cloud

$$D_{opt} = -ln\left(\frac{I(x,y)}{I_0(x,y)}\right) = \sigma \int n(x,y,z)\, dz \tag{2.50}$$

can be calculated. A second integration step extracts the atom number from the image

$$N = \int\int D_{opt}(x,y)\, dx\, dy. \tag{2.51}$$

Information about the atom number is not the only information that absorption imaging can provide. In combination with time-of-flight (TOF) imaging it is also possible to gain information about the temperature of the atomic cloud [51]. If an atomic cloud is suddenly released from all confining potentials and no external forces or atom-atom interaction influence the atomic trajectories, the atomic cloud will undergo ballistic expansion. The width σ of the atomic cloud increases then according to

$$\sigma(t) = \sqrt{\sigma(t=0)^2 + \frac{k_B T t^2}{m}}. \tag{2.52}$$

By repeating the experiment and measuring σ at different times t, the temperature of the atomic ensemble can be determined. Figure 2.24 shows an example of the raw absorption and the probe image, as well as the absorption and optical density images.

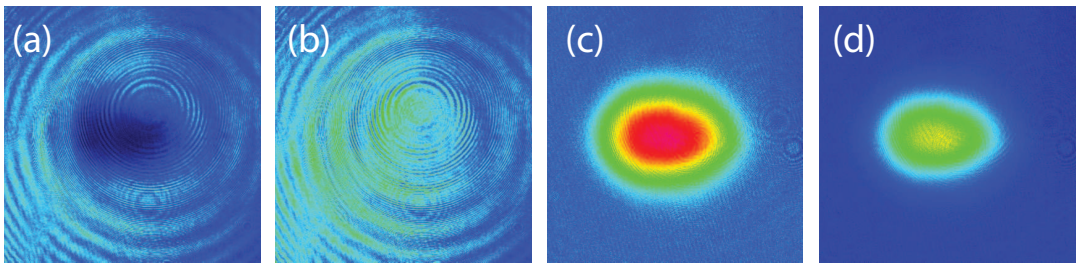

Figure 2.24: Absorption imaging pictures. (a) Raw absorption image. (b) Probe image. (c) The absorption image is calculated by the difference between the raw absorption image and the probe image. (d) The optical density is calculated from the absorption image using equation 2.50.

2.13.2 Fluorescence Imaging

Fluorescence imaging is mainly used to determine atom number. Unlike absorption imaging, fluorescence imaging is sensitive even at small atom numbers, but contains little spatial information. For fluorescence imaging the atoms are illuminated by all six MOT/molasses beams, and the scattered photons are being collected and imaged onto a camera (or photodiode). The total number of atoms can be estimated by

$$N_{atom} = \frac{8\pi}{d\Omega} \frac{1 + 4(\Delta/\Gamma)^2 + 6\, I/I_{sat}}{6 I/I_{sat}\, \Gamma} \frac{1}{t_{exp}\eta} N_{counts}. \tag{2.53}$$

I is the intensity in each individual beam, the solid angle of collected photons is $d\Omega$, t_{exp} is the exposure time of the CCD, η is the quantum efficiency of the CCD and finally N_{counts} is the number of counts of the CCD. A second image, taken without any atoms, shows the background or noise signal. Subtracting the noise image from the raw fluorescence image yields the fluorescence image, see figure 2.25.

Figure 2.25: Fluorescence Imaging pictures. (a) Raw Fluorescence Image. (b) Background Image. (c)Fluorescence Image

Chapter 3

Single-Photon Cooling

Laser cooling techniques have been a great success story in atomic physics research. However, their applicability is limited to atoms with sufficiently simple energy level structure. This chapter introduces the concept of single-photon cooling, a novel cooling technique that is applicable to almost all atoms in the periodic table, and shows how the processs of single-photon cooling can be considered a realization of Maxwell's demon.

3.1 Limitations of Laser Cooling

Standard laser cooling techniques rely on the repeated transfer of momentum from photon to atom. This is true for Zeeman slowing as well as magneto-optical trapping. To cool ^{87}Rb from room temperature (about 300 K) to near zero temperature, more than 40000 scattering events are necessary. This implies that only atoms with a simple enough level structure to drive the cooling transition in a repeatable way are amenable to laser cooling. The atoms need to have a cycling transition. A laser, or laser system, operating at the correct wavelength to drive this cycling transition is necessary. The large number of photons needed also sets a lower limit on the necessary laser power.

Unfortunately only a small number of atoms in the periodic table exhibit a simple enough level structure for laser cooling. Figure 3.1 shows which atoms have thus far been laser cooled using traditional laser cooling techniques. Elements shown on orange background have been laser-cooled in the ground state, and elements on blue background have been laser-cooled in a metastable state.

The most popular atoms are the alkali atoms. They only require two different frequencies for laser cooling (MOT and repump). More elaborate schemes are required

by more complex energy level structures, increasing the complexity of these experiments. Even hydrogen, the simplest atom in the periodic table, is not amenable to efficient laser cooling due to the lack of a sufficiently high power light source. Magnetically trapped hydrogen has been laser cooled in a pulsed scheme, however, the cooling rates are too small to efficiently increase phase-space density [52].

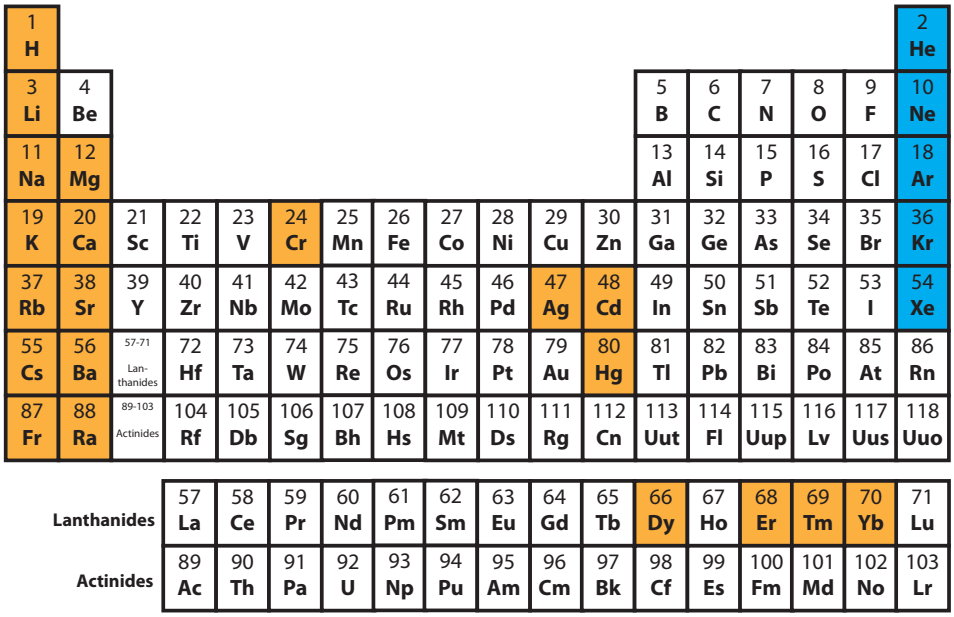

Figure 3.1: Periodic table of the elements. Elements shown on orange background have been laser-cooled in the internal ground state. See text for details on hydrogen laser cooling. Elements shown on blue background have been laser-cooled in a meta-stable state.

3.2 A One-Way Wall for Atoms

Because the requirement of having a cycling transition limits the applicability of laser cooling techniques, the question arises if it is possible to increase phase space density of a trapped cloud of atoms without a cycling transition. One solution to this problem is the concept of a one-way wall [53–56].

Consider a box filled with atoms as shown in figure 3.2. Inside this box, a one-way wall separates the volume into two parts. Assume the one-way wall allows atoms to pass from left to right, but not from right to the left. As atoms explore the trap volume,

they accumulate on the right side of the one-way wall. The atoms are thus confined to a fraction of the total volume of the trap that they occupied before. The spatial extent of the atomic cloud is reduced and the phase-space density ρ is increased.

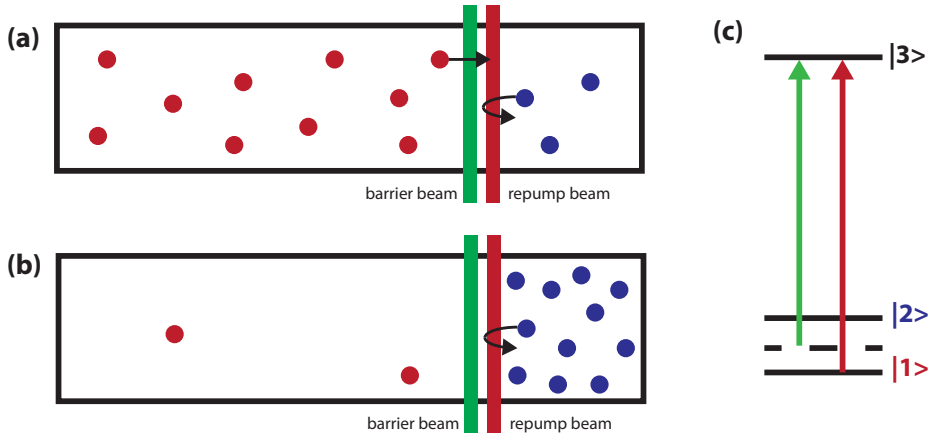

Figure 3.2: Schematic of the one-way wall phase-space compression scheme. (a) Atoms start in state $|1\rangle$ (red) on the left part of the one-way wall comprised of the barrier beam and the repumping beam. Atoms in state $|1\rangle$ can pass the barrier and are transferred to a different state $|2\rangle$ (blue). (b) Atoms in state $|2\rangle$ cannot pass the one-way wall. As atoms are exploring the trap volume, they accumulate on the right hand side of the one way wall. (c) Possible implementatin of a one-way wall. Atoms in state $|1\rangle$ see the barrier beam as red-detuned, and can pass through the barrier. The repump beam pumps the atoms into state $|2\rangle$. For atoms in state $|2\rangle$ the barrier beam is blue detuned, providing a repulsive potential that they cannot pass.

In this process the temperature of the atoms remains unchanged, and thus the thermal de-Broglie wavelength λ_{dB} stays constant. The change in phase-space density is then given by

$$\Delta\rho = \rho_i - \rho_f = (n_i - n_f)\lambda_{dB}^3 = N\left(\frac{1}{V_i} - \frac{1}{V_f}\right)\lambda_{dB}^3. \tag{3.1}$$

The amount of phase-space compression in this example is determined solely by the size of the initial and final trap volumes V_i and V_f.

This phase-space compression can be used to reduce the temperature of the ensemble of atoms. Adiabatically expanding the volume by moving the one-way wall to the left would cool the gas, but not increase the phase-space density any further.

Time reversal symmetry tells us that the process described above is unphysical, unless the atoms on the left side of the barrier differ from the atoms accumulated in the

right side of the box. An irreversible step is required to break the time-reversal symmetry. In addition, consider the effects of this process on the entropy. The decrease in entropy of the trapped atoms must be compensated by an increase in entropy somewhere else. Otherwise the second law of thermodynamics would be violated.

The entropy of an ideal gas is given by the Sackur-Tetrode equation

$$S = Nk_B \left[\ln \left(\frac{V}{N} \left(\frac{4\pi mU}{3Nh^2} \right)^{3/2} \right) + \frac{5}{2} \right], \tag{3.2}$$

where U is the internal energy of the gas, and h is Planck's constant. The change in entropy associated with the accumulation of atoms on the right hand side of the one-way barrier is thus given by

$$\Delta S = S_i - S_f = Nk_B \ln \left(\frac{V_i}{V_f} \right). \tag{3.3}$$

The answer to the question what happens to the entropy can be answered by looking at the physical realization of the one-way wall barrier.

The required energy level structure for one possible realization of the one-way wall is shown in figure 3.2 (c). This is the level structure of the alkali atoms, where the ground state is split into two hyperfine states. The one-way wall itself consists of a barrier beam, red-detuned for atoms in state $|1\rangle$, and blue-detuned for atoms in state $|2\rangle$. Atoms in state $|1\rangle$ (red) can thus pass through the attractive potential of the barrier. They then encounter a repump beam that pumps the atoms from state $|1\rangle$ (red) into state $|2\rangle$ (blue). For atoms in state $|2\rangle$ the barrier beam provides a repulsive potential, confining the atoms to the right hand side. This one-way wall scheme was realized and studied in [57–59].

As the atoms pass through the one-way wall, each atom scatters one photon. This photon is not only the irreversible step required to break time-reversal symmetry, this photon also carries away the entropy, increasing the entropy of the radiation field.

3.3 Single-Photon Cooling

The amount of phase-space compression achievable with the one-way wall is limited by the trap volumes that are reasonable to use. More phase-space compression is

possible if the internal energy of the gas, or the temperature of the atoms, could be reduced at the same time. This extension of the concept of the one-way wall is single-photon cooling. Single-photon cooling was proposed and realized in a proof-of-principle experiment at the same time the one-way wall scheme was demonstrated experimentally [60, 61].

Assume an ensemble of trapped atoms confined in a gradient potential as shown in figure 3.3. Consider first the situation shown in (a). A stationary one-way wall is placed in the center of the potential. As atoms move through the trap volume they pass the one way wall from right to left but cannot move back through the barrier and are thus accumulated on the left hand side. More efficient cooling schemes are shown in (b) and (c). In figure 3.3 (b) a moving one-way wall passes through the trap. Atoms are captured near their classical turning points and kinetic energy is removed. If the sweep of the one-way wall through the trap is adiabatic, the atoms will not regain potential energy, and the final result is an ensemble of cooled atoms at the bottom of the trap. In figure 3.3 (c) the one-way wall is placed just outside the region initially occupied by atoms. As the gradient potential collapses adiabatically, atoms cross the one-way barrier near their classical turning points. The cooled atoms are accumulated on the left side of the one-way wall.

The change in entropy, again assuming an ideal gas, is given by

$$\Delta S = S_i - S_f = N k_B \, ln \left(\frac{V_i \, U_i^{3/2}}{V_f \, U_f^{3/2}} \right), \tag{3.4}$$

where the subscripts f and i refer to the final and initial states respectively. V is the volume occupied by the trapped atoms, U is the internal energy. The maximum amount of entropy is thus removed by minimizing both the final volume V_f and the final internal energy U_f. In this sense the methods proposed in figure 3.3(b) and (c) are more efficient than the method proposed in 3.3 (a).

By translating the one-way wall or collapsing the potential slow enough, atoms are caught near their classical turning points. Increasing the translation or collapsing time sufficiently should decrease the value of U_f to arbitrarily small numbers, if one can

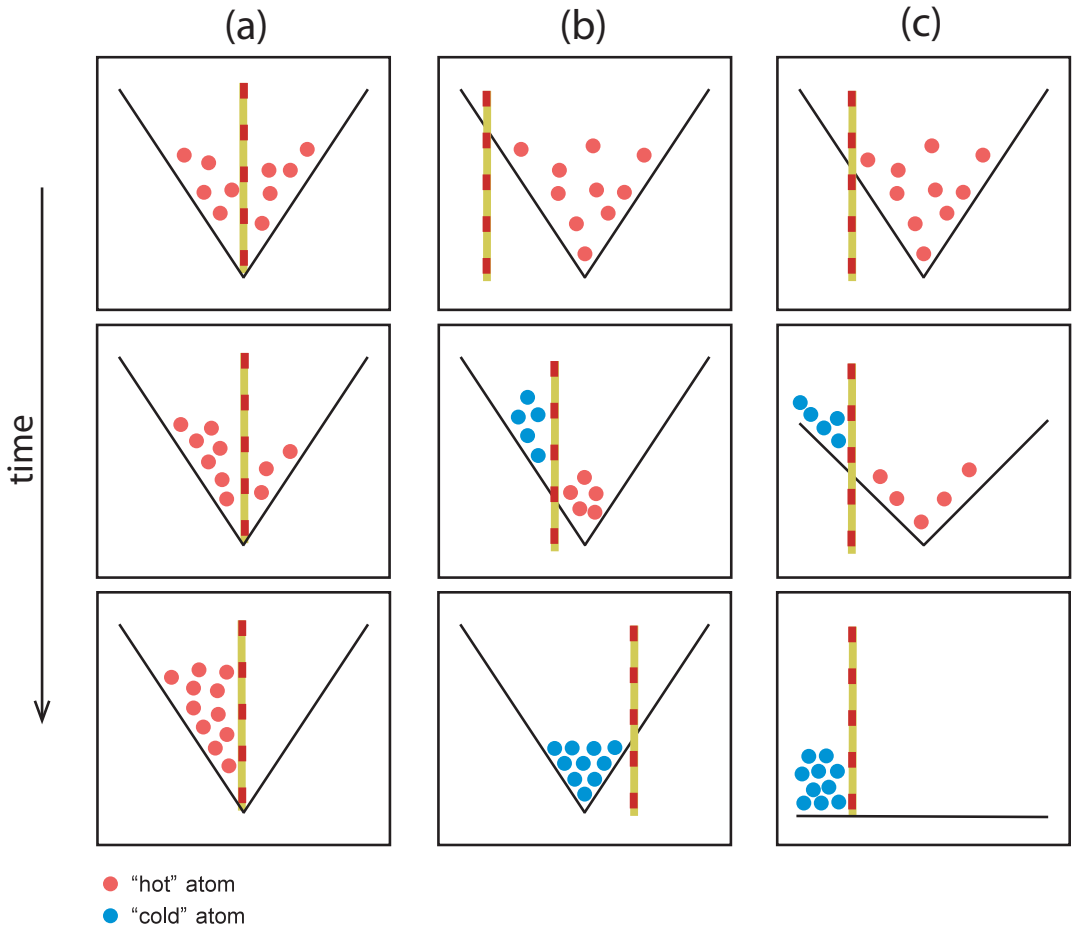

Figure 3.3: Single-photon cooling in a gradient potential. (a) A one-way wall is placed in the center of a the confining potential. As atoms explore the trap volume, they unidirectionally pass through the one-way wall. (b) The one-way wall moves adiabatically through the gradient potential. Atoms pass through the one-way wall near their classical turning points, losing kinetic energy. At the end of the sweep cold atoms are accumulated at the bottom of the gradient potential. (c) The one-way wall is stationary near the outer limits of the initial trap. The gradient potential adiabatically collapses and atoms pass through the one-way wall near their classical turning points. Cold atoms are accumulated on the left hand side of the one-way wall. Figure courtesy of Travis Bannerman.

neglect the effect of the spontaneously scattered photon. The final volume V_f occupied by the gas is now dependent only on the residual internal energy. By reducing the internal energy U_f, the final volume V_f will therefore also be minimized. The efficiency of the cooling method will therefore benefit immensely from the removal of kinetic energy from the system. Typically the spontaneously scattered photon can be neglected for the experiments presented in this dissertation, however, the single-photon recoil is the fundamental limit to phase-space densities achievable by single-photon cooling.

3.4 Maxwell's Demon

In 1867 James Clerk Maxwell proposed a gedankenexperiment commonly referred to as Maxwell's demon [62]. In the original idea a "very observant and neat-fingered being" could sort a gas of atoms or molecules according to their velocities into two separate halves of one container by operating a massless trap door. He argued that if the demon could sense the velocity of the atoms as they approached and sort them accordingly, a temperature differential between the two vessels could be created without doing any work, seemingly violating the second law of thermodynamics. An illustration of Maxwell's original demon is shown in figure 3.4.

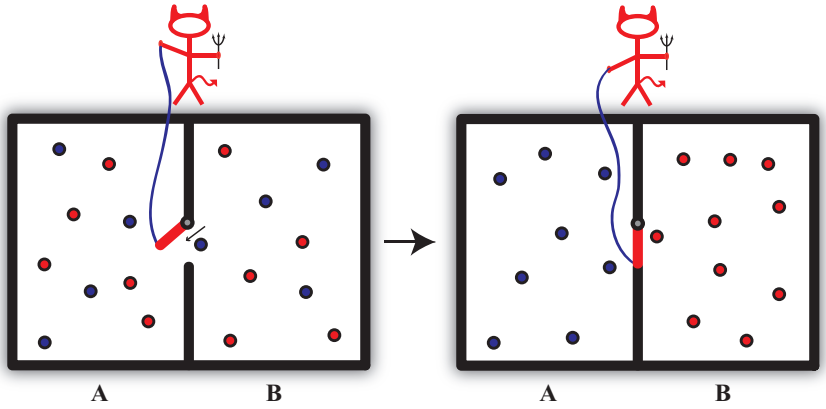

Figure 3.4: Maxwell's demon allows hot atoms (red) to move from A to B, and cold atoms (blue) to move from B to A. No work is done on the massless gate, but a temperature differential is created. Figure adapted from Travis Bannerman.

Later on Maxwell modified the original concept to a demon as illustrated in figure 3.5. In this scenario a "less intelligent" demon watches the atoms and allows

them to move from B to A, but closes the gate whenever atoms try to move from A to B, effectively creating a one-way valve. Even though no work is performed during this process, the entropy of the gas is reduced, occupying only half the original volume. This, again, is an apparent violation of the second law of thermodynamics.

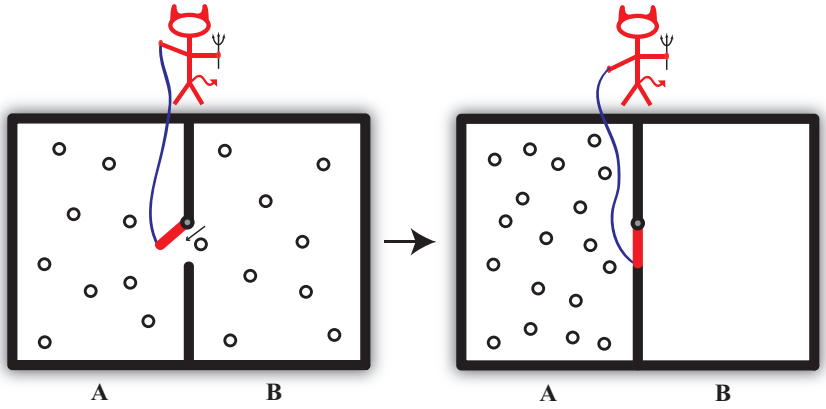

Figure 3.5: Maxwell's pressure demon allows atoms to move from B to A, but closes the gate when atoms try to move from A to B. No work is done operating the gate, and the gas occupies a smaller volume with reduced entropy. Figure courtesy of Travis Bannerman.

This thought experiment inspired many physicists to think about how Maxwell's demon can be understood without violation of the second law of thermodynamics. Leo Szilard was the first to propose to look for the missing entropy in the action of the demon [63]. He argued that in order to operate the gate correctly, the demon had to make a measurement and obtain information from the atom. Szilard claimed that this measurement was associated with an entropy increase compensating for the decrease in entropy of the atom. This concept is contemporarily known as information entropy.

Single-photon cooling is an optical realization of Maxwell's demon. As an atom reaches the one-way wall, a measurement on the atom is made and the information is carried away by the scattered photon [64]. Only one scattered photon is necessary, and in this sense single-photon cooling is a maximally efficient informational cooling technique.

Since the first demonstration of single-photon cooling, multiple proposals have been made to optimize the single-photon cooling process beyond its first limitations due to trap dynamics [65, 66].

Chapter 4

Rubidium Apparatus

A modern atomic physics experiment, even the table-top experiment, requires a large number of different technological equipment, electronics, optics and vacuum. All of these elements have to work simultaneously. It is therefore a challenge to design a system in such a way that it runs reproducibly and reliably. This chapter gives an overview of the experimental apparatus used in the single-photon cooling experiment. Details about the construnction of the setup can be found in [67–70].

4.1 Vacuum System

The vacuum system is designed for the experiment to operate in the double MOT configuration [71]. In this configuration a low background pressure is maintained in the science chamber (where the experiments are performed, in this setup the lower chamber), while rubidium atoms can quickly be accumulated in the MOT in an upper chamber, where the background pressure is higher. These two chambers are interconnected by a differential pumping tube that maintains the pressure differential while at the same time allowing for the accumulated atoms to be passed from one chamber into the other. A photograph of the rubidium vacuum chamber is shown in figure 4.1.

4.1.1 Upper Chamber

The upper chamber consists of a Pyrex glass cell with outer dimensions 4 in $\times$ 1.25 in $\times$ 1.25 in connected to a 2-3/4 CF stainless steel flange through a graded glas-to-metal seal (Larson Electronics Glass Inc, SQ-150-F2). A 6.75 in long stainless steel tube with a tapered hole (diameter between 1/8 in at the top and 3/8 in at the bottom) serves as differential pumping tube and allows the atoms to be transferred from the

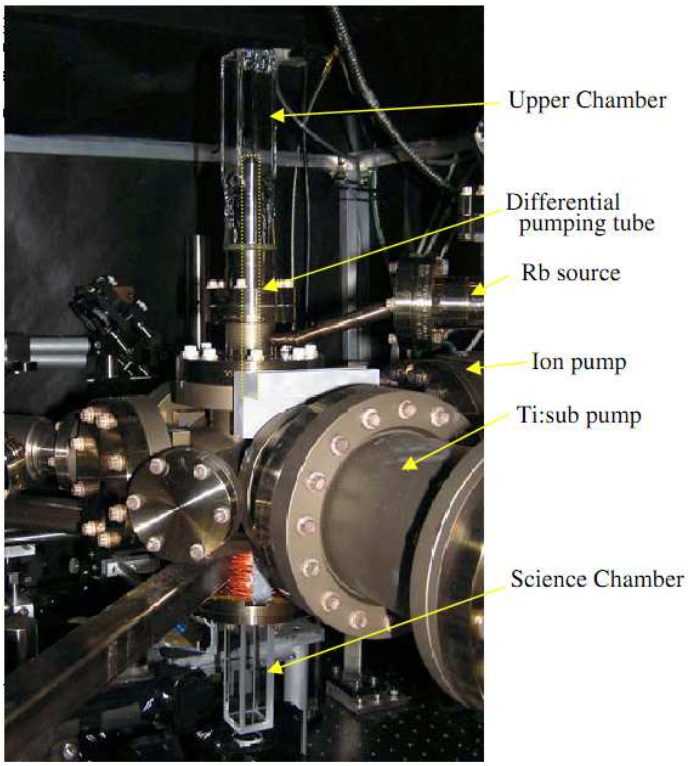

Figure 4.1: Vacuum chamber. Photograph courtesy of Todd Meyrath.

upper into the lower chamber. In this configuration a pressure gradient of more than three orders of magnitude can be maintained between the chambers.

About 200 mg of 3N5 purity solid rubidium is located in a reservoir attached to the upper vacuum chamber. At room temperature this leads to a background pressure of about 10^{-7} Torr (room temperature vapor pressure of rubidium). The metal is not isotopically enriched, so only about 28% of the rubidium consists of ^{87}Rb. However, due to the isotope shift ^{85}Rb is basically transparent to the laser beams and can be ignored for all practical purposes.

A MOT is created in this upper chamber and transferred to the lower chamber by using a resonant push-beam, which forces the atoms down the differential pumping tube by means of the scattering force.

4.1.2 Lower Chamber

The lower chamber consists of two parts: a pumping region and a glass cell, where the experiments take place. The glass cell (Hellma Cells Inc.) has outer dimensions 30 mm × 30 mm × 115 mm. The walls are 5 mm thick and consist of Spectrosil, a UV-grade synthetic fused silica. The walls are optically contacted and fused. A picture of the glass cell is shown in figure 4.2.

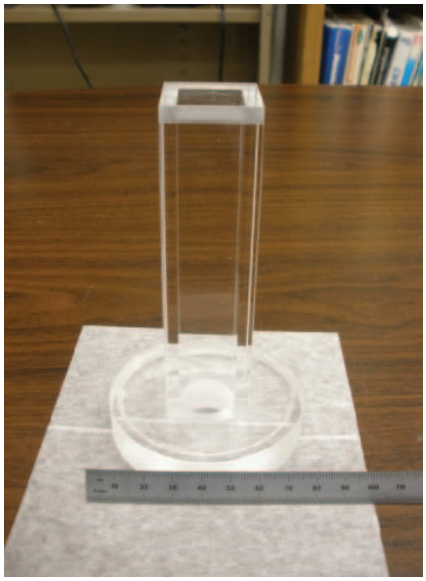

Figure 4.2: Science chamber glass cell.

A vacuum seal between the cylindrical piece of the science chamber glass cell and the stainless steel chamber is created using a Helicoflex seal (Garlock-Helicoflex H-307330 REV NC). This seal is shown in figure 4.3. The narrow ridges along the top and bottom of the seal concentrate the compression load. The metal jacket surrounds a helical spring. This spring deforms during compression creating the vacuum seal.

The pumping region of the lower chamber is a modified six-way cross with 4-1/2 and 2-3/4 CF flanges. A continously run 75 l/s ion pump (Varian 919-0103), and a titanium sublimation pump are attached to this chamber. In addition to the pumps, a nude Bayard-Alpert type ion gauge and an all-metal valve, used for initial pump-out of the vacuum chamber, are attached to the pumping region. Several blank flanges seal the remaining ports.

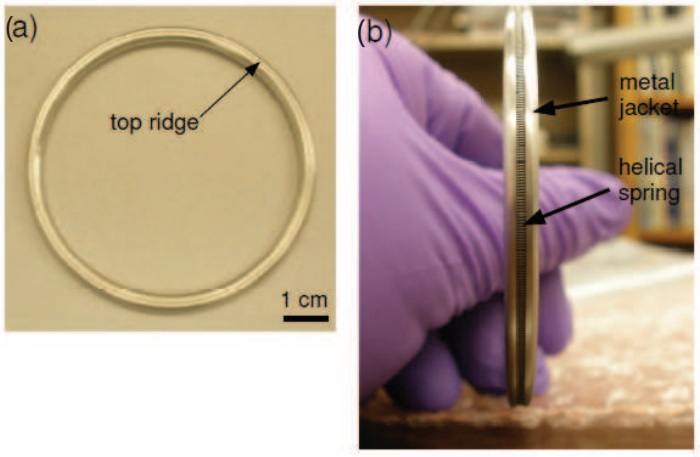

Figure 4.3: Helicoflex seal. (a) The narrow ridges along the top and bottom concentrate the compression load. (b) A metal jacket surrounds a helical spring. During compression the spring deformes, creating a vacuum seal.

4.2 Magnetic Systems

Electro-magnets create magnetic fields serving multiple purposes during the course of the experiment. These fields can be calculated using the Biot-Savart-law

$$d\vec{B} = \frac{\mu_0 I \, d\vec{L} \times \vec{I_r}}{4\pi r^2}. \tag{4.1}$$

The exact expression for the magnetic field of a circular loop of wire, through which a current I is flowing, can be derived from this equation. The axial and radial magnetic fields of a loop with radius R placed a distance D away from the origin are given by

$$B_z = \frac{\mu I}{2\pi} \frac{1}{(R+\rho)^2 + (z-D)^2} \left[K(k^2) + \frac{R^2 - \rho^2 - (z-D)^2}{(R-\rho)^2 + (z-D)^2} E(k^2) \right] \tag{4.2}$$

$$B_\rho = \frac{\mu I}{2\pi\rho} \frac{z-D}{(R+\rho)^2 + (z-D)^2} \left[-K(k^2) + \frac{R^2 + \rho^2 - (z-D)^2}{(R-\rho)^2 + (z-D)^2} E(k^2) \right], \tag{4.3}$$

where

$$k^2 = \frac{4R\rho}{(R+\rho)^2 + (z-D)^2}. \tag{4.4}$$

$K(k^2)$ and $E(K^2)$ are the complete elliptical integrals of the first and second kind. Useful approximations to this exact expression can be found in [68].

4.2.1 Upper MOT Coils

A pair of anti-Helmholtz coils creates the quadrupole field required to create a MOT in the upper chamber. The radius of these coils is 4 cm, spaced 6 cm apart. The coils consist of 91 windings of AWG 20 wire, creating a magnetic field gradient of 15 G/cm at a current of 2.5 A. To dissipate the generated heat, the coils are mounted to water-cooled copper blocks. The current in each coil is controlled individually, so that the location of the magnetic field minimum can be adjusted in space.

4.2.2 Magnetic Trap Coils

A second pair of circular coils are mounted around the science chamber cell. At small currents they create the weak magnetic field gradient required for producing a MOT in the lower chamber, at large currents these coils are able to generate the magnetic field gradients required to produce a quadrupole magnetic trap. Up to 30 A are typically used for creating the magnetic trap.

These coils are made from 176 windings of AWG 14 wire in three layers (layer A: 53 windings, layer B: 53 windings, layer C: 70 windings). They have an inner diameter of 34 mm, an outer diameter of 69 mm and a width of 42 mm. The separation between the centers of the coils is 75 mm. At large currents up to 261 W resistive heat is produced in these coils. In order to effectively cool the coils, they are surrounded by a PVC enclosure, through which a continous flow of water is directed. Figure 4.4 shows a schematic of the magnetic trap coils.

Near the center of the magnetic trap, these coils produce a magnetic field gradient of $B_z = 9.7$ G/(cm A) in the axial direction and $B_r = 4.8$ G/(cm A) in the radial direction. They are wired in series and powered by three power supplies (Lambda Gen80-19) that are wired in parallel. A home-built PID control circuit regulates the current flow using seven power op-amps (OPA549).

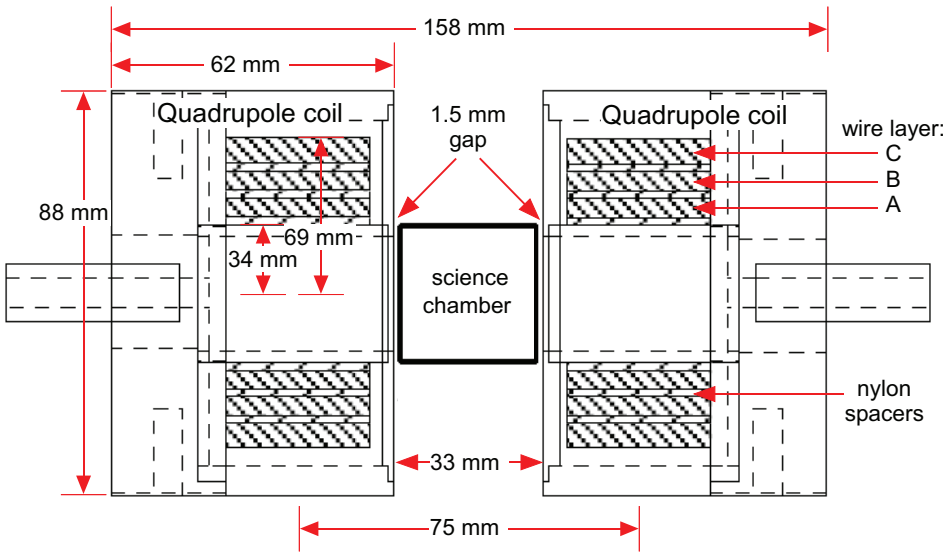

Figure 4.4: Schematic of the magnetic trap coils.

4.2.3 Auxiliary Coils

Three more coils are located around the science chamber. A pair of Helmholtz coils is aligned with the axis of the quadrupole field. The constant magnetic field offset created by these coils moves the center of the magnetic trap along this axis. They are also used to provide a homogeneous reference field during the optical pumping sequence. These Helmholtz coils consist of 30 turns of AWG 16 wire, creating a field of approximately 2.6 G/A near the trap center.

A last coil near the science chamber is mounted vertically above the cell. 150 windings of AWG 20 wire generate a field of about 1 G/A near the trap center. This coil can be used to translate the magnetic field minimum, i.e. the magnetic trap center, in the vertical direction, when superimposed to the quadrupole magnetic field. The dependence of the magnetic trap center as a function of current through this coil is shown in figure 4.5.

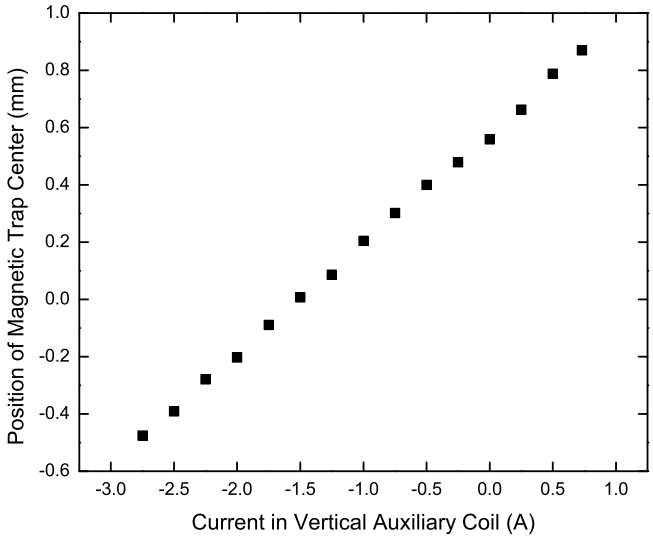

Figure 4.5: Magnetic trap center translation. Adding a uniform magnetic field shifts the position of the quadrupole field minimum. The graph shows the center of the magnetically trapped cloud of atoms as a function of the current through the vertical auxiliary coil.

4.3 Laser System

Multiple lasers with different frequencies are required during the course of the single-photon cooling experiment. They can be separated into two groups: lasers close to or at the resonance frequency of the D_2 line, near-resonant lasers, and lasers far-detuned from resonance used to create optical dipole traps.

4.3.1 Near-Resonant Lasers

Near-resonant lasers are used for a variety of purposes during the course of the experiment: creating the MOT and optical molasses beams, doing optical pumping, transferring the atoms to an optical dipole trap during the single-photon cooling process, and also for imaging. Figure 4.6 shows a diagram how each of these laser frequencies required during the experiment is related to the D_2 transition frequency.

The two fundamental frequencies, MOT and repump, of the near-resonant laser system are generated by two home-built external cavity diode lasers (ECDLs) in Littrow

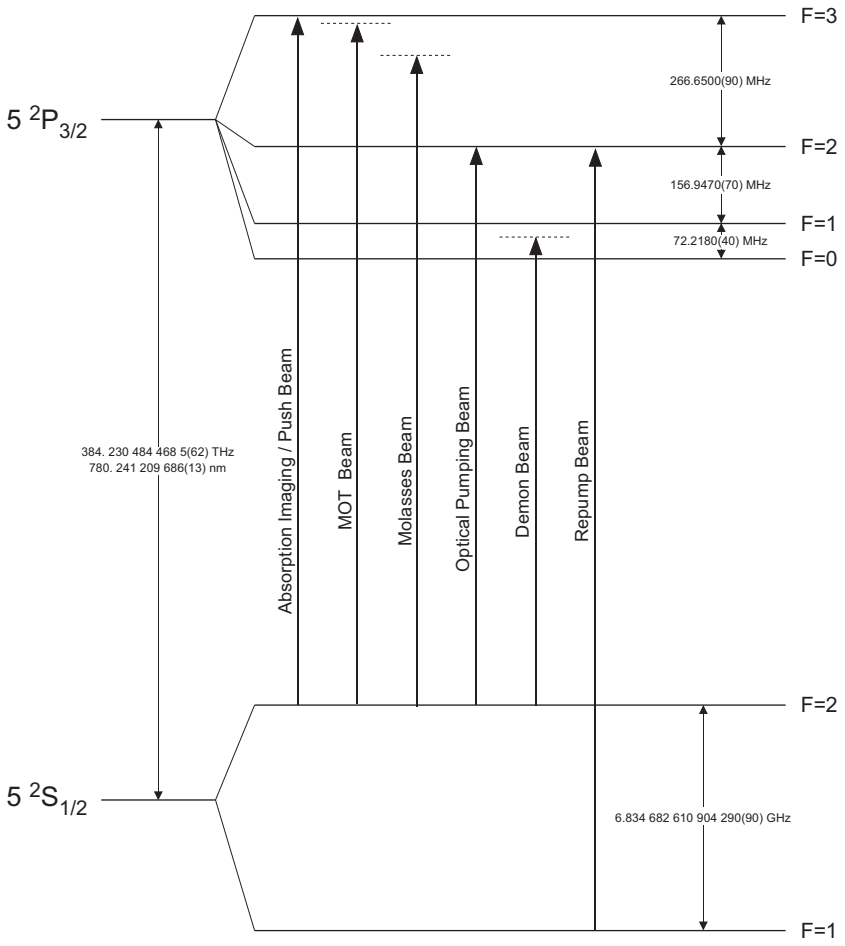

Figure 4.6: Near-resonant laser frequencies used during the single-photon cooling experiment. Figure courtesy of Travis Bannerman.

configuration [72], referred to as MOT master laser and repump laser. Each of them is locked individually to the absorption line of rubidium using saturated absorption spectroscopy. Unfortunately these diode lasers do not provide sufficient power for the experiment. Three injection-locked slave lasers seeded by the MOT master laser generate adequate power. Further changes of the laser frequencies are accomplished using acousto-optic modulators (AOMs).

4.3.1.1 MOT Master Laser

The MOT master laser, shown in figure 4.7, was built for and used in a previous experiment [73]. It is an external cavity diode laser (ECDL) in Littrow-configuration.

The laser diode (Intelite MLD-780-100S5P) has a wavelength of 780 nm and an output power of 100 mW at a current of 120 mA. The diode is mounted into the cavity by placing it in a collimation tube (Thorlabs LT230P-B). This tube also houses a broadband AR coated aspheric lens ($f = 4.5$ mm) to collimate the output beam. The collimated beam hits a gold-coated, blazed diffraction grating with 1200 grooves/mm. The zeroth-order specular reflection serves as the output beam. The first-order diffracted beam is reflected back into the diode laser, completing the external laser cavity. The laser frequency can be adjusted by changing the grating angle using a piezo stack. Thermal stability is provided by actively stabilizing the temperature of the bronze baseplate of the external cavity diode laser with a thermo-electric cooler (TEC) and a PID feedback loop. The whole setup is housed in a plexiglass cover to isolate the laser from air currents and acoustic vibrations.

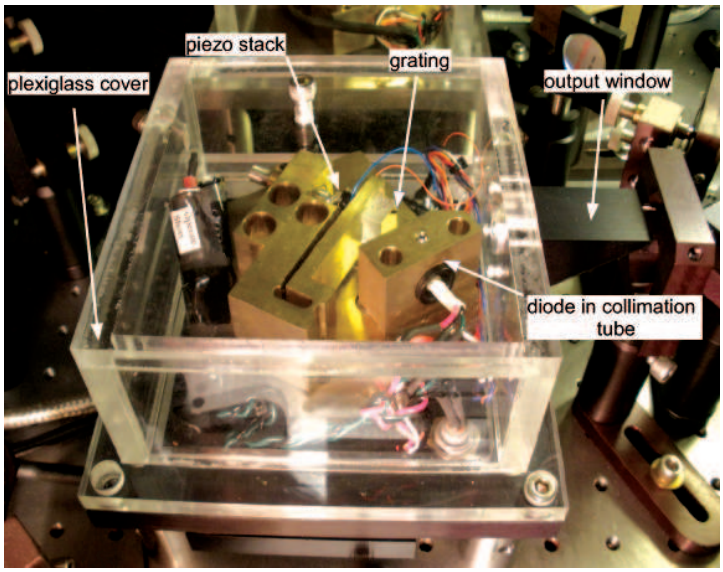

Figure 4.7: MOT master laser.

After the beam exits the diode laser housing the beam asymmetry is removed by an anamorphic prism pair. To protect the laser from damage due to back reflections, the beam passes through an optical isolator (ConOptics 712B). The beam then passes through an AOM with a frequency of 103 MHz. Only a few milliwatts of power are diffracted in this AOM, just enough to provide sufficient light for the saturated absorption spectroscopy setup used to stabilize the laser frequency. A schematic of the

distribution of the MOT master laser is shown in figure 4.8.

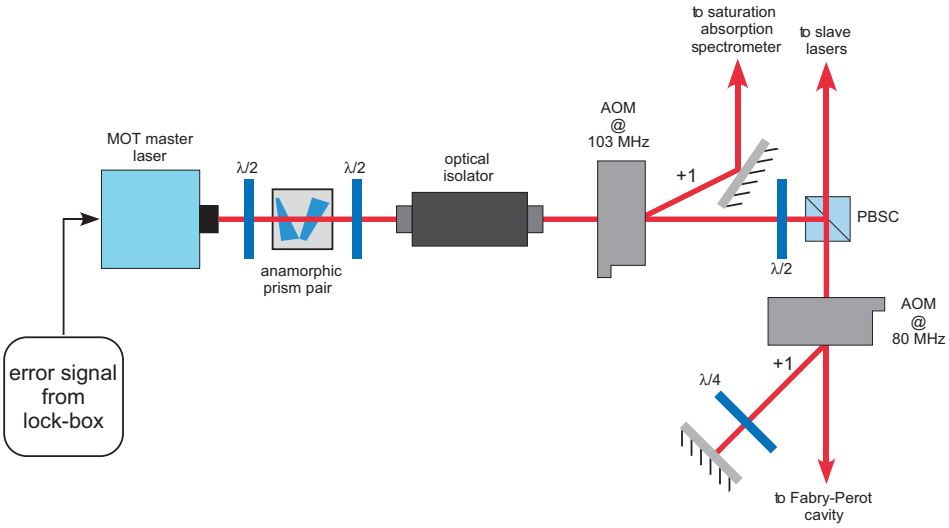

Figure 4.8: Distribution fo the MOT master laser. Figure courtesy of Gabriel Price.

Figure 4.9 shows the layout of the saturated absorption spectroscopy setup used to lock the MOT master laser. The beam is split into a pump and a probe beam using an uncoated glass plate. This ensures that the probe beam is significantly weaker than the pump beam. The pump beam is deflected by a polarizing beam splitter cube and double passes a 44 MHz AOM. This AOM is modulated with a frequency of 7 kHz and a modulation depth of 4 MHz. In the double pass the polarization of the beam is rotated by 90°, passing a quarter waveplate twice. On the second incidence on the polarizing beam splitter cube the pump beam thus passes through the cube and into the rubidium vapor cell. The pump beam is therefore counter-propagating the probe beam. At the same cube the probe beam is deflected and the signal is recorded with a fast photodiode. The signal is mixed with the FM frequency at a lock-in amplifier (Stanford Research Systems, SR510). The error signal that results from sweeping the laser across the $|F = 2\rangle \rightarrow |F' = 3\rangle$ transition is shown in figure 4.10.

The laser is locked to the $|F = 2\rangle \rightarrow |F' = 2/3\rangle$ crossover line, as this is the most prominent feature. The error signal is fed into a PID circuit and amplified by a high-voltage amplifier (Trek 601B-2) to feed back onto the grating angle.

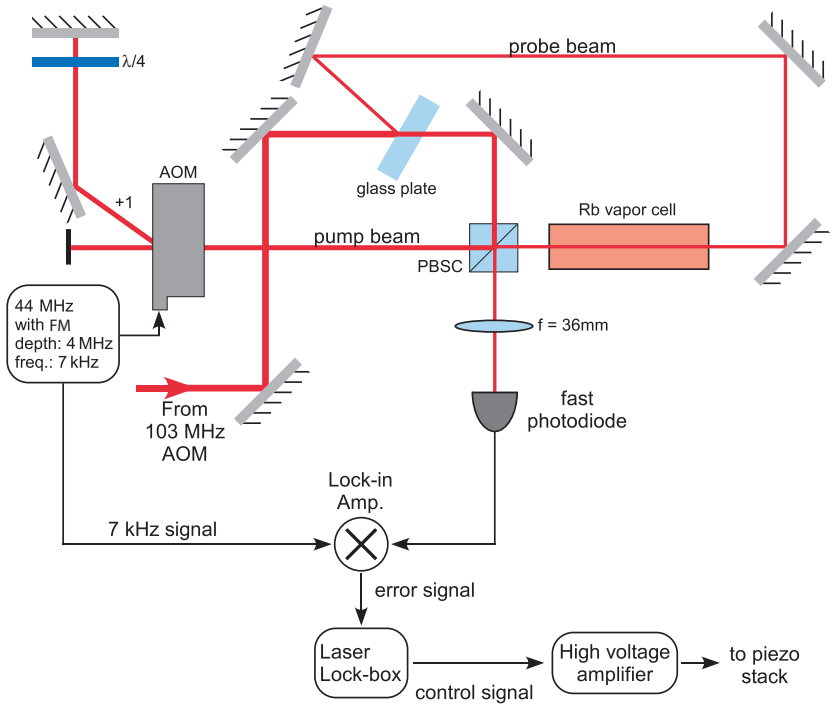

Figure 4.9: MOT master laser saturated absorption spectroscopy setup. Figure courtesy of Gabriel Price.

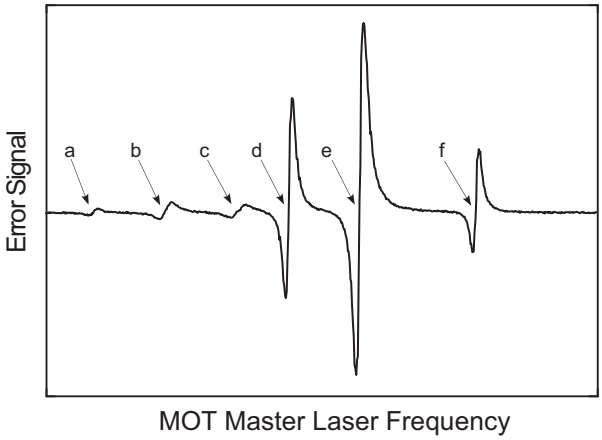

Figure 4.10: Error signal of the MOT master laser. The marked transitions are due to the following real and crossover transitions: (a) $|F = 2\rangle \rightarrow |F' = 1\rangle$, (b) $|F = 2\rangle \rightarrow |F' = 1/2\rangle$, (c) $|F = 2\rangle \rightarrow |F' = 2\rangle$, (d) $|F = 2\rangle \rightarrow |F' = 2/3\rangle$, (e) $|F = 2\rangle \rightarrow |F' = 2/3\rangle$, (f) $|F = 2\rangle \rightarrow |F' = 3\rangle$

This setup locks the laser 280 MHz to the red of the $|F = 2\rangle \rightarrow |F' = 3\rangle$ transition. The 280 MHz detuning from the transition is due to a number of frequency

shifts. First a frequency shift of 103 MHz is caused by the AOM used to pick-off the spectroscopy beam. In addition the laser is locked to the $|F = 2\rangle \rightarrow |F' = 2/3\rangle$ transition, which is detuned by 133 MHz from the $|F = 2\rangle \rightarrow |F' = 3\rangle$ transition. The pump beam is shifted by 88 MHz relative to the frequency of the probe beam by double-passing the 44 MHz AOM. This implies that the pump and the probe beam interact with atoms having a velocity such that their Dopplershift corresponds to 44 MHz. Therefore the overall error signal is shifted by 44 MHz relative to the error-signal that would result if the beam interacted with atoms with zero velocity.

Most of the light passes through the 103 MHz AOM and is deflected at a polarizing beamsplitter cube. The beam then double passes an 80 MHz AOM with a 40 MHz bandwidth. The first-order diffraction beam double-passes a quarter waveplate and thus passes straight through the polarizing beam splitter cube on the second incidence. This beam is then distributed to the three slave lasers, where it serves as the seed required for injection locking (see section 4.3.1.3). Because of the AOM double pass, the injection beam, and thus the frequency of the slave lasers, can be tuned between 80 and 160 MHz to the red of the $|F = 2\rangle \rightarrow |F' = 3\rangle$ transition. 80 MHz AOMs, used as shutters for the beam, shift the frequency of the slave lasers, so that the final detunings are between 0 and 80 MHz to the red of the $|F = 2\rangle \rightarrow |F' = 3\rangle$ transition. The zeroth order beam from the 80 MHz AOM is coupled into a Fabry-Perot cavity. This way it is easy to ensure single-mode operation of the MOT master laser.

4.3.1.2 Repump Laser

The design of the repump laser is identical to the design of the MOT master laser. The power required in the repump laser is significantly lower than the power required in the MOT laser and it is therefore not necessary to further increase the laser power.The distribution of the output power is shown in figure 4.11.

After the optical isolator a small amount of power is split off using a polarizing beam splitter cube. This beam is used in the repump spectroscopy lock, which varies slightly from the MOT master spectroscopy setup, see figure 4.12. The spectroscopy beam is split into a strong pump beam and two co-propagating weak probe beams using

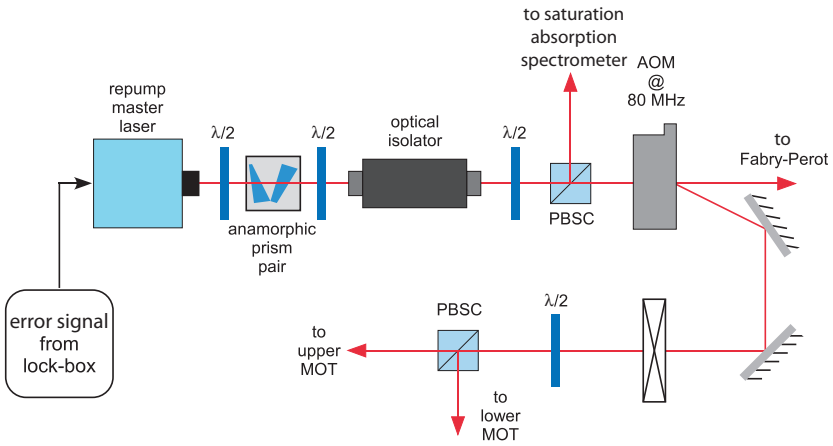

Figure 4.11: Distribution fo the repump laser. Figure courtesy of Gabriel Price.

a glass plate. The pump beam counter-propagates the probe beams but overlaps with only one of them. The difference between the two probe beams is detected using a differential photodetector to remove the Doppler-broadened background signal.

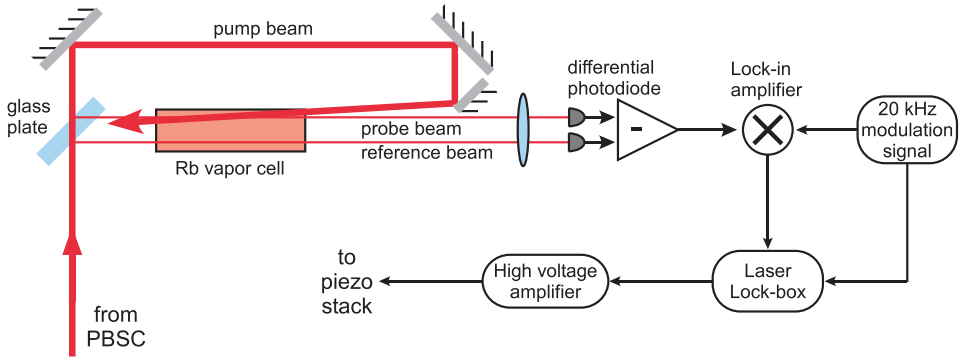

Figure 4.12: Repump laser saturated absorption spectroscopy setup. Figure courtesy of Gabriel Price.

The frequency of the laser is modulated directly by dithering the piezo stack on the diode laser cavity at 20 kHz. The disadvantage of this design is the introduction of a small amount of frequency noise on the laser. However, during normal operation of the experiment this effect is negligible.

Figure 4.13 shows the error signal for the repump laser. The laser is again locked to the most prominent line, in this case this is the $|F = 1\rangle \rightarrow |F' = 1/2\rangle$ crossover transition. This locks the laser 78.5 MHz to the red of the $|F = 1\rangle \rightarrow |F' = 2\rangle$

transition. However, the laser frequency is shifted by 80 MHz using an AOM after the polarizing beam splitter cube, see figure 4.11. Thus the final laser frequency is detuned by 1.5 MHz from resonance, negligible compared to the 6 MHz linewidth of the transition. The zeroth order signal from the 80 MHz AOM is coupled into a Fabry-Perot cavity, so that single-mode operation of the repump laser can easily be verified.

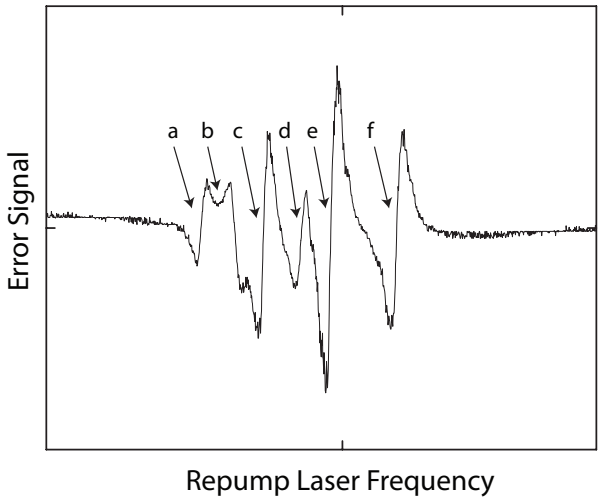

Figure 4.13: Error signal of the repump laser. The marked transitions are due to the following real and crossover transitions: (a) $|F = 1\rangle \rightarrow |F' = 0\rangle$, (b) $|F = 1\rangle \rightarrow |F' = 0/1\rangle$, (c) $|F = 1\rangle \rightarrow |F' = 1\rangle$, (d) $|F = 1\rangle \rightarrow |F' = 0/2\rangle$, (e) $|F = 1\rangle \rightarrow |F' = 1/2\rangle$, (f) $|F = 1\rangle \rightarrow |F' = 2\rangle$

4.3.1.3 Slave Lasers

Three injection-locked slave lasers amplify the MOT master laser. The heart of the slave laser is an inexpensive laser diode (Sharp GH0781JA2C) with a free-running wavelength of 784 nm and 120 mW of power at 140 mA injection current. The diode and a collimation lens are housed in a collimation tube (Thorlabs LT230P-B). The wavelength of the laser diode can be tuned close to the resonant transition of rubidium by adjusting the temperature. Good thermal control is achieved by mounting the collimation tube inside a bronze block and regulating the temperature with a TEC. Stable current to the slave lasers is provided by a PID based current controller. Figure 4.14 shows a photograph of a slave laser with and without the aluminum housing surrounding the diode laser setup.

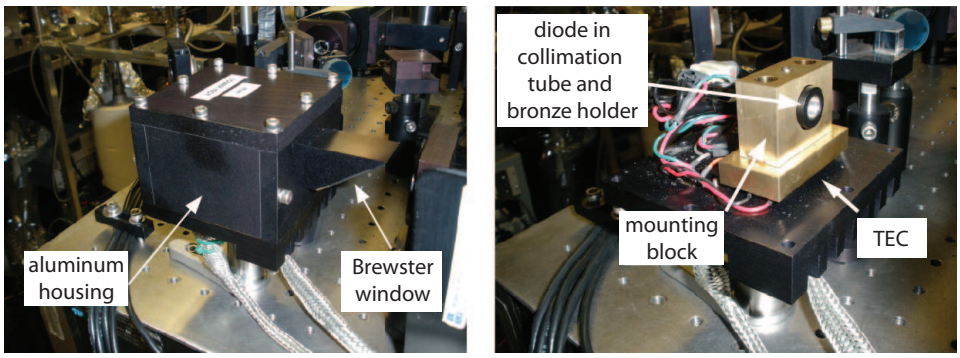

Figure 4.14: Photograph of a slave laser

Injection locking is accomplished by seeding the free-running diode laser with a weak laser beam, which spatially matches the diode laser output beam. In practice about 2 mW of power is sufficient to seed the diode lasers. When the seed beam is well aligned, about 60 mW of power at a wavelength of 780 nm are created in each of the slave lasers. Injection locked lasers can be understood as regenerative amplifiers [74]. If enough light is in the seed beam, the gain medium will amplify this frequency and the free running laser oscillation will die out.

The slave lasers are seeded by injecting a small amount of light into the rejection port of the optical isolator located directly behind the output, as shown in figure 4.15. Because the optical isolator uses the Faraday effect to rotate the polarization, the direction of rotation is independent of the propagation direction. Therefore the seed beam polarization matches the slave laser output polarization.

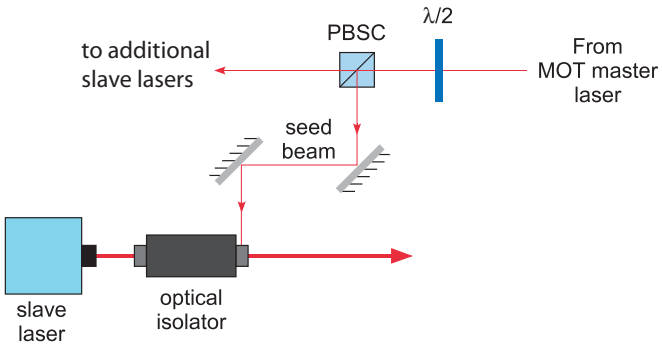

Figure 4.15: Setup for injection locking the slave lasers. Figure courtesy of Gabriel Price.

4.3.1.4 Upper MOT Horizontal Slave Laser

As the name indicates, the upper MOT horizontal slave laser's main purpose is to create the horizontal upper MOT beams. A small amount of power is diverted to create the demon beam (used to drive the transition in the single-photon cooling sequence), the push beam and the vertical absorption imaging beam. A schematic of the optical layout is shown in figure 4.16.

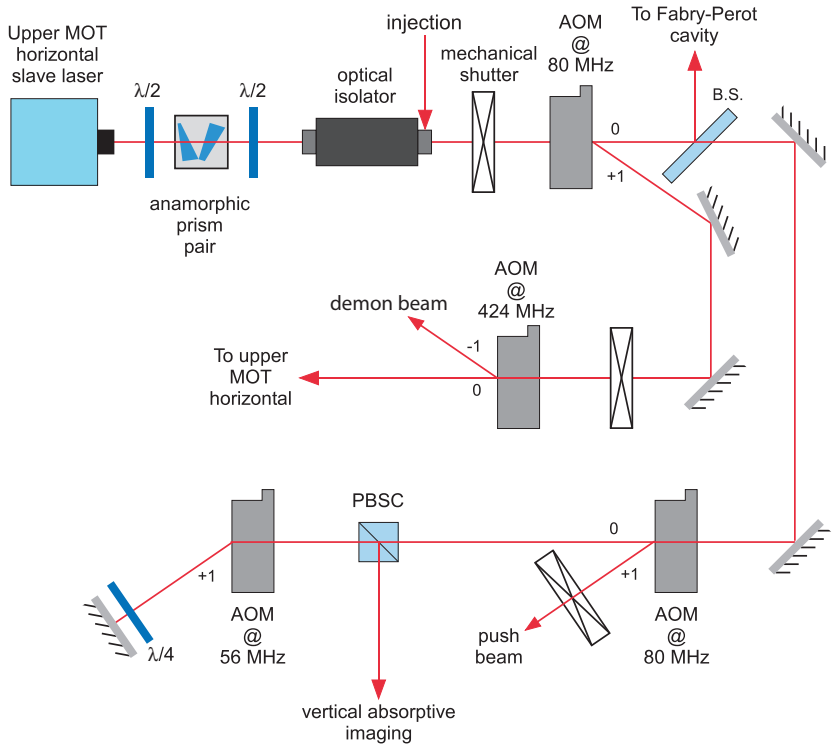

Figure 4.16: Upper MOT horizontal slave laser setup. Figure courtesy of Gabriel Price.

After the laser beam passes through the optical isolator, the first order diffraction beam of an 80 MHz AOM is used to generate the upper MOT horizontal beams. This beam is then slightly red detuned from the $|F = 2\rangle \rightarrow |F' = 3\rangle$ transition given the right injection frequency. It passes through a second AOM, this time at a frequency of 424 MHz. The zeroth order beam forms the upper horizontal MOT beam. The -1st order beam of this beam creates the demon beam, which is slightly red detuned from the $|F = 2\rangle \rightarrow |F' = 1\rangle$ transition.

A small fraction of the power of the zeroth order of the 80 MHz AOM is picked

off and coupled into a Fabry-Perot cavity. The main part of the beam goes through a second 80 MHz AOM, where the +1st order generates the push beams to move the atoms from the upper chamber into the lower chamber. With the correct injection frequency this laser beam is resonant with the $|F = 2\rangle \rightarrow |F' = 3\rangle$ transition. The zeroth order beam passes through a polarizing beam splitter cube and double passes a 56 MHz AOM and a quarter-wave plate. On the second incidence, the beam splitter cube reflects the beam. This beam is used as the vertical absorption imaging beam.

AOMs, while being very fast shutters in addition to frequency shifters, always have some leakage light in the diffraction order. A series of mechanical shutters is used throughout the laser setup to block any leakage light.

4.3.1.5 Upper MOT Diagonal Slave Laser

The upper MOT diagonal slave laser provides the power for the upper MOT diagonal MOT beams, as well as the optical pumping and horizontal absorption imaging beams. The distribution of the beams is shown in figure 4.17.

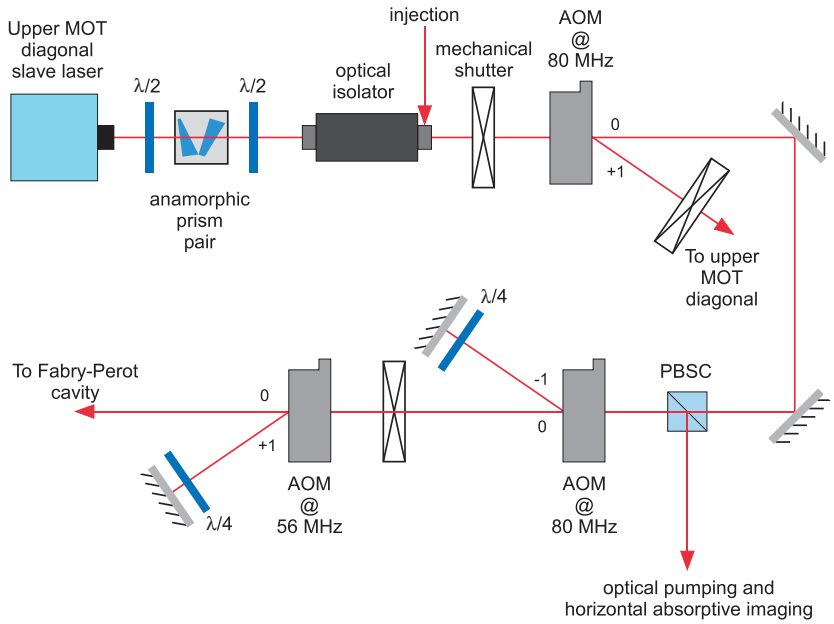

Figure 4.17: Upper MOT diagonal slave laser setup. Figure courtesy of Gabriel Price.

Upon exiting the optical isolator, the +1st diffraction order of an 80 MHz AOM

provides the beam for the upper MOT diagonal beams. The zeroth order passes through a polarizing beam splitter cube and encounters a second 80 MHz AOM. A double pass setup at this AOM shifts the frequency by 160 MHz, so that the laser is shifted into resonance with the $|F = 2\rangle \rightarrow |F' = 2\rangle$ transition given the right seed frequency. This beam is used for optical pumping. The zeroth order double passes an AOM driven at 56 MHz. This beam is used for horizontal absorption imaging. Both beams are deflected on the polarizing beam splitter cube. The zeroth order beam is coupled into a Fabry-Perot cavity.

4.3.1.6 Lower MOT Slave Laser

The lower MOT slave laser provides sufficient power for all six lower MOT beams. The beam setup is shown in figure 4.18. After passing through the optical isolator, the beam gets diffracted into the +1st order of an 80 MHz AOM. Subsequently this beam is split into the six lower MOT beams. The zeroth order is coupled into a Fabry-Perot cavity to ensure single-mode operation.

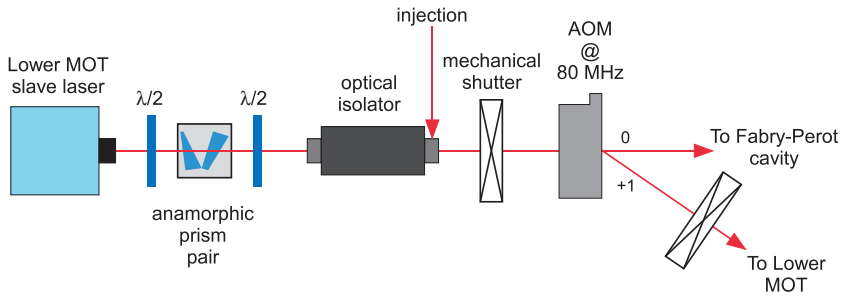

Figure 4.18: Lower MOT slave laser setup. Figure courtesy of Gabriel Price.

4.3.2 Far-Detuned Laser

A far blue-detuned laser ($\lambda = 532$ nm) creates the optical dipole trap used in the single-photon cooling sequence. This laser is a Coherent Verdi V10, a frequency-doubled Nd:Vanadate laser, with an output power of 10 W in a TEM_{00} spatial mode. The laser linewidth is less than 5 MHz.

The trap configuration used in the single-photon cooling experiment is shown in

figure 4.19. This geometry forms an open trap, where the bottom and the sides of the trap are created by laser sheets, while gravity confines atom within that trap.

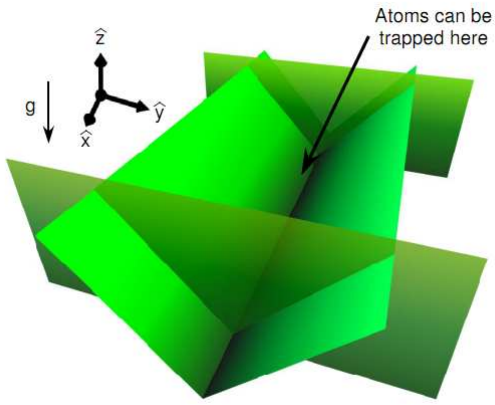

Figure 4.19: Optical trough.

The optical trap, also called optical trough due to its shape, consists of four elliptical Gaussian beams. The beams are elongated along one direction using cylindrical lenses. Two of the four beams travel along the x-direction and form a V-shape. These beams support the atoms against gravity. The other two seal off the optical trough by providing end-caps. These beams travel along the y-direction.

Each of the four beams has about 700 mW of power, and a $1/e^2$ waist of 10 μm $\times$ 100 μm. The trap depth created by this potential is approximately 10 μK.

The optical layout of the far-detuned laser is shown in figure 4.20. A series of half-wave plates and thin film polarizing beam splitters separates the beam into three paths. Beams 1 and 2 pass through a spherical telescope. By placing the first lens on a translation stage, control over the beam curvature after the telescope is obtained. This degree of freedom makes it possible to adjust the location of the focus inside the glass cell. To create the ellipticity in the beams, each beam passes through a cylindrical lens, causing astigmatism. The cylindrical lenses are rotated 90° relative to each other, so that the ellipticity in beams 1 and 2 are orthogonal after their recombination on a polarizing beam splitter cube. A $f = 63.5$ mm spherical lens focuses the beams into the glass cell.

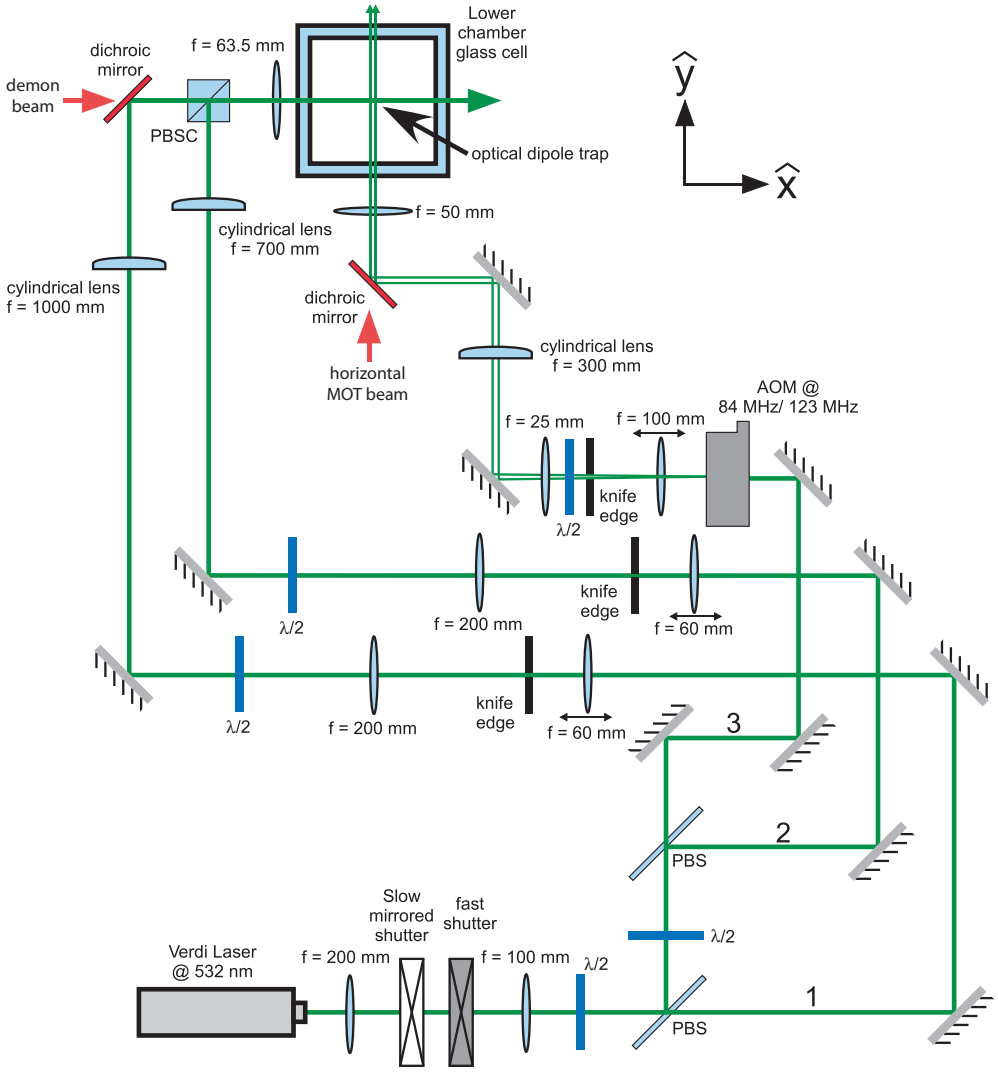

Figure 4.20: Setup of the far-detuned laser. Figure courtesy of Gabriel Price.

Beam 3 passes through an AOM, driven with two frequencies, 84 MHz and 123 MHz. This causes a slight difference in diffraction angle between the two first order spots, which is used to separate the endcaps inside the science chamber. When driving an AOM with two frequencies, a number of diffraction spots are generated. A one-dimensional spatial filter blocks out any undesired spots at the center of a telescope following the AOM. A $f = 300$ mm cylindrical lens creates the ellipticity of the laser beams. A dichroic mirror reflects the endcap beams and a 50 mm focal length spherical lens focuses the beams into the chamber such that they intersect with the V-shaped laser beams.

Dichroic mirrors are used to align near-resonant laser beams along the same optical axis used for the blue-detuned beams.

4.3.3 Imaging Setups

Both absorption and fluorescence imaging setups are implemented in the rubidium experiment along two different directions. The horizontal probe beam is combined with the beam path of one of the lower horizontal MOT beams using a polarizing beam splitter cube. A second polarizing beam splitter cube behind the glass cell picks off the imaging beam again. A series of two 120 mm lenses and a 4× objective lens image the atoms onto a CCD camera (Apogee AP9e). Because the imaging beam copropagates with the MOT/molasses beam the same optical setup cannot be used to take fluorescence images in the horizontal direction. Instead, a high solid angle collection lens collects the fluorescence light [75]. A motorized flipper mirror in front of the objective lens allows for fluorescence imaging using the same camera used for absorption imaging.

Along the vertical direction the absorption imaging beam is combined with the push beam on a polarizing beam splitter cube. For imaging the atoms the push beam is turned off, and the absorption imaging beam is tuned to the $|F = 2\rangle \rightarrow |F' = 3\rangle$ transition. The atoms are imaged onto a CCD camera (Apogee Alta U47+) with a net magnification of 4.33. The same optics used to create the absorption image along the vertical axis also allow for taking a fluorescence image along the vertical axis.

4.4 Computer Control

Precision timing and fast data-acquisition and analysis are necessary to successfully run a cold atom experiment. The experimental sequence is controlled by a PC containing several PCI boards from National Instruments (NI), two digital input/output boards (PCI-6533) and three analog output boards (PCI-6733). These cards form the heart of a home-built hardware system capable of controlling 80 digital outputs and 64 analog outputs. An additional NI card allows for communication to additional hardware via GPIB. This computer runs the program Control, written by a former postdoctoral

scholar, Florian Schreck. It is written in Visual C++ and allows control of the experiment with a timing precision of 1.6 μs.

A second PC runs the program Vision, also written by Florian Schreck. This program communicates with the cameras through a third PC. The only purpose of this computer is to ensure the communication between Vision and the cameras. Vision automatically downloads the pictures at the end of each experimental sequence, processes the images, and performs data analysis.

Chapter 5

Single-Photon Cooling of Rubidium

The first experiment showing single-photon cooling was a proof-of-principle demonstration using a magnetically trapped sample of ^{87}Rb. About 1.5×10^5 rubidium atoms were irreversibly transferred into a small optical dipole trap from a magnetic trap reservoir. The phase-space density of this trapped sample was a factor of 23 higher than the phase-space density that could be achieved by directly loading atoms into the optical dipole trap without single-photon cooling [61].

This chapter discusses the second implementation of single-photon cooling, where the amount of cooling was ultimately limited by trap dynamics [76]. Modifying the trap geometry from an all-optical trap to a gravito-optical trap increased the trap depth, allowing the capture of more atoms. In addition, a more detailed study of the cooling process was possible due to the simpler geometry.

5.1 Implementation of Single-Photon Cooling in Rubidium

The starting point of the single-photon cooling scheme is a magnetically trapped ensemble of atoms. For this proof-of-principle experiment this is achieved using standard laser cooling techniques. Atoms are captured in the upper MOT from the background rubidium vapor. The push beam transfers atoms into the glass cell, where the atoms are recaptured in the lower MOT. Typically about 10^8 atoms are loaded during a time of 1-2 seconds. The magnetic field gradient created by the lower MOT coils is about 8 G/cm. The MOT beam detuning is typically 15 MHz red detuned, and temperatures of around 150 μK are usual.

The temperature of the atoms is further reduced to between 15 and 20 μK using molasses cooling. For this stage the MOT beam detuning is usually increased to 50 MHz.

Atoms are then optically pumped to the $|F = 2, m_F = 2\rangle$ state. A weak uniform magnetic field ($B \approx 1$ G) is turned on during the optical pumping time (≈ 100 μs) to define a quantization axis. Approximately 73% of the atoms are transferred to the $|F = 2, m_F = 2\rangle$ state, while the other atoms remain in the $|F = 2, m_F = 1\rangle$ state.

All beams are then turned off and shuttered, and the magnetic field gradients are increased to 48 G/cm within a few ms, confining the atoms in the magnetic trap. To decrease the thermal equilibration time, the magnetic field gradients are increased to 96 G/cm in about 200 ms, increasing the collision rate. After about 5 seconds the atoms reach thermal equilibrium and the gradients are reduced to 72 G/cm. At this point about 10^7 Rb atoms at a temperature of 50 μK are confined in the magnetic trap. Controlling the temperature of the atoms in the magnetic trap is important for the study of single-photon cooling. By varying the detuning in the MOT beams during the loading and optical molasses phases, the temperature can be varied between about 30 and 55 μK.

Using standard laser cooling techniques is, however, not required to load atoms into a magnetic trap. It has been shown that it is feasible to decelerate a supersonic beam of atoms using an atomic coilgun [77–79]. At low velocities these atoms can then be directly loaded into a magnetic trap.

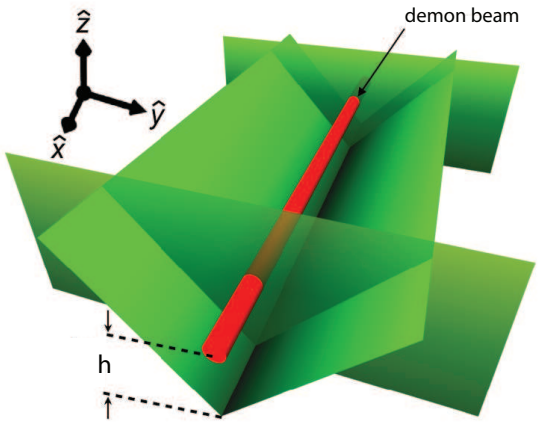

Figure 5.1: Alignment of the demon beam inside the optical trough.

Once the rubidium atoms are transferred into the magnetic trap, the optical

trough, see section 4.3.2, is placed below the ensemble, where the initial atomic density is negligible. The demon beam, see section 4.3.1.4, slightly detuned below the $|F = 2\rangle \rightarrow |F' = 1\rangle$ transition, is focused down to a final waist of 8 μm inside the trough. This setup is shown in figure 5.1.

A schematic of the implementation of single-photon cooling in rubidium using the gravito-optical trap is shown in figure 5.2. The figure shows the potentials along the gravitational axis. Atoms in the magnetic trap are predominantely trapped in the $|F = 2, m_F = 2\rangle$ state. Only the most energetic atoms have enough energy to reach the demon beam (near their classical turning points), at which point they have lost most of their kinetic energy and gained potential energy.

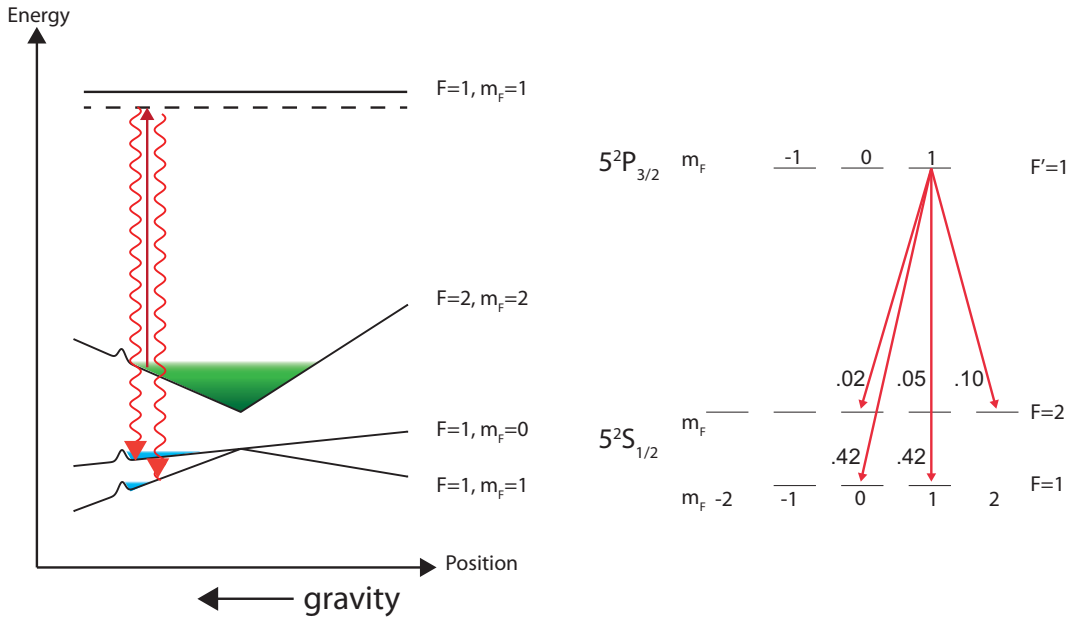

Figure 5.2: Implementation of single-photon cooling in rubidium. Near their classical turning points, atoms in the $|F = 2, m_F = 2\rangle$ state are excited to the $|F' = 1, m'_F = 1\rangle$ state and spontaneously decay. The probability to decay into the $|F = 1, m_F = 0\rangle$ and $|F = 1, m_F = 1\rangle$ states are given by the branching ratios (shown to the right). In these states the atoms are trapped in the gravito-optical trap.

When the atoms encounter the demon beam, they undergo spontaneous Raman scattering and about 84% of the atoms, as dictated by the branching ratios, are trans-

ferred into the $|F = 1, m_F = 0\rangle$ or $|F = 1, m_F = 1\rangle$ state via the single-photon cooling process. For atoms in the $|F = 1, m_F = 0\rangle$ state this is a purely gravito-optical potential, while for atoms in the $|F = 1, m_F = 1\rangle$ the magnetic interaction adds to the overall potential. Both states are trappable by the optical trough. In this new state, $|F = 1\rangle$, the atoms cannot regain the potential energy within the optical trough and are therefore effectively cooled.

The ^{87}Rb ground state hyperfine splitting is 6.8 GHz, meaning that once the atoms are transferred to the $|F = 1\rangle$ state, the demon beam is detuned by 6.8 GHz. Scattering of the demon beam of atoms in the $|F = 1\rangle$ state is therefore negligible, ensuring the irreversibility of the process.

By adiabatically reducing the current in the quadrupole coils, the magnetic potential is collapsed. During this ramp-off time t_{ramp} (typically on the order of 1 second) the atoms encountering the demon beam are always near their classical turning points, ensuring the cooling process. In order for the transfer to happen near the classical turning points, $\langle\tau\rangle \ll t_{ramp}$ must be satisfied, where $\langle\tau\rangle$ is the average oscillation period in the magnetic trap. In the rubidium magnetic trap $\langle\tau\rangle$ is about 20 ms.

Once the quadrupole coil current is reduced below 2.5 A (corresponding to a magnetic field gradient of 12 G/cm) the single-photon cooling process is complete. At this point atoms in the magnetic trap are no longer levitated against gravity and are lost from the trap. The atoms in the optical trough are then imaged to obtain information about the atom number, spatial distribution and temperature.

Figure 5.3 shows the incremental transfer of atoms into the optical trough as a function of the quadrupole coil current. The current is ramped linearly in time. The optical trough itself is a conservative trap, therefore any positive slope is indicative of successful single-photon cooling.

In the absence of any trap losses the increase in phase space density in the optical trough increases with a larger ramp time. However, unwanted scattering events and collisions with background gas lead to a finite trap life time. Balancing these effects dictates the optimum ramp time.

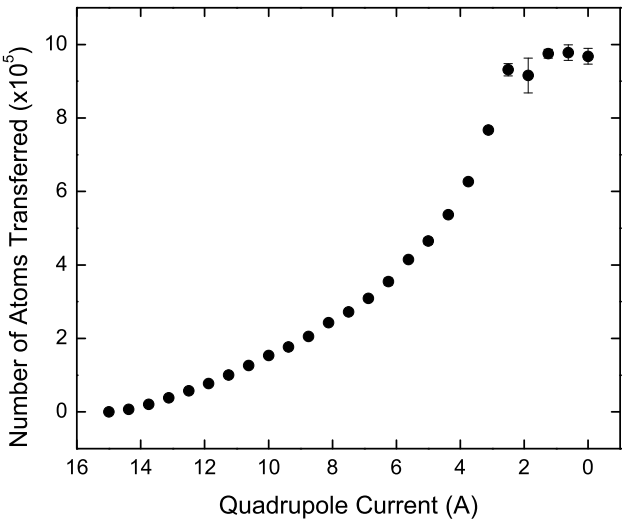

Figure 5.3: Incremental transfer of atoms into the gravito-optical trap. Below a current of 2.5A the magnetic potential does no longer support the atoms against gravity and the single-photon cooling sequence is complete.

Figure 5.4 shows an absorption image of atoms transferred into the optical trough via the single-photon cooling process. In this false color image about 1.5×10^5 atoms are trapped inside the optical trough.

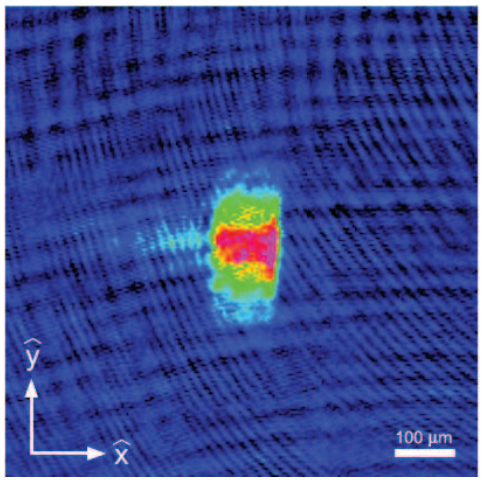

Figure 5.4: Absorption image of about 1.5×10^5 atoms transferred into the optical trough via the single-photon cooling process.

5.2 Branching Ratios and Population Distribution

The irreversible step in the implementation of single-photon cooling in rubidium lies in the spontaneous scattering event that occurs after the atom has been excited to the $|F' = 1\rangle$ state. Because of the branching ratios it is impossible to transfer all the atoms from the $|F = 2, m_F = 2\rangle$ state into one final trapped state in the gravito-optical trap. Instead they are evenly distributed between the $|F = 1, m_F = 1\rangle$ and $|F = 1, m_F = 0\rangle$ states. After completion of the single-photon cooling sequence, the distribution of atoms between the two final states is determined by applying a magnetic field gradient such that atoms in the $|F = 1, m_F = 1\rangle$ state are ejected out of the gravito-optical trap, leaving only the magnetically decoupled atoms in the $|F = 1, m_F = 0\rangle$ state in the trap. As expected about 50% of the total number of atoms are in this state. Only atoms in the $|F = 1, m_F = 0\rangle$ state are considered when calculating phase-space density.

About 10% of the atoms that encounter the demon will fall back into the $|F = 2, m_F = 2\rangle$ state, and about 5% will fall into the $|F = 2, m_F = 1\rangle$ state. These atoms are thus transferred back into the reservoir and can undergo another cycle of excitation and decay when encountering the demon beam. Only about 5% of the atoms decay into the untrapped $|F = 2, m_F = 0\rangle$ state and are lost from the system.

5.3 Effect of the Demon Beam Detuning

As mentioned before, the demon beam is slightly detuned from resonance. Naively one would assume that the beam should ideally be on resonance. This is not true, as figure 5.5 shows. The maximum number of atoms is transferred into the trough not at zero detuning, but rather at a power-dependent optimum value.

There are two reasons for this phenomenon. First, consider the scattered photon. As the density of atoms in the trap increases, the probability of reabsorption of this photon by atoms in the optical trough increases as well. If this photon is absorbed by an atom inside the trap, this additional scattering event can lead to trap loss. If the demon beam detuning Δ is away from resonance, the probability of reabsorption of this photon is dramatically decreased, as the scattering rate is roughly proportional to $1/\Delta$.

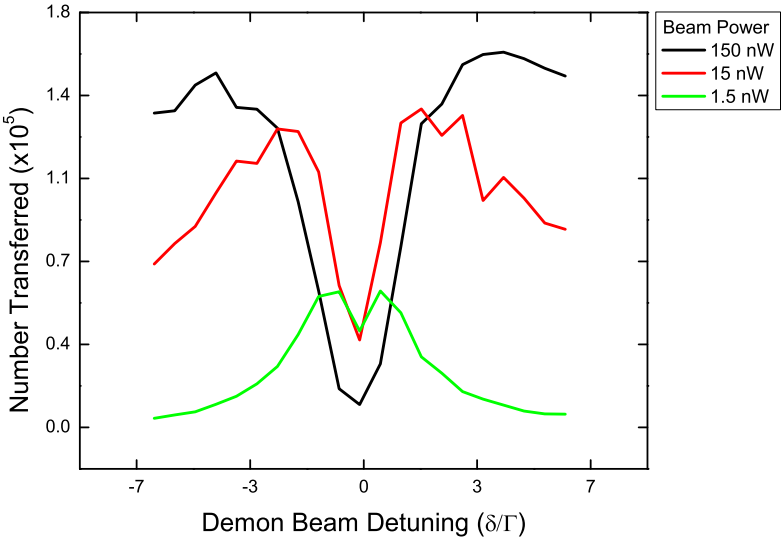

Figure 5.5: Atoms transferred into the optical trough as a function of the demon beam detuning.

This density effect is hidden underneath a second effect specific to the rubidium experimental setup. The walls of the glass cell are uncoated. This means that about 4% of the light is reflected back into the chamber at each surface. Because the demon beam is focused inside the glass cell, these reflections are divergent and are thus unfortunately incident on atoms in the magnetic trap. This leads to a trap loss of atoms inside the magnetic trap and decreases the number of atoms that can possibly be transferred into the optical trough. A calculation shows how detuning the demon beam frequency can alleviate this problem. Consider the saturation parameter $s_d = I/I_{sat}$ of the demon beam. The saturation parameter of the reflected light is then given by $s_r = \alpha s_d$, $\alpha \ll 1$. The ratio between the scattering events in the optical trough R_d to scattering events inside the magnetic trap R_{refl} as a function of the detuning is thus given by

$$\frac{R_d}{R_{refl}} = \frac{1}{\alpha} \frac{1 + \alpha s_d + (2\Delta/\Gamma)^2}{1 + s_d + (2\Delta/\Gamma)^2}. \tag{5.1}$$

Figure 5.6 shows a plot of equation 5.1 for values of $s_d = 6, \alpha = 0.01$ (blue) and $s_d = 20, \alpha = 0.01$ (red). This shows that as the detuning of the demon beam is increased, the effect of the partially reflected beam is minimized. It also shows that the negative

effect of the reflected beam at zero detuning is increased at higher beam intensities. This effect is clearly visible in figure 5.5.

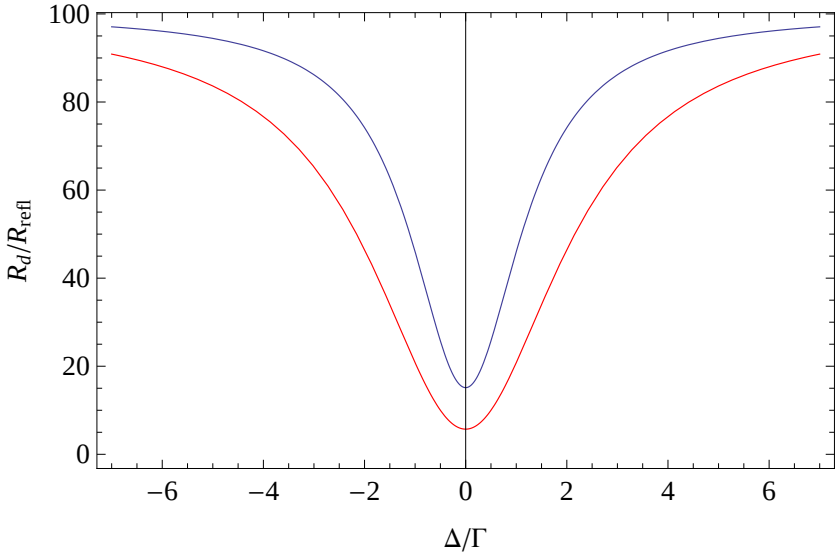

Figure 5.6: Ratio of excitation due to the demon beam and excitation in the magnetic trap for $s_d = 6, \alpha = 0.01$ (blue) and $s_d = 20, \alpha = 0.01$ (red). For larger detunings the scattering events transferring atoms into the optical trough far exceeds the scattering events leading to trap loss out of the magnetic trap. The number of detrimental scattering events at zero detunings increases with the beam power.

For a given demon beam power, an optimum detuning exists at which atoms encountering the demon beam near their classical turning point are efficiently transferred into the optical trough via Raman scattering, without depleting the atom number in the magnetic trap by unwanted scattering events.

5.4 Effect of the Demon Beam Position on Atom Number and Temperature

In order to optimize the increase in phase-space density achievable by single-photon cooling, the strategic placing of the demon beam within the optical trough needs to be considered. Figure 5.7 shows the effect of the height h_p of the demon beam above the optical trough vertex on the number N_O and the vertical temperature $T_O^{(z)}$ in the optical trough. To measure the vertical temperature $T_O^{(z)}$ the atoms are imaged before

they have time to rethermalize to thermodynamic equilibrium. Thus $T_O^{(z)}$ is a direct representation of the velocity distribution along the vertical dimension.

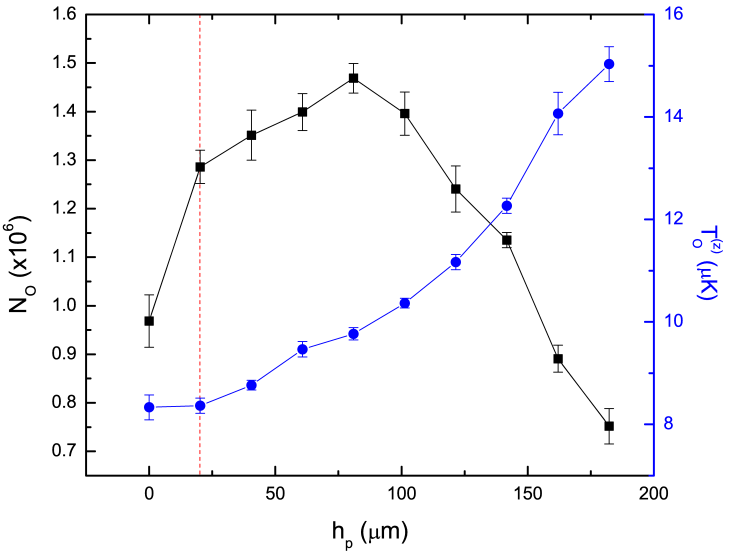

Figure 5.7: Atom number (black squares) and vertical temperature (blue circles) of atoms trapped in the optical trough as a function h_p (height above the demon beam above the trough).

The largest number of atoms can be transferred into the optical trap at a demon beam position of $h_p = 100$ μm, while the point corresponding to the highest phase-space density is located at $h_p = 41$ μm. To understand the temperature and transfer efficiency curves, consider the atoms being transferred into the $|F = 1, m_F = 1\rangle$ state. After the atoms encounter the demon beam they regain kinetic energy by falling into the bottom of the trough. For a demon beam height $h_p > 100$ μm, this energy gain is sufficient to overcome the optical potential created by the optical trough, resulting in loss from the gravito-optical trap. One might therefore think that in order to minimize this energy gain, the height of the demon beam h_p should be as close to the trough vertex as possible. However, as the demon beam gets closer to the trough vertex, the potentials of the demon beam and the optical trough beams start to overlap. This means that fewer atoms are reaching the demon beam, leading to a reduced transfer efficiency. By reducing the height h_p below zero, the atoms need to climb up the potential created

by the repulsive trough beams, gaining potential energy, before being transferred into the optical trough. The temperature $T_o^{(z)}$ of the beams will then again increase.

5.5 Transfer Efficiency and Phase-Space Compression

The fundamental limit of the temperature of single-photon cooling is given by the photon recoil temperature. For ^{87}Rb the recoil temperature is about 0.36 μK. Clearly the lowest temperatures measured along the vertical direction $T_O^{(z)}$ are far above that limit. Away from the optimum value for h_p, part of the energy can be attributed to energy regained after the transfer into the optical trough. But even at the optimum location, the temperature $T_O^{(z)}$ is above the recoil limit. The ramp time employed during the single-photon cooling sequence lies within the adiabatic regime, and the expectation is to capture atoms near their classical turning points. In fact, the energy increase due to transferring atoms away from their classical turning points is estimated to be only about $0.5\mu K$. The explanation for the excess energy lies with the geometry of the optical trough.

In this implementation, single-photon cooling is essentially a one-dimensional cooling technique, removing energy only along the vertical (z) direction. However, the optical trough geometry mixes the temperatures along the y and z dimensions quickly, due to the trough beams alignment at 45° in the y-z-plane. This leads to an increased value in the measurement of $T_O^{(z)}$.

The optical trough also has an effect on the expected temperature along the x and y dimensions. The trap depth of the optical trough is small compared to the trap depth of the magnetic trap. Hence the optical trough will necessarily truncate the transverse (x and y dimensions) temperature distribution of the atomic ensemble. The amount of truncation can be controlled by adjusting the trap depth of the optical trough (varying the beam power in the optical trough beams), as shown in figure 5.8. As the trap depth increases, atoms with higher energy along the transverse directions can be trapped, leading to an increase in the overall number of atoms trapped in the optical trough.

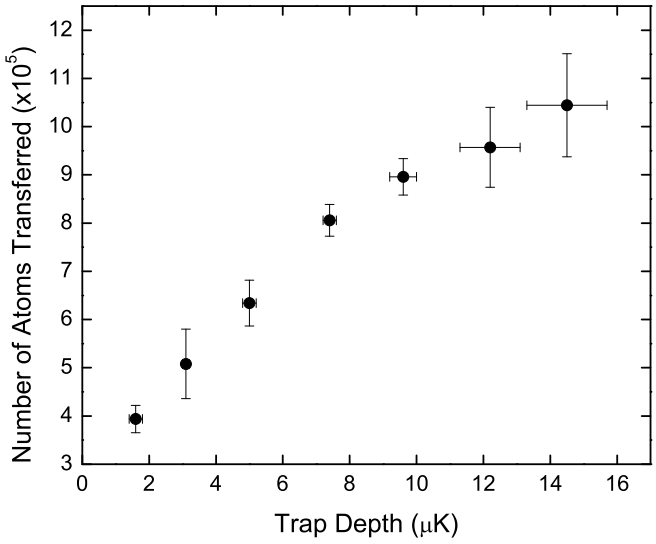

Figure 5.8: Atom number as a function of trap depth.

Additionally, the optical trough truncates the spatial distribution along the x and y directions. Figure 5.9 shows the number of atoms captured in the optical trough as a function of the separation between the end caps. A larger trap volume leads to less truncation and hence an increased number in the atoms captured from the ensemble.

This analysis shows that the final phase-space density is not necessarily the best measure to evaluate the efficiency of single-photon cooling. The final phase-space density measured is a three-dimensional quantity, while the cooling process in this implementation is only one-dimensional. To evaluate the vertical phase-space compression, it is helpful to look at the transfer efficiency η from the magnetic trap to the optical trap, $\eta = \frac{N_O}{N_B}$, N_O is the atom number in the optical trough and N_B the number of magnetically trapped atoms, and compare the measured values with the maximum values expected from an adiabatic transfer process.

The model describing the adiabatic transfer is greatly simplified by approximating the spatial distributions as Gaussian. The temperature distributions are assumed to follow Maxwell-Boltzmann velocity distributions. Neither the magnetic nor the optical trap provide harmonic potentials and thus the approximation of the spatial profile as

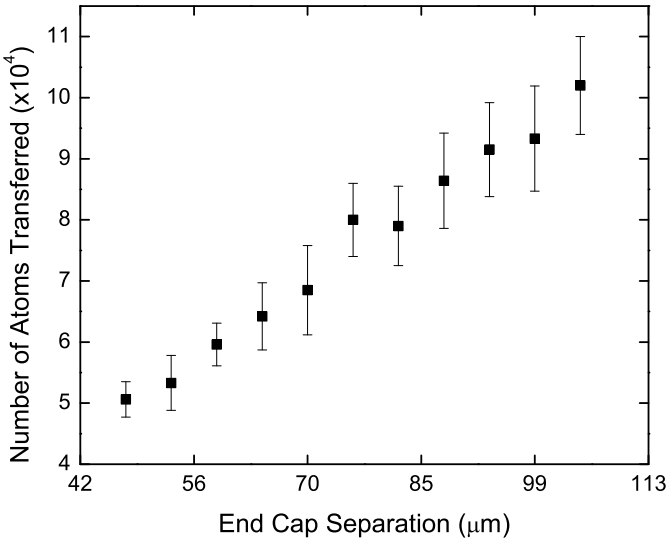

Figure 5.9: Atom number as a function of end cap separation.

Gaussian will result in a small error. In addition, any collisional interactions between the atoms are neglected in this model. Even though the model is only an approximation to the real process, it provides a simple means to gain more insight into the single-photon cooling process.

Given these assumptions, the one dimensional spatial and velocity distributions for a given atom number N

$$n_{1D}(x_i) = \frac{N}{\sqrt{2\pi\sigma_i^2}} \; e^{-\frac{x_i^2}{2\sigma_i^2}} \tag{5.2}$$

$$f_{1D}(v_i) = \sqrt{\frac{m}{2\pi k_B T_i}} \; e^{-\frac{m v_i^2}{2k_B T_i}} \tag{5.3}$$

depend only on two parameters: σ_i, defining the $1/e^2$ radius of the trap, and T_i, where the subscript i denotes the dimension.

An adiabatic process at maximum efficiency conserves the phase-space density ρ. The one dimensional phase-space density ρ_{1D}, given by

$$\rho_{1D} = n\lambda_{dB} = n\,\frac{h}{\sqrt{2\pi m k_B T}} = \frac{N}{\sigma}\,\frac{h}{\sqrt{2\pi m k_B T}} \propto \frac{N}{\sigma\sqrt{T}}, \tag{5.4}$$

is thus at best equal during the transfer from the magnetic to the optical trap. In a one-dimensional system without phase-space compression, a transfer efficiency η_i can therefore be defined as

$$\eta_i = \frac{N'}{N} = \frac{\sigma_i'}{\sigma_i}\sqrt{\frac{T_i'}{T_i}}. \tag{5.5}$$

In the three-dimensional case

$$\eta = \prod_{i\epsilon\{x,y,z\}} \frac{\sigma_i'}{\sigma_i}\sqrt{\frac{T_i'}{T_i}} \tag{5.6}$$

thus defines the transfer efficiency.

Neglecting the one photon recoil, a maximally efficient single-photon cooling sequence compresses the phase-space along the vertical (z) direction completely. In the quadrupole trap, the spatial distribution of atoms is anisotropic, $\sigma_x = 2\sigma_y \equiv \sigma$, but the atoms are in thermal equilibrium, $T_x = T_y \equiv T$. The maximum transfer efficiency is thus given by

$$\eta = \prod_{i\epsilon\{x,y\}} \frac{\sigma_i'}{\sigma_i}\sqrt{\frac{T_i'}{Ti}} = \frac{(\sigma_x'\sqrt{T_x'})(\sigma_y'\sqrt{T_y'})}{1/2\,\sigma^2\,T}. \tag{5.7}$$

Any transfer efficiencies below this value would be indicative of an incomplete phase-space compression along the vertical dimension or of an additional heating mechanism.

Equation 5.7 can be simplified even further by exploiting the linear dependence of σ on the temperature of the magnetic trap. This relationship is shown in figure 5.10. A linear regression in the relevant region of temperature leads to a fit for σ of $\sigma = (25.8 + 5.5\,T\ \mu\mathrm{K}^{-1})\mu\mathrm{m}$.

The expected transfer efficiency η, determined by the model, can now be compared with the measured transfer efficiency. The red line in figure 5.11 shows the upper limit of the transfer efficiency as given by the model. Experimentally measured transfer efficiencies are shown in black. The temperature and radius of the optical trough are given by $T_x' = 9.5\ \mu$K, $T_y' = 5.2\ \mu$K, $\sigma_x' = 63\ \mu$m and $\sigma_y' = 56\ \mu$m. The atoms in the optical trough do not have time to equilibrate, and the temperatures thus represent the strength of the trapping potential along the x and y direction respectively. In addition,

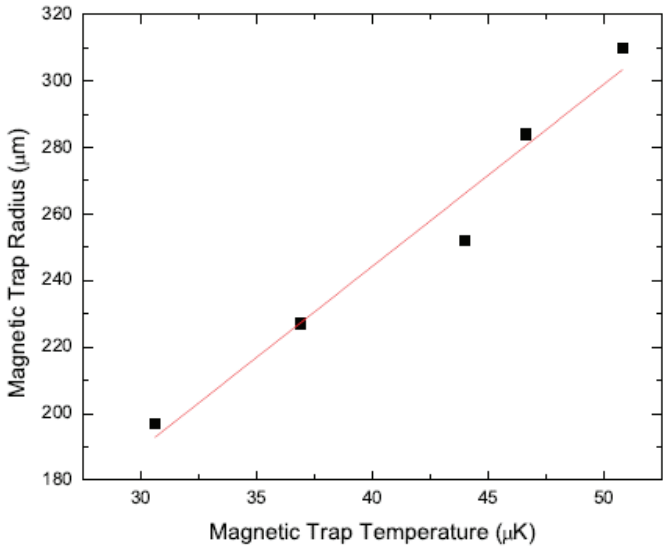

Figure 5.10: Radius of the magnetic trap as a function of temperature. A linear fit in this region results in $\sigma = (25.8 + 5.5T\ \mu\mathrm{K}^{-1})\mu\mathrm{m}$.

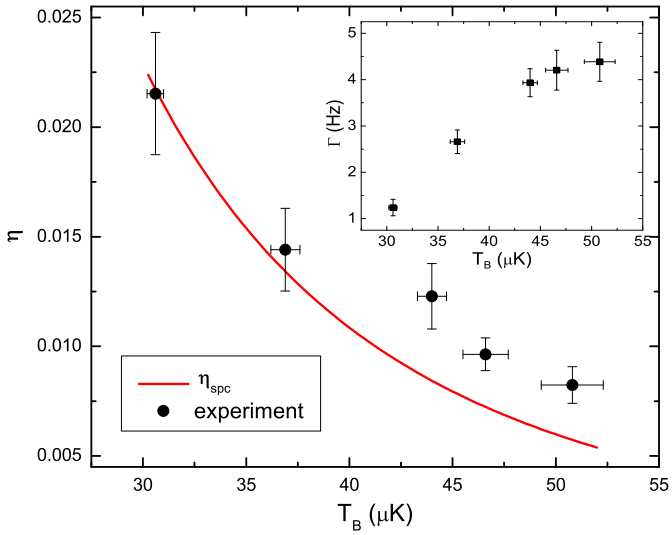

Figure 5.11: Transfer efficiency of the single photon cooling process. The red line is the expected maximum value from the model, black circles indicate data points. The inset shows calculated average single particle collision rates in the magnetic trap as a function of temperature. Rethermalization via collision leads to an increase in the transfer efficiency.

the optical trough geometry mixes the velocity distributions along the y and z directions. Because of the orientation of the optical sheet at 45°, it is reasonable to expect the measured temperature of $T'_y = 5.2$ μK to be only half of the trap depth along the y direction.

Figure 5.11 shows fairly good agreement between the model and experimental data. At higher magnetic trap temperatures, the experiment systematically exceeds the value predicted by the model. This can be explained by collisions occuring inside the magnetic trap, that are neglected in the model. The demon beam truncates the temperature distribution during the single-photon cooling sequence, and collisions between the remaining atoms in the magnetic trap lead to rethermalization. Even though the time scale for rethermalization is larger than the single-photon cooling sequence, partial thermalization occurs, as shown in figure 5.12.

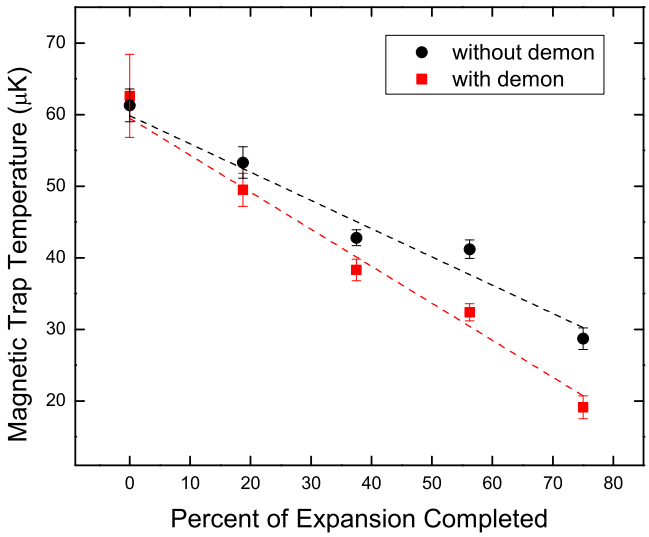

Figure 5.12: Rethermalization of the remaining atoms in the magnetic trap. In the presence of the demon beam the magnetic trap temperature decreases as the single-photon cooling process develops.

This partial rethermalization process provides additional cooling and thus phase-space compression, so that the measured transfer efficencies can surpass efficiencies predicted by the model. Obviously the strength of this rethermalization process depends

on the collision rate of atoms inside the quadrupole magnetic trap. The inset in figure 5.11 shows the calculated collision rates as a function of temperature. At higher temperatures the collision rate increases, leading to a faster thermalization time and thus additional phase-space compression.

The transfer efficiency can trivially be increased by increasing the spatial overlap between the optical trough and magnetic trap distributions, or by increasing the trap depth (or equivalently lowering the magnetic trap temperature). However, typically the amount of phase-space compression is important for cooling experiments. As discussed before, phase-space compression can be translated to a reduced temperature of the atomic ensemble.

The simple adiabatic model predicts the phase-space compression in a non-interacting ensemble to be

$$\frac{\rho'}{\rho} = \frac{\sigma}{\sigma'_z}\sqrt{\frac{T}{T'_z}}. \tag{5.8}$$

For a given optical trap geometry and trap depth, the amount of phase-space compression will thus increase with an increase in the magnetic trap temperature, despite a decreasing transfer efficiency. If collisions lead to (partial) rethermalization of the magnetically trapped atoms, the amount of phase-space compression achieved in the experiment will surpass the values predicted by the simple model.

5.6 Monte-Carlo Simulations

A series of Monte-Carlo simulations, written during the course of the experiment, give further insight into the single-photon cooling process and the trap dynamics. A Box-Mueller-algorithm creates random Gaussian distributions in velocity and position space, giving the initial conditions for the simulated magnetically trapped atoms. These initial coordinates evolve following the equation of motion inside the magnetic trap. (To ensure that this describes the situation in the experiment adequately, i.e. as long as collisions can be neglected, the spatial and velocity distributions are followed in time.)

The potentials of the optical beams are added to the overall potential, and the optical trap is defined as a subspace within the overall space. When an atom of the

ensemble walks into this region, its velocity is compared to the velocity trappable by the optical trap. If the atom is cold enough to be trapped, the single photon recoil velocity due to the demon beam is added. Following the probabilities given by the branching ratios atoms are then sorted into one of three categories: trapped in state $|F = 1, m_F = 0\rangle$, trapped in state $|F = 1, m_F = 1\rangle$, or untrapped. If its velocity is too high, the atom is removed from the simulation, mimicking trap loss.

These simulations confirm that only a subset of the total number of atoms has the chance to be transferred into the optical trap via single-photon cooling. A large number of the trajectories does not overlap with the optical trap volume or the atoms have too high a remaining velocity along the x and y directions to be trapped inside the optical trap.

These findings indicate that either an effective mixing of the atomic trajectories or a true three-dimensional cooling scheme would improve the performance of single-photon cooling.

5.7 Concluding Remarks

The largest amount of phase-space compression achieved in this implementation of single-photon cooling was a factor of 350 over the phase-space density of the magnetic trap. The final phase-space density was $4.9(3) \times 10^{-4}$, with a magnetic trap temperature of $T = 53$ μK and a corresponding radius of 515 μm. The transfer efficiency was 0.3%, leading to 3×10^5 atoms trapped in the optical trough at a temperature of $T' = 4.3$ μK.

This is a clear indication of the power of the single-photon cooling process, however, future improvements to the process should result in even larger increases in phase-space density. Even though it will probably remain challenging to generate a degenerate gas of atoms directly via single-photon cooling due to the single-photon recoil limit, it seems feasible to increase phase-space density enough to be able to initialize evaporative cooling.

This implementation was fundamentally limited by dynamics inside the magnetic trap. Only a subset of the total phase-space had the potential to be cooled and trans-

ferred via the single-photon cooling sequence. Either a randomization of trap trajectories or generalizing the cooling scheme to a fully three-dimensional cooling method should largely increase the transfer efficiency and phase space compression. A three-dimensional single-photon cooling scheme for hydrogen isotopes has already been proposed [80].

Chapter 6

Fock States and Laser Culling

In typical cold atom experiments, the number of atoms of the ensemble is unknown, and is usually determined after the experimental sequence via absorption or fluorescence imaging. Furthermore, repeating the experiment will lead to a different atom number, and the distribution will in general follow Poissonian statistics. Controlling the particle number precisely is a first step towards studying quantum entanglement and quantum collision on the few particle level, without resorting to ensemble averaged measurements, were even small variations from the average can have a large influence on the experimental result.

6.1 Atomic Fock States

In general a Fock state is a quantum state with a well-defined number of particles, e.g. photons or phonons, in a single mode. They are also frequently referred to as number states. Fock states are most commonly encountered when solving the quantum harmonic oscillator. In this case the energy levels are equally spaced, and the energy eigenstates are also the eigenstates of the number of phonons with energy equal to the energy splitting.

An N-photon Fock state in a cavity is defined as having N photons in a particular cavity mode. Photon Fock states have been realized experimentally using several different approaches, for example photon down-conversion [81], using a high-Q cavity [82], using a single atom trapped in a cavity [83], and by controlling emission from a single molecule [84]. Properties of photon Fock states have been studied in a number of experiments [85, 86], and the application of these photon Fock states to quantum computing and quantum cryptography has been considered [87, 88].

By comparison an atomic Fock state can be defined as having N atoms in a well-defined state of a trap. Photon Fock states can be achieved by creating and destroying photons directly. Atoms, in contrast, cannot be created or destroyed, and other methods are required to create an N-atom Fock state. In principle the atoms could be in any state of the trap, but the ground state appears to be the easiest to realize experimentally.

Multiple experiments have realized the production of N atoms in a trap without controlling the state [89–93]. For most quantum measurements the quantum state is very important, and the creation of a true atomic Fock state is therefore desirable.

The original proposal to generate atomic Fock States was to implement a 'quantum tweezer' to deterministically remove N atoms from a reservoir of condensate atoms through Landau-Zener tunneling [94]. In a second scheme, atoms are deterministically transferred from a Bose-Einstein condensate, confined in a weak trapping potential, to a selected state of a strongly confining potential [95].

A simpler scheme, called laser culling, has been utilized to observe sub-Poissonian number statistics in a trapped sample of bosonic ^{87}Rb [96] and to create two-atom fermionic Fock states with a fidelity (probability of finding two atoms in the ground state of the trap) of 96% [97]. The following section will describe the method of laser culling in more detail.

6.2 Laser Culling

After evaporative cooling, the atom number of a degenerate gas in a trap is unknown. If the trap depth is reduced, eventually the trap will be completely filled and any further trap reduction will force atoms to leave the trap. The atom number in this trap can be controlled, if the relation between the supported number of atoms and the trapping potential is known. Of course this implies that the potential can be controlled precisely enough, and that the trap reduction does not cause excitation within the degenerate gas.

For a quasi one-dimensional Bose-Einstein condensate in the Thomas-Fermi limit, the atom number is related to the trap depth by $N \propto U_0^{5/2}$, and thus a precise control of

the trap depth controls the atom number confined in the trap [98]. Rather than reducing the trap depth it should also be possible to control the number by squeezing the trap [99, 100]. Excitations within the degenerate gas can be avoided by adiabatic changes to the trapping potentials, however the adiabaticity requirement does not need to be fulfilled. Even sudden changes do not necessarily lead to excitation [101].

Maybe the most important question when working with Fock states of atoms is the fidelity with which they can be produced. Ultimately that will depend on the energy splitting between the two states $|N+1\rangle$ and $|N\rangle$ and the level to which the trapping potential can be controlled. From this point of view, bosons are not the ideal choice. In a BEC all atoms are in the ground state of the trap and strong interactions between the bosons are necessary to create the energy difference for the $|N+1\rangle$ and $|N\rangle$ state. Confining the atoms to a near 1-D configuration is thus required in order to maximize the energy difference.

For fermions on the other hand, the energy separation between different trap levels is enforced by the Pauli exclusion principle. These energy splittings can be orders of magnitude larger than in the boson case for similar trapping frequencies of the trap, and the production of Fock states should therefore be easier to achieve than in the bosonic case [102].

6.3 Laser Culling of ^{6}Li Atoms and Qubit Preparation

The requirement of ultrahigh-fidelity is important for continuing on with experiments on single-particle entanglement, quantum simulation and quantum computation. All these experimental results will ultimately depend on the reliability of producing a specific initial state of the system. If the initial system is flawed, the result will be drastically influenced. This section shows how one- and two-atom Fock-states of lithium atoms can be created with ultrahigh-fidelity ($> 99.99\%$). Additional details can be found in [102, 103].

Consider a degenerate gas of ^{6}Li confined in an optical dipole trap with trapping frequency ω. The degenerate gas can be created by evaporatively cooling a spin mixture

of atoms in the two hyperfine ground states $|F = 1/2, m_F = 1/2\rangle$ and $|F = 1/2, m_F = -1/2\rangle$. Each energy level will then be filled with two atoms up to the Fermi energy.

The production of a single-atom Fock state can be separated into three steps, and the fidelity of each of these steps has to be analyzed.

Step 1 is the production of the degenerate gas itself. The limit on the fidelity is given by the fidelity of having the ground state of the trap filled with two atoms.

Step 2 is the laser culling sequence or the controlled reduction of the trapping potential. In this step the fidelity will be limited by the precision with which the potentials can be controlled and by the probability of exciting atoms out of the ground state of the trap. The larger the energy splitting between different energy eigenstates, the higher the achievable fidelity. After the laser culling process the trap depth should be increased again to preserve the Fock state. This step is able to produce even number Fock states.

Step 3 allows to go from a two-atom Fock state to go to a one-atom Fock state. This is achieved by splitting the trapping potentials into two separate wells.

The ground state occupation probability in a degenerate gas will depend on the temperature of the gas. The average number of fermions with energy ϵ_i in state i is given by the Fermi-Dirac distribution

$$n_i = \frac{1}{e^{(\epsilon_i - \mu)/k_B T} + 1}. \tag{6.1}$$

Approximating the chemical potential with the Fermi energy, $\mu \approx E_F$, and assuming ϵ_1 to be negligible, the ground state occupation probability can be estimated by

$$n_1 = \frac{1}{e^{-E_F/k_B T} + 1}. \tag{6.2}$$

Temperatures of $T \approx 0.05\, T_F$ have previously been achieved in degenerate Fermi gases [104, 105]. At this temperature the ground state occupation probability is

$$n_1 \approx 1 - 2 \times 10^{-9} \tag{6.3}$$

and the loss of fidelity from vacancies in the ground state occupation are therefore negligible.

The fidelity of the laser culling process is analyzed by a 1-dimensional harmonic trap of size z, truncated at the energy E_t [102]. A schematic of the truncated potential is shown in figure 6.1.

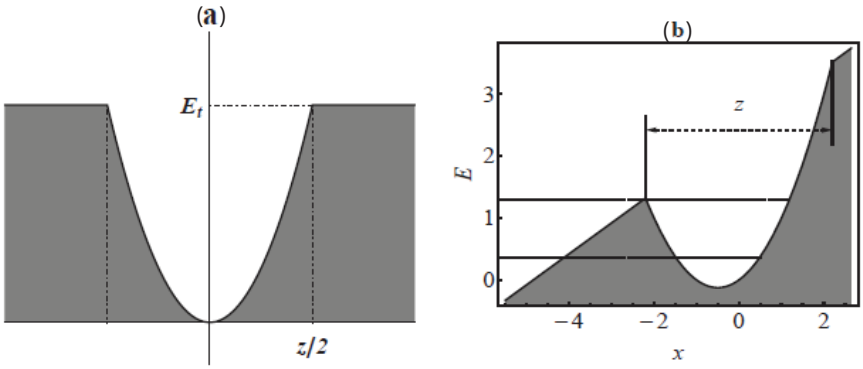

Figure 6.1: Trapping potentials used to calculate the fidelity of laser culling in ^{6}Li. (a) Truncated harmonic trap. The truncation energy is E_t and the trap size is z. (b) Truncated harmonic trap with a magnetic field gradient. The trap size z is defined as the length of the parabolic part of the potential profile. The lines represent the ground and first excited state energy levels. The unit of length is given by $x_0 = \sqrt{\hbar/m\omega}$, the unit of energy is $\hbar\omega$. Figure courtesy of Shoupu Wan.

Controlling the strength of the trapping potential is not the only option one has to control the number of trapped atoms. In addition, a magnetic field gradient can be applied, see figure 6.1 (b). This has two effects: all atoms that are no longer held within the trapping potential will be moved away from the system quickly. In addition, the magnetic field gradient allows for additional control of the overall trapping potential. In the presence of a magnetic field gradient true bound states no longer exist. Instead a series of quasi-bound states exists (figure 6.1 shows the ground and first excited state). In this situation the atoms can tunnel out of the trap. However, the atoms in the first excited state will tunnel out much faster than atoms bound more deeply. Once the excited state atoms have left the trap, the magnetic field gradient can be removed and the trap depth deepened to protect the remaining ground state atoms (the Fock state).

The difference in the lifetimes of the ground and first excited quasi-bound states determines the fidelity of creating a pair of atoms in the ground state of the trap. The

difference in the lifetimes is determined by the energy splitting between the energy levels. A tight confining potential is therefore desirable.

Figure 6.2 shows the fidelity of the laser culling process as a function of trap size and applied magnetic gradient force.

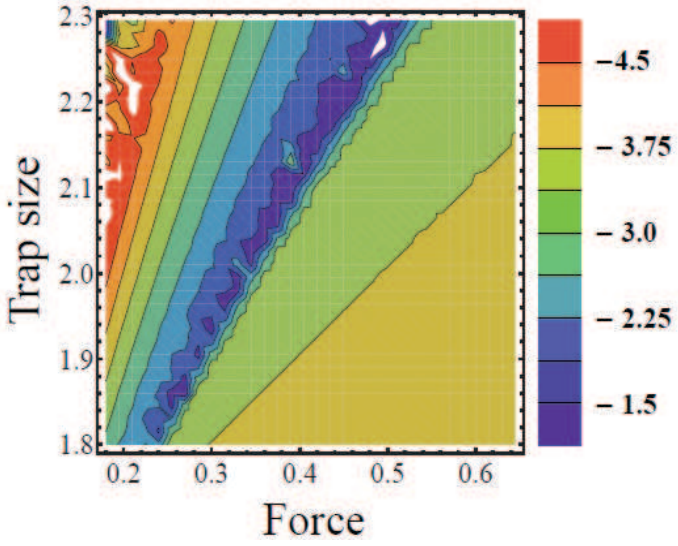

Figure 6.2: Fidelity of laser culling. Shown is the ground state fidelity loss in base-10 logarithm. Red (blue) represents high (low) fidelity. The white areas are out-of-range clippings and should be more intense than the color surrounding them. The unit of length is given by $x_0 = \sqrt{\hbar/m\omega}$, the unit of force is $\hbar\omega/x_0$. Figure courtesy of Shoupu Wan.

For an experimentally feasible set of parameters with trapping frequency $\omega = 2\pi \times 1$ kHz, magnetic field gradient $dB/dz = 0.66$ G/cm, a truncated trap size $z = 8.8$ μm and a tunneling time of 218 ms the fidelity of creating the two-atom Fock state is predicted to be larger than 0.99998 [102].

One additional step is required to create a one-atom Fock state: adiabatic splitting of the optical dipole trap into two separate wells. This step can be achieved with ultrahigh fidelity [106] and it is thus possible to initialize a qubit pair or an entangled (EPR) pair of atoms. At very low magnetic fields, one of the two atoms will be a high-field seeker, the other will be a low-field seeker. By applying a weak magnetic field gradient during the separation process, the high-field seeker and the low-field seeker can

be split deterministically, initializing a pair of qubits.

The entangled pair of atoms can be created in the presence of a stronger homogeneous magnetic field. At larger fields both atoms are high-field seekers, but more importantly they exhibit strong repulsive interactions. This interaction can be used to separate the atoms into the two separate wells. Under these conditions, where no preference of the atoms exists to go on way or the other, an entangled pair of atoms is created.

Experimentally, additional effects influence the fidelity. Atoms will scatter light from the trap beam. These scattering events lead to vacancies within the Fermi distribution and can thus lead to a reduction in the fidelity of the laser culling process. The use of far-detuned laser beams, where scattering is suppressed, mitigates this problem. Another source of possible fidelity loss stems from collisions of the trapped atoms with background gas. Ultra-high vacuum is therefore a requirement to create an atomic Fock state with ultra-high fidelity.

Chapter 7

Lithium Apparatus

Creating Fock states of lithium atoms requires a complex series of experimental steps, and many different sub-systems of the experimental apparatus have to work together. Even though great effort was made to keep the experimental setup as simple as possible, a large number of different devices are required. This chapter summarizes the design and construction of the experimental apparatus and details the methods employed for detection of the atomic ensemble.

7.1 Vacuum Chamber

Three main requirements determine the design of the vacuum chamber: the desired vacuum pressure, sufficient optical access, and ease of building and assembly. Collisions between the atoms of interest and background gas atoms are detrimental to the creation of Fock states of atoms. Therefore, vacuum pressures in the low 10^{-10} Torr range or better are necessary. Optical access is required for cooling and trapping the atoms, creating the optical dipole traps for evaporative cooling and laser culling, and for detection of the atoms.

The design of our vacuum chamber consists of two main parts: the oven chamber and the science chamber. They are connected through a differential pumping tube which also serves as the Zeeman slower. A complete drawing of the vacuum chamber is shown in figure 7.1. With the experience gained from previous cold atom experiments, the vacuum chamber is designed to rely almost exclusively on passive alignment. This, however, places tight requirements on the dimensions for machining of the parts. Most particularly, the parallelism of opposing flanges has to be precisely controlled to ensure a straight beam path for the effusive lithium beam.

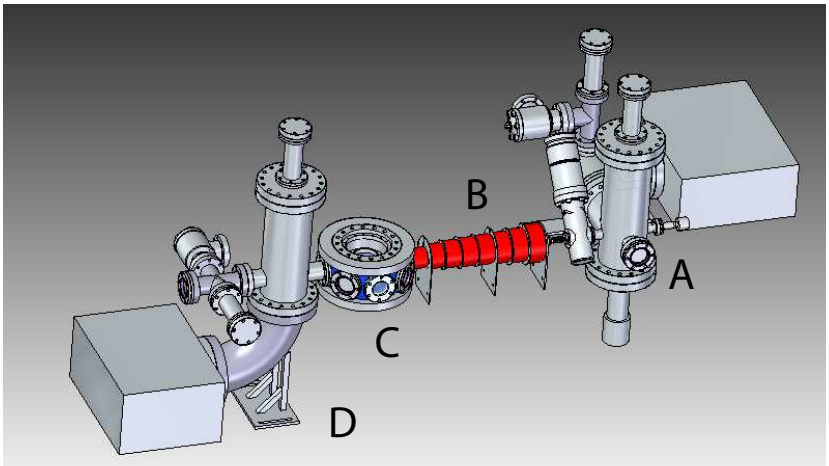

Figure 7.1: Design of the lithium vacuum chamber. A. Oven chamber, B. Differential pumping tube and Zeeman slower, C. Spherical octagon, D. Pumping chamber

During the assembly of the vacuum chamber, the horizontal and vertical position of the oven chamber with respect to the science chamber can be adjusted using a support structure constructed of 80/20 T-slot framing. A small bellows on the oven side of the differential pumping tube allows for angular adjustment, see chapter 7.1.2. The alignment is checked carefully using a telescope. Once the complete vacuum chamber is assembled and the support structure locked down, no further adjustment to the alignment of the atomic beam is possible.

7.1.1 Oven Chamber

The front end of the vacuum chamber houses the lithium reservoir (oven) and an atomic beam shutter allows for blocking of the effusive beam of the atoms. The rest of the oven chamber allows for attachment of an ion pump, titanium sublimation pump, an ion gauge and an angle valve required for the initial pump-out. The design of the oven chamber is shown in figure 7.2.

The design of the lithium reservoir is shown in figure 7.3. The outer diameter of the oven is 1.5 in. The oven can easily be heated to temperatures of 350°C and above using a band heater. Several layers of fiber glass and aluminum foil serve as insulation. In order to limit the heat flow from the lithium reservoir to the rest of the vacuum

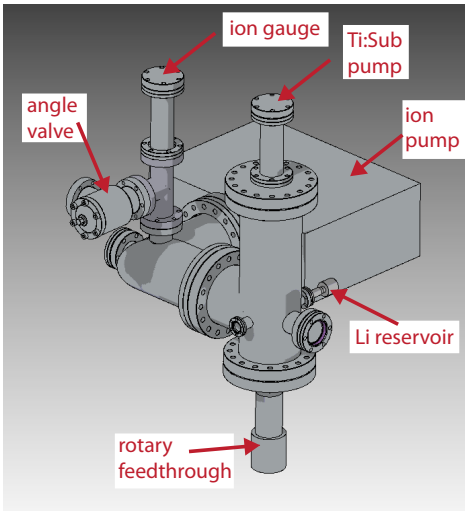

Figure 7.2: Oven chamber.

chamber, the wall thickness is decreased above the reservoir. The oven is attached to a modified 6 inch nipple with a nickel gasket. The choice of gasket material is based on the fact that hot lithium can attack copper gaskets, which, over time, can lead to a vacuum leak. This can be avoided by the use of the nickel gasket.

Figure 7.3: Lithium oven. The lithium is loaded into the reservoir which is heated to create an effusive beam of lithium atoms. Decreased wall thickness close to the reservoir (right) limits the heat flow from the reservoir to the rest of the vacuum chamber. The outer diameter of the reservoir is 1.5 in.

A rotary feedthrough (Accuglass Products Inc., HTR-133) is attached to the bottom of the 6 inch nipple. This feedthrough is controlled by a stepper motor. Due to space constraints, a custom coupling is located between the stepper motor and the rotary feedthrough. The rotary feedthrough blocks and unblocks the effusive atomic

beam using an atomic beam shutter, see figure 7.4. The top of the atomic beam shutter was polished to achieve a mirror-like finish, so that it is possible to look into the oven chamber as well as into the differential pumping tube. This greatly simplifies the initial alignment of the Zeeman slower beam through the vacuum chamber.

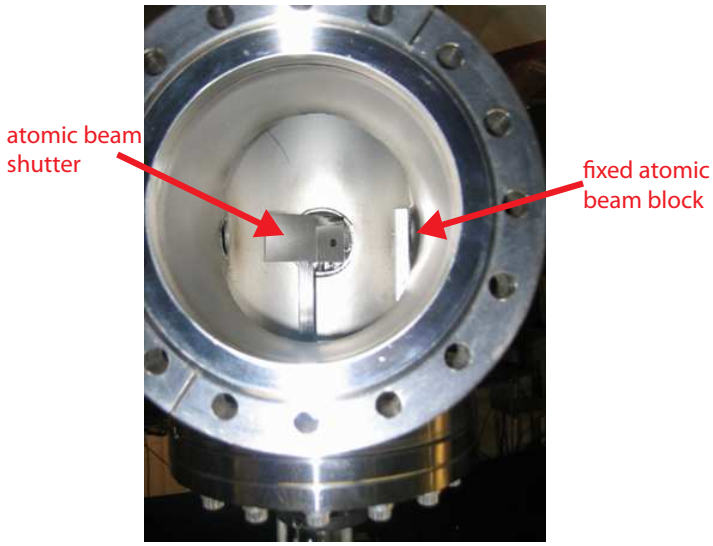

Figure 7.4: Atomic beam shutter and fixed atomic beam block inside the 6 inch nipple.

In addition to the movable atomic beam shutter, a fixed atomic beam block is mounted to a 6 inch flange at the bottom of the 6 inch nipple, see figure 7.4. At the atomic beam height the beam block has a 5 mm diameter hole. This setup only allows atoms within a small divergence angle to enter the differential pumping tube. The beam block reduces the flux of atoms to the science chamber by selecting only atoms within a small divergence angle around the Zeeman slower axis.

A titanium sublimation pump is mounted on top of the 6 inch nipple. In between the 6 inch nipple and the differential pumping tube, an all-metal gate valve (VAT Valve, 48124-CE01) allows for separation of the vacuum chamber into two separate chambers. This way the vacuum pressure in the science chamber can be maintained, even when vacuum needs to be broken on the oven chamber side to refill lithium.

Perpendicular to the Zeeman slower axis a 90° elbow is attached. An ion pump (Duniway Stockroom, VA-60-TR), an ion gauge (Duniway Stockroom, I-NUDE-F) with

an ion gauge controller (Granville Phillips, 350), and an angle valve (VAT valve, 54032-GE02) are connected via this elbow.

The entire oven chamber setup is supported by an 80/20 support structure.

7.1.2 Differential Pumping Tube

The differential pumping tube is located between the oven chamber and the science chamber. There is a small bellows (Standard Bellows Company, 64-34-1-EE) at the front end, see figure 7.5. This bellows allows for angular adjustment of the oven chamber relative to the science chamber. To achieve maximum differential pumping the diameter of the opening in the tube should be minimized and its length maximized. However, a longer length leads to a larger angular spread of the atoms, reducing the atomic flux in the science chamber. Ultimately the length of the differential pumping tube is determined by the length of the Zeeman slower.

Figure 7.5: The small bellows at the end of the differential pumping tube allows for the alignment of the atomic beam axis between the oven chamber and the science chamber.

To minimize the conductivity between the two parts of our vacuum setup, the profile inside the differential pumping tube matches the expected atomic beam profile. The initial opening in the differential pumping tube is 5 mm in diameter and it expands to a final diameter of 13 mm in 9 steps, as shown in figure 7.6. These steps approximate the ideal tapered profile. The groove in the back flange and the groove at the beginning of the differential pumping tube allow for mounting of the Zeeman slower coils on an additional tube.

A tube holding the Zeeman slower coils has to slide over the differential pumping

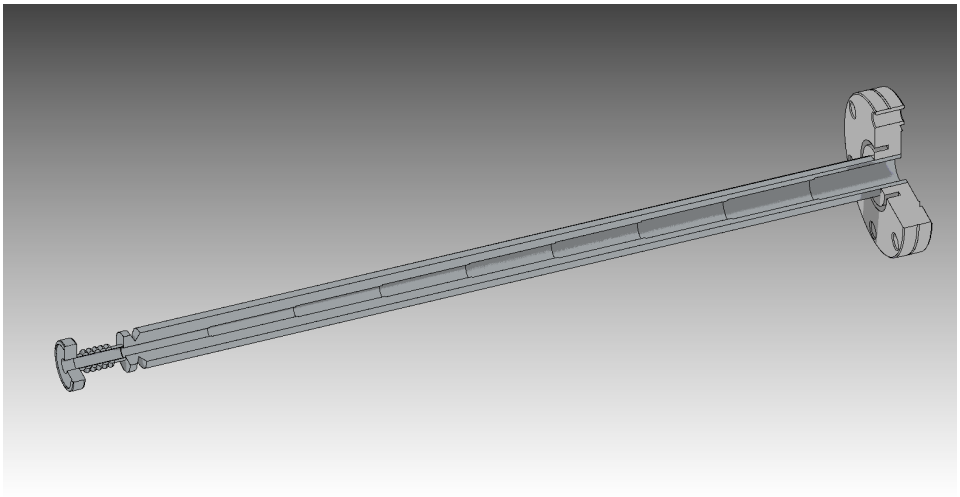

Figure 7.6: Differential pumping tube. The inner diameter changes from 5 mm to 13 mm in 9 steps. The groove in the back flange (right) allows for mounting of the Zeeman slower tube.

tube. Thus, the assembly requires the removal of the flange from the front end of the differential pumping tube; only then can the Zeeman slower tube (inner diameter = 25.53 mm) slide over the differential pumping tube. The flange is therefore cut in half, and the two halves are reassembled and connected to the gate valve after the Zeeman slower coils are in place. A photograph of the cut flange is shown in figure 7.7.

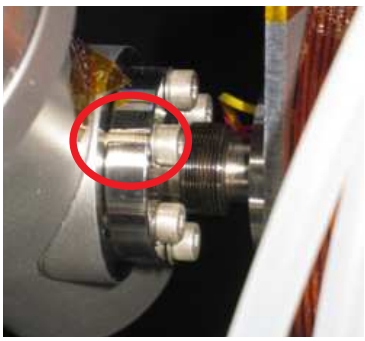

Figure 7.7: Cut flange on the differential pumping tube. After the Zeeman slower coils are in place, the two halves are assembled and connected to the gate valve.

7.1.3 Science Chamber

The science chamber consists of a "spherical octagon" chamber manufactured by Kimball Physics (MCF600-SO200800). Broadband anti-reflection (BBAR) coated

viewports (MDC, 450002) are attached to four of the eight 2-3/4 CF sealing surfaces. The coating covers the wavelength range from 650 to 1200 nm and was done by Thinfilm Labs. All viewports that can potentially come in contact with lithium have to be coated to prevent damage of the glass due to the deposition of lithium. Perpendicular to the Zeeman slower axis, two zinc-selenide (ZnSe) viewports (VG Scienta) are mounted. These viewports are used for the CO_2 laser beam access to the vacuum chamber. The ZnSe viewports are AR coated for 10.6 μm by the manufacturer. Figure 7.8 shows a schematic of the spherical octagon assembly.

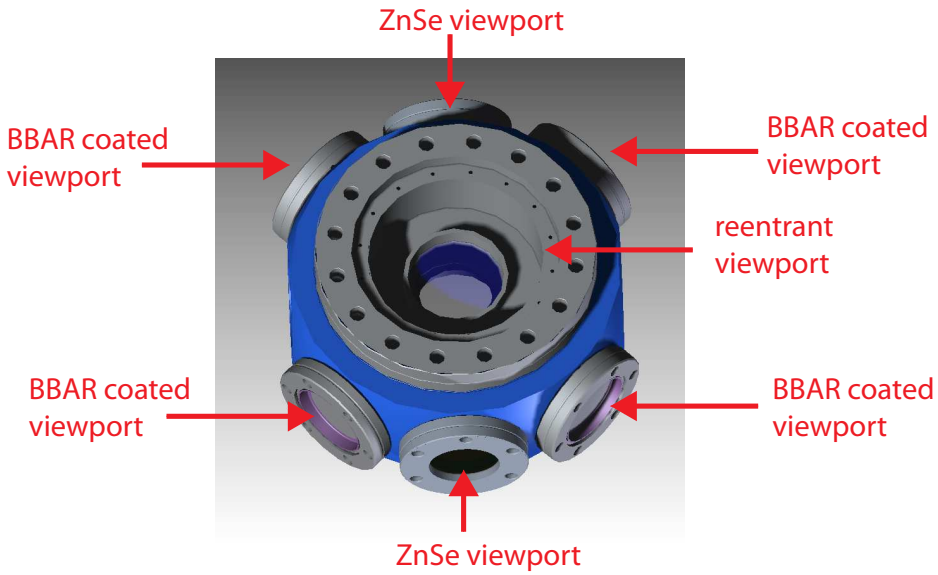

Figure 7.8: Octagon assembly. A second reentrant viewport is at the bottom of the spherical octagon, not visible in this schematic.

Two custom reentrant viewports (Special Techniques Group, Culham Centre for Fusion Energy, United Kingdom Atomic Energy Authority) seal the two 6 in CF ports. Because optical access should be close to the trapped atoms, the windows on these viewports reach into the spherical octagon. However, neither the Zeeman slower beam nor the MOT beams should be blocked, and this dictates the minimum distance between the windows of the reentrant viewports. The final distance between the viewports was thus chosen to be 16.6 mm. The windows on the reentrant viewport are coated with

the same BBAR coating that is applied to the standard viewports. Figure 7.9 shows a photograph of one of the reentrant viewports.

Figure 7.9: Photograph of the reentrant viewport. The size of the flange is nominally 6 in.

An additional feature of the design is that it allows mounting of the Feshbach coils inside the reentrant viewports. These coils need to be mounted in Helmholtz-configuration to produce the homogeneous magnetic field for tuning the Feshbach resonance during the evaporation sequence. Because the coils can be mounted inside the reentrant viewport, both the radius of the coils and the distance between the coils can be small, thus reducing the current required to generate fields of up to 850 G. A ring of bolt holes simplifies the mounting of the Feshbach coils, see figure 7.8.

Opposing the Zeeman slower port, a second 6 inch nipple, customized in our machine shop, connects to an ion pump, a titanium sublimation pump, an ion gauge and an angle valve for the initial pump-out of the vaccum chamber. The ion pump (Duniway Stockroom, RVIP-75-S) is connected through an elbow to the bottom of this 6 inch nipple. The titanium sublimation pump (Duniway Stockroom, TSP-275-003) is mounted on top of the 6 inch nipple. Along the Zeeman slower axis, a 2-3/4 inch cross connects to the ion gauge (Duniway Stockroom, I-NUDE-F with Granville Phillips Controller, 350) and an all-metal angel valve (Vat-Valve, 54032-GE02). This assembly is shown in figure 7.10. At the end of the cross, another 2-3/4 inch viewport, identical to the ones connected to the spherical octagon, seals the last vacuum port. This viewport is used by the Zeeman slower beam. The lithium atoms not slowed by the Zeeman slower or

not trapped by the MOT impinge on this viewport. It is therefore constantly heated to a temperatue of about 120°C with a band heater to avoid coating of the window. Both the 6 inch custom nipple and the 6 inch elbow are electropolished (Central Electropolishing Co.) to reduce outgassing in the science chamber.

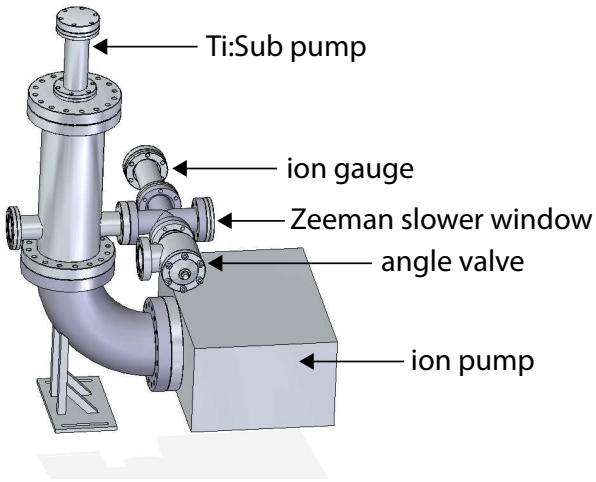

Figure 7.10: Science chamber assembly.

7.1.4 Bake-Out

To achieve vacuum pressures in the 10^{-10} Torr range or better, ion pumps and titanium sublimation pumps, rather than turbo-pumps, are connected to the vacuum system. This also eliminates moving pumps, reducing vibrations. However, for the initial pump-out a turbo pump is necessary. The turbo-pump is connected to the vacuum chamber through two angle valves. After bake-out these valves are closed, and the turbo-pump can be disconnected.

Ultra-high vacuum pressures would be difficult to reach without baking of the chamber. Baking increases the outgassing speed, especially for water attached to the stainless steel walls of the vacuum chamber parts, thus drastically decreasing the amount of time necessary to reach the desired pressure. At pressures of 10^{-6} Torr or better the baking of the chamber can start. Typically the chamber is wrapped with heater-tapes and insulated using aluminum foil. The higher the temperature during the bake-out,

the shorter the bake can be. However, multiple elements in the chamber limit both the maximum temperature and the maximum temperature gradients during the baking process. A multiple step bake-out is therefore used.

Even before the assembly of the vacuum chamber, an air-bake of the differential pumping tube is done to remove any residual oil deposited by the machining process. The differential pumping tube, after thorough cleaning with acetone and methanol, is thus heated to about 200°C for about 24 hours.

For the first bake-out the ZnSe viewports are not attached to the vacuum chamber. The maximum baking temperature of the ZnSe viewports is low (120°C) due to the AR coating, and would limit the overall temperature of the vacuum chamber during the bake. Two blank flanges seal the ports typically occupied by the ZnSe viewport. The chamber is wrapped in flexible heater-tapes and covered in aluminum foil before being heated to 200°C, the maximum temperature specified for the rotary feedthrough and the highest recommended temperature for the reentrant viewports.

After the initial bake, the ZnSe viewports are attached to the spherical octagon. To minimize the contact of any chamber walls with air, the whole chamber is vented with high-purity argon gas and the viewports are attached as quickly as possible. The thick AR coating on the ZnSe viewports is extremely sensitive to any spatial and temporal temperature gradients. To minimize the risk of damaging the coating, a brick oven surrounds the spherical octagon. The bricks are made from an insulating ceramic and wrapped in aluminum foil to minimize the release of dust. The large air volume inside the brick oven mitigates temperature gradients. The final baking temperature with the ZnSe viewports attached is about 100°C.

The lithium reservoir is run at a temperature of 350°C during the experiment. It is therefore necessary to outgas the lithium to at least this temperature. The lithium used in the experiment is 95% enriched ^{6}Li from Sigma-Aldrich and Medical Isotopes Inc. The enriched lithium is stored in oil to avoid oxidation. Even after multiple cleaning cycles, involving removal of the outermost layer of the chunk of lithium and chemical cleaning of the metal, oil contamination cannot be completely ruled out. Before outgassing the lithium at a temperature of up to 400°C, the gate valve to the science chamber is closed.

Should contamination of the vacuum system happen, it would be confined to the oven chamber only, where the requirements for the vacuum pressure are not as stringent.

After the complete bake-out process ultra-high vacuum condition are achieved throughout the vacuum system.

7.2 Magnetic Systems

Magnetic fields are used to manipulate the atomic structure or atomic interactions during various stages of the experiment. All magnetic fields are produced by electromagnetic coils. Before winding the coils from copper wire, the ideal magnetic fields are calculated and subsequently approximated as well as possible by coils that are reasonable to fabricate.

7.2.1 Zeeman Slower

There are different types of Zeeman slowers, increasing-field, spin-flip, and decreasing-field Zeeman slower. The lithium Zeeman slower falls into the category of decreasing-field slowers, meaning that the atoms encounter the strongest magnetic field first.

Figure 7.11 shows the ideal magnetic field of a decreasing field Zeeman slower for lithium. This magnetic field can be well approximated by a tapered coil, where the number of turns decreases along the axis of the Zeeman slower. However, due to ease of construction, a set of eight individual coils is used to approximate the field instead. The field generated by each individual coil is shown in green, the field due to the pair of MOT coils in anti-Helmholtz configuration is shown in red. More details on the MOT coils are given in chapter 7.2.2. The total magnetic field due to all coils in the assembly is shown in blue.

The eight individual coils are separated by an aluminum spacer, as shown in figure 7.12. The first seven coils are run in series at a current of 5.8 A. The last coil is operated separately at a current of 4.3 A. Each coil is wound with square wire (MWS Wire Industries, 40039). The bare wire is an AWG 18 wire and has dimensions of 1.29 mm$\times$1.29 mm. The copper wire is coated with Polyimide-ML, which can withstand

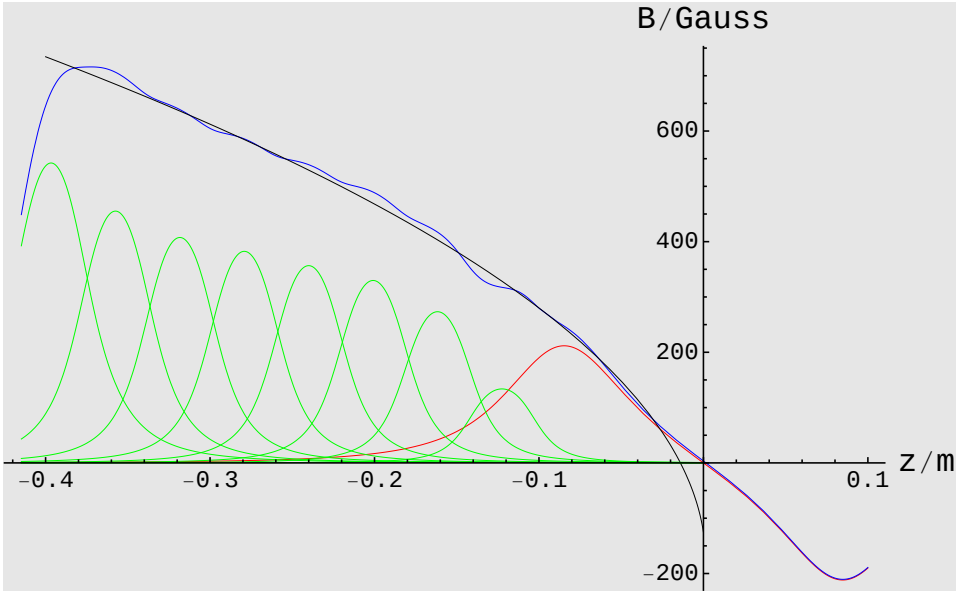

Figure 7.11: Simulation of the Zeeman slower magnetic field profile. The black line shows the ideal magnetic field for decelerating atoms in the Zeeman slower. The green line shows the field of each of the eight individual Zeeman slower coils, the red line shows the field due to the MOT coils. Together the Zeeman slower coils and the MOT coils lead to the blue line. The origin is at the center of the MOT.

temperatures of up to 200°C. Including the coating, the outer dimensions of the wire are 1.45 mm × 1.45 mm. A layer of epoxy (Epoxy Technology, 360) is applied after each individual layer of the coil is wound to ensure mechanical stability and durability of the coils. Once the coil is finished, the epoxy is allowed to dry at room temperature over night. Subsequently the coils are baked at 100°C for one hour to cure the epoxy completely. The finished coils are then assembled onto a tube and mounted around the differential pumping tube.

The length of the Zeeman slower is 312 mm and the total distance from the start of the Zeeman slower to the center of the MOT is 414.7 mm. Each coil has 26 turns axially and between 5 and 19 layers radially. The inner radius of the coils is 15.5 mm. The Zeeman slower has a resistance of approximately 3.5 Ω, leading to a power dissipation of roughly 120 W. The individual parameters of each coil are listed in table 7.1.

Before attaching the Zeeman slower to the vacuum chamber, the magnetic field

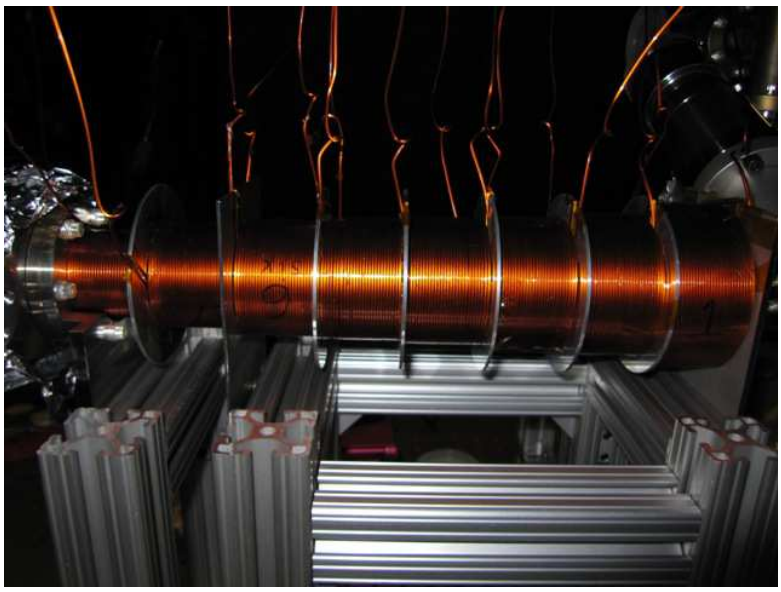

Figure 7.12: The assembled Zeeman slower. The total length of the slower is 312 mm.

along the axis is measured using a Gaussmeter. The data (blue) is shown in figure 7.13 and compared to the expected field (grey) and the ideal magnetic field profile (black).

Coil #	Radial turns	Resistance	Current	Power	Outer diameter
1	19	0.87 Ω	5.8 A	29.3 W	85.9 mm
2	15	0.62 Ω	5.8 A	20.9 W	74.4 mm
3	13	0.51 Ω	5.8 A	17.2 W	68.6 mm
4	12	0.46 Ω	5.8 A	15.4 W	65.7 mm
5	11	0.41 Ω	5.8 A	13.7 W	62.8 mm
6	10	0.36 Ω	5.8 A	12.1 W	59.9 mm
7	8	0.26 Ω	5.8 A	9.1 W	54.1 mm
8	5	0.15 Ω	4.3 A	2.8 W	45.5 mm

Table 7.1: Properties of the Zeeman slower coils

Using the combination of the MOT coils and the Zeeman slower coils to produce the Zeeman slower field profile has some advantages over other designs. In this setup the Zeeman slower finishes deceleration of the atoms right at the location of the MOT. If the Zeeman slower ended before the trapping volume of the MOT, the decelerated and thus slow atoms would still have to travel some distance before being captured by the MOT beams. Due to the transverse velocity of the atoms, the density of atoms at the center of the MOT would therefore be reduced, potentially leading to smaller trapped

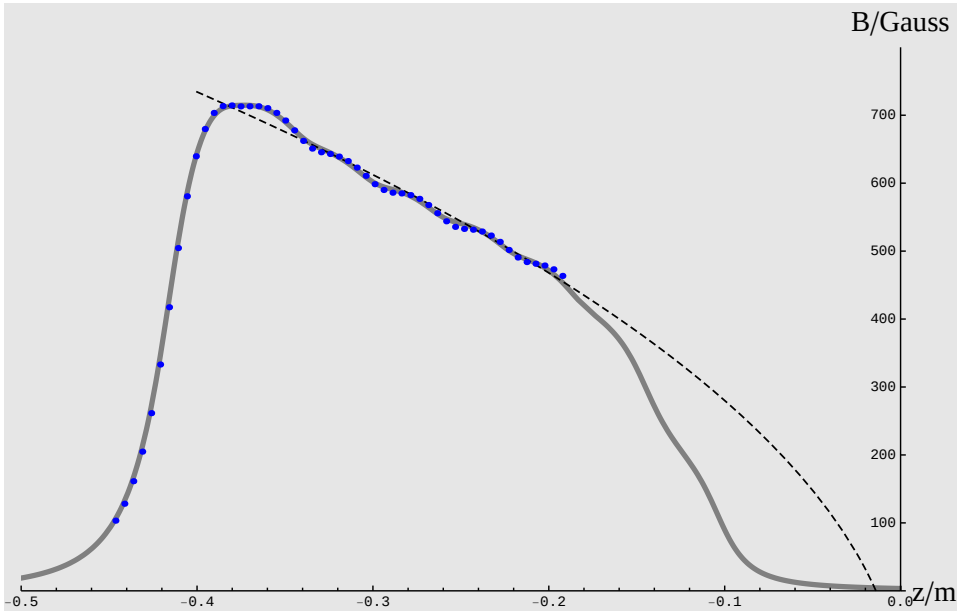

Figure 7.13: Measured Zeeman slower field profile. The ideal beam profile (black) and the expected profile (grey) are compared to experimental data (blue).

atom numbers.

During the experiment the Zeeman slower does not run continuously, but turns on only for one to two seconds during each experimental cycle. It is therefore not necessary to cool the Zeeman slower coils. However, during the alignment procedure the Zeeman slower is frequently run at a larger duty cycle. In order to avoid overheating of the Zeeman slower coils, an interlock system is installed that will automatically shut-off the current if the temperature of the coils exceeds 65°C. It also limits the time the Zeeman slower can be run continously to 15 minutes.

The current to the Zeeman slower is provided by two separate power supplies. Coils 1-7 are driven by a Sorensen power supply (DCR40-35A), the current to coil 8 is provided by a Kepco power supply (36-15M). To improve the current stability, a PID current controller regulates the current [68]. In addition this current controller is TTL-controlled by the computer control program, so that the current to the Zeeman slower coils can be turned on and off remotely.

7.2.2 MOT Coils

A second set of coils used during the experimental sequence is a pair of anti-Helmholtz coils that creates the quadrupole magnetic field of the MOT. These coils are designed to fit around the flange of the reentrant viewport, see figure 7.14. Each MOT coil is comprised of four individual coils, which are then stacked and wired in series. The individual coils have 22 windings made from flat wire with dimensions 4.85 mm $\times$ 1.12 mm (MWS Wire Industries, 41172) and polyimide-220 coating. The inner radius of the coils is 152 mm, just large enough to slide over the flange of the reentrant viewport. The coil windings are connected using Epoxy Technology 360 epoxy. The individual layers are then glued together using a thermally conductive epoxy (Epoxy Technology, 920) and attached to a copper plate. This copper plate is water-cooled to avoid overheating of the coils. The flow rates through the copper plate are 2.4 l/min and 2.6 l/min for the lower and upper MOT coils respectively.

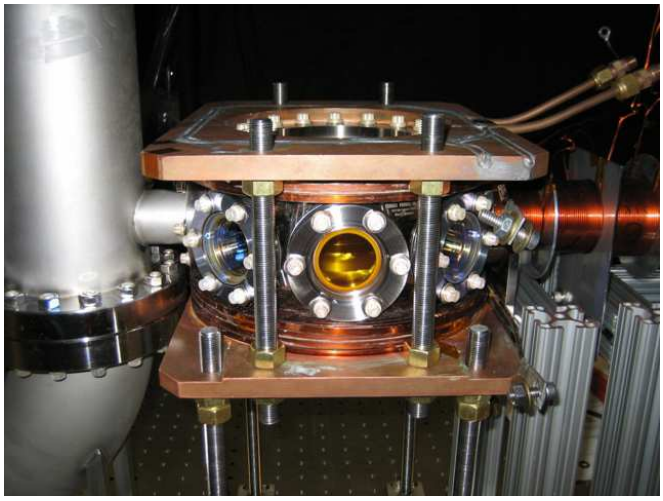

Figure 7.14: MOT coils mounted around the reentrant viewport.

The MOT coils are separated by 70.6 mm, the height of the spherical octagon. At a current of 36 A, the gradients near the center of the trap are 43.7 G/cm axially, and 21.9 G/cm radially. The coils are wired in series, and the current is supplied by three power supplies (Lambda, GEN80-19) wired in parallel. One of the power supplies is programmed as the master power supply, the other two as slave power supplies. In this configuration only one of the power supplies needs to be controlled; the other two will

follow the master supply. This setup allows for an increase of the output current at the cost of reducing the available voltage. The properties of the MOT coils are summarized in table 7.2.

Number of coils	2
Number of layers per coil	4
Number of turns per coil	22
Current through each coil	36 A
Axial gradient	43.7 G/cm
Radial gradient	21.9 G/cm
Inner diameter of the coils	152 mm

Table 7.2: Properties of the MOT coils

The calculated magnetic field profiles of the MOT coils in radial and axial directions are shown in figures 7.15 and 7.16. Experimental data (blue) are measured using a Gaussmeter.

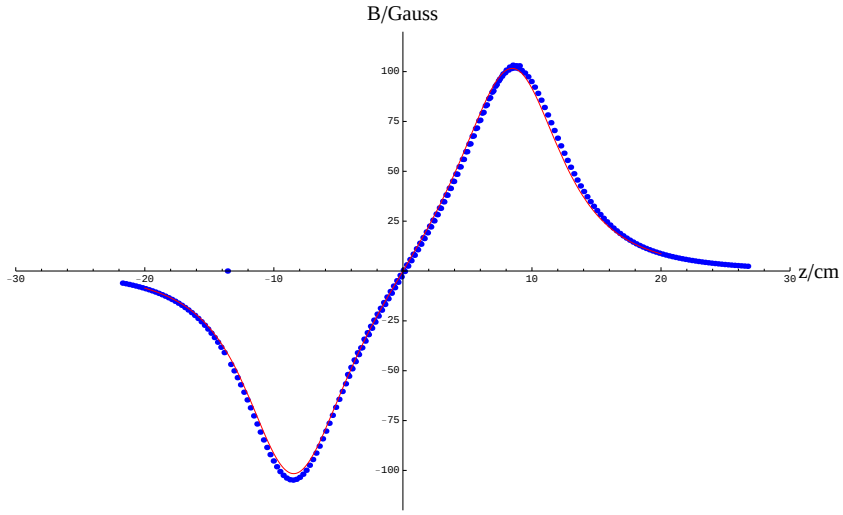

Figure 7.15: Radial field profile of the MOT coils. The solid line is the calculated field, experimentally determined field strengths are shown in blue.

Under normal operation the coils will not exceed a temperature of 30°C. During alignment of the MOT, when the coils are run continously, the temperature of the MOT coils can, however, be quite high. Unfortunately, a heating of the coils is closely coupled to a heating of the ZnSe viewports due to their proximity to each other. To avoid any

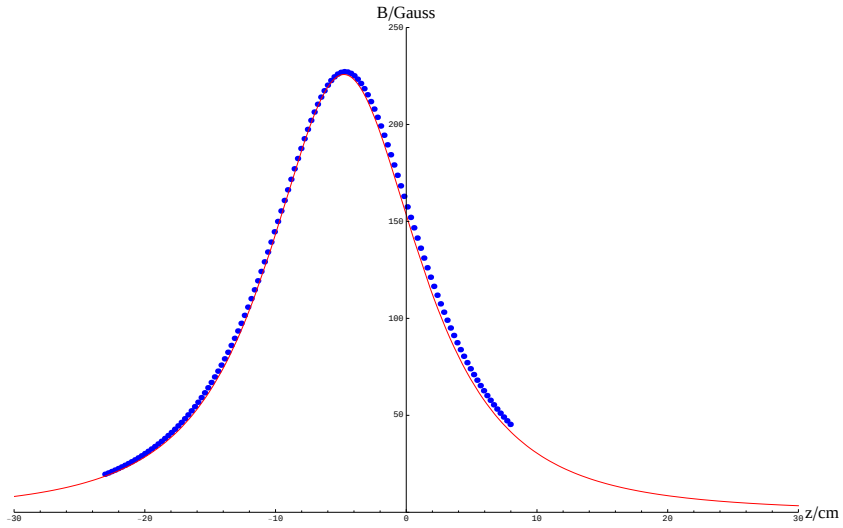

Figure 7.16: Axial field profile of the MOT coils. The solid line is the calculated field, experimentally determined field strengths are shown in blue.

large temperature gradients an interlock system is installed. The interlock stops the current to the MOT coils if either the cooling water is not flowing or the temperature of the coils is exceeding 30°C.

7.2.3 Feshbach Coils

The most difficult set of coils to design is the pair of Feshbach coils which are located inside the reentrant viewport, as shown in figure 7.17. For fast evaporative cooling a constant magnetic field must be tuned near the Feshbach resonance located at 834 G. Because the trap depth of the optical dipole trap is significantly lowered during the evaporation sequence, any forces exerted by magnetic field gradients can possibly lead to traploss. A homogeneous field is therefore necessary. The Feshbach coils are consequently designed in Helmholtz-configuration.

The inner diameter of the coils is 29.5 mm, fitting around the window of the reentrant viewport; the outer diameter is about 45 mm. They are separated by approximately 36 mm. The coils are wound from flat copper wire with dimensions 0.43 mm × 7.6 mm, (MWS Wire Industries, 41137). Each coil has 26 windings, leading to a magnetic field strength of 6.34 G/A. To create the required fields strengths, a current of up

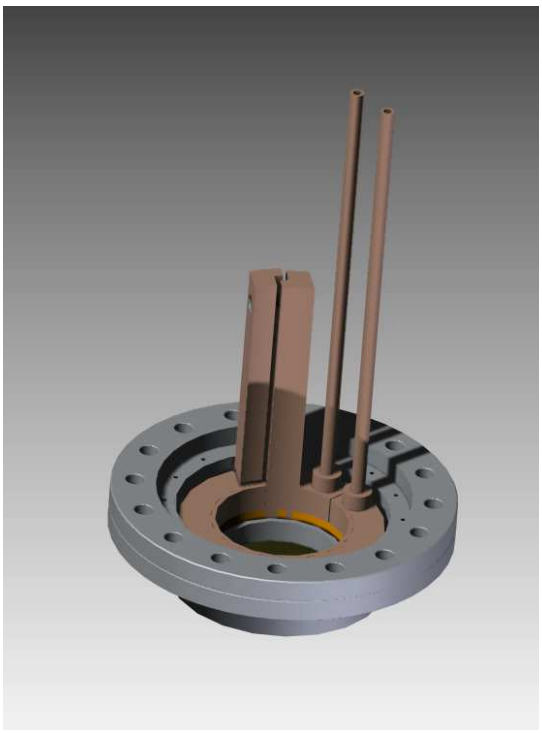

Figure 7.17: Feshbach coils located inside the reentrant viewport.

to 150 A is necessary. Figure 7.18 shows the calculated magnetic field.

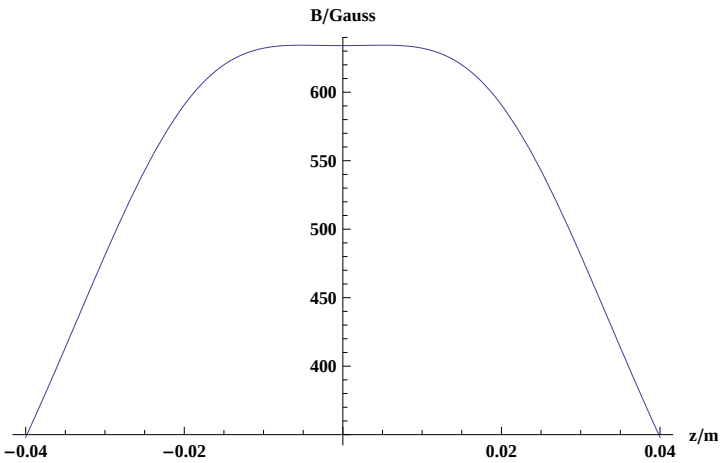

Figure 7.18: Feshbach field along the axial directio. Near the origin, at the location of the atom, a homogeneous field of 634 G is created for a current of 100 A.

The coils are wound around a winding tool made of Teflon. The individual windings are glued together using epoxy (Epoxy Technology 360). After winding, the coils are baked for one hour at a temperature of 100°C to cure the epoxy. High currents

are required to create the high magnetic fields and resistive heat therefore has to be efficiently removed from the coils by a water cooled copper heat sink (see below for details of the heat sink). Good thermal contact between the heat sink and the coil is necessary, otherwise the coil will overheat during the experiment. After winding and curing, the coating of the copper wire of the coils is removed on the lathe, and the copper surface is polished to minimize any irregularities. The same polishing step is applied to the bottom of the heat sink, shown in figure 7.19. The coil and the heat sink are then attached using a diamond filled epoxy (AI Technology, Primabond ME 7159). This epoxy has a very large thermal conductivity (11.4 W/(m°C)), while being electrically insulating (electrical resistivity $> 1 \times 10^{24}$ Ωcm). The epoxy is applied to the heat sink and the coil and prebaked for 30 min at 60°C before joining the two parts together. The epoxy is then cured for 2 hours at a temperature of 140°C. To minimize variations from the perfect homogenous magnetic field desired, the two coils are wound and the heat sinks designed to mirror each other in the setup.

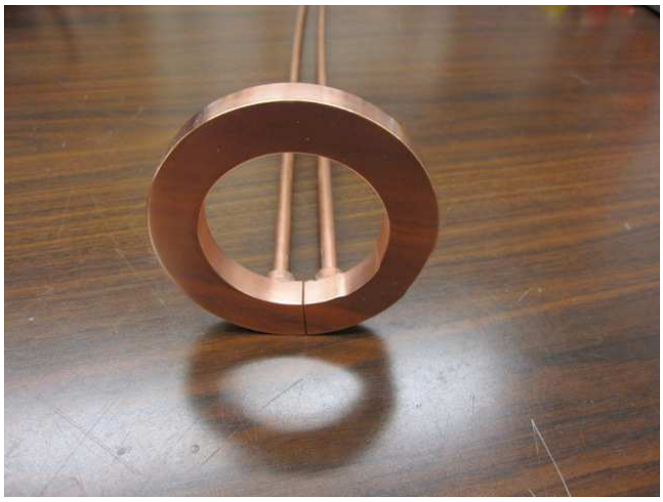

Figure 7.19: The bottom of the Feshbach coil is polished until a mirror finish is achieved.

The design of the inside of the heat sink is shown in figure 7.20 (a). To reduce eddy currents the heat sink is not a completely closed ring, but has a small spacing in-between the water connectors. The inside is hollow so that water can flow through the heat sink and carry away the resistive heat. The coils are typically cooled with water at a temperature between 17°C and 20°C. The indentations on the side of the

heat sink allow for the connection of current connectors to the coil without establishing an electrical connection between the current supply and the heat sink.

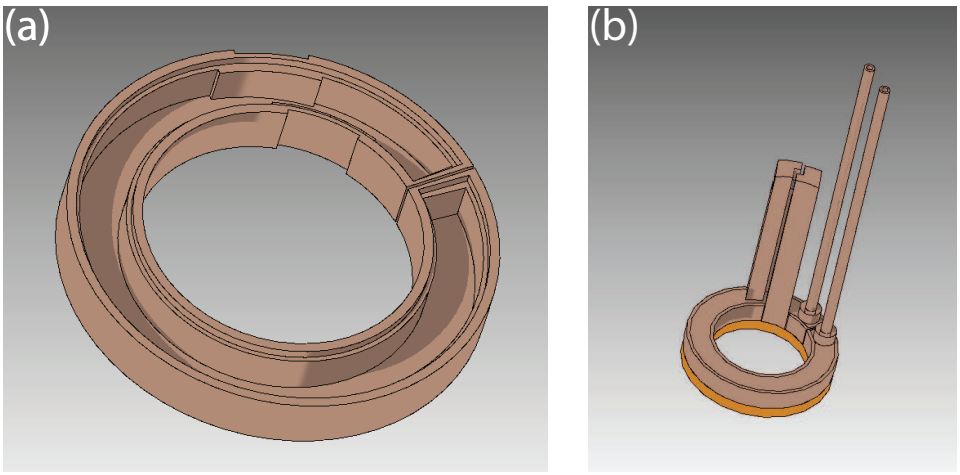

Figure 7.20: Feshbach coil heat sink. (a) A small gap in the heat sink reduces eddy currents. The inside is hollow so that water can remove resistive heat from the coils. (b) The current connectors are attached to the Feshbach coil (orange), without establishing an electric contact between the current supply and the heat shink.

The current connectors are soldered to the coil with Indium solder (Indium Corporation of America, alloy 58Bi 42Sn). This epoxy has a lower electrical resistance than regular solder and a lower melting point (138°C). Both the coil and the copper current connectors have a large volume of copper that need to be heated, and it is impossible to directly solder the current connector to the coil. Standard soldering irons are not able to produce enough heat, even with the reduced melting point of the solder. The Feshbach coil with the heat sink connected is therefore heated to 130°C using heater tape. The current connectors are heated separately in the oven typically used for curing of epoxy. With both coil and connector close to the melting point temperature of the solder the electrical connection can be made with a standard soldering iron. Before attaching the two pieces together, diamond filled epoxy is applied to the indentation of the heat sink. This stabilizes the current connector to the heat sink and provides a large resistivity between the two parts. To further support the weight of the current connectors, epoxy putty (Loctite, Fixmaster underwater repair epoxy) is used to create another mechanical support between the current connectors and the heat sink.

The coils are then checked for shorts and the resistance of the coils and the heating of the coils is measured. The resistance is approximately 0.03 Ω. Figure 7.21 shows the temporal evolution of the temperature for different currents. The steady state temperature remains below 70°C even at a current of 150 A ($B \approx 951$ G). The water flow through the heat sink is between 2.1 and 2.4 l/min, and the water temperature is set to 18°C. High currents in the Feshbach coils are only required during the evaporation stage of the experiment. It is therefore estimated that during the experiment the steady state temperature will not exceed 35°C.

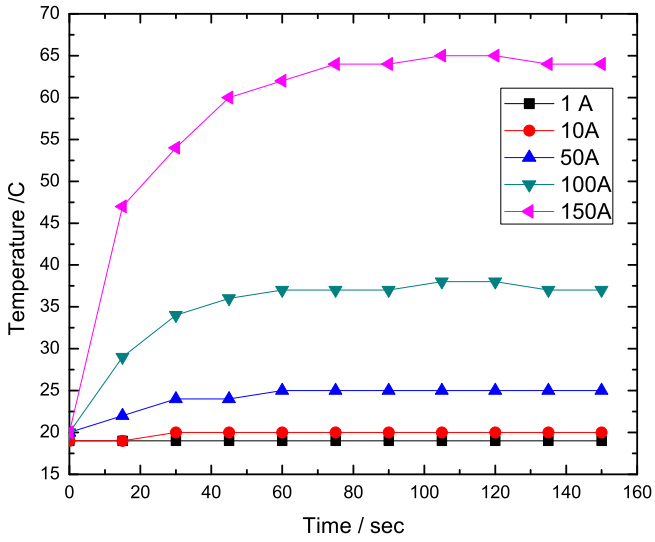

Figure 7.21: Temperature increase in the Feshbach coils at several current values.

The current to the Feshbach coils is provided by a Lambda power supply (ESS 20-500). This power supply is able to provide up to 500 A of current at 20 V, and the current is stabilized to within 0.1%.

In addition to running the coils in Helmholtz configuration during evaporation, they can also operate in anti-Helmholtz configuration. This is achieved by an H-bridge setup built from a group of MOSFETs. The MOSFET setup with water-cooling is shown in figure 7.22. Each MOSFET (IRF1324PbF) can in principle take a current of 195 A. However, the maximum current is limited by the quality of the connections as well. A

large safety margin on the current is implemented by using 10 MOSFETs in parallel.

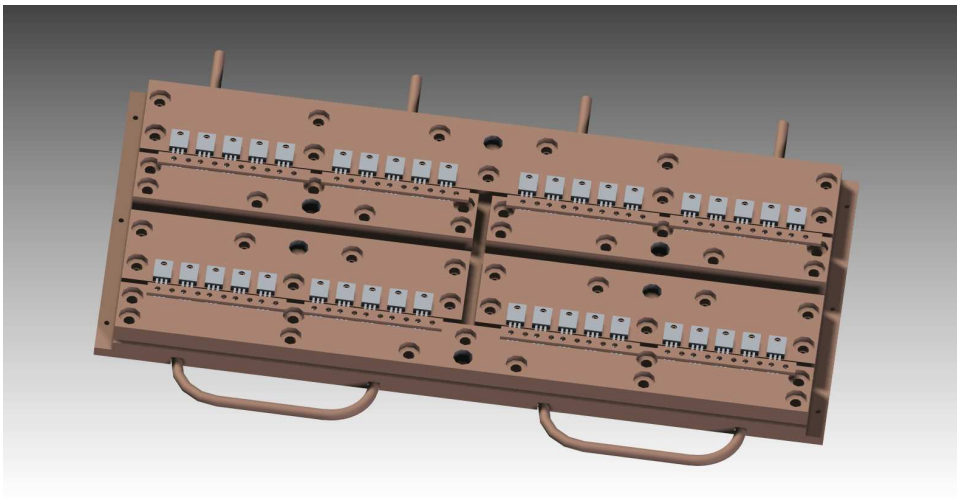

Figure 7.22: MOSFET H-bridge setup.

The electrical circuit for the switching of the current direction through one of the Feshbach coils is shown in figure 7.23. This design allows for switching from Helmholtz- to anti-Helmholtz-configuration in only a few ms. The current direction is controlled by a TTL input to the H-bridge driving circuit. The H-Bridge driver (HIP4081) opens either the MOSFET groups A and D (each MOSFET symbol figure 7.23 represents a group of 10 MOSFETs run in parallel), or B and C simultaneously, switching the current direction through Feshbach coil 2. To reduce switching and turn-off times the overall inductance of the setup is minimized. Therefore all current carrying wires run in pairs with minimal distance between them.

Because of the ability to switch the Feshbach coils between Helmholtz- and anti-Helmholtz configuration it is possible to use the Feshbach coils to create the quadrupole field for the MOT. In contrast to the MOT coils, the Feshbach coils can be run continously at the current required to generate the MOT magnetic field gradients (20 A). The loading rate and the atom number in both situations is comparable. The speed at which the system can be aligned however, is greatly increased when the quadrupole fields can be run continously. The experiment therefore now typically uses the Feshbach coils to create the MOT magnetic field gradients.

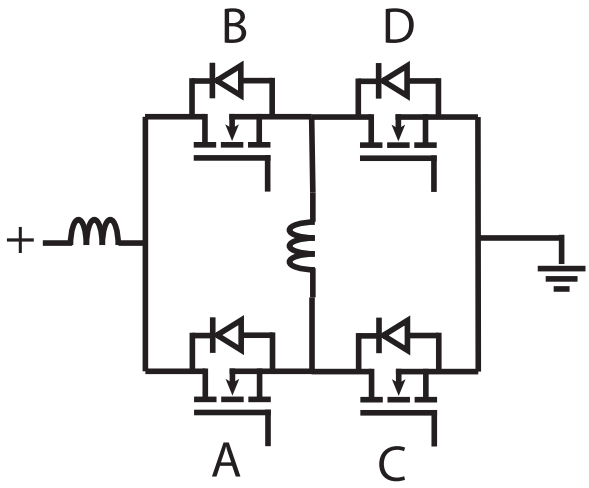

Figure 7.23: Feshbach coil H-bridge circuit. Using the H-bridge driver either MOSFETs A and D, or MOSFETs B and C open simultaneously, allowing the reversal of the current through the second Feshbach coil. Each MOSFET symbol represents 10 MOSFETs wired in parallel.

For safety reasons an interlock system is installed. As with all of the interlocks it is based on the Arduino micro-controller. This interlock ensures that the Feshbach coils are not continously run above a current of 50 A. Below this current no significant temperature increase was measured and it is therefore not necessary to limit the time the coils are running below 50 A. Above a current of 100 A the interlock turns off the current after 10 s. If the current is between 50 A and 100 A the interlock turns off the current after 20 s. The interlock also monitors the cooling water temperature and the water flow.

Table 7.3 summarizes the properties of the Feshbach coils.

Number of coils	2	Magnetic field strength	6.34 G/A
Number of layers per coil	1	Coil separation	36.0 mm
Number of turns per coil	26	Water flow through each coil	>2 l/min
Inner diameter of the coils	29.5 mm	Axial gradient	1.9 G/cm/A
Outer diameter of the coils	45.0 mm	Radial gradient	1.1 G/cm/A

Table 7.3: Properties of the Feshbach coils

7.2.4 Water-Cooling of MOT and Feshbach Coils

The Feshbach coils, the Feshbach coil H-bridge, and the MOT coils are all water-cooled to avoid overheating during the experimental sequence. Sufficient cooling capability is provided by a heat-exchanger (Affinity, EWA-04AA-CE56CB). Originally the heat exchanger used a valve to control the water flow of chilled university water through the heat exchanger. This provided control of the temperature of the water used for cooling the coils. Unfortunately that valve is no longer functional. An external valve (Johnson Controls, VA-4233-6GA-24) and a thermocouple measuring the water temperature of the cooling water are therefore added to the circuit. A home-built controller box based on an Arduino microcontroller controls the temperature of the chilled water running through the coils by adjusting the water flow from the university water lines. Temperature stabilization of the cooling water is important to ensure that all coils are sufficiently cooled without causing condensation. The water temperature is typically set to approximately 18°C. Figure 7.24 shows the layout of the water-cooling system.

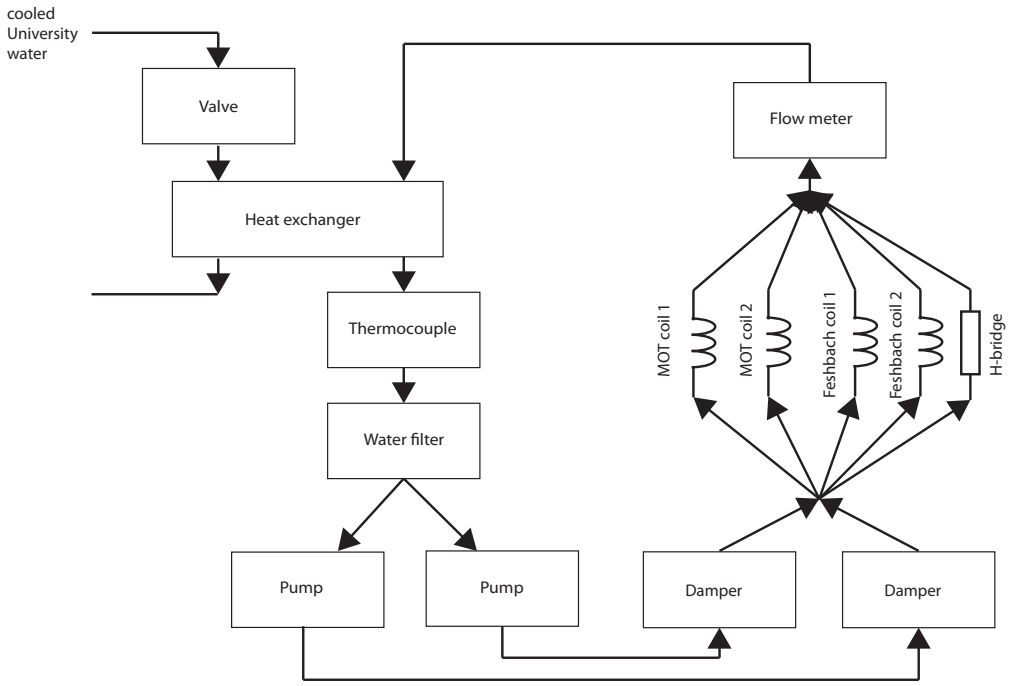

Figure 7.24: Water cooling for the MOT coils, Feshbach coils, and the Feshbach coil H-bridge.

Directly behind the water output of the heat exchanger a water filter is installed to

ensure that no particulates build up inside the water cooling lines, potentially disrupting the water flow through the lines and coils. The heat-exchanger provides sufficient cooling capabilities but is not able to generate sufficient pressures for the required water flow through the coils and the H-bridge. A pair of pumps (Tuthill, TXS2.6PPPT3WN1C000) increase the water flow rate significantly. These pumps add mechanical vibrations to the system, so pulsation dampers (FlowGuard) are added in series with the pumps.

The coils and the H-bridge are run in parallel. To simplify the splitting and combining of the water lines a home-built distribution system made from brass is used. A photograph of this splitter is shown in figure 7.25.

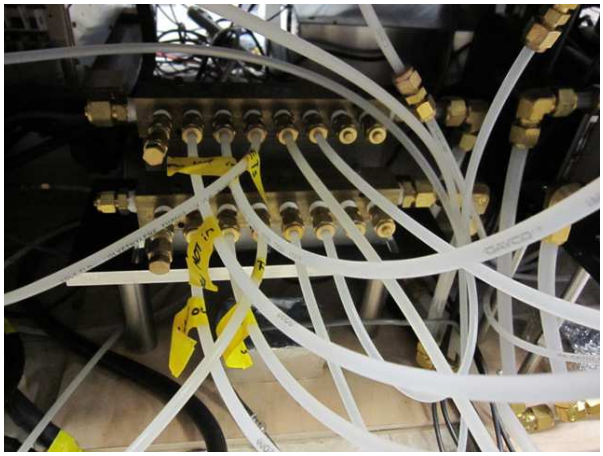

Figure 7.25: Water splitter made from brass. The upper part splits the water into five separate water lines leading to the coils and the H-bridge, the lower part recombines the water lines.

The last part of the water cooling circuit is a flowmeter. It outputs an analog voltage proportional to the flow rate that is used in the MOT and Feshbach interlock boxes. If the flowmeter indicates that no or too little water is flowing, either because the heat exchanger and the water pumps are not turned on or because a leak developed, the interlock boxes will prevent the current from flowing through any of the coils, protecting the experiment from potential damage.

7.3 Optical Setup

Multiple laser systems, operating at different frequencies, and imaging setups are required to trap, cool, manipulate and image the atomic ensemble. A near-resonant laser system is used in the Zeeman slower, the MOT setup, and for imaging. A far-detuned CO_2 laser provides the optical potential for evaporative cooling, and an Nd:YAG laser will be used to create the tweezer trap for laser culling.

7.3.1 Near-Resonant Laser System

Two low-power diode lasers (Toptica, DLpro), each with an output power of approximately 20 mW, and one tapered amplifier with its own master laser diode (Toptica, TApro) with an output power of approximately 400 mW constitute the near resonant laser system. A schematic of the near-resonant laser table is shown in figure 7.26.

7.3.1.1 Spectroscopy Setup

A phase modulation spectroscopy setup is used in the lithium experiment. The optical layout is shown in figure 7.27. A pair of anamorphic prism pairs (Thorlabs, PS871-B) shapes the elliptical beam of the laser diode to a more circular beam shape. After the prism pair, the beam passes through an optical isolator (Conoptics, model 712B). This optical isolator protects the diode from potentially harmful back-reflections. Using a half-wave plate (CVI-MellesGriot, QWPM-670-05-2) and a polarizing beam splitter cube (CVI-MellesGriot, PBS-670-050) the beam is distributed into two beam paths. About 5 mW of power are transmitted through the cube for the spectroscopy setup, the rest of the power (about 15 mW) is diverted to the frequency offset lock (see chapter 7.3.1.3).

The current of the laser diode is modulated at 20 MHz by the PDD module of the laser electronics (Toptica). This causes sidebands at ± 20 MHz of the carrier frequency. The beam (with all three frequency components) double passes the spectroscopy cell and the signal is detected in a fast photodiode (New Focus, model 1801). The voltage signal is transmitted to the PDD module, which generates the error signal. Figure 7.28

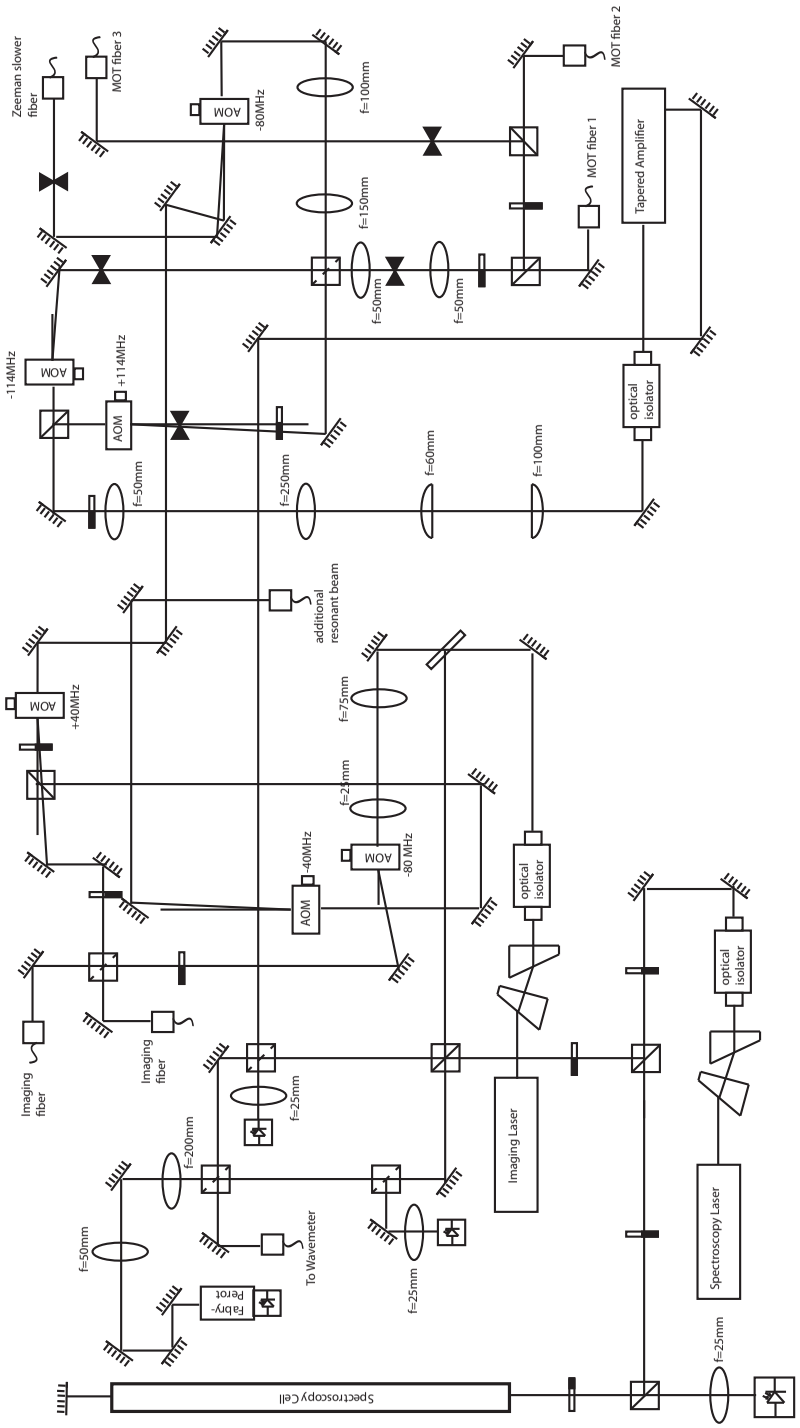

Figure 7.26: Optical layout of the near-resonant laser system.

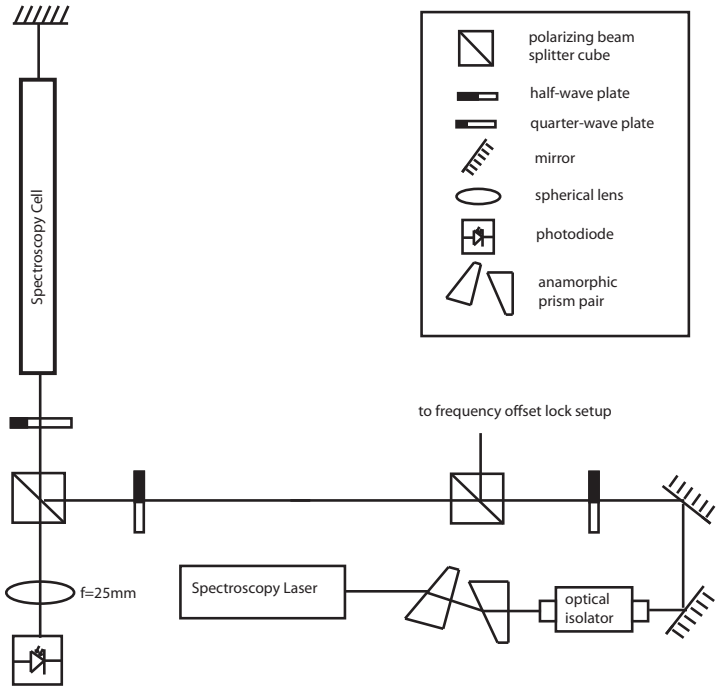

Figure 7.27: Phase modulation spectroscopy setup.

shows the error signal. The laser is typically locked to the $|F = 3/2\rangle \rightarrow |\text{excited state}\rangle$ transition of the D_2 line.

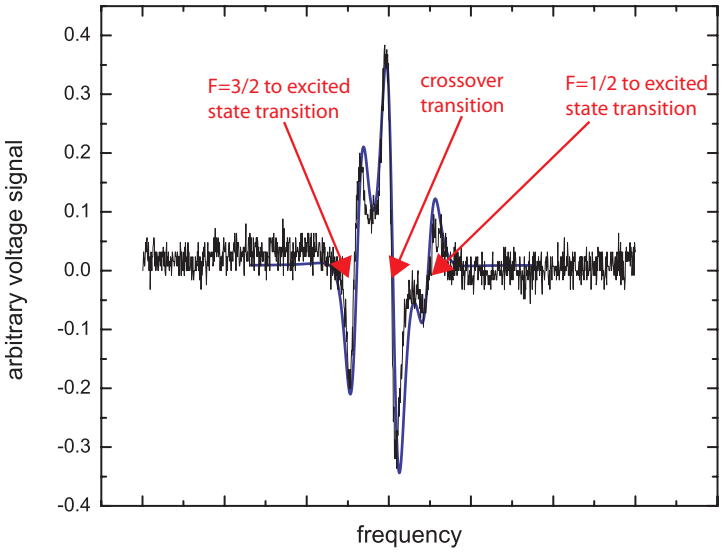

Figure 7.28: Error signal generated by the phase modulation spectroscopy setup. The three transition lines correspond to the $|F = 3/2\rangle$, $|F = 1/2\rangle$ and the crossover transitions. The blue line represents the predicted error signal.

The error signal shows three lines, corresponding to the $|F = 3/2\rangle$ to the excited state, from $|F = 1/2\rangle$ to the excited state as well as the crossover transition. The branching ratios determine the strength of the different transitions, and in the case of ^{6}Li the $|F = 3/2\rangle$ to the excited state transition is stronger than the $|F = 1/2\rangle$ to the excited state transition. Given the relative strength of the transitions and the amount of power-broadening, it is possible to calculate a theoretical error signal [22, 44]. The power-broadened linewidth is estimated to be 45 MHz. The predicted signal is shown in blue in figure 7.28.

7.3.1.2 Spectroscopy Cell

The spectroscopy cell is filled with a small amount of 95% isotopically enriched ^{6}Li placed in the lithium reservoir. The vapor pressure of lithium at room temperature is very low (4.4×10^{-20} Torr [20]), and the spectroscopy cell is therefore heated to a temperature of 390°C. The vapor pressure at this temperature is approximately 6×10^{-5} Torr.

The spectroscopy cell is made of a 1.5 inch outer diameter, 48.1 cm long, stainless steel tube. Approximately at half the length an additional nipple is attached. This nipple is used to attach the lithium reservoir. On one side of this stainless steel tube a 2-3/4 flange tee is attached. A small valve for pump-out (VAT Valve, 54024-GE02-0001) of the spectroscopy cell is mounted to the tee. The overall length of the spectroscopy cell is thus 63.2 cm. The viewports on the spectroscopy cell are broadband anti-reflection coated ($400\text{ nm} - 700\text{ nm}$) (Larson glass). A schematic of the spectroscopy cell is shown in figure 7.29.

After checking for leaks on the spectroscopy cell assembly, the cell is back-filled with argon gas and lithium is added to the reservoir. The argon is then pumped-out until a pressure of approximately 35 mTorr is reached. The remaining gas inside the spectroscopy cell serves as a buffer gas. Having the right amount of buffer gas is important in lithium spectroscopy cells. If the pressures are too high, broadening effects will severly decrease the quality of the spectroscopy signal. If the pressure is too small however, the mean free path of lithium atoms is sufficient to reach the end of the cell

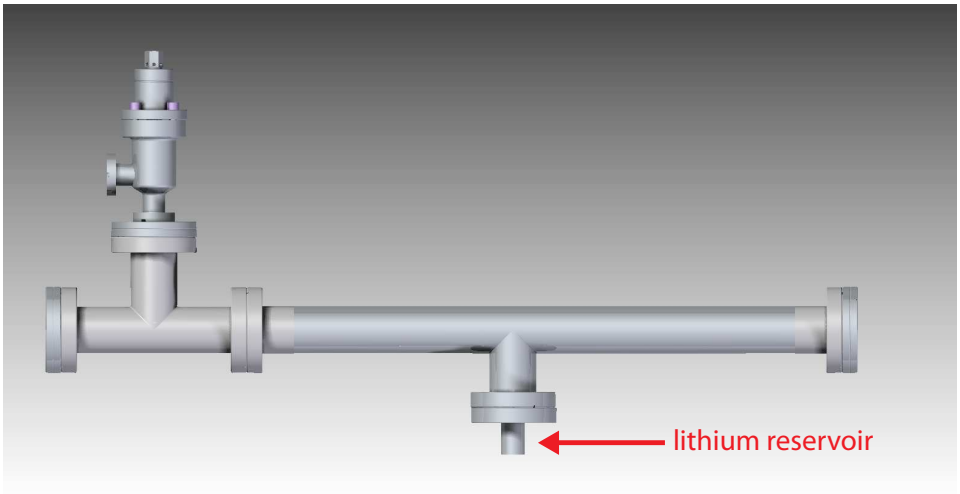

Figure 7.29: Spectroscopy cell.

and thus to coat the viewports.

The spectroscopy cell is heated near the lithium reservoir with high-temperature heater tape. It is insulated using fiber glass. To avoid frequency shifts due to the presence of magnetic fields, the heater tape is wound around the cell in such a way as to minimize the resulting magnetic fields due to currents flowing through the tape. Except near the lithium reservoir the spectroscopy cell is kept near room temperature. Lithium atoms therefore stick to the walls of the cell, which reduces the risk of coating the viewports with lithium. The first time the lithium reservoir is heated to a temperature of about 450°C. This breaks any oxide layer that might have been formed on the surface of the lithium metal during the preparation and loading into the cell.

7.3.1.3 Frequency-Offset Lock Setups

Frequency-offset locking has many applications in atomic physics experiments. Most importantly for the lithium setup, it is an easy method to lock the imaging diode laser and the master laser, used to seed the tapered amplifier, relative to the spectroscopy laser with a frequency offset Δf. Using a tunable scheme, it is possible to dynamically change the laser frequency during the course of the experimental sequence. This is important especially for the master laser, where the frequency offset Δf controls the MOT detuning. Δf can then be changed to compress the MOT prior to loading atoms

into the CO_2 laser. The optical layout for the frequency-offset lock is shown in figure 7.30.

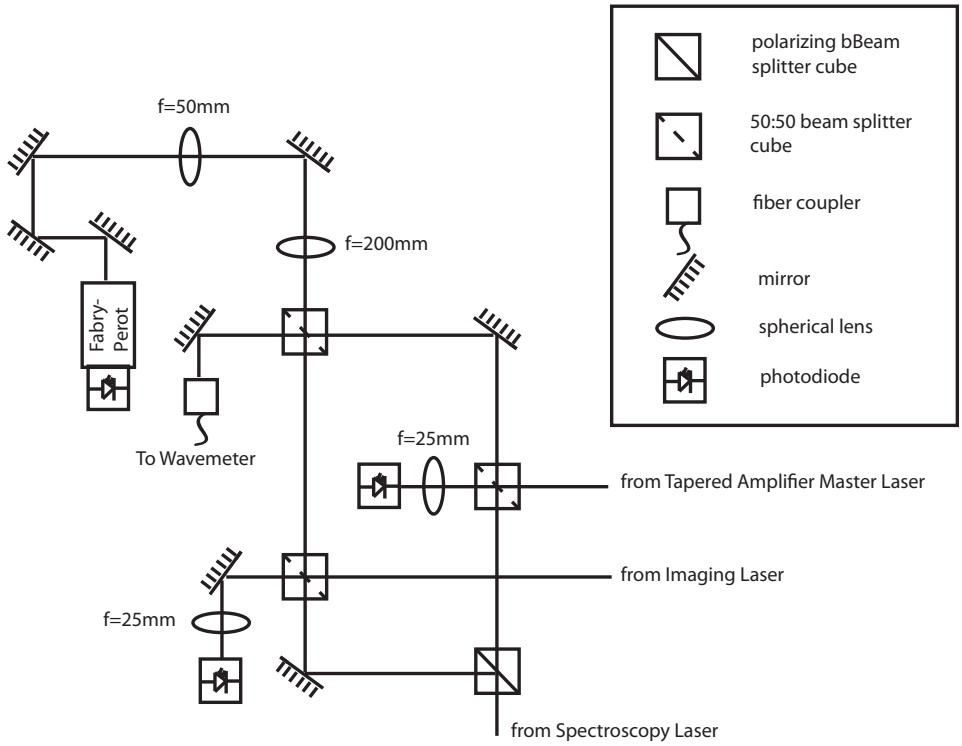

Figure 7.30: Optical layout of the frequency-offset lock optics.

A 50:50 fixed ratio beamsplitter (Edmund Optics, NT49-005) distributes the spectroscopy laser into two beam paths. A second 50:50 fixed ratio beamsplitter cube then combines the spectroscopy laser with the imaging laser beam. An identical setup overlaps the spectroscopy laser with the master laser seeding the tapered amplifier. After the beams are combined, they are focused onto photodiodes that detect the interference signal between the spectroscopy and the imaging laser, and the spectroscopy and the master laser respectively. To create the interference signal, the polarizations of the beams have to be aligned.

The remaining beam power from all three beams, spectroscopy, imaging and master, is then combined at a third 50:50 beamsplitter cube. The beam from one of the two output ports of this beam splitter is then coupled into the wavemeter using a multimode fiber. The second beam is coupled into a home-built Fabry-Perot cavity.

Single-mode operation of all lasers can thus easily be verified.

The beat frequency of the lasers determines the required bandwidth of the photodiodes. For detecting the beat of the spectroscopy and the master laser a Thorlabs photodiode (PDA10A) is used. The bandwidth of this photodiode is 150 MHz. However, for the beat of the spectroscopy and the imaging laser much larger beat frequencies have to be detected. A faster photodiode (Hamamatsu, G4176-03) with a bandwidth of 10 GHz is therefore used.

The beat frequency f_1 of the lasers is mixed with the frequency f_2 supplied by a voltage controlled oscillator (VCO) [107]. The mixed signal is then low-pass filtered. The remaining frequency component after this filter is $f_1 - f_2$. This signal is subsequently split into two, and recombined at a phase detector. One of the signals passes through a delay line, so that the signals arrive with a different phase at the phase detector. This phase is given by $\phi = 2\pi(f_1 - f_2)\tau$, where τ is the time delay between the signals. The phase signal is sent to the PID regulator used to lock the laser frequency.

The beat frequency can be directly measured using a frequency counter. Therefore a coupler is added to the electronics to divert a small amount of signal to frequency counters.

A schematic of the electronics used to create the frequency-offset lock signals are shown in figures 7.31 and 7.32. All components are manufactured by minicircuits.

The value of ϕ can be changed by manipulating either f_1 or f_2. f_1 can be modulated by changing the current in the laser diode and/or changing the grating angle in the laser cavity using the piezo actuator. With a constant f_2 this method is used to generate the error signals shown in figure 7.33. During the experimental sequence the frequency f_1 is fixed and f_2 is changed. The VCO frequency f_2 is controlled by an analog out of the experiment control electronics. Because the phase ϕ is fixed as the lock point, the PID will feedback onto the piezo actuator to keep $f_1 - f_2$ constant, changing the laser frequency f_1 in the process. Using this method the frequency of the master laser can be changed by 50 MHz in a few ms without unlocking.

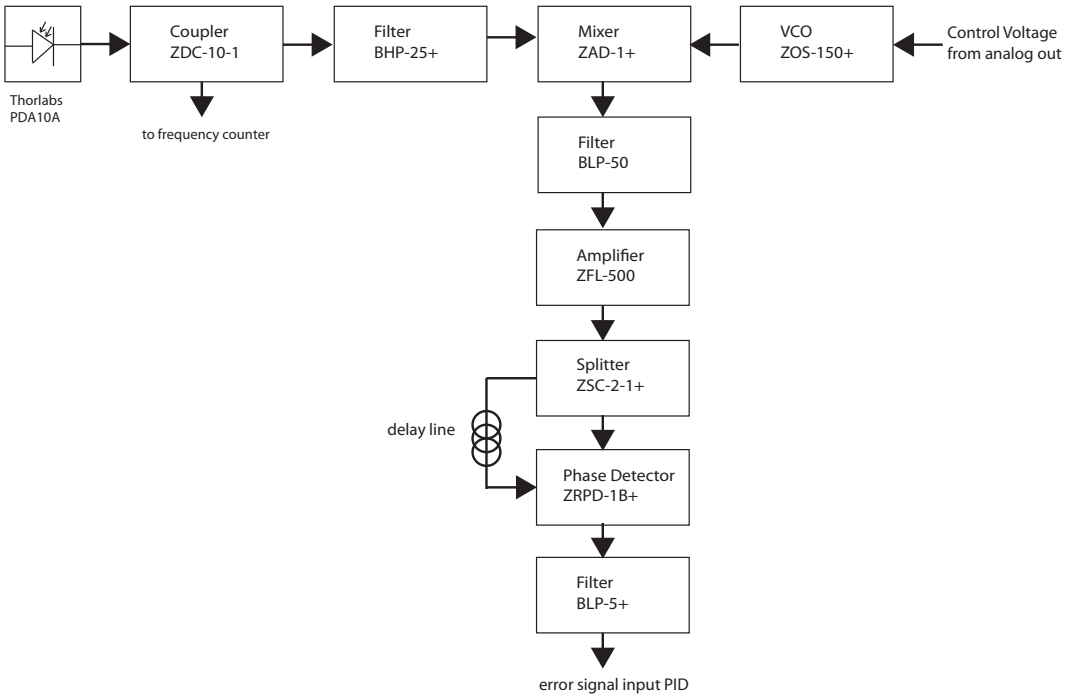

Figure 7.31: Frequency-offset lock electronics for the tapered amplifier master laser All components are manufactured by minicircuits.

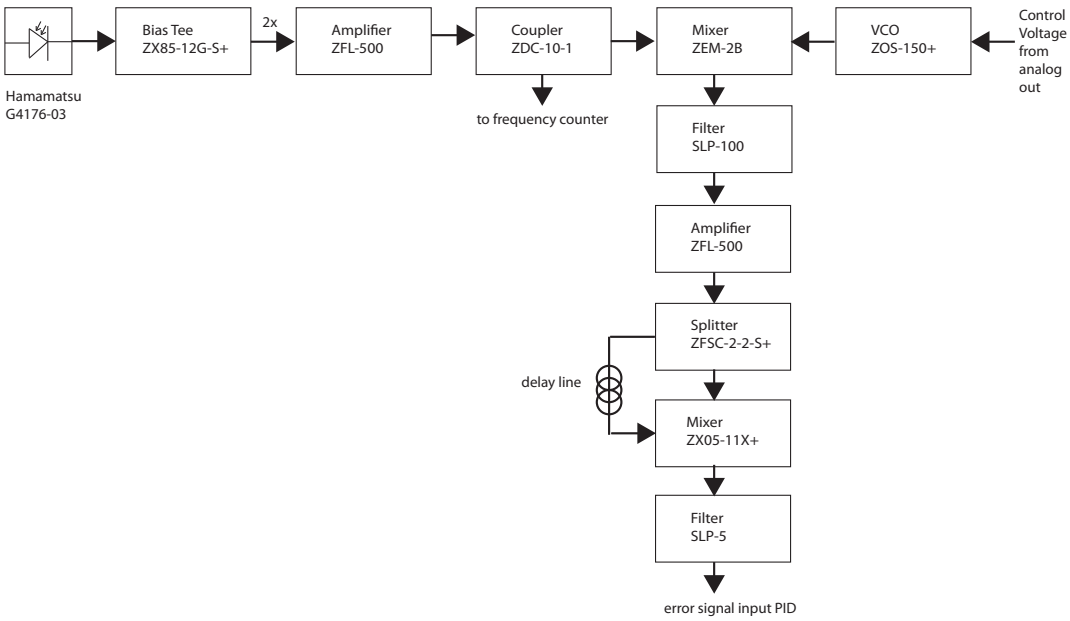

Figure 7.32: Frequency-offset lock electronics for the imaging laser. All components are manufactured by minicircuits.

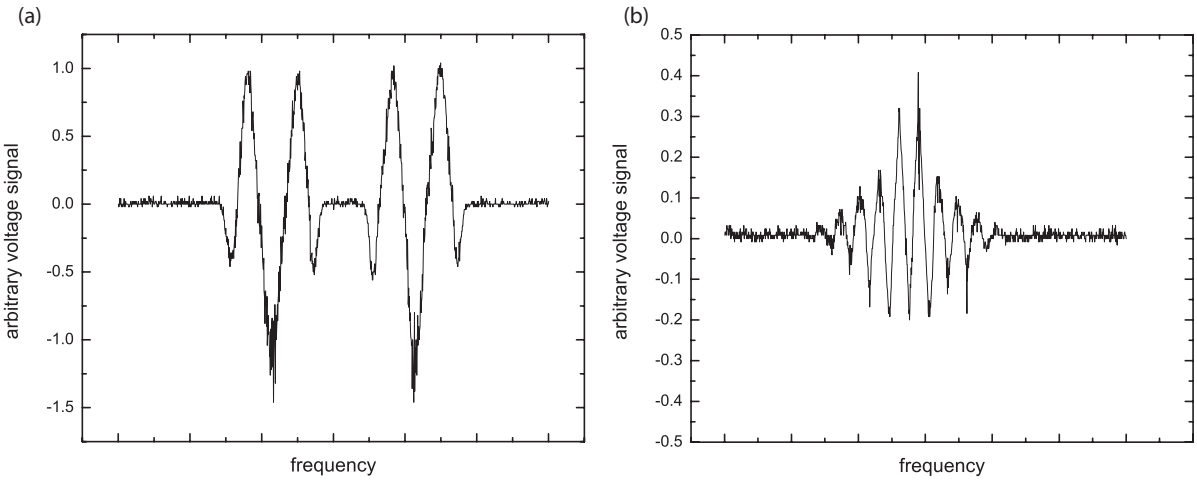

Figure 7.33: Frequency-offset lock error signals. (a) Tapered amplifier master laser error signal. (b) Imaging laser error signal.

7.3.1.4 Tapered Amplifier Setup

The tapered amplifier provides sufficient power for the MOT and the Zeeman slower beam. Additionally, the laser is used for imaging at zero magnetic field, where both MOT and repump frequency components are necessary for absorption imaging. It also provides a resonant beam used for various alignment procedures. The optical layout is shown in figure 7.34.

To protect the tapered amplifier from back reflections an optical isolator (ConOptics, model 716) is placed behind the tapered amplifier output. Because tapered amplifier chips are even more sensitive to back-reflections than laser diodes, the isolation of this isolator is 56 to 60 dB. All other isolators in the setup have a 37 to 40 dB isolation. Even though the tapered amplifier beam is well collimated by a lens system inside the laser housing, the vertical and horizontal beam waists are different. To improve the beam profile, especially important to achieve good coupling efficiencies into fibers, a 5:3 cylindrical telescope optimizes the beam shape. Directly behind the cylindrical telescope, a 5:1 spherical telescope matches the beam diameter to the active area of two 114 MHz AOMs (IntraAction, ATM114-A1). Using a half-wave plate and a polarizing beam splitter cube, the beam from the tapered amplifier is split into two beam paths, the MOT and the repump arm. A typical ratio of powers is 3:1. The AOM in the MOT

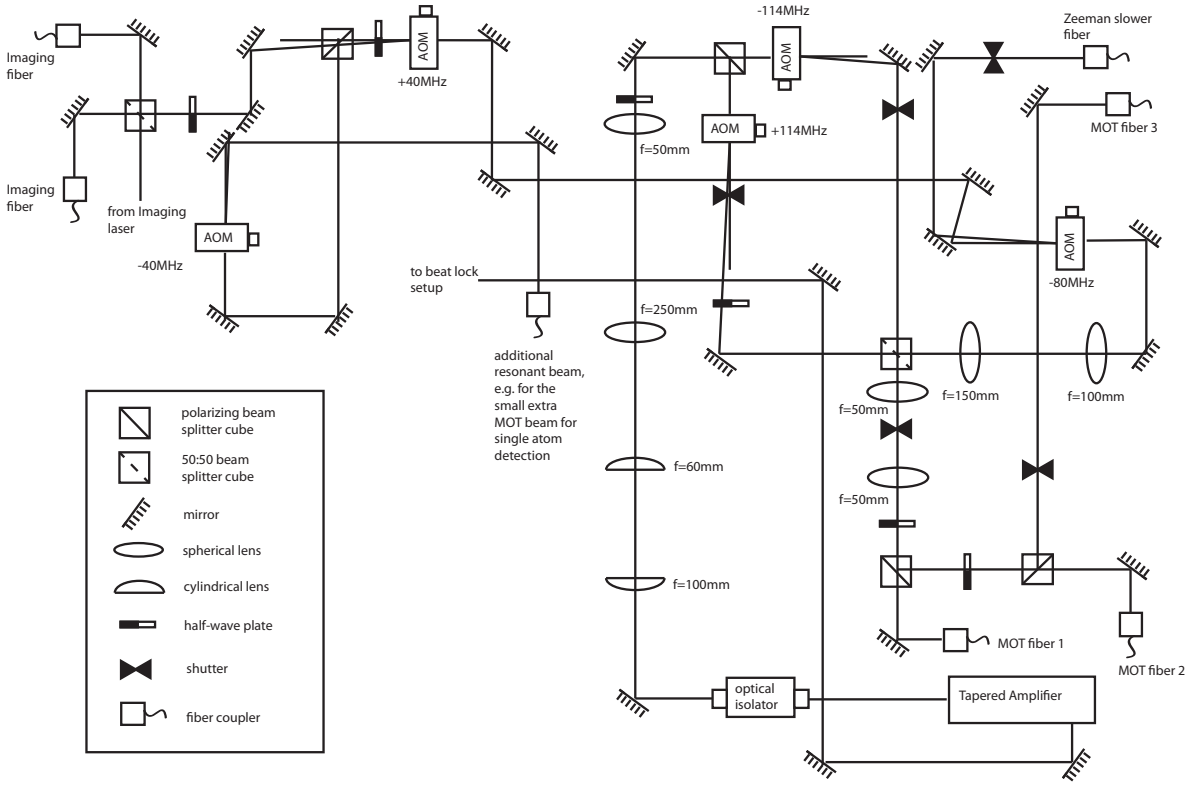

Figure 7.34: Optical layout of the tapered amplifier

arm shifts the laser frequency by −114 MHz, the AOM in the repump arm shifts the frequency by +114 MHz. Combined this produces a frequency difference of 228 MHz, the hyperfine splitting of the ground state of ^{6}Li. All three MOT beams and the Zeeman slower beam need a repump frequency component as well as the MOT frequency. The MOT arm and the repump arm are therefore recombined on a 50:50 beam splitter cube. To align the polarization of the two beams, a half-wave plate is added to the repump arm.

One of the output ports of the 50:50 beam splitter cube provides the power for the three MOT beams, the second one provides the power for the Zeeman slower beam. In the beam path for the MOT beams, a series of half-wave plates and polarizing beam splitter cubes separate the beam into three beams. Each of these is individually coupled into a single-mode polarization-maintaining fiber. The beam of the second output port, used for the Zeeman slower beam, passes through another spherical telescope, again used to match the beam size to the active area of an 80 MHz AOM (IntraAction, AOM802).

The -1st order of this AOM is coupled into a single-mode polarization-maintaining fiber.

The zeroth order from the Zeeman slower AOM is used for imaging the atoms at zero magnetic field. This beam is frequency shifted by +40 MHz (IntraAction, AOM402AF3-10), and coupled into the imaging fibers. Part of this beam is picked off before the beam is combined with the imaging laser beam path and aligned to a second 40 MHz AOM (IntraAction, AOM-40). The laser frequency of this beam then matches the laser frequency of the MOT beams. In the future this beam will become important to detect the fluorescence signal of single atoms. Throughout the setup shutters are added to block leakage light from the AOMs that cannot be eliminated otherwise.

Figure 7.35 summarizes the different frequencies of the MOT, repump and Zeeman slower beams. In this example the frequency offset from the laser lock is 76 MHz, typical detuning during the MOT loading stage of the experimental sequence. However, the detuning can be changed to 114 MHz, in which case the MOT and repump frequencies are exactly on resonance with the atomic transition.

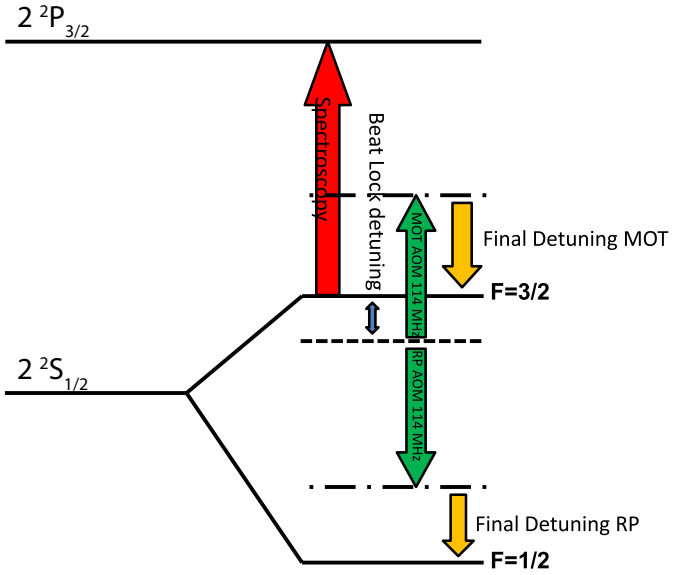

Figure 7.35: Frequency detunings of the MOT, repump and Zeeman slower beam. The spectroscopy laser is locked to the $|F = 3/2\rangle$ transition. The detuning due to the frequency-offset lock is typically 76 MHz during the MOT loading stage of the experimental sequence. However, the frequency offset can be changed to 114 MHz, in which case the MOT and repump frequencies are exactly on resonance.

Table 7.4 summarizes the beam powers in the different fibers.

Fiber	MOT power (mW)	repump power (mW)	total power (mW)
MOT #1	12.0	4.0	16.0
MOT #2	10.6	7.0	17.6
MOT #3	10.2	6.3	16.5
Zeeman slower	34	10	44

Table 7.4: Typical beam powers after the fibers

7.3.1.5 Imaging Laser Setup

The optical layout of the imaging laser is shown in figure 7.36.

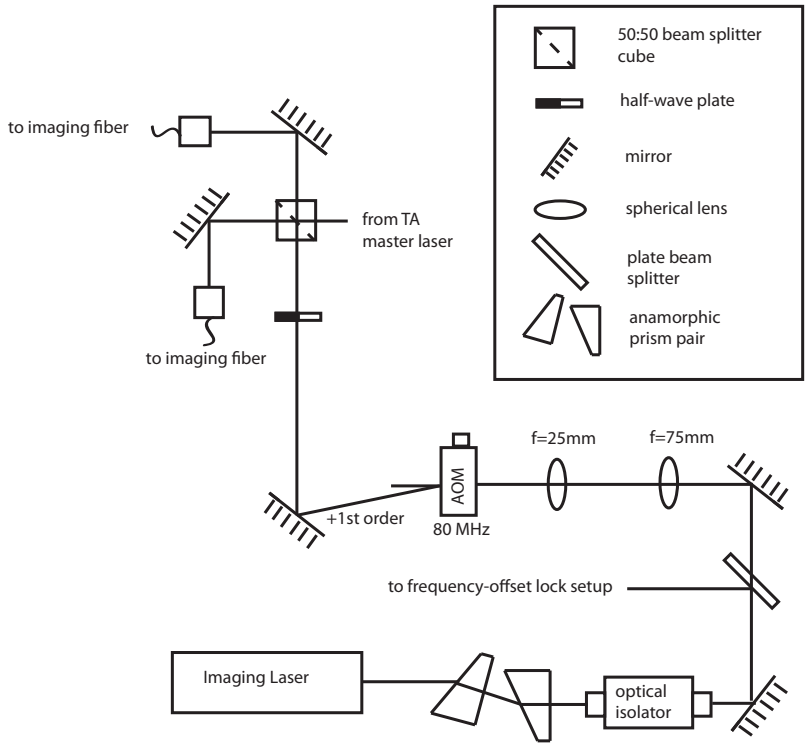

Figure 7.36: Optical layout of the imaging laser.

Leaving the diode laser head, the beam has an elliptical beam profile that is corrected by an anamorphic prism pair. To avoid damage to the laser from back reflections, an optical isolator (Conoptics, model 712B) is added to the beam path after the prism pair. A plate beamsplitter picks off a small amount of power ($\approx$ 1.5 mW)

for the frequency-offset lock, the wavemeter and the Fabry-Perot cavity. The main part of the beam passes through an 80 MHz AOM (IntraAction, model ATM801-A1). This AOM can turn the beam on and off quickly, creating the short pulses ($\approx 10\ \mu$s) required for absorption imaging. The beam is split into two by a half-wave plate and a polarizing beam splitter cube and coupled into a single-mode polarization-maintaining fiber to provide the capability of imaging along two different directions.

7.3.2 CO_2 Laser System

A CO_2 laser (Coherent GEMSelect) creates the optical dipole trap for evaporative cooling of the trapped sample of lithium atoms. This laser is chosen because the scattering rate of atoms in this laser beam is negligible due to the extremely large detuning. At a wavelength of 10.6 μm the scattering rate is reduced to a few photons per hour. In addition intensity noise in the laser is minimal.

To create a deep enough optical dipole trap to trap atoms from the MOT, a significant amount of power is required. The output power of the laser is about 130 W. The beam power is controlled with an optical single crystal germanium acousto-optic modulator (IntraAction, AGM-4010BJ1) with a center frequency of 40 MHz. Even though germanium has a relatively high transmission at 10.6 μm, the absorbed power cannot be neglected and it is necessary to cool the AOM with water. The flow rate through the AOM is set to about 1 l/min. The diffraction efficiency of this AOM is up to 85%. The 0th order beam is dumped into a water-cooled beam block. An optical layout of the CO_2 laser setup is shown in figure 7.37.

A cylindrical 1:1 telescope is placed into the diffracted beam path as close to the AOM as possible. Because the AOM crystal is water-cooled on top and on the bottom a thermal gradient in the vertical direction is likely to occur. The associated change in the index of refraction of the crystal can lead to a thermal lensing effect and cause the beam to diverge or converge along the vertical direction. The cylindrical telescope is adjusted to minimize any difference in the horizontal and vertical divergence angles.

A 1:4 spherical telescope increases the beam diameter, before the final $f = 5$ in focal length lens focuses the beam into the vacuum chamber. To measure the beam

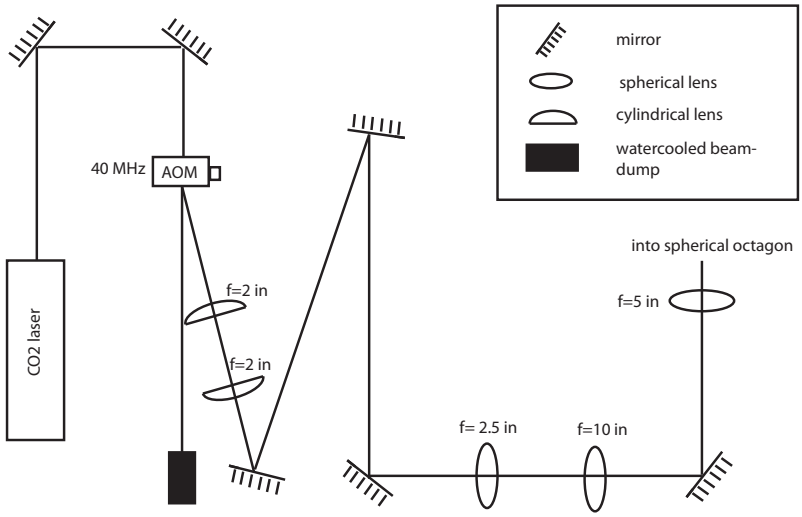

Figure 7.37: Optical layout for the CO_2 laser.

waist after the focusing lens, a knife-edge setup is used. The beam power is reduced by inserting a beam splitter into the beam path after the spherical telescope. This beam splitter reflects approximately 99% of the beam power. The transmitted beam is then focused with the same lens at the same distance as it is in the experimental setup. To simulate the viewport a ZnSe window of the same thickness is added after the focusing lens. The measured beam waists are 61 μm horizontally and 42 μm vertically.

The CO_2 laser is water-cooled by a chiller (Lytron, model RC022J03BF2C031) provided by Coherent. In addition, several beam-dumps and the AOM require water cooling. A second chiller (Neslab, model M33) provides sufficient cooling capacity. The main water line is split using a similar setup as is used to cool the MOT and Feshbach coils. A second home-built splitter, identical to the one described in chapter 7.2.4, simplifies the setup.

To ensure safe operation of the CO_2 laser, an interlock can disable laser emission, if the laser warning sign is turned off, the water flow through the chilling lines is insufficient, or the water temperature exceeds 22°C. In addition, an emergency shut-off can stop emission at any time.

7.3.3 Optical Setup around the Spherical Octagon

Around the science chamber octagon both laser system, the resonant laser system and the CO_2 laser system are combined to create all necessary optical forces and potentials for the experiment, as well as providing the necessary beams for imaging purposes. In the near future an Nd:Yag laser will be added to provide the small optical dipole trap required for laser culling. The optical layout in the horizontal plane around the spherical octagon is shown in figure 7.38.

The CO_2 setup consists of a $f = 5$ in plano-convex lens, which focuses the CO_2 beam at the location of the atoms. In order to be able to align the beam to the atoms, the lens is mounted on an x-y-z-translation stage. On the opposite side of the spherical octagon, a water-cooled beam dump collects the CO_2 beam.

The beams coming out of the MOT fibers are collimated by $f = 50$ mm lenses housed inside the fiber output coupler. Coming out of the fiber, the beam is linearly polarized. To change the polarization to circularly polarized light, MOT beam 1 passes through a quarter-wave plate before the spherical octagon. The beam is retro-reflected. In each pass the beam passes through a quarter-wave plate on the other side of the chamber to obtain the correct polarization for the retro-reflected beam.

The second MOT beam is collimated the same way as MOT beam 1. However, before passing through the mandatory quarter-wave plate, the beam is transmitted through a polarizing beam splitter cube. On the other side of the vacuum chamber two lenses ($f = 125$ mm and $f = 400$ mm) are mounted directly onto the viewport for imaging purposes. These lenses focus the MOT beam onto a reflective polarizer (Moxtek, WGP00015). Before the polarizer, a quarter-wave plate changes the polarization to s-polarized light, which is reflected by the polarizer.

The beam splitter cube is used to combine the absorption imaging beam with the MOT beam. After the quarter-wave plate the MOT and imaging beam polarizations have opposite handedness, and at the location of the reflective polarizer the imaging beam will be p-polarized and thus transmitted. This setup allows to image along a MOT beam axis. The two lenses mounted onto the viewport magnify the object by a

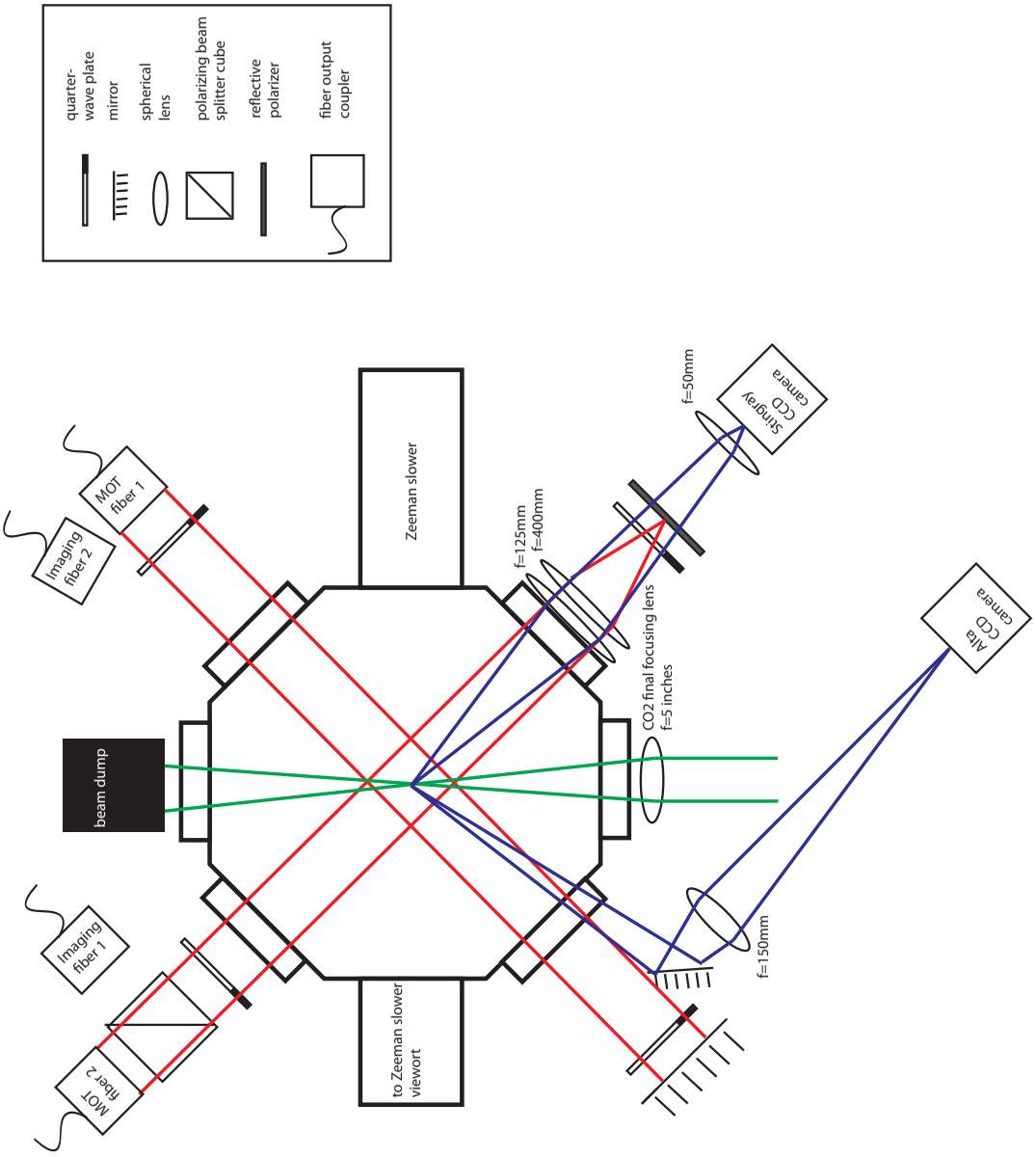

Figure 7.38: Optical layout around the spherical octagon. The horizontal MOT beams are shown in red, the CO_2 beam in green. The blue lines show how images are formed along the two imaging axes.

factor of 4. To image the MOT and measure its temperature this magnification is too large, and another lens ($f = 50$ mm) is added to the setup, changing the magnification to 0.5. A fire-wire camera (Allied Vision Technologies, Stingray F-33B/C) records the image along this axis. For imaging atoms in the CO_2 beam this lens is removed from the setup.

A second imaging axis, mostly used for fluorescence imaging, is at a slight axis of the direction of MOT beam 1. A mirror mounted as close as possible to the MOT beam and a $f = 150$ mm lens collect the light and image it onto the CCD camera (Alta U47+).

A retro-reflected MOT beam is currently the only beam using the vertical axis.

7.3.4 Laser Culling Dipole Trap Setup

The vertical axis will be used in the near future for a number of different purposes. Most importantly, it is the axis along which the small tweezer beam used for laser culling will be focused into the degenerate Fermi gas. To focus this laser beam a self-designed objective consisting of an aspheric lens and a meniscus lens was designed. A schematic of the setup within the reentrant viewport is shown in figure 7.39. In addition this axis will be used to collect the fluorescence light for single- and few-atom detection. Of course the third MOT beam will still be along this axis as well.

The custom objective therefore has to fulfill many requirements: The working distance has to be larger than 14.3 mm, the spot size should be as small as possible, the numerical aperture should be as large as possible to collect as many photons as possible, and the MOT beam has to be retro-reflected. The objective consists of two stock lenses, an aspheric lens (Thorlabs AL4532-B) and a meniscus lens (CVI MellesGriot MENP-50.0-4.8-300.0-C-670-1064) and is designed using Zemax optical design software. The diffraction limited beam waist of this objective using a YAG beam with a waist of 8 mm is exptected to be 1.7 μm. The spacing between the two lenses is 2 mm. To focus at the location of the atoms the objective needs to be mounted 2.8 mm above the window of the reentrant viewport.

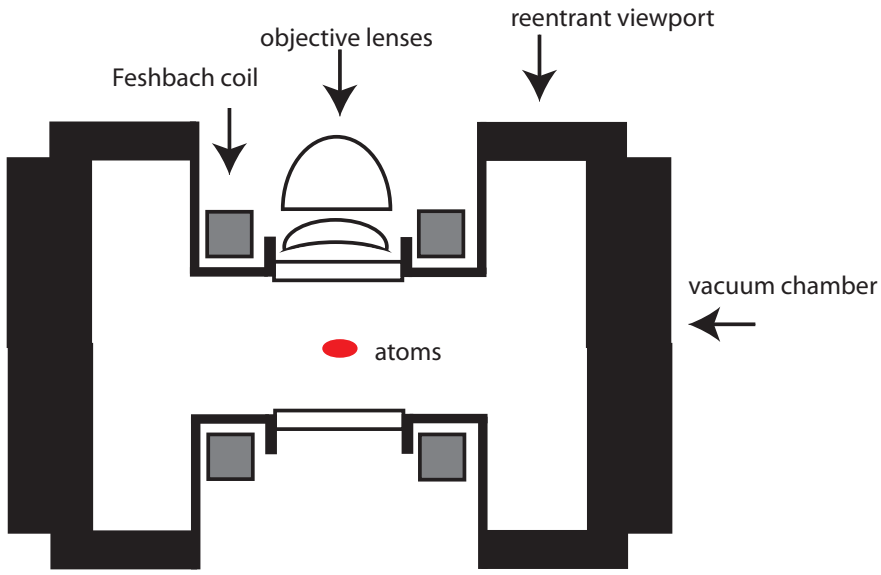

Figure 7.39: Future vertical axis optics. The Nd:YAG tweezer beam will be focused through the objective lens unto the atoms. The MOT beam will come from the bottom and be retroreflected above the vacuum chamber with the help of additional optics. The objective will also be used to collect the fluorescence signal for single-atom detection.

In principle aspheric lenses are designed to minimize aberrations to generate the smallest spot size possible. However, these lenses are not designed having the glass of the vacuum viewport in mind. The meniscus lens is therefore added to compensate for the effect of that window.

The objective will also be used to collect the fluorescence light for single-atom detection. A large numerical aperture of the objective is therefore important and the diameter of the objective lenses should be kept as large as possible. With this objective it is expected to collect about 10% of the scattered photons. These photons can then be spatially filtered and focused onto the avalanche photo diode (APD, Perkin Elmer, SPCM-AQR-14) for single-atom detection. A dichroic mirror combines the YAG beam and the scattered photon beam paths.

The MOT beam will be focused by the objective lens. Additional lenses can recollimate the beam, before it is retro-reflected. An optical layout of the envisioned optical setup is shown in figure 7.40. A mirror required for the MOT loading stage can be moved away after the MOT is loaded.

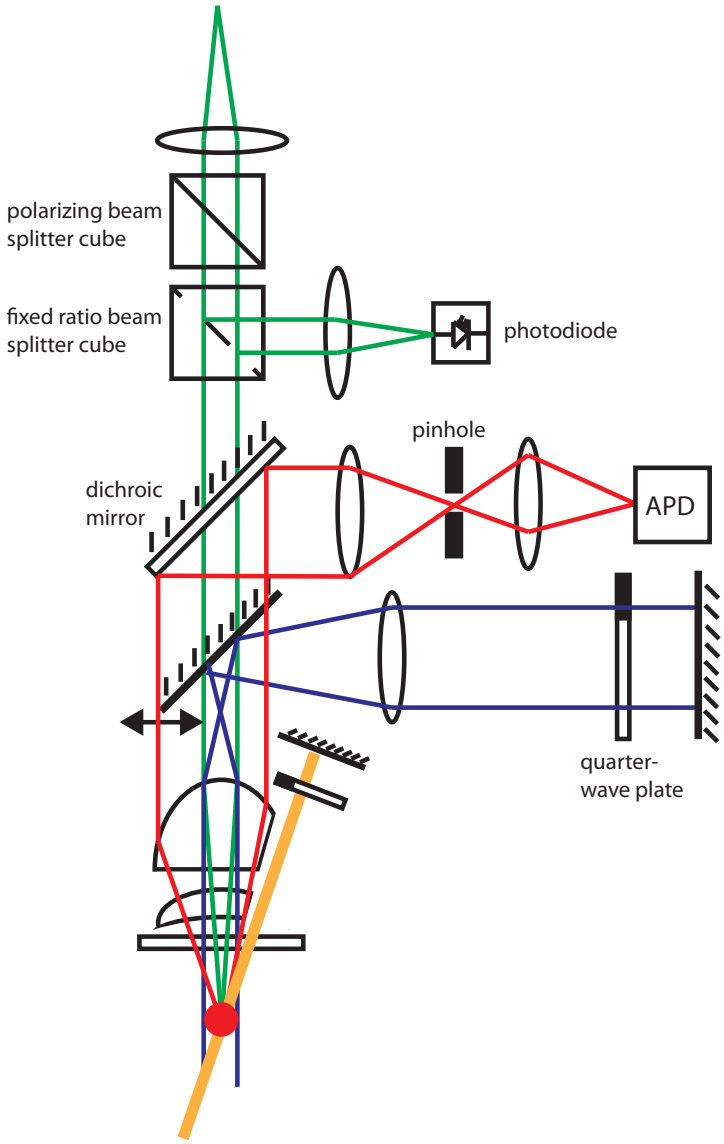

Figure 7.40: Optics along the vertical axis. The main MOT beam is shown in blue, the small MOT beam is shown in orange, the YAG tweezer beam is shown in green, and the scattered light collection is shown in red.

There is however one more problem that needs to be addressed by the objective. In order to detect single atoms, the atoms will have to be trapped in a small MOT and excited so that they scatter photons. This means that a small MOT beam is required along the vertical axis even during single-atom detection. To overcome this problem part of the lenses had to be removed to allow for the alignment of a small MOT beam at an angle of 38° relative to the vertical axis. That way the scattered photons and the

MOT beams are no longer traveling along the same beam path. In addition, the outer diameter of the meniscus lens has to be reduced for the lens to fit close enough to the vacuum viewport. The final diameter of the lens is 40 mm. These modifications to the lenses were done in the physics department machine shop. Special care had to be taken that the AR coating of the lenses would not be damaged during the machining process. Photographs of the lenses are shown in figure 7.41.

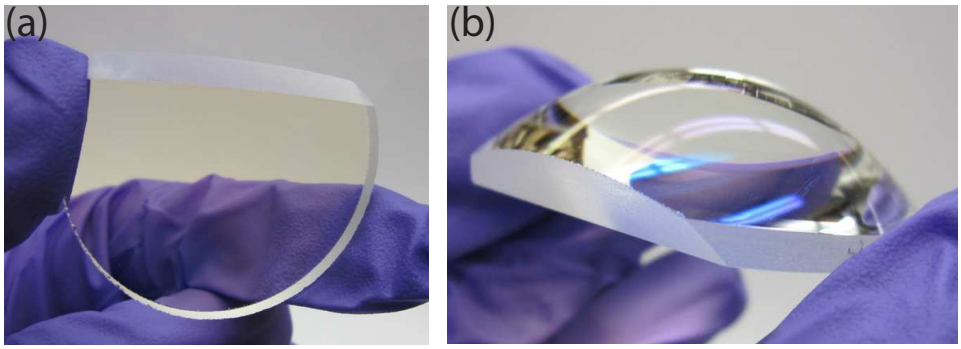

Figure 7.41: Photograph of the objective lenses: a) Meniscus lens. b) Aspheric lens.

The two lenses are housed in a specially designed objective holder. The meniscus lens sits at the bottom of the holder and is held in place by a Delrin sleeve. This sleeve also houses the aspheric lens. This Delrin sleeve allows for easy mounting of the aspheric lens inside the objective holder. It also determines the distance between the meniscus lens and the aspheric lens. The asphere is fixed to the objective holder by set screws.

After the lenses are machined and assembled inside the objective holder, the performance of the objective is tested by measuring the final waist of a YAG laser beam. The YAG laser is first fiber-coupled into a single-mode polarization-maintaining fiber and then collimated to a waist of 8.4 mm using an achromat doublet lens (Thorlabs AC254-100). To simulate the reentrant viewport window, a window of the same thickness and material is implemented into the test setup. Even without optimizing the alignment, waists of 2.1 μm and 2.0 μm are measured horizontally and vertically.

Two beam splitter cubes, the first a polarizing beam splitter cube, and the second a fixed ratio beam splitter cube, shown in figure 7.40 can be used to stabilize the beam power in the YAG using a PID feedback loop. The first beam splitter cleans the polar-

ization of the beam. The second cube reflects a fixed amount of power. Fluctuations in this power can be measured with the photodiode and fed back to an AOM used to stabilize the power.

7.4 Computer Control and Data Acquisition

The computer control and data acquisition software and hardware is an updated version of the rubidium system. A newer version of Control, a Visual C++ program originally written by Florian Schreck, a former postdoctoral scholar, offers precision timing of 500 ns of the experimental sequence, and a user-friendly graphical interface. Control communicates with three different National Instruments cards, NI6533, NI6733 and NI PCI-GPIB. It generates a waveform of the experimental sequence and sends the infromation as 25 bit data to the NI cards. The first 16 bits are used for data, the next 8 address the different outputs and the last bit is used as a strobe bit to synchronize the outputs. This is necessary to achieve a timing precision of 500 ns. All 25 bits from Control are sent to all of the outputs, however, only the one with the matching address will respond.

The first of the NI cards (NI6533) controls 16 analog outs, 32 digital outs and 9 direct digital synthesizer (DDS) boards. The output from the NI card first goes to a bus driver/buffer card. Here the signal is amplified and connected to flat ribbon cables, that connect to the home-built digital/analog out cards and the DDS. The analog and digital out cards from the rubidium experiment have to be modified to allow for the increased timing precision. The design of these boards can be found at [108]. The setup currently has two analog out cards, each with 8 channels per board, and two digital out cards with 16 digital outs each. The analog boards provide an output voltage between -10 V and $+10$ V, the digital outs work as TTL signals with a high of around 3.5 V. In addition 9 DDS boards are currently installed. These are based on the AD9852 DDS IC and provide frequencies up to 135 MHz. A commercial frequency generator (Wavetek 2407) provides a 300 MHz reference signal to the DDS boards. The DDS are used as frequency sources for the AOMs.

The second card (NI6733) offers eight digital in/out and two 24 bit counters. This card will be used for acquiring single atom detection data. For each detected photon the avalanche photodiode (APD) generates a pulse. These pulses can then be counted with the help of this card.

The last card (NI PCI-GPIB) is able to control GPIB-cabale devices and is used to interface with GPIB devices. Thus far it was mainly used to communicate with an arbitrary function generator (Agilent 33250A).

A second PC runs a program called Apogee Server. This program controls the two cameras in the experimental setup: The USB camera Apogee Alta U47+ and the FireWire camera Stingray F033B/C from Allied Vision Technologies. A third computer, running the software Vision, also written by Florian Schreck, communicates both with Control and Apogee Server. If a picture is to be taken during the experimental sequence, Control sends this information to Vision, which in turn tells Apogee Server to prepare the camera. Control then triggers the camera and Apogee Server downloads the picture information from the camera and sends the data to Vision.

The main purpose of Vision is data evaluation. Depending on the type of image taken, Vision automatically displays the fluorescence image, or uses the raw absorption, the probe, and the noise image of absorption imaging to calculate the optical density. It also fits the data to determine atom number, the spatial extent of the cloud, etc. Vision automatically stores all the images and all the variables with values used in the experimental sequence. This allows a complete reconstruction of the experimental sequence at any time.

7.5 Imaging

Imaging of lithium atoms using absorption imaging techniques is more complicated than for rubidium, due to the differences in energy level structure. Corrections to the simple formulas given before are therefore required. In addition it can be very helpful to image the atoms at a homogeneous magnetic field, and the presence of the field has to be taken into account during the imaging process.

7.5.1 Absorption Imaging

Determining the absorption scattering cross section in the case of lithium, especially in the presence of external magnetic fields, is not as straight forward as it is for rubidium. The excited states are not resolved, thus making the two-level assumption used to calculate the scattering cross-section invalid. In addition the existence of the second hyperfine ground state cannot be neglected.

7.5.1.1 Absorption Scattering Cross Section at Zero Magnetic Field

For imaging the atoms at zero magnetic field, for example for measuring the temperature of the MOT, both MOT and repump light are required. Without repump light, the atoms will only scatter a few photons and then fall into the lower state, where they are transparent to the MOT light. The absorption imaging beam used at zero magnetic field is thus derived from the tapered amplifier, which has both MOT and Repump frequencies.

In a multi-level atom, the on-resonance scattering cross section will differ from the two-level approximation ($\sigma_0 = \frac{3\lambda^2}{2\pi}$), and all possible transitions have to be taken into account. The transition matrix element is given by

$$\mu = \langle (J_2 I) F_2 m_{F_2} | \hat{\mu}(1,q) | (J_1 I) F_1 m_{F_1} \rangle, \tag{7.1}$$

where the subscript 1 corresponds to the ground state, the subscript 2 to the excited state respectively.

In lithium the excited state energy levels are degenerate to within the transition linewidth, so all possible values for F_2 have to be taken into account. The transition matrix element will be shown to be independent of the polarization of the laser light, and a random mixture of polarizations is therefore assumed. In addition, the magnetic sublevels of the ground state will be mixed. An even mixture of these states is assumed in the following calculation.

$$\hat{e} = \sum_q a(q) \hat{e}_q \tag{7.2}$$

$$\sum_q |a(q)|^2 = 1. \tag{7.3}$$

Averaging over the magnetic sublevels requires each component of the transition matrix element to be weighed with the degeneracy factor $\frac{1}{2F_1+1}$. The possible values for the quantum number are $I = 1$,$F_1 = 3/2$, $F_1 = 1/2$, $F_2 = 1/2$, $F_2 = 3/2$, $F_2 = 5/2$ $J_1 = 1/2$ and $J_2 = 3/2$. The transition matrix element is then given by

$$\mu^2 = \frac{1}{2F_1+1} \sum_q |a(q)|^2 \sum_{F_2, m_{F_2}, m_{F_1}} |\langle (J_2 I) F_2 m_{F_2} | \hat{\mu}(1,q) | (J_1 I) F_1 m_{F_1} \rangle|^2. \tag{7.4}$$

This matrix element can be rewritten using the Wigner-Eckhart-Theorem [26],

$$\mu^2 = \frac{1}{2F_1+1} \sum_q |a(q)|^2 \sum_{F_2} \sum_{m_{F_2}, m_{F_1}} (-1)^{2(F_2 - m_{F_2})} \begin{pmatrix} F_2 & 1 & F_1 \\ -m_{F_2} & q & m_{F_1} \end{pmatrix}^2 \times |\langle (J_2 I) F_2 | \hat{\mu}(1) | (J_1 I) F_1 \rangle|^2, \tag{7.5}$$

where the term in parenthesis is known as Wigner-3j-symbol.

The sum over the magnetic sublevels is independent of the polarization and the final level. The equation thus reduces to

$$\mu^2 = \frac{1}{3(2F_1+1)} \sum_{F_2} |\langle (J_2 I) F_2 | \hat{\mu}(1) | (J_1 I) F_1 \rangle|^2. \tag{7.6}$$

Using further angular momentum coupling, equation 7.6 can be simplified using the reduced dipole matrix element of the D_2 line, $\langle (L_2 S) J_2 || \hat{\mu}(1) || (L_1 S) J_1 \rangle$:

$$\mu^2 = \frac{1}{3(2F_1+1)} \sum_{F_2} \delta_{I_2 I_1} (-1)^{2(J_2 + I_1 + F_1 + 1)} (2F_1+1)(2F_2+1) \times \left| \begin{Bmatrix} J_2 & I & F_2 \\ F_1 & 1 & J_1 \end{Bmatrix} \right|^2 |\langle (L_2 S) J_2 || \hat{\mu}(1) || (L_1 S) J_1 \rangle|^2 . \tag{7.7}$$

The transition matrix element for the MOT light ($F_1 = 3/2$) and the repump light ($F_1 = 1/2$) are therefore

$$\begin{aligned} \mu^2 &= \frac{1}{6} |\langle (L_2 S) J_2 || \hat{\mu}(1) || (L_1 S) J_1 \rangle|^2 \\ &= \frac{2}{3} \mu_0^2, \end{aligned} \tag{7.8}$$

The on-resonance absorption scattering cross section is thus given by

$$\sigma_{MOT} = \sigma_{Repump} = \frac{2}{3}\, \sigma_0 = \frac{\lambda^2}{\pi} \tag{7.9}$$

where $\sigma_0 = \frac{3\lambda^2}{2\pi}$.

7.5.1.2 Absorption Scattering Cross Section at Large Magnetic Fields

In the presence of a magnetic field, the effective scattering cross section differs from the scattering cross section at zero magnetic field. The energy levels at high fields are separated by more than the transition linewidths and thus individual transitions can be resolved. The energy level splitting as a fuction of an external magnetic field is shown in figure 7.42.

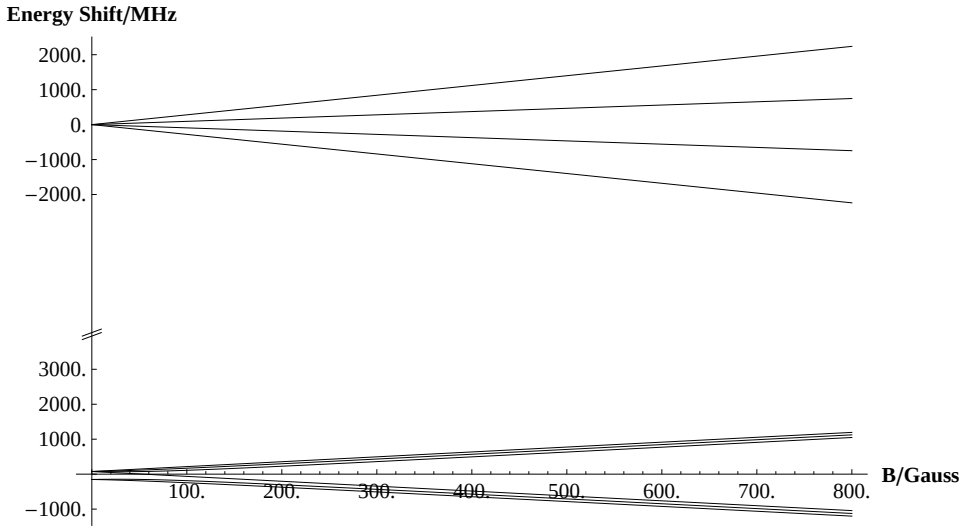

Figure 7.42: Energy level splitting as a function of an external magnetic field. At high magnetic fields the energy levels split to more than the transition linewidth.

Prior to optical evaporation, the atoms are pumped into the $|F = 1/2\rangle$ state. At large magnetic fields they will therefore occupy the two lowest states. In this regime a closed cycling transition exists. This means that a repump beam is not necessary. Because the two states are energetically separated ($\Delta f \approx 76$ MHz), atoms can be imaged separately in each state. The cycling transition drives the atoms from the $|(L = 0, S = 1/2)J = 1/2, m_J = -1/2\rangle$ to the $|(L = 1, S = 1/2)J = 3/2, m_J = -3/2\rangle$ state, as shown in figure 7.43.

Unfortunately, the transition frequency is slightly dependent on the magnitude of the magnetic fields. It tunes with approximately 1.4 MHz/G. However, knowing the magnetic field, the frequency of the imaging laser can be adjusted using the frequency-offset lock.

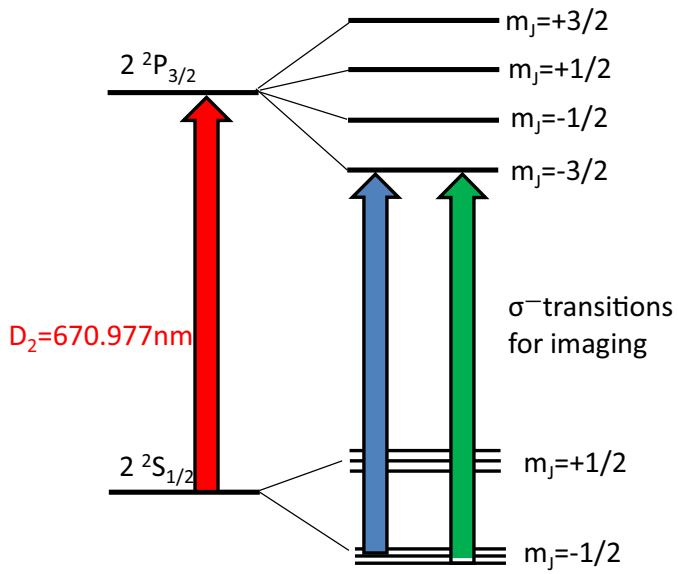

Figure 7.43: Imaging transitions at high magnetic field.

The quantization axis is defined by the magnetic field orientation of the Feshbach coils, which is chosen along the $\hat{z}$-axis. To take advantage of the maximum scattering cross section the imaging beam would have to be σ^- polarized and traveling along the quantization axis. Unfortunately, this axis is reserved for doing the laser culling and single atom detection, and imaging along this axis is therefore not easily implemented. The imaging axis is perpendicular to the quantization axis instead. Because this axis is also used for a MOT beam and MOT and imaging beam share optics, the imaging beam is circularly polarized with opposite handedness than the MOT beam. Because of these complications the full vector nature of the field amplitude $\vec{\mathcal{E}}$ has to be considered [109].

The calculations are performed in a rotated (primed) coordinate system as shown in figure 7.44.

In the lab frame the polarization of the atomic transition is given by $\sigma^- = 1/\sqrt{2}(\hat{x} - i\hat{y})$. In the primed coordinate system the transition is hence $\sigma^{-'} = 1/\sqrt{2}(\hat{x}' - i\hat{z}')$. The scattering cross section, as will be shown below, is independent on the handedness of the incident polarization, σ^+ or σ^- polarized, and the handedness will therefore

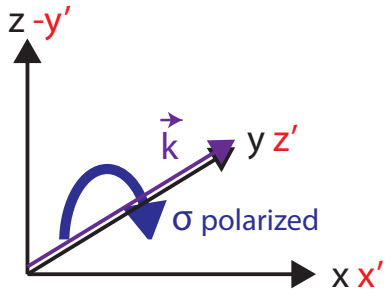

Figure 7.44: Coordinate systems at high magnetic fields. The quantization axis is determined by the magnetic field and is along the z axis. The black coordinates are in the lab-frame, the red primed coordinates represent the rotated frame used for calculating the scattering cross section.

not be specified. The incident polarization is $\hat{\epsilon}_{inc} = 1/\sqrt{2}(\hat{x} \pm i\hat{z})$ in the lab frame, which corresponds to $\hat{\epsilon}'_{inc} = 1/\sqrt{2}(\hat{x}' \mp i\hat{y}')$ in the rotated frame.

The effect of the atomic cloud on the field is described by the differential equation [109]

$$\frac{\partial \mathcal{E}(x', y', z')}{\partial z'} = -\left(\frac{n(x', y', z')\,\sigma_0}{2(1+\delta^2)}\right)(1+i\delta)(\mathbb{I} - \hat{z}'\hat{z}') \cdot \hat{\sigma}^-\,\hat{\sigma}^{-*} \cdot \mathcal{E}(x', y', z'). \tag{7.10}$$

$\mathbb{I}$ is the identity matrix, $\delta \equiv \frac{2\Delta}{\Gamma}$ is the detuning from resonance in units of half linewidth, and $\hat{\sigma}^-$ is the left-circular unit vector. Taking a closer look at this differential equation one important physical conclusion can be drawn immediately: only the projection of the field onto the excitation vector $\hat{\sigma}^{-*} \cdot \mathcal{E}(x', y', z')$ can excite the atom.

This differential equation can be solved by looking for eigenvector solutions for which the incoming polarization is preserved. This leads to the following ansatz

$$\mathcal{E}(x', y', z') = \mathcal{E}_0\, exp\left[\left(\frac{-n\,\xi\sigma_0}{2(1+\delta^2)}\right)(1+i\delta)\right]\hat{\epsilon}. \tag{7.11}$$

$\sigma_0 = 3\lambda^2/(2\pi)$ is the on-resonance scattering cross section of a two-level atom and $n = n(x', y') = \int_{-\infty}^{\infty} n(x', y', z')dz'$ is the atomic column density. ξ has been added as a factor to account for the difference to the effective scattering cross section σ_0. $\hat{\epsilon}$ is the polarization unit vector of the field. Using this ansatz in equation 7.10 leads to the following eigenvalue equation

$$\xi\hat{\epsilon} = (\mathbb{I} - \hat{z}'\hat{z}') \cdot \hat{\sigma}_-\,\hat{\sigma}^*_- \cdot \hat{\epsilon}. \tag{7.12}$$

The right hand side of equation 7.12 consists of a vector $(\mathbb{I} - \hat{z}'\hat{z}') \cdot \hat{\sigma}_-$ and a scalar $\hat{\sigma}_-^* \cdot \hat{\epsilon}$. The first solution is hence

$$\hat{\epsilon}_1 = \gamma(\mathbb{I} - \hat{z}'\hat{z}') \cdot \hat{\sigma}_- = \hat{x}' \tag{7.13}$$

$$\xi_1 = \left(\frac{1}{\gamma}\right) \hat{\sigma}_-^* \cdot \hat{\epsilon} = \frac{1}{2} \tag{7.14}$$

Here γ is the normalization constant.

The second solution is easily found as it has to be perpendicular to the propagation direction ($\hat{z}' \cdot \hat{\epsilon}_2 = 0$) and the already known solution ($\hat{\epsilon}_2^* \cdot \hat{\epsilon}_1 = 0$). The solutions are thus

$$\hat{\epsilon}_2 = \hat{y}' \tag{7.15}$$

$$\xi_2 = 0. \tag{7.16}$$

Every polarization can be decomposed into the two eigenpolarizations, one interacting with the atoms ($\hat{\epsilon}_1$), and one not ($\hat{\epsilon}_2$).

In general the incident field is given by

$$\mathcal{E}_{inc} = \mathcal{E}_0 \, \hat{\epsilon}'_{inc} = \mathcal{E}_0 \frac{1}{\sqrt{2}} (\hat{\epsilon}'_1 \mp i\hat{\epsilon}'_2). \tag{7.17}$$

Expanding this field in terms of the eigenpolarization leads to

$$\mathcal{E}_{inc} = \mathcal{E}_0 \, (\hat{\epsilon}_{inc} \cdot \hat{\epsilon}_1^*) \, \hat{\epsilon}_1 + \mathcal{E}_0 \, (\hat{\epsilon}_{inc} \cdot \hat{\epsilon}_2^*) \, \hat{\epsilon}_2. \tag{7.18}$$

The field in the object plane of the imaging system can then be derived by applying the same ansatz to each term:

$$\mathcal{E}_{obj} = \mathcal{E}_0(\hat{\epsilon}'_{inc} \cdot \hat{\epsilon}_1^*) \, exp\left[\left(\frac{-n\xi_1\sigma_0}{2(1+\delta^2)}\right)(1+i\delta)\right] \hat{\epsilon}_1 + \mathcal{E}_0(\hat{\epsilon}'_{inc} \cdot \hat{\epsilon}_2^*) \, \hat{\epsilon}_2 \tag{7.19}$$

For the incoming polarization in the experimental setup, $\hat{\epsilon}'_{inc} = 1/\sqrt{2}(\hat{x}' \mp i\hat{y}')$, the field in the object plane simplifies to

$$\mathcal{E}_{obj} = \frac{\mathcal{E}_0}{\sqrt{2}} \, exp\left[\left(\frac{-n\xi_1\sigma_0}{2(1+\delta^2)}\right)(1+i\delta)\right] \hat{\epsilon}_1 \mp \frac{i\mathcal{E}_0}{\sqrt{2}} \, \hat{\epsilon}_2, \tag{7.20}$$

where

$$\hat{\epsilon}'_{inc} \cdot \hat{\epsilon}^*_1 = \frac{1}{\sqrt{2}}(\hat{x}' \mp i\hat{y}') \cdot \hat{x}' = \frac{1}{\sqrt{2}} \tag{7.21}$$

$$\hat{\epsilon}'_{inc} \cdot \hat{\epsilon}^*_2 = \frac{1}{\sqrt{2}}(\hat{x}' \mp i\hat{y}') \cdot \hat{y}' = \mp\frac{i}{\sqrt{2}} \tag{7.22}$$

is used.

The scattered field is then found by subtracting the incident field:

$$\begin{aligned}
\mathcal{E}_{scat} &= \mathcal{E}_{obj} - \mathcal{E}_{inc} \\
&= \frac{\mathcal{E}_0}{\sqrt{2}}\, exp\left[\left(\frac{-n\xi_1\sigma_0}{2(1+\delta^2)}\right)(1+i\delta)\right]\hat{\epsilon}_1 \mp \frac{i\mathcal{E}_0}{\sqrt{2}}\,\hat{\epsilon}_2 - \left(\mathcal{E}_0\frac{1}{\sqrt{2}}(\hat{\epsilon}'_1 \mp i\hat{\epsilon}'_2)\right) \\
&= \frac{\mathcal{E}_0}{\sqrt{2}}\left\{exp\left[\left(\frac{-n\xi_1\sigma_0}{2(1+\delta^2)}\right)(1+i\delta)\right] - 1\right\}\hat{\epsilon}_1
\end{aligned} \tag{7.23}$$

To derive the intensity profile in the imaging plane, the effect of the imaging optics on the fields has to be taken into account. In the thin lens approximation [110] the scattered and incident fields are thus given by

$$\mathcal{E}_{scat}(x', y') = \frac{\mathcal{E}_0}{\sqrt{2}}\left\{exp\left[\left(\frac{-n\xi_1\sigma_0}{2(1+\delta^2)}\right)(1+i\delta)\right] - 1\right\} exp\left[\frac{ik}{2f}(x'^2 + y'^2)\right]\hat{\epsilon}_1 \tag{7.24}$$

$$\begin{aligned}
\mathcal{E}_{inc} &= \mathcal{E}_0\, exp\left[\frac{ik}{2f}(x'^2 + y'^2)\right]\hat{\epsilon}'_{inc} = \mathcal{E}_0\, exp\left[\frac{ik}{2f}(x'^2 + y'^2)\right]\frac{1}{\sqrt{2}}(\hat{\epsilon}'_1 \mp i\hat{\epsilon}'_2) \\
&= \mathcal{E}_0\, exp\left[\frac{ik}{2f}(x'^2 + y'^2)\right]\frac{1}{\sqrt{2}}(\hat{x}' \pm i\hat{y}').
\end{aligned} \tag{7.25}$$

The total electric field in the image plane is determined by the sum of the scattered and the incident field:

$$\begin{aligned}
\mathcal{E}_{tot} &= \mathcal{E}_{scat} + \mathcal{E}_{inc} \\
&= \frac{\mathcal{E}_0}{\sqrt{2}}\left\{exp\left[\left(\frac{-n\xi_1\sigma_0}{2(1+\delta^2)}\right)(1+i\delta)\right] - 1\right\} exp\left[\frac{ik}{2f}(x'^2 + y'^2)\right]\hat{\epsilon}_1 + \\
&\quad \mathcal{E}_0\, exp\left[\frac{ik}{2f}(x'^2 + y'^2)\right]\frac{1}{\sqrt{2}}(\hat{\epsilon}'_1 \mp i\hat{\epsilon}'_2) \\
&= \frac{\mathcal{E}_0}{\sqrt{2}}\left\{exp\left[\left(\frac{-n\frac{1}{2}\sigma_0}{2(1+\delta^2)}\right)(1+i\delta)\right] - 1\right\} exp\left[\frac{ik}{2f}(x'^2 + y'^2)\right]\hat{x}' + \\
&\quad \mathcal{E}_0\, exp\left[\frac{ik}{2f}(x'^2 + y'^2)\right]\frac{1}{\sqrt{2}}(\hat{x}' \pm i\hat{y}')
\end{aligned}$$

$$= \frac{\mathcal{E}_0}{\sqrt{2}} exp\left[\left(\frac{-n\frac{1}{2}\sigma_0}{2(1+\delta^2)}\right)(1+i\delta)\right] exp\left[\frac{ik}{2f}(x'^2+y'^2)\right]\hat{x}'$$
$$\pm\frac{i\mathcal{E}_0}{\sqrt{2}} exp\left[\frac{ik}{2f}(x'^2+y'^2)\right]\hat{y}' \tag{7.26}$$

Defining $I = k|\mathcal{E}_{tot}|^2$ and $I_0 = k|\mathcal{E}_{inc}|^2$ leads to

$$I_0 = k\left(\frac{|\mathcal{E}_0|^2}{2}+\frac{|\mathcal{E}_0|^2}{2}\right) = k|\mathcal{E}_0|^2 \tag{7.27}$$

$$I = k\left(\frac{|\mathcal{E}_0|^2}{2} exp\left[\frac{-n\frac{1}{2}\sigma_0}{1+\delta^2}\right]+\frac{|\mathcal{E}_0|^2}{2}\right) \tag{7.28}$$

and thus

$$\frac{I}{I_0} = \frac{1}{2} exp\left[\frac{-n\frac{1}{2}\sigma_0}{1+\delta^2}\right]+\frac{1}{2} = \frac{1}{2} exp\left[\frac{-n\sigma^*}{1+\delta^2}\right]+\frac{1}{2}. \tag{7.29}$$

The effective scattering cross section σ^* is only half of σ_0. In addition, only half the light interacts with the atoms. The temperature of the MOT and the compressed MOT is measured using the setup shown in 7.38, where this calculation applies.

For imaging atoms trapped in the CO_2 laser a few changes to the optical setup shown in figure 7.38 are necessary. First, the $f = 50$ mm lens is removed, changing the magnification to be roughly 1:4. Because of the lower atom number and the increased magnification the signal-to-noise ratio is reduced as compared to imaging of the MOT. Instead of using a polarizing beam splitter cube to combine the MOT and the imaging beam, a mirror mounted on a motorized flipper is added to the setup. It is then possible to use linearly polarized light for imaging the atoms. The intensity in the image plane is then given by [109]

$$\frac{I}{I_0} = exp\left(\frac{-n\frac{1}{2}\sigma_0}{1+\delta^2}\right). \tag{7.30}$$

The disadvantage of this setup is that atoms cannot be imaged in the MOT, because the time the flipper requires exceeds the storage time of the atoms.

Lithium atoms expand faster than other alkali atoms. This means that especially at MOT temperatures the atoms can move a significant distance even during the imaging exposure time. The imaging pulse duration is therefore restricted to between 10 μs and 20 μs to minimize this effect.

In the derivation for the optical density, it was assumed that the probe beam intensity I satisfies $I \ll I_{sat}$. Unfortunately this is not the regime with the best signal-to-noise ratio. The best signal-to-noise ratio is found for intensities $I \approx I_{sat}$. However, for a large enough number of atoms it is possible to achieve adequate signal-to-noise ratios even in the low-intensity regime.

7.5.2 Fluorescence Imaging and Calibration

Fluorescence imaging of lithium atoms is very straight forward, and no special considerations have to be made. Even though fluorescence imaging is simple it is very useful for finding the image plane and calibrating the magnification of the imaging system.

The image plane, and thus the position of the camera, can be found using a split-imaging technique. A mask with two or more holes is placed directly behind the imaging lens, as shown in figure 7.45. The fluorescence signal is then collected only through those two holes. If the camera is not placed in the image plane, the two images formed by the two spots will not overlap; they coincide only in the image plane. This method is a quick and easy way to locate the image plane.

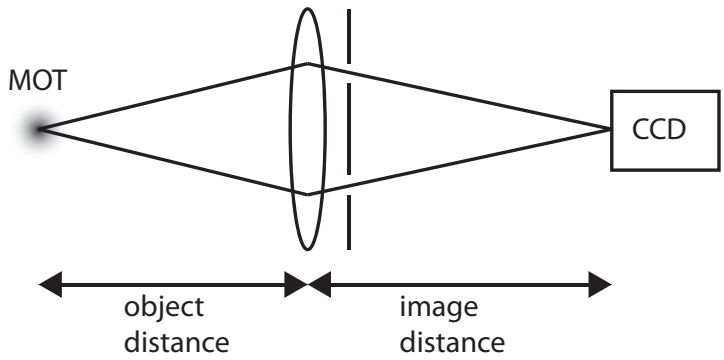

Figure 7.45: Schematic setup for finding the imaging plane using a split-imaging technique. A mask with two or more holes is placed behind the imaging lens. The two images of the MOT coincide only in the imaging plane.

The magnification of an imaging system is typically determined by taking a series of images showing atoms in free fall. The center of mass position can then be used to calibrate the magnification. This method, however, has a couple of problems. Any

residual potentials besides gravitation can lead to errors in the measured magnification. In addition, the determination of the center of mass of the atomic cloud is not always trivial, especially if the atoms are expanding as quickly as they do in a lithium MOT. A different method is therefore used in this experiment. A tightly collimated resonant laser beam (waist $w_0 \ll 1$ mm), traveling perpendicular to the imaging axis, is aligned to the center of the MOT. Atoms are loaded into the MOT. The MOT beams and the magnetic field gradients are then turned off so that the atoms expand. The resonant laser beam is pulsed and the fluorescent signal recorded. The laser beam is then translated vertically by a known amount, and a second image is taken. The fluorescence signal recorded by the camera moves by the same amount by which the laser was translated. Doing this measurement for multiple vertical positions, one can easily determine the magnification of the imaging system.

Chapter 8

Towards Fock States of Lithium Atoms

Even though the lithium experiment has not been able to create Fock states yet, significant progress towards this goal has been made. This chapter summarizes this progress, showing data on MOT properties, CO_2 laser alignment, dipole trap loading and initial signs of evaporative cooling.

8.1 MOT Properties

The lithium oven typically operates at a temperature of 350°C. At this temperature about 1.5×10^8 atoms/second are loaded into the MOT. If everything is aligned optimally this number is frequently exceeded. Figure 8.1 shows the MOT loading. The MOT is loaded for a time t before the MOT and Zeeman slower light are turned off. Fluorescence imaging then determines the atom number. The MOT typically saturates around 5×10^8 atoms, at optimum alignment the saturation value can be higher. Loading rates up to 3×10^8 atoms and saturation values of up to 1×10^9 atoms have been achieved. At a higher oven temperature the MOT loads faster, however, the lithium reservoir will be depleted faster and the current loading rate is sufficient for the experiment.

The lifetime of the magneto-optically trapped atoms can be used as a direct measure to determine the collision rate with background atoms. In a MOT there are two processes that can lead to traploss. At high atomic densities, the loss is dominated by two-body loss, which occurs when two trapped atoms collide with each other. At lower densities, two-body collisions are reduced and collisions with atoms from the background gas are the dominating loss mechanism. The lifetime of the MOT in the low density limit is thus a good indication of the background pressure and how this pressure will limit the lifetime in the optical dipole trap.

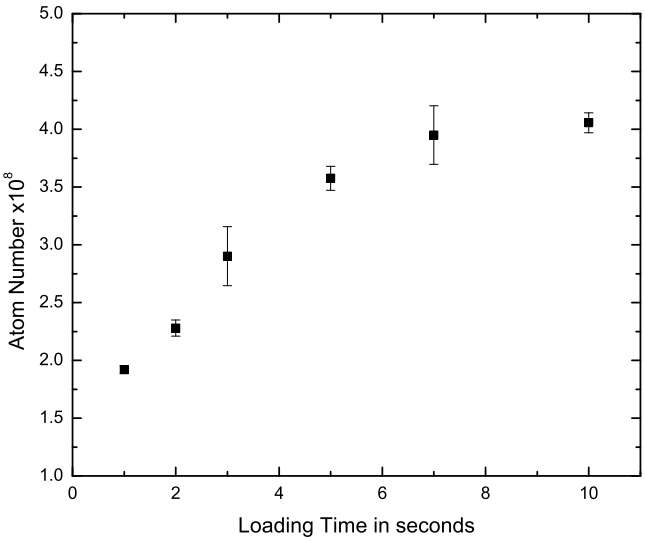

Figure 8.1: MOT loading. Typical loading rates are about $1.5 \cdot 10^9$ atoms/second and saturation values lie around $5 \cdot 10^8$ atoms.

In order to measure the lifetime in the low-density regime, the magnetic field gradient of the quadrupole field and the beam power in the MOT beams are reduced. Under these conditions and with short loading times (300 ms or less), only a small number of atoms is loaded into the MOT, leading to a low density of atoms inside the trap. The lifetime is determined to be around 27 s, in good agreement with the lifetime expected from the pressure reading from the ion gauge. The vacuum pressure in the oven chamber is currently limited by outgassing of the ZnSe viewports. This hypothesis is supported by the fact that the vacuum pressure in the science chamber increases slightly when the viewports are heated by absorption of photons from the CO_2 laser beam. However, a lifetime of 27 s is sufficient and the experiment is not currently limited by the background pressure.

8.2 Compressed MOT

Unfortunately, direct loading out of this MOT into the CO_2 laser dipole trap is not feasible. The temperature of the MOT at a detuning of 38 MHz, the typical detuning

used for loading, is above 2 mK. The trap depth of the optical dipole trap, however, is only about 700 μK. A simple model estimates the equilibrium atom number trapped in an optical dipole trap [28]

$$N = N_0 \, F\left[\frac{U_0}{k_B T}\right] = n_{MOT} V_{trap} \, F\left[\frac{U_0}{k_B T}\right], \tag{8.1}$$

where N_0 is the number of atoms within the volume V_{trap} of the dipole trap at the density $n_{MOT} = N_0/V_{trap}$. $F[q]$ is given by

$$F[q] = \frac{q^{3/2}}{2} \int_0^1 dx \, x^2 g_1(x) exp[q(1-x)], \tag{8.2}$$

with

$$g_1(x) = \frac{(-ln(1-x))^{3/2}(1-x)^{1/2}}{x^2} \frac{16}{\pi} \int_0^1 du \, u^2 \sqrt{exp[(\ln(1-x))(1-u^2)] - 1}. \tag{8.3}$$

Figure 8.2 shows F as a function of $U_0/k_B T$.

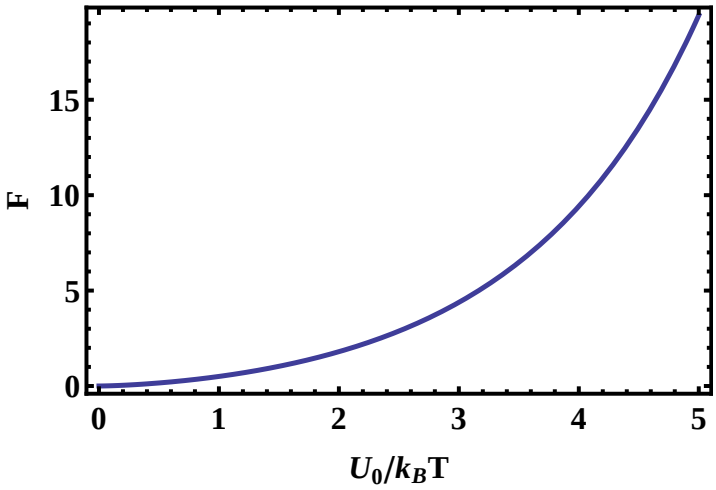

Figure 8.2: Dipole trap loading efficiency as a function of $U_0/k_B T$.

The number of atoms loaded into the into the CO_2 dipole trap is greatly enhanced as the temperature of atoms in the MOT is reduced. It is therefore necessary to compress the MOT in order to reduce the temperature and increase the number of atoms in the optical dipole trap, even though compressing the MOT leads to atom loss. Typically the compression sequence is run after the MOT is loaded at a detuning of 38 MHz. The Zeeman slower beams and field are turned off and the atomic beam shutter is closed.

A linear ramp typically changes the MOT beam detuning from 38 MHz to the final detuning in 3 to 10 ms using the frequency-offset lock.

Figure 8.3 shows the temperature of the atoms in the MOT as a function of the detuning and clearly indicates that changing the detuning is able to reduce the temperature drastically. The temperatures are measured using time-of-flight techniques. At larger detunings the uncertainty in the measurement is large, as only very short expansion times can be realized. The higher the temperature, the faster the atomic cloud expands, reducing the atomic density. Determining the size of the atomic cloud is more difficult at lower atomic densities. In addition, the maximum size of the atomic cloud that can be measured is determined by the size of the chip in the CCD camera.

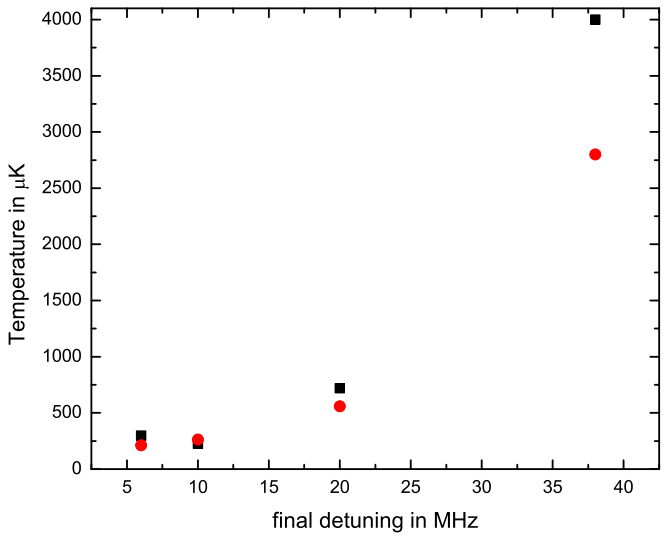

Figure 8.3: MOT temperature as a function of the MOT beam detuning. The black squares (red circles) represent T_x (T_y).

Along with changing the beam detuning, it is necessary to reduce the beam power in the MOT beams at the same time. Too large an intensity in the beams will heat the atoms, rather than achieving the desired cooling effect. Figure 8.4 shows the temperature at a fixed final detuning (6 MHz) as a function of final beam power. At -30 dB only about 40 μW (31 μW) of MOT (repump) power are in each of the MOT beams.

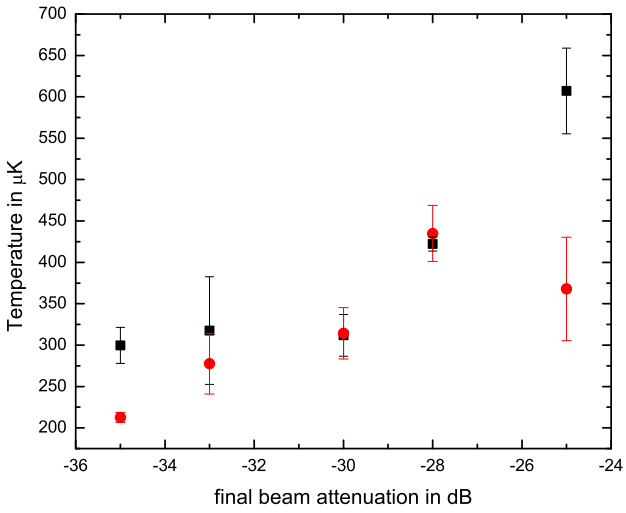

Figure 8.4: MOT temperature as a function of beam power at a fixed detuning of 6 MHz. Black squares (red circles) represent T_x (T_y).

By decreasing the detuning, the size of the MOT is also reduced. This behaviour is shown in figure 8.5.

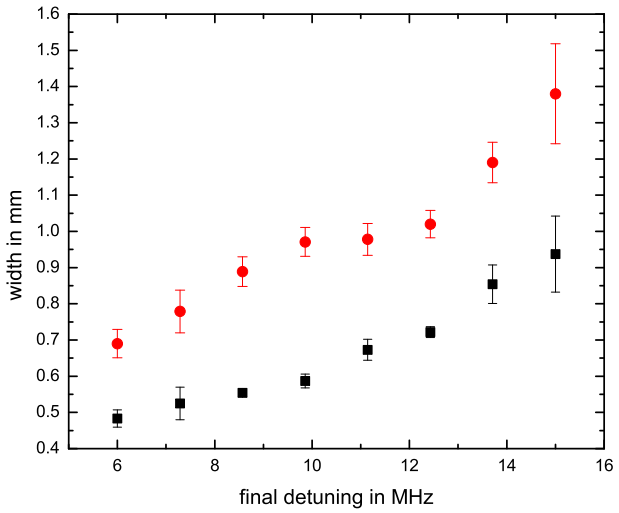

Figure 8.5: $1/e^2$ width of the MOT as a function of detuning. Red circles (black squares) represent σ_x (σ_y).

A typical MOT is density-limited at a density around 10^{11} cm^{-3}. Thus, a density-limited MOT will experience atom loss as the capture volume of the MOT is reduced by tuning the beams closer to resonance. This phenomenon is shown in figure 8.6. At $t = 0$ the final detuning is reached. Due to the density-limit, the atom number decreases very quickly in the first few ms, until the atom number is reduced to the density-limited value. Any further atom loss is then due to two-body collisions.

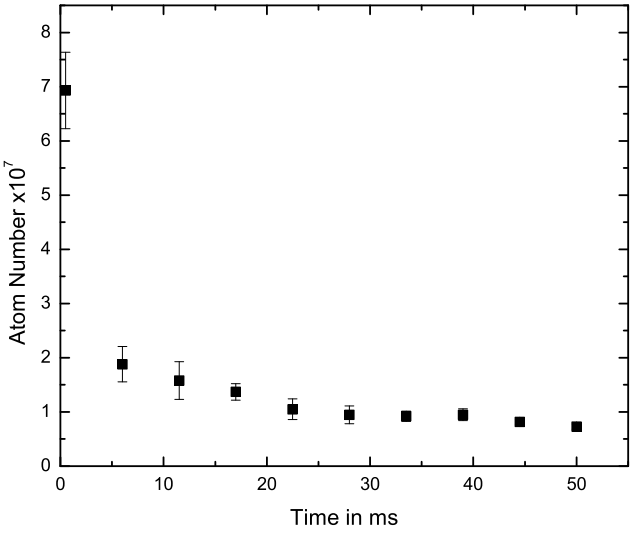

Figure 8.6: Atom number as a function of time after MOT compression. At the reduced trap size the density-limited atom number is exceeded, leading to fast trap loss until the density-limited value is reached.

To measure the MOT temperature, typical expansion times are between 50 and 1000 μs. This poses a number of technical challenges. First, a really fast camera shutter is required to be able to take those images. The Alta U47+ (Apogee) camera uses a mechanical shutter with an opening time of approximately 5 ms. This implies that the shutter is partially open for a few ms before the picture is taken. During those ms scattered light from the MOT, i.e. a fluorescence image, is recorded on the camera, that will overlap with the absorption image. Cameras with mechanical shutters are therefore not suitable for this kind of measurement. Rather than using a mechanical shutter, the Stingray camera (Allied Vision Technologies, Stingray F-033B/C) uses an electronic

shutter instead. The shutter speed is less than 1 μs, enabling this camera to image atoms at very short times after the MOT beams are turned off.

The second problem results from the particular imaging setup in this experiment. Figure 7.38 shows that the imaging beam axis coincides with one of the three MOT beam axes. Even though more than 95% of the MOT beam power are reflected at the reflective polarizer, approximately 5% of the power is transmitted and photons impinge on the CCD chip of the Stingray camera, saturating the pixels. Before an image is taken, all prior charge built-up has to be removed. Unfortunately not all charges can be removed during the brief shutter time. An image of the remaining charge built-up is shown in figure 8.7.

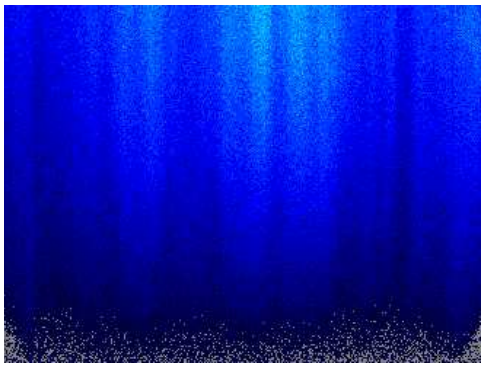

Figure 8.7: Charge built-up on the Stingray CCD camera.

This effect on the raw absorption image leads to a lot of noise in the absorption and optical density pictures, if the same effect is not visible in the probe image. It is therefore necessary to turn on the MOT beams again before taking the probe image. About 10 ms of MOT beam exposure prior to taking the probe image are sufficient to introduce the same effect on the probe image, so that this imaging artifact can successfully be removed from the absorption images.

8.3 Alignment of the CO_2 Laser Dipole Trap

Optical evaporation of atoms trapped in a red-detuned focused laser beam has been a very powerful technique to create degenerate gases. Using optical evaporation, degenerate gases of alkali atoms have been created in lithium [39, 111], sodium [112],

rubidium [113–115] and cesium[116]. Creating the tweezer trap using CO_2 lasers ($\lambda \approx 10\ \mu$m) has been particularly interesting because of the low noise of these lasers as well as the very low scattering rate due to the large detuning. However, aligning the CO_2 laser beam to the trapped cloud of atoms remains a challenging task.

A standard technique to align an optical dipole trap beam is to image this beam at the location of the atoms directly onto a camera. This method is however not employable when working with a wavelength larger than the mid-infrared, due to the limited wavelength sensitivity of a CCD or CMOS camera and thus does not work for aligning a CO_2 laser beam. The second technique is to look for a change in the scattering rate of the atoms in the presence of the CO_2 laser beam. Any laser beam causes a change in the polarizabilites of the atoms by the AC-Stark shift, thus effectively changing the transition frequency. Therefore the scattering rate of atoms in the MOT changes, as the detuning of the MOT laser beams is varied. This technique has been used successfully in [117]. However, for lithium atoms the change in the scattering rate in the presence of the CO_2 laser is vanishingly small, because the ground ($^2S_{1/2}$) and excited ($^2P_{3/2}$) state polarizabilities are nearly equal. For a 50 W laser beam focused to a waist of 50 μm the change in transition frequency at the peak intensity of the CO_2 laser is less than 10 MHz. The overall change in scattering rate is therefore negligible and makes alignment using this technique unviable for lithium atoms. In [118] an additional laser beam at a wavelength of 610 nm was therefore added. The scattering rate for this transition is highly sensitive to the alignment of the CO_2 laser and quick alignment using this technique could be achieved. However, this method requires an additional laser system to drive the sensitive transition and is therefore in general difficult and expensive to implement.

Instead the CO_2 laser beam is aligned by using balanced lock-in detection from a split-image of the fluorescence signal. This method requires only a few optics, two photodiodes and a lock-in amplifier.

Figure 8.8 shows a schematic of the experimental setup. About 3×10^8 ^{6}Li atoms are loaded in a MOT during the course of 2 s. The fluorescence light of the MOT is collected at an angle from underneath the vacuum chamber using a mirror (M1) and a 25 mm diameter lens with focal length $f = 75.6$ mm (L1). This setup is determined by

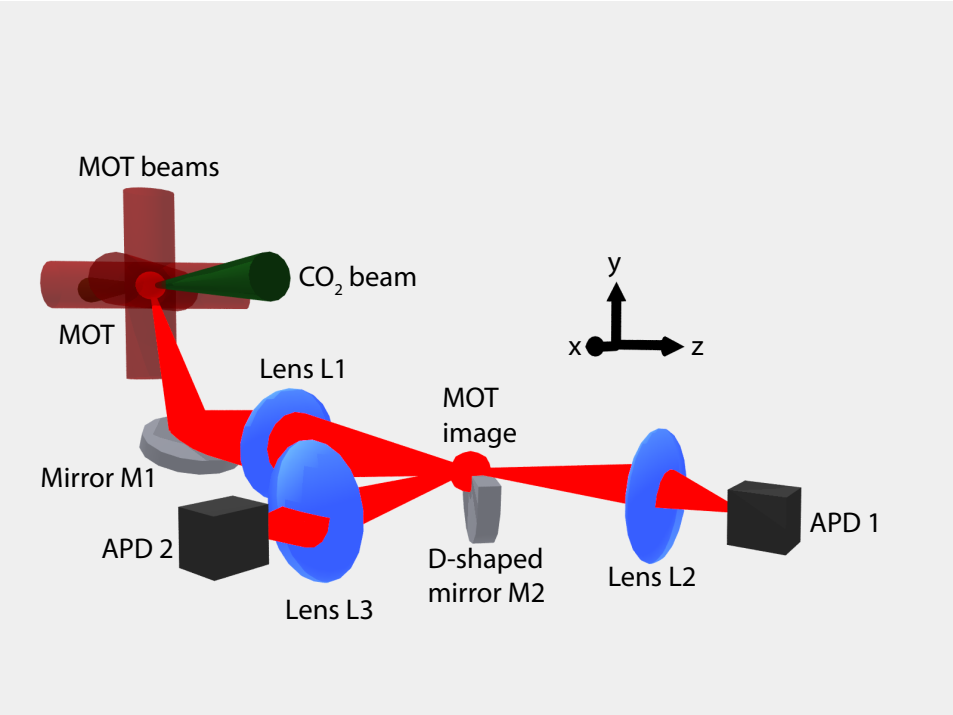

Figure 8.8: Experimental setup for locating the CO_2 laser beam within the trapped cloud of MOT atoms. The three pairs of retro-reflected MOT beams excite fluorescence in the atoms of the MOT. The CO_2 beam is located in the general vicinity of the trapped cloud of atoms. The mirror M1 reflects the fluorescence light from the MOT. The lens L1 collects the fluorescence light and creates an image of the MOT. In the image plane a D-shaped mirror (M2) cuts the fluorescent signal into two halves. These are individually focused by two lenses (L2 and L3) onto two avalanche photodiodes (APD1 and APD2).

the optical access that is available to collect the fluorescence light. Ideally the collection angle is maximized to capture a large number of scattered photons from the MOT atoms. Particular care is taken to reduce any scattered light from the MOT beams as much as possible in order to optimize the signal to noise ratio. In the image plane of the lens L1 the signal of the MOT is split 50:50 in the vertical dimension. The light is then collected with two $f = 25$ mm lenses (L2 and L3) and focused onto two avalanche photodiodes (APDs). To do balanced detection the signals of the two APDs are substracted from each other.

Figure 8.9 shows the measured noise spectra of (a) the electronic noise in combination with the noise caused by scattered light without atoms trapped in the MOT and (b) the noise of the system with atoms trapped in the MOT. These spectra clearly show

that most of the noise is due to the scattering of photons from the atoms. Most of the noise occurs at frequencies below 2 kHz. This is explained by the timescales with which the atoms move within the capture volume of the MOT.

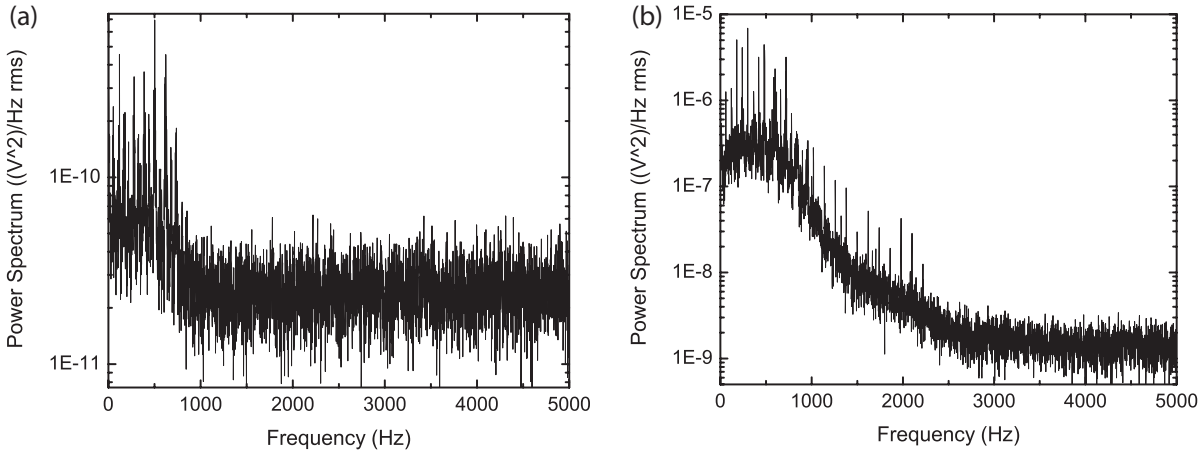

Figure 8.9: (a) Electronic noise and noise caused by scattered light. (b) Noise Spectrum in the presence of the MOT. In both cases the signal of the two APDs are substracted and the difference is recorded.

At this point it is possible to start the balanced lock-in detection. The CO_2 laser is pulsed at a frequency f_1 by turning the AOM on and off using an RF switch. The presence of the CO_2 laser beam slightly changes the spatial distribution of the atoms within the MOT, causing a slight imbalance in the previously balanced signal from the APDs. Because this change is very small lock-in detection at the frequency f_1 is used to filter the small signal out of the large background noise.

The ideal pulsing frequency is in principle determined by three factors: the electronic noise in the APDs and the lock-in amplifier, which can be neglected in this case, the noise caused by fluctuations in the MOT, and the timescale at which the atoms will be able to react to the presence of the CO_2 laser beam. The ideal pulsing frequency is determined to be around 2.4 kHz.

Figure 8.10 (a) shows a sketch of how the coordinate system at the lens used to focus the CO_2 laser into the vacuum chamber is seen at the image location of the MOT. The horizontal black line indicates where the signal of the MOT is split into the two separate halves. z is the propagation axis of the laser beam and passes through the

center of the MOT. As an example it is shown how the CO_2 laser beam moves within the cloud of atoms when the lens is moved along the y-axis (labeled (1)-(3)). The axes are defined as shown in figure 8.8.

Figure 8.10 (b) - (d) shows the signal due to the imbalance caused by the pulsed CO_2 laser as a function of position. The signal of the lock-in amplifier is recorded with a time constant of 1 s and a sensitivity of 2 mV. The focus of the beam is moved by translating the CO_2 laser focusing lens using an X-Y-Z-translation stage. As long as the laser beam hits the lens with normal incidence the translation of the lens will correspond to a 1:1 movement of the focus inside the vacuum chamber. The lens moves along one axis, leaving the other two dimensions constant. The numerical values of the fixed dimensions are shown in the top left corner of each graph. The error bars indicate statistical uncertainties.

Figure 8.10 (b) shows the position dependence along the x-axis. The position of the focus along the y-axis is at $y = -0.8$ mm, 0.8 mm away from the center of the MOT. This implies that the laser beam is focused predominantely into the lower half of the MOT. As the laser focus is scanned from $x = -1.0$ mm to $x = 0$ mm an increase in the signal is seen. At $x = 0$ mm the signal is maximum. Here the focus is aligned to the center of the MOT along the x-axis and therefore the laser beam affects the largest number of atoms, leading to the largest imbalance signal. If the focus is scanned further ($x > 0$ mm) the signal decreases again, as the number of affected atoms decreases. If the CO_2 laser focus was aligned to the center of the MOT along the vertical dimension ($y = 0$ mm), the imbalance caused by the laser beam would be expected to be the same in both halves of the MOT. This would mean that the average signal would be zero.

In figure 8.10 (c) the CO_2 laser beam is translated along the y-axis. This is the dimension along which the fluorescence image is split in the image plane of the lens L1. The effect on the imbalance of the laser beam is therefore expected to be different than for the scan along the x-axis. At $y = 0$ mm both halves of the MOT will experience the same disturbance due to the laser beam, leading to a vanishing overall signal. As the laser focus is moved into the upper half of the MOT ($y > 0$ mm), the disturbance caused by the CO_2 laser is no longer balanced and a signal is observed. If the focus is moved

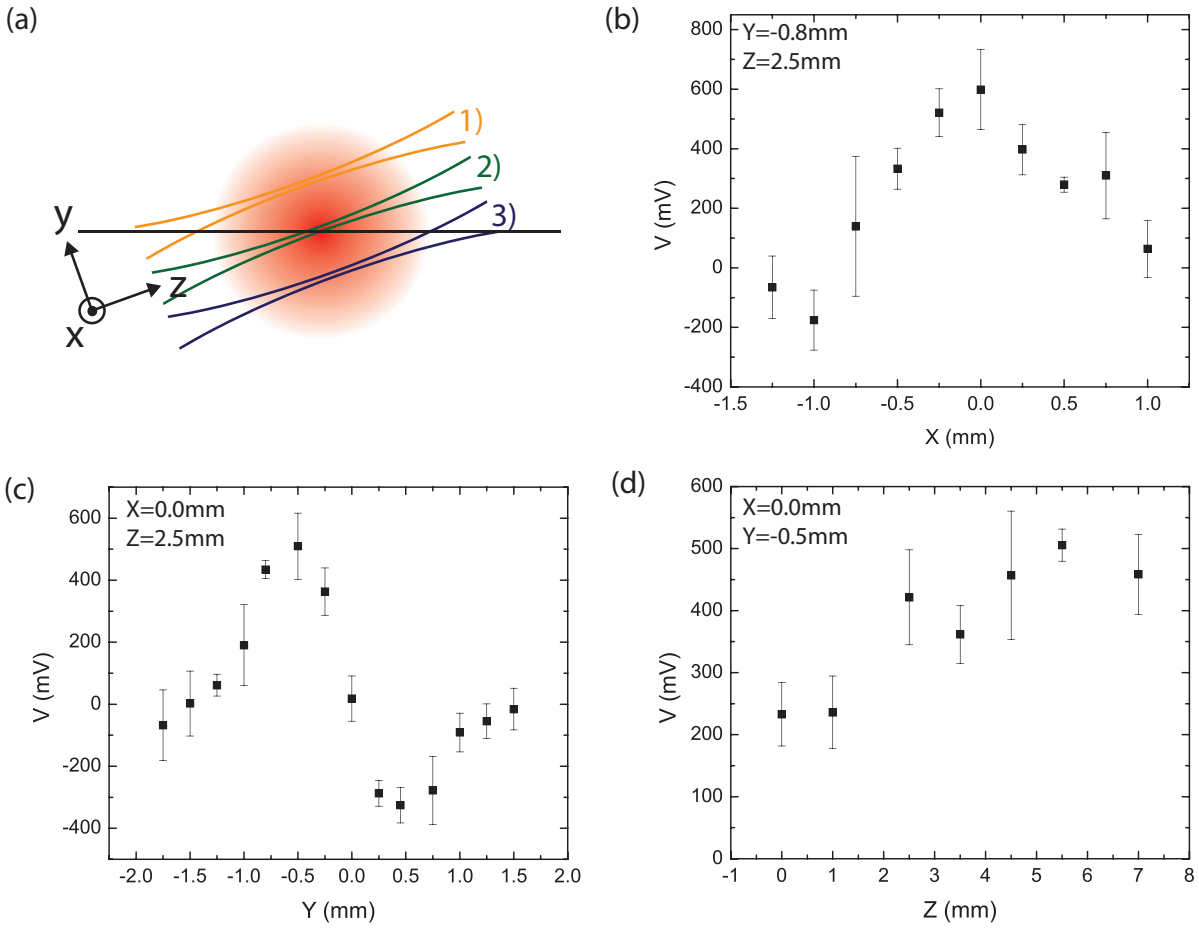

Figure 8.10: (a) Geometry of the split image and laser alignment. The horizontal black line symbolizes where the D-shaped mirror M2 splits the image into two halves. The two halves of the image are then detected with the two APDs. The coordinate system indicates how the coordinates at the CO_2 laser focusing lens translate at the MOT image plane. z is the propagation axis of the laser beam and passes through the center of the MOT. x (y) is the horizontal (vertical) axis at the lens position. The three focused laser beams (1-3) show the location of the CO_2 focus within the cloud for three differnet positions along the y-axis. The green beam (2) corresponds to the focus being aligned to the center of the MOT along the y-dimension, where the overall signal vanishes (see (c)) (b)-(d)Signal due to the imbalance caused by the pulsed CO_2 laser as a function of position. The focus of the laser beam is moved along one dimension, while the other two are held constant. (b) The focus of the laser beam is moved along the x-axis. (c) The focus of the laser beam is moved along the y-axis. (d) The focus of the laser beam is moved along the z-axis (along the beam propagation axis). Error bars indicate statistical uncertainties. The inset in the upper left corner indicates the alignment in the other two dimensions.

past $y = 0.5$ mm the signal starts to decrease again. This is due to two reasons: the total number of atoms affected by the CO_2 laser decreases as the laser beam is moved away from the center of the MOT. In addition the effect of the disturbance of the CO_2 focus is only local. This means that even though the atomic distribution is affected by the presence of the laser beam, the overall effect is limited to only one half of the MOT and thus does not lead to an imbalance in the scattered light between the two halves. The same phenomenon is visible if the focus is moved to the lower half of the MOT ($y < 0$ mm). However, the sign of the observed signal has changed, because this system detects the difference in the APD signals, not the absolute value.

Figure 8.10 (d) shows that the method described is not very sensitive to the alignment of the focus along the beam propagation axis, as expected from the long Rayleigh length along this dimension. The Rayleigh lengths of the CO_2 are 522 μm and 1102 μm respectively.

8.4 Loading of the Optical Dipole Trap

After aligning the CO_2 laser beam to the MOT and compressing the MOT to reduce the temperature, atoms are successfully loaded into the optical dipole trap. Once a first signal of the atoms is obtained it is possible to optimize the transfer into the trap in multiple ways. Before going into more details about this, it should be pointed out that one important step needs to happen after compressing the MOT and before turning the MOT beams off completely. Optical evaporation happens using atoms in the $|F = 1/2, m_F = \pm 1/2\rangle$ states. It is therefore necessary to optically pump the atoms into the lower state. This is done by turning the repump beam off before the MOT beam is turned off. Typical optical pumping times are on the order of ten to hundred of μs.

The location of the optical dipole trap is optimized first by moving the final focusing lens of the CO_2 laser beam. Additionally, the way the power in the MOT beams is decreased during the MOT compression stages is varied and the different curves of beam power as a function of time is shown in figure 8.11. The standard shape that was used for measuring the compressed MOT temperatures is shown in blue. Curve 1

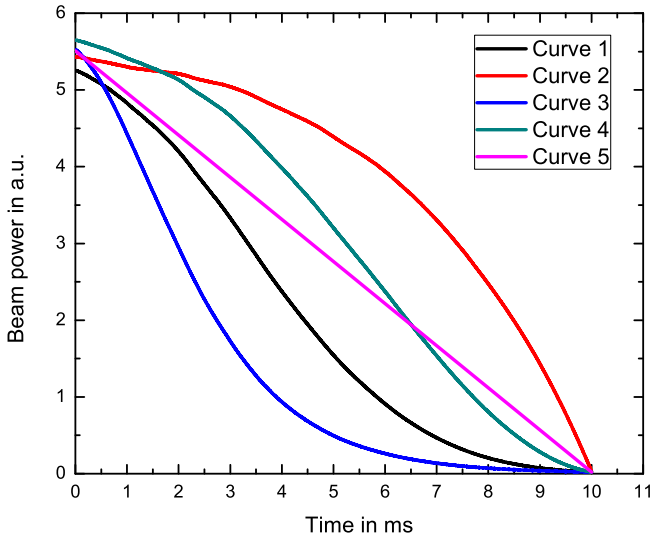

Figure 8.11: Different shapes of MOT compression curves. The detuning of the MOT beams is ramped linearly in all of these cases.

(black) leads to the best atom number in the optical dipole trap. (The number of atoms in the MOT before loading, and the final MOT beam detuning is kept constant to ensure fair comparison.) Table 8.1 summarizes the different shapes of the compression curves used and the corresponding atom number loaded into the optical dipole trap. The atom number is determined after 1 second holding in the CO_2 dipole trap. This ensures that all atoms not captured in the dipole trap are removed. This data was taken before the problem of the optical dipole trap lifetime was solved, see section 8.5, and thus the number loaded into the trap was actually larger than the numbers reported in table 8.1.

Curve	Fitted curve shape	atom number
1	$6.22 - 6.20 \cdot \sin^2(0.00115 \cdot (t + 55.199)^2)$	$(8.19 \pm 0.72) \times 10^5$
2	$5.80 - 0.340 \cdot \exp(\frac{t}{3.53})$	$(3.38 \pm 0.04) \times 10^5$
3	$0.0146 + 646 \cdot (1 - \exp(-\frac{(t+4.30)}{2.51}))^{7.69} \cdot \exp(-\frac{(t+4.30)}{1.32})$	$(5.34 \pm 0.68) \times 10^5$
4	$-0.160 + 5.69 \cdot \sin^2(0.147(t + 10.5))$	$(7.97 \pm 0.60) \times 10^5$
5	$5.51 - 0.549 \cdot t$	$(3.78 \pm 0.56) \times 10^5$

Table 8.1: Transfer into optical dipole trap for different compression curves. The atom number is determined 1 second after the MOT has been turned off, to ensure that only atoms in the optical dipole trap are counted.

In equilibrium, the temperature of the MOT is determined by the combination of beam intensities and beam detuning. At any given point during the compression ramp too large an intensity leads to heating of the atoms, while too low an intensity leads to traploss. The ideal ramp shape therefore balances those two competing effects, and the ideal ramp shape will minimize the temperature and maximize the number of atoms in the MOT.

8.5 Lifetime of the Optical Dipole Trap

After the successful loading of atoms into the optical dipole trap, the lifetime of atoms in the trap is measured. Unfortunately, the determined lifetime was only on the order of 15 seconds, much lower than the expected value. The main reason for chosing the CO_2 laser to create the optical dipole trap is its low intensity noise. The low intensity noise of the laser should, in principle, translate into a long lifetime in the optical dipole trap.

With the assumption that the laser itself has low intensity noise, the most likely source of noise is the RF source driving the CO_2 amplifier. The original RF source is a homebuilt DDS board. Noise near the trapping frequencies of the optical dipole trap is the most detrimental, so frequency spectra around the 40 MHz driving frequency are taken. However, the noise spectra are inconclusive.

The next step is to directly measure the noise in the laser beam itself. To measure noise in the kHz range of the infrared laser beam a Vigo system photodiode (PVM-10.6) is used. The photocurrent is then amplified with a low-noise amplifier (Stanford Research Systems SR560). Special care is taken to not exceed the saturation value of this photodetector. A schematic of the optical setup is shown in figure 8.12.

99% of the beam power are reflected out of the beam using a ZnSe beam splitter (not shown figure 8.12). The experimental setup is then simulated using an identical lens ($f = 5$ in) to the lens in the experimental setup to focus the laser beam. A ZnSe window with a thickness of 3 mm imitates the ZnSe window in the viewport. The light then passes through an uncoated CaF_2 window with a thickness of 5 mm. This window is

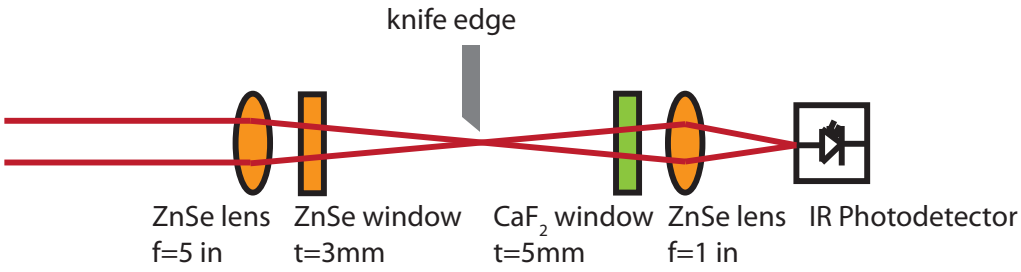

Figure 8.12: CO_2 noise measurement setup. The beam is first attenuated with a beam-splitter reflecting 99%, transmitting 1% of the power (not shown). The beam is then focused by the same lens as it is in the experimental setup to create the optical dipole trap. The ZnSe window simulates the viewport. A second ZnSe lens focuses the light onto the IR photodetector. In order to not exceed the maximum intensity at the photodetector a CaF_2 window is placed in the beam path. The thickness of the window is chosen such that it absorbs enough power to not damage the photodiode while transmitting enough power for a good signal to noise ratio. The knife edge is inserted at the focus of the beam to block half the light for the measurement of spatial fluctuations.

used to further reduce the power in the CO_2 laser beam to a value below the photodiode saturation value. CaF_2 absorbs light at 10.6 μm, the absorption coefficient is 3.6 cm^{-1} [119], so the thickness has to be chosen correctly as to reduce the beam power sufficiently and at the same time maintaining the best beam power to optimize the signal-to-noise ratio on the photodiode. A second ZnSe lens ($f = 1$ in) is used to collect the light and focus it onto the photodetector.

A reduced lifetime could not only stem from intensity noise, but also in position noise of the laser foces. To measure position noise the option of inserting a knife-edge at the focus of the laser beam, blocking half the beam power, is added. Any additional intensity fluctuations as compared to the case without the knife-edge then have to be due to changes in the position of the focus of the laser beam or to vibrations of the knife-edge itself.

Figure 8.13 shows the measured noise spectrum of the laser beam after passing through the CO_2 AOM (blue) and the background noise spectrum (green). Clearly there is noise around 1 kHz, close to the expected trapping frequency of the dipole trap. (Measuring the position noise spectrum only reveals fluctuations due to vibrations of the knife-edge, with is confirmed by taking the measurement with two knife-edges of

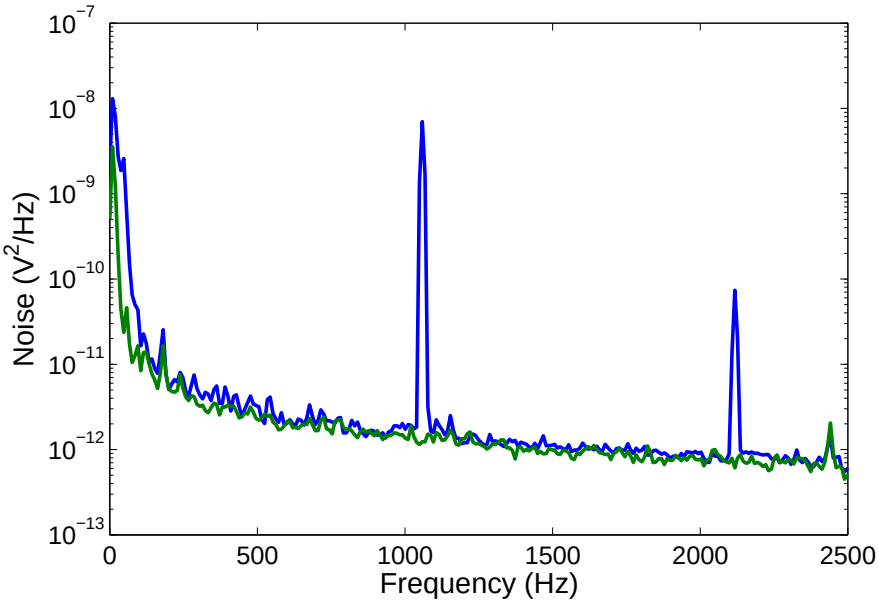

Figure 8.13: CO_2 laser intensity noise spectrum. Background noise is shown in green, the laser noise is shown in blue.

different mass and thus different oscillation frequencies.)

Three additional RF sources are then analyzed: an HP signal generator (HP 8657B), a Fluke signal generator (Fluke 6060B) and lastly a Wavetek generator (Wavetek 2405). The RF output of these sources around 40 MHz is determined by a a fast data acquisition card and subsequent data analysis using fast Fourier transform algorithms. The background noise level on these sources varies by orders of magnitude, the HP generator being the most quiet.

However, measuring the intensity noise in the laser beam reveals a noise peak around 1 kHz again. Clearly the source of the noise is thus not the RF source itself. The current hypothesis is that the reason for the noise peak is located within the CO_2 AOM amplifier box itself. The amplifier box (IntraAction GE-4050H), does not only house a high-power amplifier, but also an RF oscillator which can be used for driving the amplifier without needing an external RF source. This source oscillates not exactly at 40 MHz, but rather about 1 kHz above. Even though this oscillator is disconnected from the amplifier itself, which is directly driven by the external RF source, a small amount of this signal is most likely being picked up by the amplifier, leading to the noise

shown in figure 8.13. By matching the two frequencies it is thus possible to eliminate any intensity noise signal in the laser.

The reason for using an external RF source has to do with the thermal lensing effect of the CO_2 AOM mentioned in chapter 7.3.2. To avoid temporal changes to the lensing effect, the RF power to the AOM should be kept at a constant value. Rather than turning the AOM off completely when the CO_2 beam should be off, the driving frequency is switched to 50 MHz. This beam is blocked in a water-cool beam dump. In order to do this frequency switch, two separate RF sources are connected to an RF switch, and then combined on a power combiner prior to the CO_2 AOM amplifier. This setup is not possible with the internal frequency source of the CO_2 amplifier box. By changing the state of the RF switches, the driving frequency can be changed quickly from 40 to 50 MHz during the experimental sequence.

After the elimination of the intensity noise peak, the lifetime of the optical dipole trap increases to 27 seconds. This is the same number as the lifetime of the low-density MOT. This implies that the lifetime of the optical dipole trap is now limited by the background pressure inside the vacuum chamber.

8.6 Evaporative Cooling and Trapping Frequencies Measurement

The first stage of optical evaporation is free evaporation. To decrease thermalization times, the scattering length a is increased to approximately $300\,a_0$ by setting the Feshbach field to 300 G. At this magnetic field strength, the lifetime in the trap is reduced to 9.5 seconds. A decrease in the lifetime could have multiple reasons, one of them being heating of the atoms due to fluctuations in the magnetic field. To eliminate this as a cause for the reduced lifetime, the Feshbach field is increased further to 530 G, where the scattering length is again close to zero. The lifetime of atoms in the dipole trap then increases to 17 seconds, indicating that not noise, but rather free evaporation leads to the reduced lifetime at a field of 300 G.

Figure 8.14 shows the remaining number of atoms in the optical dipole trap as a function of free evaporation time at a magnetic field of 300 G. This figure shows an

initial fast atom loss, after which the atom number remains approximately constant. This is the behaviour one expects from free evaporation, where the evaporation stops once the temperature of the atoms is sufficiently reduced, and the tail of the thermal distribution no longer extends above the trap depth. After 700 ms of free evaporation the temperature of the ensemble is reduced to 58 μK.

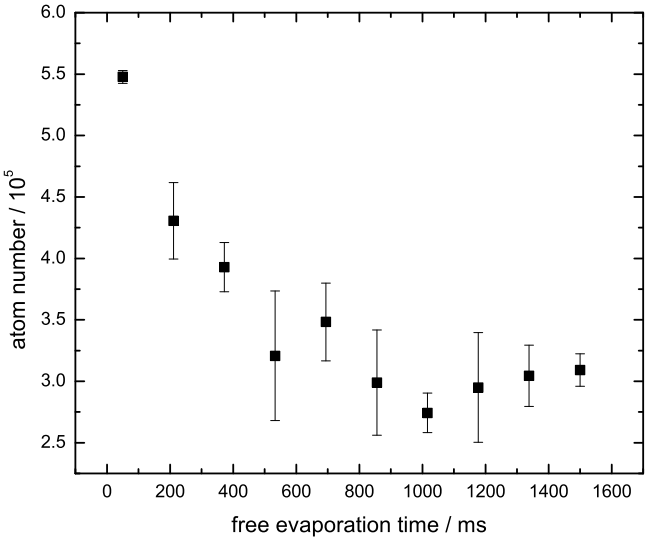

Figure 8.14: Atom number as a function of free evaporation time at a field of 300 G. Error bars indicate statistical uncertainties.

Once free evaporation levels off, around 700 ms, the trap depth is lowered to force evaporation to continue. The trap depth of the laser is lowered according to equation 2.36 with $\tau = 400$ ms and $\eta = 10.9$. Figure 8.15 shows the atom number and temperature as a function of forced evaporation time, again at $B = 300$ G. The decrease in temperature is a clear indication that evaporative cooling is reducing the temperature of this system.

However, the goal of evaporative cooling is not to reduce the temperature but to increase the phase-space density $\rho \propto N/(V \cdot T^{3/2})$ of the trapped atomic ensemble. Figure 8.16 shows the temperature as a function of atom number during the forced evaporative cooling sequence. The reduction in temperature is larger than the loss in atom number, and the evaporative cooling sequence therefore does increase the phase-space density.

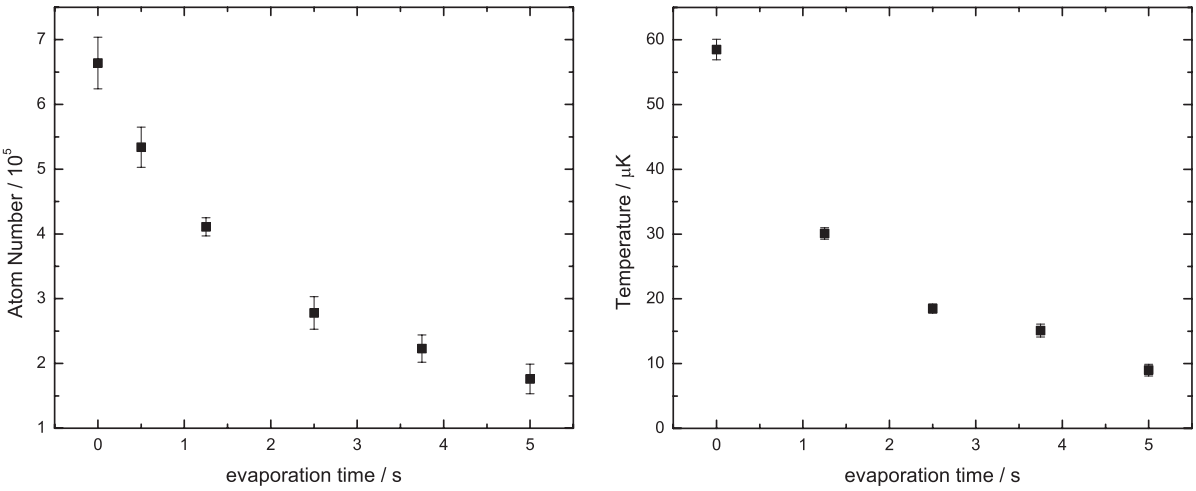

Figure 8.15: Atom number and temperature as a function of forced evaporation time at a field of 300 G. Error bars indicate statistical uncertainties.

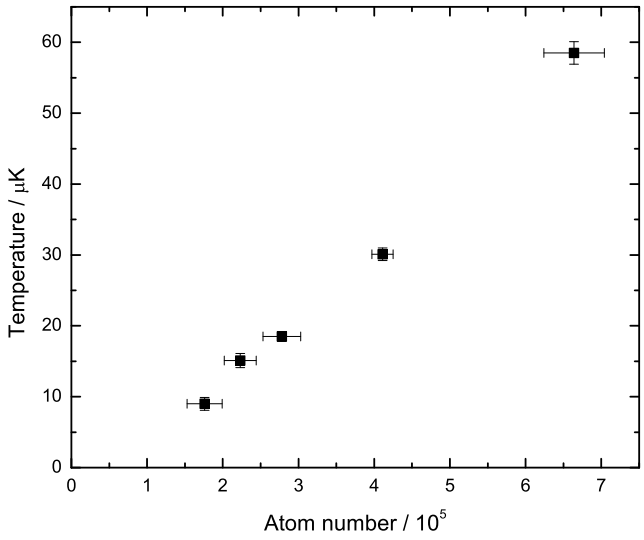

Figure 8.16: Temperature as a function of atom number at a field of 300 G. Error bars indicate statistical uncertainties.

Determining the trap frequencies of the optical dipole trap is important for being able to calculate the degeneracy factor T/T_F. The first method is to shake the optical dipole trap. This can be done by frequency modulating the AOM driving frequency. The focusing lens will translate the angular modulation to a transverse movement of the trap.

Modulations of the trapping potential heats the atoms, if the modulation frequency is close to the trap frequency.

To measure the trap frequency in the vertical direction, a cold atomic sample is produced by evaporating at 300 G for 500 ms and then increasing the trap depth to its maximum value again. The driving frequency of the AOM is then modulated using the RF frequency generator for the CO_2 AOM (HP8657B) and the trap is shaken for 1 second with a modulation depth of ± 20 kHz. Figure 8.17 shows resonant excitation at $f = 5.3$ kHz.

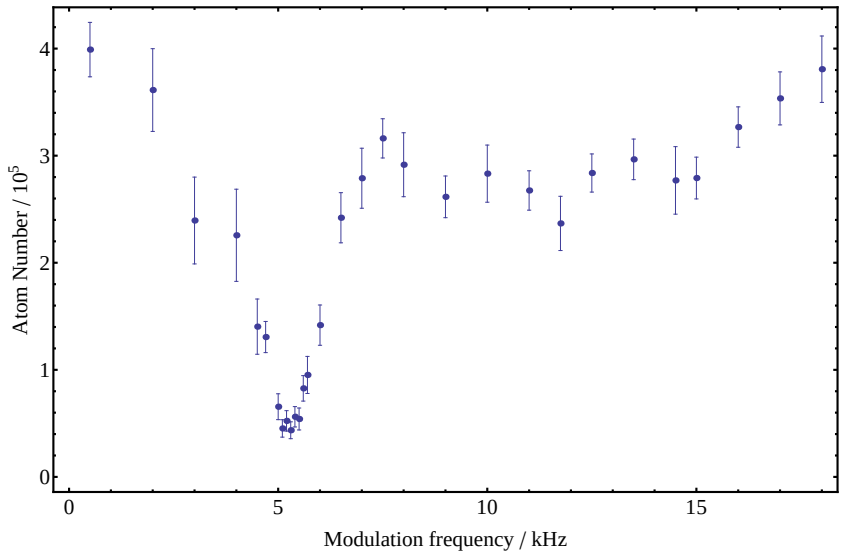

Figure 8.17: Atom number as a function of modulation frequency. The frequency in the AOM is modulated by ± 20 kHz causing a vertical shaking of the dipole trap. Error bars indicate statistical uncertainties.

Unfortunately modulating the frequency only excites the vertical oscillation. To measure the trapping frequency along the axis of the beam and in the horizontal direction, amplitude modulation of the trap depth is used. In this case, modulation at twice the trap frequency heats the atoms via parametric resonance.

The atomic ensemble is prepared using the same experimental sequence. The intensity of the CO_2 laser beam is then modulated by changing the RF amplitude going to the AOM by 20% (10%). Figure 8.18 shows the remaining atom number as a function of the modulation frequency. The resonances are located at 10.5 kHz, 7.0 kHz and

275 Hz. Using these values the beam waist of the CO_2 laser is estimated to be 54 μm vertically and 67 μm horizontally. The beam waists are most likely smaller than these values. Amplitude modulation causes the trapping frequencies to vary during the course of the experiments and the consequence of this variation is difficult to understand [109]. Measuring trap frequencies and beam waists using amplitude modulation is therefore only an estimate.

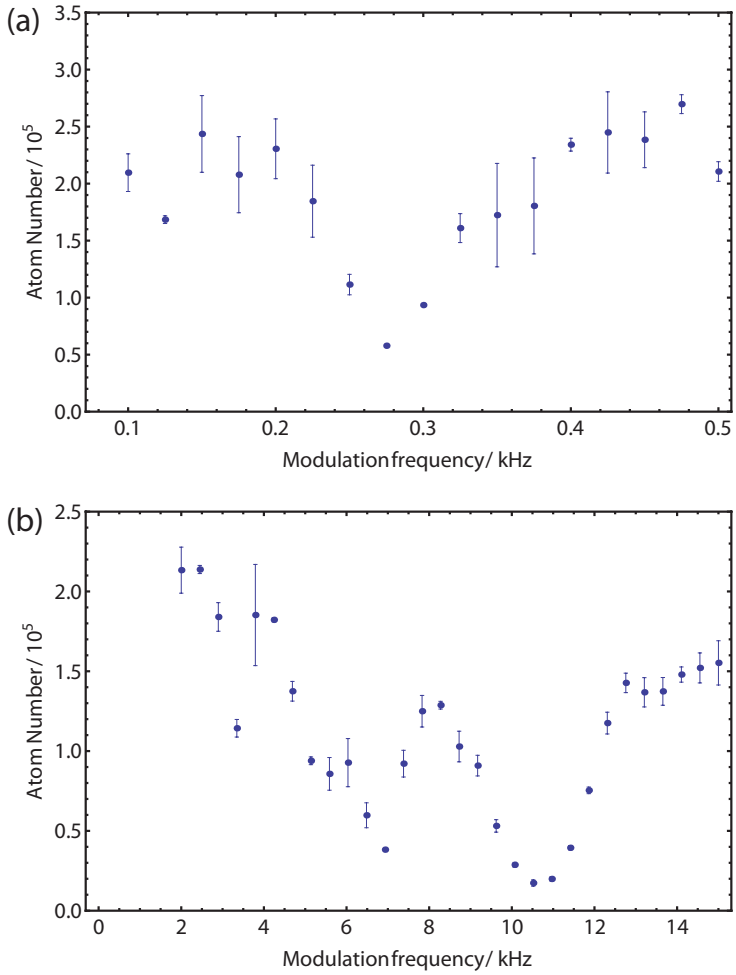

Figure 8.18: Atom number as a function of amplitude modulation frequency. The amplitude is modulated at the modulation frequency by 20% (a) or 10% (b). Error bars indicate statistical uncertainties.

8.7 Future Outlook

With the current progress towards generating a degenerate gas and the demonstrated ability to create a small dipole trap for laser culling, the experiment should be able to generate atomic Fock states of lithium atoms in the near future.

Evaporation until degeneracy is reached is work in progress. To reduce the evaporation time, evaporation will be done closer to the Feshbach resonance, in the 750 to 834 G range. However, close to resonance the scattering length is positive and molecules can be formed [30]. Evaporation to degeneracy will therefore be finished at 300 G, where the scattering length is negative.

Once degeneracy is verified, the objective and the other optics shown in figure 7.40 will be added to the experimental setup and lithium atoms can be loaded from the CO_2 optical dipole trap to the small YAG dipole trap to initialize the laser culling sequence. How to best load this small dipole trap is still an open question. Especially the timing of the turn on and the turn on speed will have to be determined, keeping in mind that excitations especially to the lowest energy levels have to be avoided. With the right combination of laser power, magnetic field gradient, offset magnetic field, and culling time Fock states of atoms can then be created.

Having achieved the milestone of Fock state production, many different experiments can be envisioned. The study of quantum entanglement on the single particle level using neutral atoms is one path to follow. Creating an entangled pair of atoms in the lithium system will involve splitting the 2-atom Fock state into two separate traps. This splitting can be done by "painting" a time-averaged potential of the traps with the use of an AOM. Changing the driving frequency of the AOM on time scales faster than the trapping frequencies will avoid heating of the atoms but instead they will experience the time-averaged potential. It has been shown that this method is indeed applicable to degenerate gases [120].

The generation of scalable quantum entanglement is the ultimate goal of the lithium experiment. Once the production of a Fock state in a single site and the splitting into separate wells are well understood, multiple sites can be implemented into the

system. Maybe the easiest way to achieve multiple sites is again to paint the laser culling dipole potential with the use of an AOM.

Having the ability of dynamically changing the location and number of sites provides great flexibility to the type of experiments that can be envisioned. Studying collisional entanglement is just one possibility among many [121–126].

Appendix

Appendix A

Magic Wavelength of Hydrogen

The concept of a magic wavelength is important for precision frequency measurements of optically trapped atoms. In general, an optical potential will introduce an AC-Stark shift of the energy levels, leading to a spatial dependence of the transition frequency within the trapped cloud, and limiting the precision achievable. Many new technologies rely on precision time; the Global Positioning System (GPS) is just one important example.

This section introduces the idea of a magic wavelength trap, and how this provides a unique environment for precision spectroscopy. Subsequently, the magic wavelength for hydrogen is determined theoretically.

A.1 Magic Wavelength

An optical clock using trapped neutral atoms is desirable for two main reasons: long interaction times and high short-term stability [127, 128]. Because trapped neutral atoms exhibit both qualities, they can potentiall provide a frequency standard superior to single-ion and atomic fountain clocks. This would be an important step towards new tests of fundamental physics and improved measurements of fundamental constants.

Chapter 2.6.2 showed that the shift of atomic energy levels of an atom in the presence of an external light field due to the AC-Stark effect is given by (compare equation 2.26)

$$\Delta E_{AC} = -\frac{1}{2\epsilon_0 c} Re(\alpha) I \tag{A.1}$$

$$= -\frac{1}{4\epsilon_0 \hbar c} \sum_k |\langle k|\vec{\mu}|j\rangle|^2 \left(\frac{1}{\omega_{kg} + \omega} + \frac{1}{\omega_{kg} - \omega} \right) I. \tag{A.2}$$

In general the polarizability, and thus the energy shift, is different for all atomic energy levels. It is thus possible for the ground and excited state to have opposite signs, and in general the energy shift of the two levels will not be identical.

The AC-Stark effect poses a number of challenges for spectroscopic measurements. Since the AC-Stark shift depends on the intensity of light, the transition frequency will vary inside the trap, leading to a broadening of the observed transition linewidth. In addition, the absolute value of the frequency will depend on the trapping laser intensity, and will be broadened by any intensity fluctuations in the trapping potential. If the polarizability has different signs for the two states involved in the transition, it is possible to drive an atom to an anti-trapped state, leading to trap loss.

The special wavelength at which the ground and excited state polarizabilities are identical is called the "magic" wavelength. At the magic wavelength the transition frequency is independent of the laser intensity, and broadening mechanisms are suppressed. It is possible to extend this concept and impose additional requirements, such as coincidence between the magnetic dipole or electric quadrupole interactions [129, 130]. For the purpose of this dissertation the analysis is restricted to the electric dipole moment. Magic wavelengths have been calculated and measured for a number of elements, mostly alkaline and alkaline earth elements [83, 131–135].

A.2 Calculations for Hydrogen

Hydrogen is the simplest atom in the periodic table of elements. Due to its simplicity it allows precise comparison between theory and experiment, and the spectroscopy of hydrogen has led to precise measurements of fundamental constants such as the Rydberg constant [136]. The spectroscopy of hydrogen and its isotopes is therefore of tremendous value to fundamental physics research.

Using equation A.1 the scalar polarizability of the $1s$ and $2s$ states of atomic hydrogen are calculated. The polarizability α is approximated using the leading terms in the sum. Figure A.1 shows the polarizability as a function of the wavelength when the first 12 transitions are included for the ground state polarizability, and the first 10

transitions for the excited state polarizability (data taken from [137]). At wavelengths where the $2s$ polarizability matches the $1s$ polarizability, a magic wavelength exists. In the range from 400 nm to 1 μm and above three distinct magic wavelengths exist. The broadest of these is located around 512.4 nm.

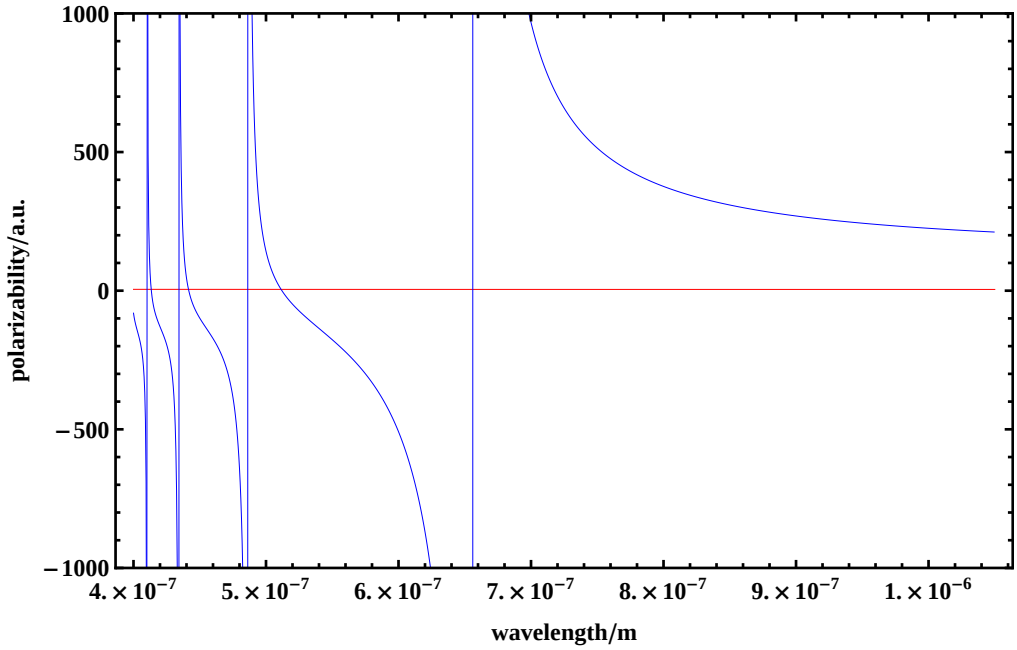

Figure A.1: Scalar polarizability of the $1s$ (red) and $2s$ (blue) states of atomic hydrogen, calculated using equation A.1.

The method outlined above is limited in precision by the number of states that are included in the sum. Fortunately, there are other approaches to calculating the scalar polarizability of hydrogenic atoms [138, 139]. A closed analytical expression for the scalar polarizability (in atomic units) is given by [138]

$$\alpha_{1s}(\omega) = -\frac{1}{\omega^2} - \sum_{m=1}^{2} \frac{512\,\nu_{1m}^9}{(\nu_{1m}^2-1)^2(\nu_{1m}+1)^8(\nu_{1m}-2)} \cdot {}_2F_1\left(4, 2-\nu_{1m}, 3-\nu_{1m}; \left(\frac{\nu_{1m}-1}{\nu_{1m}+1}\right)^2\right) \tag{A.3}$$

$$\alpha_{2s}(\omega) = -\frac{1}{\omega^2} - \sum_{m=1}^{2} \frac{2^{18}\,\nu_{2m}^9}{(\nu_{2m}^2+2)^7(\nu_{2m}-4)^3} \cdot {}_2F_1\left(4, 2-\nu_{2m}, 3-\nu_{2m}; \left(\frac{\nu_{2m}-2}{\nu_{2m}+2}\right)^2\right), \tag{A.4}$$

with

$$\nu_{11} = \frac{1}{\sqrt{-2(-\frac{1}{2}+\omega+i0)}} \tag{A.5}$$

$$\nu_{12} = \frac{1}{\sqrt{-2(-\frac{1}{2}-\omega)}} \tag{A.6}$$

$$\nu_{21} = \frac{1}{\sqrt{-2(-\frac{1}{8}+\omega+i0)}} \tag{A.7}$$

$$\nu_{22} = \frac{1}{\sqrt{-2(-\frac{1}{8}-\omega)}}, \tag{A.8}$$

and ${}_2F_1(a,b,c;x)$ being Gauss's hypergeometric function.

Using this formalism the magic wavelength is determined to be located around 514.4 nm.

Bibliography

[1] J.J. Thomson. Cathode rays. *Philosophical Magazine*, 44:293, 1897.

[2] E. Rutherford. The scattering of α and β particles by matter and the structure of the atom. *Philosophical Magazine*, 21:669, 1911.

[3] M. Planck. Ueber das Gesetz der Energieverteilung im Normalspectrum (on the law of distribution of energy in the normal spectrum). *Annalen der Physik*, 309:553, 1901.

[4] N. Bohr. On the constitution of atoms and molecules. *Philosophical Magazine*, 26:1, 1913.

[5] W.D. Phillips. Laser cooling and trapping of neutral atoms. Proposal to the Office of Naval Research, 1979.

[6] W.D. Phillips and H. Metcalf. Laser deceleration of an atomic beam. *Phys. Rev. Lett.*, 48:596, 1982.

[7] J.V. Prodan, W.D. Phillips, and H. Metcalf. Laser production of a very slow monoenergetic atomic beam. *Phys. Rev. Lett.*, 49:1149, 1982.

[8] S. Chu, L. Hollberg, J.E. Bjorkholm, A. Cable, and A. Ashkin. Three-dimensional viscous confinement and cooling of atoms by resonance radiation pressure. *Phys. Rev. Lett.*, 55:48, 1985.

[9] M.H. Anderson, J.R. Ensher, M.R. Matthews, C.E. Wieman, and E.A. Cornell. Observation of Bose-Einstein Condensation in a Dilute Atomic Vapor. *Science*, 269:198, 1995.

[10] K.B. Davis, M.-O. Mewes, M.R. Andrews, N.J. van Druten, D.S. Durfee, D.M. Kurn, and W. Ketterle. Bose-Einstein Condensation in a Gas of Sodium Atoms. *Phys. Rev. Lett.*, 75:3969, 1995.

[11] C.C. Bradley, C.A. Sackett, J.J. Tollett, and R.G. Hulet. Evidence of Bose-Einstein Condensation in an Atomic Gas with Attractive Interactions. *Phys. Rev. Lett.*, 75:1687, 1995.

[12] B. DeMarco and D.S. Jin. Onset of Fermi Degeneracy in a Trapped Atomic Gas. *Science*, 285:1703, 1999.

[13] B. DeMarco, S.B. Papp, and D.S. Jin. Pauli Blocking of Collisions in a Quantum Degenerate Atomic Fermi Gas. *Phys. Rev. Lett.*, 86:5409, 2001.

[14] A.G. Truscott, K.E. Strecker, W.I. McAlexander, G.B. Partridge, and R.G. Hulet. Observation of Fermi Pressure in a Gas of Trapped Atoms. *Science*, 291:2570, 2001.

[15] D.R. Lide (Ed.). *CRC Handbook of Chemistry and Physics*. CRC Press, Boca Raton, 79th edition, 1998.

[16] C.B. Alcock, V.P. Itkin, and M.K. Horrigan. Vapor pressure equations for the metallic elements: 298 2500 k. *Canadian Metallurgical Quarterly*, 23:309, 1984.

[17] D.A.Steck. Rubidium 87 D line data. steck.us/alkalidata/rubidium87numbers.pdf, September 2010.

[18] M.P. Bradley, J.V. Porto, S. Rainville, J.K. Thompson, and D.E. Pritchard. Penning trap measurements of the masses of ^{133}Cs, $^{87,85}Rb$, and ^{23}Na with uncertainties $\leq$0.2 ppb. *Phys. Rev. Lett.*, 83:4510, 1999.

[19] A.N. Nesmeyanov. *Vapour Pressure of the Elements*. Academic Press, New York, 1963.

[20] M.E. Gehm. Properties of ^{6}Li. physics.ncsu.edu/ jet/techdocs/pdf/ PropertiesOfLi.pdf, February 2003.

[21] I. Mills, T. Cvitas, K. Homann, N. Kallay, and K. Kuchitsu. *Quantities, Units, and Symbols in Physical Chemistry*. Blackwell Scientific Publishing, Oxford, 1988.

[22] C.J. Foot. *Atomic Physics*. Oxford University Press, New York, 2005.

[23] J.J. Sakurai. *Modern Quantum Mechanics*. Addison Wesley, Reading, 1994.

[24] D. Budker, D.F. Kimball, and D. DeMille. *Atomic Physics*. Oxford University Press, New York, 2004.

[25] B.H. Bransden and C.J. Joachain. *Physics of Atoms and Molecules*. Prentice Hall, Harlow, 2003.

[26] A.R. Edmonds. *Angular momentum in quantum mechanics*. Princeton University Press, Princeton, 1974.

[27] A.L. Migdall, J.V. Prodan, W.D. Phillips, T.H. Bergeman, and H.J. Metcalf. First observation of magnetically trapped neutral atoms. *Phys. Rev. Lett.*, 54:2596, 1985.

[28] K.M. O'Hara. *Optical Trapping and Evaporative Cooling of fermionic atoms*. PhD thesis, Duke University, 2000.

[29] H. Feshbach. A unified theory of nuclear reactions. *Ann. Phys.*, 5:337, 1958.

[30] C. Chin, R. Grimm, P.S. Julienne, and E. Tiesinga. Feshbach resonances in ultracold gases. *Rev. Mod. Phys.*, 82:1225, 2010.

[31] A.J. Moerdijk, B.J. Verhaar, and A. Axelsson. Resonances in ultracold collisions of ^{6}Li, ^{7}Li, and ^{23}Na. *Phys. Rev. A*, 51:4852, 1995.

[32] M. Houbiers, H.T.C. Stoof, W.I. McAlexander, and R.G. Hulet. Elastic and inelastic collisions of ^{6}Li atoms in magnetic and optical traps. *Phys. Rev. A*, 57:R1497, 1998.

[33] M. Bartenstein, A. Altmeyer, S. Riedl, R. Geursen, S. Jochim, C. Chin, J. Hecker Denschlag, R. Grimm, A. Simoni, E. Tiesinga, C.J. and Williams, and P.S. Julienne. Precise determination of ^{6}Li cold collision parameters by radio-frequency spectroscopy on weakly bound molecules. *Phys. Rev. Lett.*, 94:103201, 2005.

[34] T.B. Ottenstein. *Few-body physics in ultracold Fermi gases.* PhD thesis, University of Heidelberg, 2010.

[35] H.J. Metcalf, and P. van der Straten. *Laser cooling and trapping.* Springer, New York, 1999.

[36] R. Grimm, M. Weidemueller, and Y.B. Ovchinnikov. Optical dipole traps for neutral atoms. *Adv. At., Mol. and Opt. Phys.*, 42:95, 2000.

[37] E.L. Raab, M. Prentiss, A. Cable, S. Chu, and D.E. Pritchard. Trapping of Neutral Sodium Atoms with Radiation Pressure. *Phys. Rev. Lett.*, 59:2631, 1987.

[38] C.G. Townsend, N.H. Edwards, C.J. Cooper, K.P. Zetie, C.J. Foot, A.M. Steane, P. Szriftgiser, H. Perrin, and J. Dalibard. Phase-space density in the magneto-optical trap. *Phys. Rev. A*, 52:1423, 1995.

[39] S.R. Granade, M.E. Gehm, K.M. O'Hara, and J.E. Thomas. All-Optical Production of a Degenerate Fermi Gas. *Phys. Rev. Lett.*, 88:120405, 2002.

[40] K.M. O'Hara, M.E. Gehm, S.R. Granade, and J.E. Thomas. Scaling laws for evaporative cooling in time-dependent optical traps. *Phys. Rev. A*, 64:051403, 2001.

[41] L. Luo, B. Clancy, J. Joseph, J. Kinast, A. Turlapov, and J.E. Thomas. Evaporative cooling of unitary Fermi gas mixtures in optical traps. *New Jour. Phys.*, 8:213, 2006.

[42] K. Huang. *Statistical Mechanics.* John Wiley and Sons, 1987.

[43] C.J. Pethick and H. Smith. *Bose-Einstein Condensation in Dilute Gases.* Cambridge University Press, Cambridge, 2002.

[44] W. Demtroeder. *Laser Spectroscopy: basic concepts and instrumentation.* Springer, Berlin, 2003.

[45] F. Riehle. *Frequency Standards.* Wiley-VCH, Weinheim, 2004.

[46] E.D. Black. An introduction to Pound-Drever-Hall laser frequency stabilization. *Am. J. Phys.*, 69:79, 2001.

[47] G.C. Bjorklund. Frequency-modulation spectroscopy: a new method for measuring weak absorptions and dispersions. *Optics Letters*, 5:15, 1980.

[48] G.C. Bjorklund, M.D. Levenson, W. Lenth, and C. Ortiz. Frequency modulation (fm) spectroscopy. *Appl. Phys. B*, 32:145, 1983.

[49] R.W.P. Drever, J.L. Hall, F.V. Kowalski, J. Hough, G.M. Ford, A.J. Munley, and H.Ward. Laser phase and frequency stabilization using an optical resonator. *Appl. Phys. B*, 31:97, 1983.

[50] E.D. Black. Notes on the Pound-Drever-Hall technique. Technical Note LIGO-T980045-00-D, 1998.

[51] W. Ketterle, D.S. Durfee, and D.M. Stamper-Kurn. Making, probing and understanding Bose-Einstein condensates. *Course CXL (IOS Press Amsterdam), Proceedings of the International School of Physics Enrico Fermi*, 1999.

[52] I.D. Setija, H.G.C. Werij, O.J. Luiten, M.W. Reynolds, T.W. Hijmans, and J.T.M. Walraven. Optical cooling of atomic hydrogen in a magnetic trap. *Phys. Rev. Lett.*, 70:2257, 1993.

[53] M.G. Raizen, A.M. Dudarev, Q. Niu, and N.J. Fisch. Compression of Atomic Phase Space Using an Asymmetric One-Way Barrier. *Phys. Rev. Lett.*, 94:053003, 2005.

[54] A. Ruschhaupt and J.G. Muga. Atom diode: A laser device for a unidirectional transmission of ground-state atoms. *Phys. Rev. A*, 70:061604, 2004.

[55] A. Ruschhaupt, J.G. Muga, and M.G. Raizen. Improvement by laser quenching of an 'atom diode': a one-way barrier for ultra-cold atoms. *J. Phys. B: At. Mol. Opt. Phys.*, 39:L133, 2006.

[56] A.M. Dudarev, M. Marder, Q. Niu, N.J. Fisch, and M.G. Raizen. Statistical mechanics of an optical phase compressor. *Europhys. Lett.*, 70:761, 2005.

[57] J.J. Thorn, E.A. Schoene, T. Li, and D.A. Steck. Experimental Realization of an Optical One-Way Barrier for Neutral Atoms. *Phys. Rev. Lett.*, 100:240407, 2008.

[58] J.J. Thorn, E.A. Schoene, T. Li, and D.A. Steck. Dynamics of cold atoms crossing a one-way barrier. *Phys. Rev. A*, 79:063402, 2009.

[59] E.A. Schoene, J.J. Thorn, and D.A. Steck. Cooling atoms with a moving one-way barrier. *Phys. Rev. A*, 82:023419, 2010.

[60] G.N. Price, S.T. Bannerman, E. Narevicius, and M.G. Raizen. Single-photon atomic cooling. *Laser Physics*, 17:1, 2007.

[61] G.N. Price, S.T. Bannerman, K. Viering, E. Narevicius, and M.G. Raizen. Single-Photon Atomic Cooling. *Phys. Rev. Lett.*, 100:093004, 2008.

[62] C.G. Knott. *Life and Scientific Work of Peter Gutherie Tait.* Cambridge University Press, Cambridge, 1911.

[63] L. Szilard. On the decrease of entropy in a thermodynamic system by the intervention of intelligent beings. (In H.S. Leff and A.F. Rex, ed.). *Maxwell's Demon 2: Entropy, Classical and Quantum Information.* Institute of Physics, Philadelphia, 2003.

[64] A. Ruschhaupt, J.G. Muga, and M.G. Raizen. One-photon atomic cooling with an optical Maxwell demon valve. *J. Phys. B: At. Mol. Opt. Phys.*, 39:3833, 2006.

[65] S. Choi, B. Sundaram, and M.G. Raizen. Single-photon cooling in a wedge billiard. *Phys. Rev. A*, 82:033415, 2010.

[66] V.P. Singh and A. Ruschhaupt. Optimizing Single-Photon Cooling. *arXiv: 1204.0352v1*, 2012.

[67] J.L. Hanssen. *Controlling Atomic Motion: From Single Particle Classical Mechanics to Many Body Quantum Dynamics*. PhD thesis, The University of Texas at Austin, 2004.

[68] T.P. Meyrath. *Experiments with Bose Einstein Condensation in an optical box*. PhD thesis, The University of Texas at Austin, 2005.

[69] C.-S. Chuu. *Direct Study of Quantum Statistics in a Degenerate Bose Gas*. PhD thesis, The University of Texas at Austin, 2006.

[70] G.N. Price. *Single-Photon Atomic Cooling*. PhD thesis, The University of Texas at Austin, 2008.

[71] W. Wohlleben, F. Chevy, K. Madison, and J. Dalibard. An atom faucet. *Eur. Phys. J. D*, 15:237, 2001.

[72] C.E. Wieman and L. Hollberg. Using diode lasers for atomic physics. *Rev. Sci. Inst.*, 62:1, 1991.

[73] D.A. Steck. *Quantum Chaos, Transport, and Decoherence in Atom Optics*. PhD thesis, The University of Texas at Austin, 2001.

[74] A.E. Siegman. *Lasers*. University Science Books, Sausalito, 1986.

[75] W. Alt. An objective lens for efficient fluorescence detection of single atoms. *Optik*, 113:142, 2002.

[76] S.T. Bannerman, G.N. Price, K. Viering, and M.G. Raizen. Single-photon cooling at the limit of trap dynamics: Maxwell's demon near maximum efficiency. *New Journal of Physics*, 11:063044, 2009.

[77] E. Narevicius, A. Libson, C.G. Parthey, I. Chavez, J. Narevicius, U. Even, and M.G. Raizen. Stopping Supersonic Beams with a Series of Pulsed Electromagnetic Coils: An Atomic Coilgun. *Phys. Rev. Lett.*, 100:093003, 2008.

[78] E. Narevicius, A. Libson, C.G. Parthey, I. Chavez, J. Narevicius, U. Even, and M.G. Raizen. Stopping supersonic oxygen with a series of pulsed electromagnetic coils: A molecular coilgun. *Phys. Rev. A*, 77:051401, 2008.

[79] E. Lavert-Ofir, S. Gersten, A.B. Henson, I. Shani, L. David, J. Narevicius, and E. Narevicius. A moving magnetic trap decelerator: a new source of cold atoms and molecules. *New Journal of Physics*, 13:103030, 2011.

[80] A. Libson, S.T. Bannerman, R.J. Clark, T.R. Mazur, and M.G. Raizen. The atomic coilgun and single-photon cooling. *Hyperfine Interactions*, 2012. 10.1007/s10751-012-0586-7.

[81] C.K. Hong and L. Mandel. Experimental realization of a localized one-photon state. *Phys. Rev. Lett.*, 56:58, 1986.

[82] B.T.H. Varcoe, S. Brattke, M. Weidinger, and H. Walther. Preparing pure photon number states of the radiation field. *Nature*, 403:743, 2000.

[83] J. McKeever, J.R. Buck, A.D. Boozer, A. Kuzmich, H.-C. Naegerl, D.M. Stamper-Kurn, and H.J. Kimble. State-Insensitive Cooling and Trapping of Single Atoms in an Optical Cavity. *Phys. Rev. Lett.*, 90:133602, 2003.

[84] C. Brunel, B. Lounis, P. Tamarat, and M. Orrit. Triggered Source of Single Photons based on Controlled Single Molecule Fluorescence. *Phys. Rev. Lett.*, 83:2722, 1999.

[85] A.I. Lvovsky, H. Hansen, T. Aichele, O. Benson, J. Mlynek, and S. Schiller. Quantum State Reconstruction of the Single-Photon Fock State. *Phys. Rev. Lett.*, 87:050402, 2001.

[86] P. Bertet, A. Auffeves, P. Maioli, S. Osnaghi, T. Meunier, M. Brune, J.M. Raimond, and S. Haroche. Direct Measurement of the Wigner Function of a One-Photon Fock State in a Cavity. *Phys. Rev. Lett.*, 89:200402, 2002.

[87] W. Tittel, J. Brendel, H. Zbinden, and N. Gisin. Quantum Cryptography Using Entangled Photons in Energy-Time Bell States. *Phys. Rev. Lett.*, 84:4737, 2000.

[88] D.S. Naik, C.G. Peterson, A.G. White, A.J. Berglund, and P.G. Kwiat. Entangled State Quantum Cryptography: Eavesdropping on the Ekert Protocol. *Phys. Rev. Lett.*, 84:4733, 2000.

[89] Z. Hu and H.J. Kimble. Observation of a single atom in a magneto-optical trap. *Opt. Lett.*, 19:1888, 1994.

[90] D. Frese, B. Ueberholz, S. Kuhr, W. Alt, D. Schrader, V. Gomer, and D. Meschede. Single Atoms in an Optical Dipole Trap: Towards a Deterministic Source of Cold Atoms. *Phys. Rev. Lett.*, 85:3777, 2000.

[91] C.J. Hood, T.W. Lynn, A.C. Doherty, A.S. Parkins, and H.J. Kimble. The Atom-Cavity Microscope: Single Atoms Bound in Orbit by Single Photons. *Science*, 287:1447, 2000.

[92] N. Schlosser, G. Raymond, I. Protsenko, and P. Grangier. Sub-poissonian loading of single atoms in a macroscopic dipole trap. *Nature*, 411:1024, 2001.

[93] S. Kuhr, W. Alt, D. Schrader, M. Mueller, V. Gomer, and D. Meschede. Deterministic Delivery of a Single Atom. *Science*, 293:278, 2001.

[94] R.B. Diener, B. Wu, M.G. Raizen, and Q. Niu. Quantum Tweezer for Atoms. *Phys. Rev. Lett.*, 89:070401, 2002.

[95] B. Mohring, M. Bienert, F. Haug, G. Morigi, W.P. Schleich, and M.G. Raizen. Extracting atoms on demand with lasers. *Phys. Rev. A*, 71:053601, 2005.

[96] C.-S. Chuu, F. Schreck, T.P. Meyrath, J.L. Hanssen, G.N. Price, and M.G. Raizen. Direct observation of sub-poissonian number statistics in a degenerate bose gas. *Phys. Rev. Lett.*, 95:260403, 2005.

[97] F. Serwane, G. Zuern, T. Lompe, T.B. Ottenstein, A.N. Wenz, and S. Jochim. Deterministic Preparation of a Tunable Few-Fermion System. *Science*, 332:336, 2011.

[98] A.M. Dudarev, M.G. Raizen, and Q. Niu. Quantum Many-Body Culling: Production of a Definite Number of Ground-State Atoms in a Bose-Einstein Condensate. *Phys. Rev. Lett.*, 98:063001, 2007.

[99] A. del Campo and J.G. Muga. Atom Fock-state preparation by trap reduction. *Phys. Rev. A*, 78:023412, 2008.

[100] M. Pons, A. del Campo, J.G. Muga, and M.G. Raizen. Preparation of atomic Fock states by trap reduction. *Phys. Rev. A*, 79:033629, 2009.

[101] D. Sokolovski, M. Pons, A. del Campo, and J.G. Muga. Atomic Fock states by gradual trap reduction: From sudden to adiabatic limits. *Phys. Rev. A*, 83:013402, 2011.

[102] M.G. Raizen, S.-P. Wan, C. Zhang, and Q. Niu. Ultrahigh-fidelity qubits for quantum computing. *Phys. Rev. A*, 80:030302, 2009.

[103] S. Wan. *Atomic Fock States and Quantum Computing.* PhD thesis, The University of Texas at Austin, 2009.

[104] J. Kinast, A. Turlapov, J.E. Thomas, Q. Chen, J. Stajic, and K. Levin. Heat Capacity of a Strongly Interacting Fermi Gas. *Science*, 25:1296, 2005.

[105] W. Li, G.B. Partridge, Y.A. Liao, and R.G. Hulet. Pairing of a trapped Fermi gas with unequal spin populations. *Nuclear Physics A*, 790:88c, 2007.

[106] S.-P. Wan, M.G. Raizen, and Q. Niu. Calculation of atomic number states: a Bethe ansatz approach. *J. Phys. B: At. Mol. Opt. Phys.*, 42:195506, 2009.

[107] U. Schuenemann, H. Engler, R. Grimm, M. Weidemueller, and M. Zielonkowski. Simple scheme for tunable frequency offset locking of two lasers. *Rev. of Sci. Instr.*, 70:242, 1999.

[108] F. Schreck. iqoqi006.uibk.ac.at/users/c704250.

[109] M.E. Gehm. *Preparation of an optically-trapped degenerate Fermi gas of 6Li: finding the route to degeneracy.* PhD thesis, Duke University, 2003.

[110] J.W. Goodman. *Introduction to Fourier Optics*. McGraw-Hill, New York, 1996.

[111] K.M. O'Hara, S.L. Hemmer, M.E. Gehm, S.R. Granade, and J.E. Thomas. Observation of a Strongly Interacting Degenerate Fermi Gas of Atoms. *Science*, 298:5601, 2002.

[112] R. Dumke, M. Johanning, E. Gomez, J. D. Weinstein, K. M. Jones, and P.D. Lett. All-optical generation and photoassociative probing of sodium Bose-Einstein condensates. *New J. Phys.*, 8:64, 2006.

[113] M.D. Barrett, J.A. Sauer, and M.S. Chapman. All-optical formation of an atomic Bose-Einstein condensate. *Phys. Rev. Lett.*, 87:010404, 2001.

[114] G. Cennini, G. Ritt, C. Geckeler, and M. Weitz. Bose-Einstein condensation in a CO_2-laser optical dipole trap. *Appl. Phys. B: Lasers Opt.*, 77:773, 2003.

[115] G. Cennini, G. Ritt, C. Geckeler, and M. Weitz. All-Optical Realization of an Atom Laser. *Phys. Rev. Lett.*, 91:240408, 2003.

[116] T. Weber, J. Herbig, M. Mark, H.-C. Naegerl, and R. Grimm. Bose-Einstein condensation of Cesium. *Science*, 299:232, 2003.

[117] T. Takekoshi, B.M. Patterson, and R.J. Knize. Observation of Optically Trapped Cold Cesium Molecules. *Phys. Rev. Lett.*, 81:5105, 1998.

[118] K.M. O'Hara, S.R. Granade, M.E. Gehm, T.A. Savard, S. Bali, C. Freed, and J.E. Thomas. Ultrastable CO_2 Laser Trapping of Lithium Fermions. *Phys. Rev. Lett.*, 82:4204, 1999.

[119] A. Hordvik and H. Schlossberg. Photoacoustic technique for determining optical absorption coefficients in solids. *Appl. Opt.*, 16:101, 1977.

[120] K. Henderson, C. Ryu, C. MacCormick, and M.G. Boshier. Experimental demonstration of painting arbitrary and dynamic potentials for Bose-Einstein condensates. *New Jour. Phys.*, 11:043030, 2009.

[121] D. Jaksch, H.-J. Briegel, J.I. Cirac, C.W. Gardiner, and P. Zoller. Entanglement of atoms via cold controlled collisions. *Phys. Rev. Lett.*, 82:1975, 1999.

[122] D. Jaksch, J.I. Cirac, P. Zoller, S.L. Rolston, R. Cote, and M.D. Lukin. Fast Quantum Gates for Neutral Atoms. *Phys. Rev. Lett.*, 85:2208, 2000.

[123] G.K. Brennen, C.M. Caves, P.S. Jessen, I.H. Deutsch. Quantum Logic Gates in Optical Lattices. *Phys. Rev. Lett.*, 82:1060, 1999.

[124] L.You and M.S. Chapman. Quantum entanglement using trapped atomic spins. *Phys. Rev. A*, 62:052302, 2000.

[125] M.D. Lukin and P.R. Hemmer. Quantum Entanglement via Optical Control of Atom-Atom Interactions. *Phys. Rev. Lett.*, 84:2818, 2000.

[126] J. Mompart, K. Eckert, W. Ertmer, G. Birkl, and M. Lewenstein. Quantum Computing with Spatially Delocalized Qubits. *Phys. Rev. Lett.*, 90:147901, 2003.

[127] H. Katori, M. Takamoto, V.G. Pal'chikov, and V.D. Ovsiannikov. Ultrastable Optical Clock with Neutral Atoms in an Engineered Light Shift Trap. *Phys. Rev. Lett.*, 91:173005, 2003.

[128] M. Takamoto, F.-L. Hong, R. Higashi, and H. Katori. An optical lattice clock. *Nature*, 435:03541, 2005.

[129] H. Katori, K. Hashiguchi, E.Y. Il'inova, and V.D. Ovsiannikov. Magic Wavelength to Make Optical Lattice Clocks Insensitive to Atomic Motion. *Phys. Rev. Lett.*, 103:153004, 2009.

[130] A. Brusch, R. Le Targat, X. Baillard, M. Fouche, and P. Lemonde. Hyperpolarizability Effects in a Sr Optical Lattice Clock. *Phys. Rev. Lett.*, 96:103003, 2006.

[131] M. Takamoto and H. Katori. Spectroscopy of the $^1S_0$-$^3P_0$ Clock Transition of ^{87}Sr in an Optical Lattice. *Phys. Rev. Lett.*, 91:223001, 2003.

[132] C. Degenhardt, H. Stoehr, U. Sterr, F. Riehle, and C. Lisdat. Wavelength-dependent ac Stark shift of the $^1S_0$-$^3P_1$ transition at 657 nm in Ca. *Phys. Rev. A*, 70:023414, 2004.

[133] B. Arora, M.S. Safronova, and C.W. Clark. Magic wavelengths for the *np*-*ns* transitions in alkali-metal atoms. *Phys. Rev. A*, 76:052509, 2007.

[134] N. Lundblad, M. Schlosser, and J.V. Porto. Experimental observation of magic-wavelength behavior of ^{87}Rb atoms in an optical lattice. *Phys. Rev. A*, 81:031611, 2010.

[135] U. Dammalapati, B. Santra, and L. Willmann. Light shifts and magic wavelengths for heavy alkaline earth elements: Ba and Ra. *J. Phys. B: At. Mol. Opt. Phys.*, 45:025001, 2012.

[136] F. Biraben, et al. Precision spectroscopy of atomic hydrogen. In: S.G. Karshenboim, F.S. Pavone, G.F. Bassani, M. Inguscio, T.W. Haensch (eds.) The Hydrogen Atom: Precision Physics of Simple Atomic Systems. Lecture Notes in Physics, vol. 570, p. 17, Springer, Berlin 2001.

[137] O. Jitrik, and C.F. Bunge. Transition Probabilities for Hydrogen-Like Atoms. *J. Phys. Chem. Ref. Data*, 33:1059, 2004.

[138] V. Yakhontov and K. Jungmann. Light-shift calculation in the ns-states of hydrogenic systems. *Z. Phys. D*, 38:141, 1996.

[139] A.Z. Tang and F.T. Chan. Dynamic multipole polarizability of atomic hydrogen. *Phys. Rev. A*, 33:3671, 1986.